Shallow Neural Networks and High-Density Electromyography for Proportional Control of Hand Kinematic State: Applications in Healthy Subjects and Upper-Limb Impaired Patients

Giovanni Rolandino

St Edmund Hall

University of Oxford

A thesis submitted for the degree of

Doctor of Philosophy

Trinity 2025

To my parents
for any possible reason

„Zwar weiß ich viel, doch möcht' ich alles wissen."

"Much do I know, but to know all is my ambition."

— Wagner, *Faust I* by Johann Wolfgang von Goethe

Acknowledgements

The quote above, taken from the first volume of Faust, is not spoken by the eponymous character but by one of his students, Wagner, who represents what learning should not become: the relentless accumulation of knowledge in pursuit of completeness. This quote holds particular meaning for me because it encapsulates one of the most valuable insights gained through the doctoral journey, or indeed, any educational path: it is impossible to know everything. This seemingly trivial realisation may appear a modest return on over two decades of study, yet its implications are profound: it is not necessary to know everything. A doctoral journey teaches that progress arises from deep specialisation in a narrow field, leading, if all goes well, to a modest advancement. Knowledge does not grow by mastering everything at once, but rather through countless individual contributions, each extending human understanding in multiple directions. The sum of these small, dedicated efforts is what allows knowledge to evolve and expand.

This brings me to a second, perhaps even more important, lesson I carry with me from four years in Oxford, and from all the years of study preceding them, is that no achievement is ever truly individual. Nothing is accomplished without the support of those around us. With this awareness, I would like to dedicate the following lines to the people who made this personal milestone possible.

I would like to express my heartfelt gratitude to my supervisors, Prof. James FitzGerald, Prof. Brian Andrews, and Dr. Taian Martins, for their unwavering support throughout these four and a half years. By giving me the opportunity to pursue a research project so personally meaningful, allowing me the freedom to shape it according to my own ideas, and offering continuous guidance to help me grow, they made this endeavour possible, first by enabling it, and ultimately by contributing to its success.

This research would not have been possible without the deep and sustained collaboration with members of my own research group as well as with colleagues from other institutions, both in the UK and abroad. I am especially grateful to everyone at the Oxford Neural Interfacing Group for their invaluable advice and support throughout my doctoral studies. Internal collaborations within Oxford, particularly with Oxford Functional Neurosurgery and the Oxford Robotics Institute, were instrumental in completing much of the work presented in this thesis. In this regard,

I wish to extend my special thanks to Prof. Alex Green, Mr. Martin Gillies, and Dr. Ioannis Havoutis, along with my deep appreciation to all members of the two groups.

A special mention goes to the entire LISiN group at Politecnico di Torino. At the very beginning of my project, they welcomed me generously and provided everything I needed to begin shaping my research. Without our collaboration, this project would have taken a very different form. In addition to Dr. Martins, my supervisor, I am particularly grateful to Prof. Marco Gazzoni, Dr. Giacinto Luigi Cerone, and Dr. Alberto Botter for their constant guidance, unwavering support, and warm hospitality.

As my doctoral journey began with a collaboration, it felt fitting that it should conclude with one. I would like to express my sincere thanks to Prof. Alberto Cliquet Jr. and all members of the Departments of Orthopaedics, Rheumatology, and Traumatology at UNICAMP. Thank you for offering me the opportunity to finish my studies with such a fascinating and enriching experience, and for your generous support throughout my work.

Last, but by no means least, a heartfelt thank you to my truly invaluable students and co-authors: Marco, Giuseppe, Chiara, Leonardo, and Vinicius. Your constant support during the long days in the lab, and the privilege of working alongside such bright and dedicated individuals, remain among the most treasured aspects of my entire doctoral experience.

My DPhil was, thankfully, not spent entirely in the hospital or in a lab. These four years have been the most rewarding experience of a lifetime, and I would like to spend many words thanking the people who, beyond my colleagues and collaborators, made it all possible.

First and foremost, I would like to thank my dearest mum, dad, and sister. By supporting me in my studies throughout my whole life up to now, they have given me the greatest gift a son could wish for. I truly could not have hoped for a better family, and everything this path has been, and whatever may come of it, is your merit as much as it is mine.

At this point, it is impossible to establish a fair order in which to thank every person who made these four years so special, rewarding, and memorable. A chronological order of appearance might be the best option. First, my friends from Italy: as exciting and fulfilling as moving to a new country can be, it is only made easier when one's roots run deep. Despite my continuous absence from Milan, you never missed a chance to remind me that, no matter how far I was, I always had a place to return to.

Next, all of my friends in London. While mostly overlapping with the previous group, I feel these friends deserve a special mention for their continued, at times weekly, friendship and hospitality. Even more so, I am grateful to those adventurous enough to come and visit me in Oxford.

Following them, in order of appearance, are my flatmates of four years. From Norham Gardens to the smaller cohort in Cowley Road, none of this would have been as pleasant or as fun without so many people waiting for me at home each evening. Among them, I found some of my deepest and truest friendships, and I will carry them with me forever.

Next, my great passion: St Edmund Hall and its Middle Common Room. I would like to thank both the institution itself and every member of the MCR for welcoming me as one of their own and for ensuring that I could truly call Oxford my home. I am especially grateful to everyone who served with me on the MCR committee, for offering me three rewarding years of helping to shape something greater than myself.

No Oxford experience would be complete without rowing. I would like to thank the St Edmund Hall Boat Club for providing a much-needed distraction from long days of work, and for introducing me to friends I hope to keep for a lifetime.

These four years in Oxford have been life-changing and inspiring, and I wish to thank all those, casual encounters and colleagues alike, who may not be listed above but who certainly made a difference along the way.

I would also like to thank the team at the Creative Destruction Lab, both in Berlin and Oxford, for giving me the opportunity to support myself during my studies and for offering the promise of an exciting path beyond them.

Finally, I would like to thank Aimée, who, during this final period of writing, has been a constant and invaluable source of support, both practical and emotional. She has made this past year truly unforgettable.

Abstract

Upper limb impairments significantly compromise functional independence and quality of life for individuals, yet current assistive technologies often fail to meet expectations of users for intuitive, effective control. This thesis addresses this gap through the development of the RPC-Net/HDE-Array system, a unified platform combining High-Density surface Electromyography (HD-sEMG) with a physiologically inspired regression-based neural controller. The system includes a dry-electrode, circumferentially distributed bracelet (HDE-Array) designed for user-friendly signal acquisition, and RPC-Net, a recursive, shallow neural network that decodes HD-sEMG into online, multi-degree-of-freedom (DoF) hand kinematics. Six experimental studies validate the accuracy of the system, its robustness to electrode variability, and its usability by both able-bodied and tetraplegic participants. Findings demonstrate that the platform matches or exceeds state-of-the-art decoding performance, maintains stability under non-ideal conditions, and enables effective real-time control using both forearm and neck muscles. Novel contributions include recursive signal integration, PCA-driven dimensionality reduction, and the demonstration of neck-based control for inclusive rehabilitation. The thesis provides open-source code and datasets to support reproducibility and outlines pathways for future clinical deployment, including integration with prosthetic and FES devices. Collectively, this work establishes a viable, user-centred control interface for upper-limb rehabilitation, bridging the gap between laboratory-grade systems and practical, real-world applications.

Contents

List of Figures **xix**

List of Tables **xxi**

1 State of the Art **1**

1.1 Anatomy and Kinematic Models of the Upper Limb and Neck . . . 2
1.1.1 Overview of the Upper Limb . . . 2
1.1.2 Overview of the Neck . . . 7
1.1.3 Kinematic Models . . . 11
1.1.4 Summary . . . 13
1.2 Epidemiology and Global Burden of Upper-Limb Impairment . . . 14
1.2.1 Musculoskeletal causes . . . 14
1.2.2 Nervous System . . . 16
1.2.3 Summary . . . 19
1.3 Needs of Upper Limb Rehabilitation Device Users . . . 20
1.3.1 Amputation . . . 20
1.3.2 Non-amputation loss of function . . . 24
1.3.3 Summary . . . 28
1.4 Upper Limb Prosthetic Devices . . . 29
1.4.1 Passive (Cosmetic) Upper Limb Prosthetic Devices . . . 30
1.4.2 Body-Powered Prosthetic Devices . . . 31
1.4.3 Active Prosthetic Devices . . . 31
1.4.4 Summary . . . 34
1.5 Non-amputation rehabilitation solutions . . . 35
1.5.1 Mechanical Assistive Devices . . . 35
1.5.2 Electrophysiological Interventions . . . 37
1.5.3 Summary . . . 39
1.6 Biosignal Interfaces for Intent Detection in Upper-Limb Devices . . . 40
1.6.1 Central Nervous System Signals . . . 40
1.6.2 Peripheral Nervous System Signals . . . 42
1.6.3 Summary . . . 44
1.7 Electromyography (EMG): Principles and Instrumentation . . . 44

1.7.1 Muscle and Motor-Unit Physiology 45
1.7.2 Origin of the Electromyographic Signal 46
1.7.3 Recording Modalities 46
1.7.4 Signal Properties and Interference 48
1.7.5 Electrode Technologies and Interface Models 48
1.7.6 Summary 50
1.8 Developments in Machine Learning 51
1.8.1 Neural Networks 51
1.8.2 Classical Machine Learning Methods 55
1.8.3 Relevance to Electromyography 56
1.9 Machine Learning applications in EMG-Based Control 57
1.9.1 Pattern Recognition 57
1.9.2 Classification 58
1.9.3 Regression 58
1.9.4 Current Challenges 60
1.10 Summary 61

2 Introduction **63**
2.1 Problem Statement and Identified Gaps 63
2.2 Proposed Approach 65
2.2.1 Overview 65
2.2.2 Operational Definitions: Online and Real-time 65
2.2.3 Signal Source: High-Density Surface EMG 66
2.2.4 Neural Architecture: Shallow Regression Networks 67
2.2.5 Control Strategy: Regression over Classification 69
2.2.6 Choice of Output: Kinematic Model 69
2.2.7 Software Development: Temporal Continuity 70
2.2.8 Hardware Innovation: Dry Electrodes 70
2.2.9 Integrated Component: EMG Amplifier 72
2.2.10 Summary 72
2.3 Research Objectives and Hypotheses 73
2.3.1 Performance Criteria 76
2.4 Contributions 77
2.5 Thesis Structure 77
2.6 Data Availability 78

3 RPC-Net: HD-EMG and ML for Hand Position Estimation 79
3.1 Introduction . . . 79
3.2 Materials and Methods . . . 82
3.2.1 Instrumentation . . . 82
3.2.2 Experimental Approach . . . 83
3.2.3 Comparison with State of the Art Solutions . . . 94
3.2.4 Variations of RPC-Net . . . 95
3.3 Results . . . 98
3.3.1 Performance of RPC-Net . . . 98
3.3.2 Variations of RPC-Net and Comparison with Other Solutions 98
3.4 Discussion . . . 102
3.5 Conclusion . . . 113

4 HDE-Array: A Dry Electrode System for HD-sEMG Acquisition 115
4.1 Introduction . . . 115
4.2 Materials and Methods . . . 117
4.2.1 Instrumentation . . . 117
4.2.2 RPC-Net Performance: HDE-Array and Gel Electrodes . . . 119
4.2.3 Variance Analysis Across Columns and Rows for Gel Electrodes 126
4.2.4 Skin-Electrode Impedance Characterisation . . . 127
4.3 Results . . . 129
4.3.1 Variance Analysis . . . 129
4.3.2 Impedance Characterisation . . . 129
4.3.3 RPC-Net Performance . . . 130
4.4 Discussion . . . 133
4.5 Conclusion . . . 138

5 PCA-Based Synergies for Hand Kinematic Control 139
5.1 Introduction . . . 139
5.2 Materials and Methods . . . 141
5.2.1 Instrumentation . . . 141
5.2.2 Experimental Protocol . . . 141
5.3 Results . . . 149
5.3.1 Analysis of Variance Explained by Different PCs . . . 149
5.3.2 Performance of RPC-Net with PCA . . . 150
5.3.3 Performance Comparison of 5 PCs vs Full Model . . . 152
5.4 Discussion . . . 155
5.5 Conclusion . . . 160

6 ANNs for HD-sEMG: Inter-/Intra-Subject Variability 163
6.1 Introduction . . . 163
6.2 Materials and Methods . . . 165
6.2.1 Instrumentation . . . 165
6.2.2 Experimental Protocol . . . 165
6.3 Results . . . 176
6.3.1 Robustness of RPC-Net Against Electrode Repositioning . . 176
6.3.2 Effect of Repositioning on Intra-Session Learning . . . 177
6.3.3 Effect of Repositioning on Cross-Session Performance . . . 180
6.3.4 Effect of Inter-Subject Training on System Generalisation . . 181
6.4 Discussion . . . 182
6.5 Conclusion . . . 188

7 Real-Time Control: Multi-Subject Training and Feedback 191
7.1 Introduction . . . 191
7.2 Materials and Methods . . . 193
7.2.1 Instrumentation . . . 194
7.2.2 Experimental Protocol . . . 194
7.3 Results . . . 204
7.3.1 Real-time vs. Offline Performance . . . 204
7.3.2 Subject-specific vs. Generalised Training . . . 204
7.3.3 Influence of Visual Feedback . . . 206
7.4 Discussion . . . 208
7.5 Conclusion . . . 212

8 Neck Muscle HD-sEMG for Rehab-Oriented Control 213
8.1 Introduction . . . 213
8.2 Materials and Methods . . . 216
8.2.1 Instrumentation . . . 216
8.2.2 Experimental Protocol . . . 217
8.3 Results . . . 228
8.3.1 Assessment of Hand Control Performance . . . 229
8.3.2 Healthy vs. Tetraplegic Subjects: Hand Position Control . . 229
8.3.3 Assessment of Cursor Control Performance . . . 230
8.3.4 Healthy vs. Tetraplegic Subjects: Cursor Control . . . 232
8.4 Discussion . . . 232
8.5 Conclusion . . . 238

9 Discussion **241**
9.1 Integrated Findings and Thematic Insights . . . 243
9.1.1 Theme 1: Decoding Accuracy Across Configurations . . . 243
9.1.2 Theme 2: Robustness Under Non-ideal Conditions . . . 245
9.1.3 Theme 3: User-centred Control Efficacy . . . 246
9.1.4 Theme Summary . . . 247
9.2 Theoretical Integration and Contribution . . . 248
9.2.1 Alignment and Divergence with Existing Literature . . . 248
9.2.2 New Insights Beyond the Literature . . . 250
9.2.3 Synthesis . . . 251
9.3 Methodological Strengths and Shared Limitations . . . 252
9.3.1 Cross-Study Methodological Strengths . . . 252
9.3.2 Shared Limitations . . . 253
9.3.3 Synthesis . . . 254
9.4 Implications and Concluding Synthesis . . . 255
9.4.1 Practice, Policy, and Management . . . 255
9.4.2 Directions for Future Research . . . 255
9.5 Concluding Synthesis . . . 259

10 Conclusion **261**

References **265**

Appendices

A Ethics and Acknowledgments **301**
A.1 Acknowledgment Chapter 3 . . . 301
A.1.1 Publication acknowledgment . . . 301
A.2 Acknowledgment Chapter 4 . . . 302
A.2.1 Publication acknowledgment . . . 302
A.3 Acknowledgment Chapter 5 . . . 302
A.3.1 Publication acknowledgment . . . 302
A.4 Acknowledgment Chapter 6 . . . 303
A.4.1 Publication acknowledgment . . . 303
A.5 Acknowledgment Chapter 7 . . . 303
A.5.1 Publication acknowledgment . . . 304
A.6 Acknowledgment Chapter 8 . . . 304
A.6.1 Publication acknowledgment . . . 304
A.7 Ethics Documentation . . . 305

List of Figures

1.1 Incidence of traumatic upper-limb amputations 16

2.1 Kinematic model 71

3.1 Subject setup 84
3.2 Instrumentation and electrode placement 86
3.3 RPC-Net architecture 91
3.4 Schematic definition of MD and MPCC 93
3.5 Estimation error of RPC-Net 100
3.6 Comparison between RPC-Net estimates and target values 101
3.7 Performance of RPC-Net (comparison with state of the art) 103
3.8 Performance of RPC-Net as a function of EMG input signal length 104
3.9 Comparative analysis (EMG input signal length) 105
3.10 Performance of RPC-Net as a function of EMG layer width 106
3.11 Comparative analysis (EMG layer width) 107
3.12 Performance of RPC-Net as a function of the subset of electrodes used 108
3.13 Performance of RPC-Net-I, RPC-Net-W, and RPC-Net 109
3.14 Comparative analysis (RPC-Net-W, RPC-Net-I, and RPC-Net) . . 110

4.1 HDE-Array 118
4.2 Subject setup 121
4.3 Electrical model of the skin-electrode interface 128
4.4 Variance analysis results 130
4.5 Impedance characterisation results 131
4.6 Direct signal comparison 132
4.7 RPC-Net performance results (dry vs gel electrodes) 133
4.8 SPM analysis results 134

5.1 Subject setup 143
5.2 RPC-Net and PCA implementation 146
5.3 Variance explained by principal components 151
5.4 Representation of main principal components 152
5.5 Principal component heatmap 153

5.6 Case 1. Performance as a function of PCs considered 154
5.7 Case 2. Performance as a function of PCs considered 155
5.8 Case 3. Performance as a function of PCs considered 156
5.9 Direct comparison between full and reduced models 158

6.1 HDE-Array configuration 166
6.2 Subject setup 168
6.3 Comparison of RPC-Net performance under different conditions . . 177
6.4 Intra-session performance with and without electrode repositioning 179
6.5 Performance as a function of number of training subjects 183
6.6 RPC-Net performance with one and sixteen training subjects 184

7.1 HDE-Array configuration 194
7.2 Subject setup 197
7.3 Prompted hand positions 200
7.4 Visual interface for real-time testing 201
7.5 Movement-wise real-time performance results 205
7.6 Comparison between specific and generalised testing 207
7.7 Comparison between testing with and without feedback 209

8.1 Electrode placement 218
8.2 Directions of movement and corresponding labels 220
8.3 Tasks prompted during testing phase 222
8.4 Testing phase example 224
8.5 Hand control tasks 225
8.6 Hand control task performance results 230
8.7 Cursor control task performance results 233

9.1 Conceptual map of the thesis 244

List of Tables

1.1 Motor innervation of forearm and hand muscles 6
1.2 Motor innervation of neck muscles 8
1.3 Estimated annual incidence of chronic upper-limb impairment . . . 18

3.1 Input electrode subsets 97
3.2 Performance indicators for RPC-Net across subjects 99

4.1 RPC-Net performance 135

5.1 Fitted parameters of the exponential performance model 157

6.1 Effect of session variability on RPC-Net performance 178
6.2 Fitted parameters of the exponential performance model 180
6.3 Fitted parameters for the linear performance model 181

7.1 Subject performance with RPC-Net-S 205
7.2 Performance comparison between RPC-Net variants 206

8.1 Hand control results 231
8.2 Cursor position control results 234

9.1 Summary of the six experimental chapters and their through-line . 242

10.1 Summary of the hypotheses assessed in the six experimental chapters 262

Acronyms

2D Two-Dimensional

3D Three-Dimensional

AC Alternating Current

ADL Instrumental Activities of Daily Living

ADL Activities of Daily Living

AnC Ansa Cervicalis

AR Autoregressive Coefficients

BCI Brain-Computer Interface

BLDC Brushless DC motors

BMI Brain Machine Interface

BPI Brachial Plexus Injury

CJD Cross-Joint Derivative

CMC Carpometacarpal

CMCJD Cross-Movement Cross-Joint Difference

CN Cranial Nerve

CNN Convolutional Neural Network

CNS Central Nervous System

CPM Continuous Passive Movement

CPU Central Processing Unit

CSN Cervical Spinal Nerve

DC Direct Current

DIP Distal Interphalangeal

DL Deep Learning

DoF Degree of Freedom

DT Decision Tree

ECoG Electrocorticography

EEG Electroencephalography

EMG Electromyography

FES Functional Electrical Stimulation

FKA Forward Kinematic Algorithm

fNIRS Functional Near-Infrared Spectroscopy

GBD Global Burden of Disease

GPU Graphics Processing Unit

GRU Gated Recurrent Unit

HD-sEMG High Density surface Electromyography

HDE-Array High-Density Electrode Array

HRQoL Health-Related Quality of Life

iEMG Intramuscular Electromyography

IKA Inverse Kinematic Algorithm

IP Interphalangeal

IQR Inter-Quartile Range

IT Inference Time

KNN K-Nearest Neighbour

LDA Linear Discriminant Analysis

LMT Logistic Model Tree

LSTM Long Short-Term Memory

MAD Mean Angular Distance

MAV Mean Absolute Value

MCP Metacarpophalangeal

MCS Mental Component Score

MD Mean Distance

MGD Mean Global Distance

ML Machine Learning

MLP Multi-Layer Perceptron

MP Metacarpo-phalangeal

MPCC Mean Pearson Correlation Coefficient

MS Multiple sclerosis

MUAP Motor Unit Action Potential

NB Naive Bayes

ND Normalised Distance

ND-C ND-Complex

ND-S ND-Simple

NDV Normalised Dimensional Variance

NiTi-SMA Nickel-Titanium Shape Memory Alloy

PC Principal Component

PCA Principal Component Analysis

PCC Pearson Correlation Coefficient

PCS Physical Component Score

PD Parkinson's Disease

PIP Proximal Interphalangeal

PNS Peripheral Nervous System

PR Pattern Recognition

PTSD Post-Traumatic Stress Disorder

QoL Quality of Life

ReLU Rectified Linear Unit

RFC-Net Recursive Functional electrical stimulation Control Network

RIC Research Institute of Chicago

RMS Root Mean Square

RMSE Root Mean Square Error

RNN Recurrent Neural Network

RPC-Net Recursive Prosthetic Control Network

SCI Spinal Cord Injury

SD Standard Deviation

SDI Socio-Demographic Index

sEMG surface Electromyography

SLR Simple Logistic Regression

SPM Statistical Parametric Mapping

SSC Slope Sign Changes

STFT Short-Time Fourier Transform

SU Sensor Unit

SVM Support Vector Machine

TCS Task Completion Score

TCS-C TCS-Complex

TCS-S TCS-Simple

TMC Trapeziometacarpal

UI Uncertainty Interval

UL Upper Limb

UMD Unweighted Mean Distance

WFD Weighted Fingertip Distance

WHOQOL-BREF World Health Organization Quality of Life - BREF version

WL Waveform Length

WPT Wavelet Packet Transform

WT Wavelet Transform

ZC Zero Crossing

1 State of the Art

This chapter offers an overview of the fundamental concepts established in the academic literature that underpin this thesis. Given the highly interdisciplinary nature of this research project, it is appropriate to provide essential background across all fields contributing to its development.

This section addresses the following topics:

1. Anatomy and Kinematic Models of the Upper Limb and Neck
2. Epidemiology and Global Burden of Upper-Limb Impairment
3. Needs of Upper Limb Rehabilitation Device Users and Impact on Quality of Life
4. Upper Limb Prosthetic Devices
5. Non-Amputation Rehabilitation Solutions
6. Biosignal Interfaces for Intent Detection in Upper-Limb Devices
7. Electromyography: Principles and Instrumentation
8. Developments in Machine Learning
9. Machine Learning applications in EMG-Based Control of Upper Limb Rehabilitation Devices

The information included in this chapter is referenced in the Introduction chapter to highlight current gaps in existing solutions and to justify the approach chosen.

1.1 Anatomy and Kinematic Models of the Upper Limb and Neck

The human upper limb plays a fundamental role in facilitating interaction with the environment, with the hand serving as its most functionally versatile component. The capacity of the hand to perform precise and complex movements is enabled by an intricate interplay of musculoskeletal and neural structures, extending from the neck and shoulder girdle to the distal phalanges. In particular, coordination between the forearm musculature, hand joints, and associated nerves underlies fine motor control. Additionally, cervical musculature often provides accessible proxy signals for gesture decoding in assistive technologies.

As this thesis focuses on technologies aimed at restoring upper limb function following injury or impairment, a foundational understanding of the relevant anatomical structures is essential. The rehabilitation approaches discussed in this thesis depend on bioelectrical signals primarily derived from the forearm and neck muscles and are directed towards reconstructing natural hand kinematics. Accordingly, this section presents an overview of the anatomical components most relevant to these objectives. This includes the bones and joints of the hand and forearm, the corresponding flexor and extensor musculature, and the cervical muscles commonly used for signal acquisition. Neural structures critical to motor control are also addressed. Other anatomical domains, such as the vascular and lymphatic systems, are excluded from this discussion as they fall beyond the scope of the thesis.

The anatomical overview draws upon a range of classical and contemporary references and is intended to provide the reader with the necessary background to understand the principles and challenges underlying the development of advanced rehabilitation systems [1–3]. Relevant tables from the Netter Atlas of Human Anatomy are referenced throughout [4].

1.1.1 Overview of the Upper Limb

The upper limb is a highly specialised appendage that supports a wide range of motor functions, from gross movement and object manipulation to the fine precision

required for tasks such as tool use, writing, and grasping. It consists of 32 bones, distributed across four anatomical regions: the shoulder girdle, arm (brachium), forearm (antebrachium), and hand (manus).

Bones of the Upper Limb

- Shoulder girdle: clavicle and scapula (2)
- Arm: humerus (1)
- Forearm: radius and ulna (2), see Plate 449 [4].
- Hand: 27 bones (see Subsection 1.1.1 for detailed breakdown)

Muscles of the Upper Limb

The upper limb contains over 50 skeletal muscles that facilitate movement across multiple joints. These muscles support three primary functional categories:

- Positioning: movement of the limb through space via shoulder and elbow articulation
- Manipulation: wrist and finger control for object handling
- Sensory interaction: fine motor control that enables exploratory and communicative behaviours, such as gesture production

Motor control is mediated by complex neuromuscular pathways, with segmental innervation primarily provided by the brachial plexus (Plate 439), a network of spinal nerve roots (C5-T1) that converge and branch to innervate the muscles and skin of the shoulder, arm, and hand [4].

Bones of the Hand

The human hand comprises 27 bones, organised into three functional groups:

- Carpal bones (8): arranged in two rows
  - Proximal row (lateral to medial): scaphoid, lunate, triquetrum, pisiform
  - Distal row (lateral to medial): trapezium, trapezoid, capitate, hamate
- Metacarpal bones (5): numbered I to V from thumb to little finger
- Phalanges (14): each finger contains three (proximal, middle, distal), except the thumb, which has two

See Plate 466 for a visual depiction [4]. Although the following discussion emphasises the osseous arrangement of the hand, each degree of freedom is mechanically delimited by ligaments, joint capsules, and other passive soft-tissue structures. These constraints couple adjacent joints and restrict extreme ranges of motion; a detailed description of ligamentous anatomy lies beyond the scope of the present thesis.

Muscles of the Hand

Muscles contributing to hand function are divided into two primary groups: extrinsic muscles, which originate in the forearm, and intrinsic muscles, which are located entirely within the hand. The extrinsic muscles provide strength and positioning for gross hand movements, while the intrinsic muscles enable fine motor control and digital precision.

Extrinsic Muscles:

- Superficial flexors of the hand (anterior compartment of the forearm, Plate 452 and Plate 456) [4]:
  - Flexor carpi radialis: flexes and abducts the wrist
  - Palmaris longus: tenses the palmar aponeurosis and flexes the wrist
  - Flexor carpi ulnaris: flexes and adducts the wrist
- Intermediate flexor of the hand (anterior compartment of the forearm):
  - Flexor digitorum superficialis: flexes the Metacarpophalangeal (MCP) and Proximal Interphalangeal (PIP) joints of digits II to V
- Deep flexors of the hand (anterior compartment of the forearm, Plate 453 and Plate 458) [4]:
  - Flexor digitorum profundus: flexes the Distal Interphalangeal (DIP) joints of digits II to V
  - Flexor pollicis longus: flexes the Interphalangeal (IP) joint of the thumb
- Superficial extensors of the hand (posterior compartment of the forearm, Plate 451 and Plate 454) [4]:
  - Extensor digitorum: extends the MCP and IP joints of digits II to V
  - Extensor digiti minimi: extends the fifth digit

  - Extensor carpi ulnaris: extends and adducts the wrist
  - Extensor carpi radialis longus: extends and abducts the wrist
  - Extensor carpi radialis brevis: extends and abducts the wrist
- Deep extensors of the hand (posterior compartment of the forearm, Plate 455) [4]:
  - Extensor indicis: extends the second digit
  - Abductor pollicis longus: abducts and extends the thumb at the Carpometacarpal (CMC) joint
  - Extensor pollicis brevis: extends the MCP joint of the thumb
  - Extensor pollicis longus: extends the IP and MCP joints of the thumb

Intrinsic Muscles:

- Thenar group (Plate 475) [4]:
  - Abductor pollicis brevis: abducts the thumb
  - Flexor pollicis brevis: flexes the thumb at the MCP joint
  - Opponens pollicis: opposes the thumb
- Hypothenar group:
  - Abductor digiti minimi: abducts the fifth digit
  - Flexor digiti minimi brevis: flexes the fifth digit at the MCP joint
  - Opponens digiti minimi: opposes the fifth digit
  - Palmaris brevis: wrinkles the skin of the hypothenar eminence and protects the ulnar nerve
- Central compartment:
  - Lumbricals (4): flex the MCP joints and extend the PIP and DIP joints of digits II to V
- Interossei:
  - Palmar interossei (3): adduct digits II, IV, and V and assist the lumbricals
  - Dorsal interossei (4): abduct digits II to IV and assist the lumbricals
- Adductor compartment:
  - Adductor pollicis: adducts the thumb towards the palm; essential for pinching and grip

Muscle	M	U	R
Abductor digiti minimi		X	
Abductor pollicis brevis	X		
Abductor pollicis longus			X
Adductor pollicis		X	
Dorsal interossei		X	
Extensor carpi radialis brevis			X
Extensor carpi radialis longus			X
Extensor carpi ulnaris			X
Extensor digiti minimi			X
Extensor digitorum			X
Extensor indicis			X
Extensor pollicis brevis			X
Extensor pollicis longus			X
Flexor carpi radialis	X		
Flexor carpi ulnaris		X	
Flexor digiti minimi brevis		X	
Flexor digitorum profundus (lateral half)	X		
Flexor digitorum profundus (medial half)		X	
Flexor digitorum superficialis	X		
Flexor pollicis brevis (deep head)		X	
Flexor pollicis brevis (superficial head)	X		
Flexor pollicis longus	X		
Lumbricals I-II	X		
Lumbricals III-IV		X	
Opponens digiti minimi		X	
Opponens pollicis	X		
Palmar interossei		X	
Palmaris brevis		X	
Palmaris longus	X		

Table 1.1: Motor innervation of forearm and hand muscles across the three main nerves. An *X* indicates innervation. M: Median nerve; U: Ulnar nerve; R: Radial nerve

Motor Innervation of the Forearm and Hand

Motor control of the forearm and hand is primarily mediated by three terminal branches of the brachial plexus: the median, ulnar, and radial nerves. While each

nerve innervates a broad set of muscles, often with overlapping or complementary functions, it is possible to associate each with a general functional domain:

- Median nerve: responsible for flexion of the wrist and fingers, particularly the lateral digits; thumb opposition; and precision grip (Plate 486) [4]
- Ulnar nerve: flexes the ring/little fingers, cups the palm, and draws the thumb hard across the palm, creating a strong, cupped power-grip posture (Plate 487) [4]
- Radial nerve: supplies the extensor muscles of the elbow, wrist, and fingers, enabling limb extension and release of grasp (Plate 489)

See Plate 484 for a visual overview of the upper limb, and Table 1.1 for a detailed breakdown of innervation by muscle [4]. The thesis focuses on the efferent (motor) functions of the median, ulnar, and radial nerves; however, each nerve also conveys afferent fibres that supply cutaneous and proprioceptive feedback to the central nervous system. Although these sensory branches are crucial for closed-loop prosthetic control, their detailed anatomy and physiology are not elaborated here.

1.1.2 Overview of the Neck

The neck forms a critical transitional region between the head and the thorax. It supports essential structures such as the airway, oesophagus, major blood vessels, and spinal cord, while also enabling a wide range of movement. Structurally, it comprises bones, multiple muscular layers, and complex neurovascular networks. In the context of this thesis, neck muscles are particularly relevant due to their accessibility for surface Electromyography (sEMG) signal acquisition, especially in individuals with impaired upper limb function.

Bones of the Neck

The skeletal framework of the neck primarily includes (Plate 43, Plate 44, and Plate 45) [4]:

- Cervical vertebrae (7): C1 to C7, forming the cervical spine

Muscle	CN	AnC	CSN
Digastric (anterior belly)	X		
Digastric (posterior belly)	X		
Geniohyoid	X		
Interspinales cervicis			X
Intertransversarii colli			X
Longus capitis			X
Longus colli			X
Multifidus cervicis			X
Mylohyoid	X		
Omohyoid		X	
Platysma	X		
Scalenus anterior			X
Scalenus medius			X
Scalenus posterior			X
Semispinalis capitis			X
Semispinalis cervicis			X
Sternocleidomastoid	X		X
Sternohyoid		X	
Sternothyroid		X	
Stylohyoid	X		
Thyrohyoid	X		
Trapezius	X		X
Splenius capitis			X
Splenius cervicis			X
Suboccipital muscles			X
Scalenus medius			X

Table 1.2: Motor innervation of neck muscles by major nerve groups. Cranial Nerve (CN) (VII, XI, XII); Ansa Cervicalis (AnC) (C1-C3); Cervical Spinal Nerves (CSNs) (C1-C8).

- Hyoid bone: located anteriorly at the level of C3; serves as an attachment point for tongue and neck muscles

Muscles of the Neck

The muscles of the neck are organised into three principal groups based on anatomical position and function: anterior neck muscles, lateral (vertebral) neck muscles, and

posterior neck muscles. These muscles contribute to head and neck movement, respiration, swallowing, and postural support.

Anterior Neck Muscles

- Superficial neck muscles (Plate 49 and Plate 54) [4]:
  - Platysma: tenses the skin of the neck
  - Sternocleidomastoid: rotates the head contralaterally and flexes the neck
- Suprahyoid neck muscles:
  - Digastric (anterior and posterior bellies): depresses the mandible and elevates the hyoid bone
  - Mylohyoid: elevates the floor of the mouth during swallowing
  - Geniohyoid: pulls the hyoid bone anteriorly and elevates it
  - Stylohyoid: elevates and retracts the hyoid bone
- Infrahyoid neck muscles:
  - Sternohyoid: depresses the hyoid after swallowing
  - Omohyoid: depresses and stabilises the hyoid bone
  - Sternothyroid: depresses the thyroid cartilage
  - Thyrohyoid: depresses the hyoid and elevates the larynx

Lateral Muscles:

- Cervical muscles: located along the sides of the neck, extending between the cervical transverse processes and the first two ribs (Plate 55) [4].
  - Scalenus anterior: elevates the first rib; flexes and rotates the neck
  - Scalenus medius: elevates the first rib; contributes to lateral neck flexion
  - Scalenus posterior: elevates the second rib; assists in neck flexion

Posterior muscles:

- Superficial neck muscles: span from the skull and cervical vertebrae to the pectoral girdle (Plate 195, Plate 196, and Plate 197) [4]:
  - Trapezius: elevates and retracts the scapula; assists with head extension
  - Splenius capitis: extends and laterally rotates the head
  - Splenius cervicis: extends and laterally flexes the cervical spine
- Deep neck muscles:

  - Semispinalis capitis: extends the head and neck
  - Semispinalis cervicis: extends and rotates the cervical spine
  - Multifidus cervicis: stabilises and rotates the cervical vertebrae
- Deepest neck muscles:
  - Suboccipital muscles: provide fine control of head movement (rectus capitis posterior major and minor, obliquus capitis superior and inferior)
  - Interspinales cervicis: extend the cervical spine
  - Intertransversarii colli: laterally flex the cervical spine

Nerve Supply of the Neck

Motor innervation of the neck musculature is derived from three principal sources (Plate 56 and Plate 57) [4]. A detailed summary of muscle innervation is provided in Table 1.2.

- Cranial Nerve (CN), including:
  - Facial nerve (CN VII): innervates platysma, stylohyoid, and the posterior belly of digastric
  - Mandibular nerve (CN VIII): supplies mylohyoid and the anterior belly of digastric
  - Accessory nerve (CN XI): innervates sternocleidomastoid and trapezius
  - Hypoglossal nerve (CN XII): carries C1 fibres to geniohyoid and thyrohyoid
- Ansa Cervicalis (AnC): a motor loop formed by cervical roots C1 to C3. It innervates most infrahyoid muscles, including sternohyoid, omohyoid, and sternothyroid
- Cervical Spinal Nerve (CSN): direct motor branches from C1 to C8. These innervate:
  - Deep prevertebral muscles, such as longus colli and longus capitis
  - Lateral neck muscles, including the scalenes
  - Posterior cervical muscles, such as splenius, semispinalis, and the suboccipital group

1.1.3 Kinematic Models

The anatomical overview presented above establishes the structural and neuromuscular constraints that govern movement of the upper limb and neck. In order to simulate these constraints, predict reachable postures, and design control algorithms for assistive devices, the continuous anatomy must be abstracted into a finite set of mechanical degrees of freedom. The following section therefore reviews existing kinematic models. A similar analysis is also performed for neck kinematics.

Hand

Accurate modelling of the kinematics of the human hand is essential for simulating and controlling upper limb function, particularly in rehabilitation and prosthetic systems. A wide range of hand kinematic models has been proposed in the literature, differing in the distribution of Degrees of Freedom (DoFs) across the anatomical joints of the hand and wrist.

Lee and Kunii proposed a 24-DoF model [5], assigning four DoFs to each finger (including two at the MCP joint and one at each IP joint), and five DoFs to the thumb, to account for the unique mobility of its CMC and MCP joints. An additional three DoFs were allocated to the wrist. Cobos et al. expanded upon this with a 27-DoF model [6], introducing a virtual joint at the CMC junction of each finger, resulting in five DoFs per finger and four for the thumb, along with three wrist DoFs. Bray et al. also described a 27-DoF model [7], in which each finger was assigned five joint angles: three for flexion, one for abduction, and one for axial twist. The thumb was modelled with four joint angles: three for flexion and one for abduction. Their model included three wrist DoFs.

Chalfoun et al. proposed a 26-DoF model [8], assigning four DoFs to each finger and five to the thumb (two at the Trapeziometacarpal (TMC) joint, two at the MCP joint, and one at the IP joint). This model also included two internal palm DoFs to account for metacarpal mobility and three wrist DoFs. Kuch et al. described a 24-DoF model [9], which included two DoFs in the forearm, two in the wrist, two in the CMC joint of the thumb, two at the MCP joints of each finger (for

flexion/extension and abduction/adduction), and one DoF at each IP joint. Du et al. proposed a 27-DoF model [10], allocating one DoF to each distal and proximal IP joint and two DoFs to each MCP joint (except for the thumb, which had only one DoF at the MCP joint). The TMC joint of the thumb was modelled with two DoFs (abduction/adduction and axial twist), and three DoFs were assigned to the wrist. Renault et al. presented a detailed 27-DoF model [11], incorporating realistic joint axes for the forearm, wrist, CMC joints, and finger articulations. Their model included two DoFs at the elbow, two at the wrist, two rotational joints at the CMC joints of the ring and little fingers, two DoFs at each MCP joint, and one at each IP joint. The thumb was modelled with five joints.

Taken together, these models exhibit a broad consensus in assigning three degrees of freedom to the wrist and recognising the increased joint complexity of the thumb relative to the fingers; however, they also differ substantially in how they allocate degrees of freedom across joints, particularly in modelling finger abduction, axial rotation, and palm dynamics. Most models attribute between four and five DoFs to each finger, with variation introduced through the inclusion of abduction/adduction and axial rotation at the MCP joints. Several authors incorporate virtual or anatomical joints at the CMC level to account for transverse plane motion, while a subset explicitly models internal palm dynamics or forearm contributions. The total number of DoFs ranges from 24 to 27 in most cases, reflecting a balance between anatomical fidelity and computational tractability. The diversity of modelling choices, particularly in how they treat MCP mobility, thumb opposition, and non-planar finger motion, underscores the absence of a universal standard and motivates the development of a unified model that aggregates the most functionally relevant features.

All models considered exclude the three global positional DoFs (translation along the x, y, and z axes), which are typically associated with the placement of rigid bodies in space. These translational components are not intrinsic to hand biomechanics and are instead related to overall body movement.

Neck

The cervical spine is a biomechanically complex structure composed of seven vertebrae, each contributing to the overall flexibility of the neck through multiple articulating joints. In high-fidelity models, up to 16 mechanical DoFs are used to represent the individual segmental motions of the cervical vertebrae. However, many simplified neck models treat the head-neck connection as a single joint with three rotational DoFs, corresponding to the anatomically observable motions of pitch (flexion and extension), yaw (axial rotation), and roll (lateral bending). In these models, the head is treated as a rigid body, and its orientation relative to the trunk is described using three Euler angles. This 3-DoF representation effectively captures the visible movement of the neck, since the multiple joints of the cervical spine collectively allow three independent head rotations [12, 13]. Translational displacements of the head relative to the torso are generally minor under normal conditions and are therefore often neglected. The resulting kinematic simplification treats the neck as a ball-and-socket joint, permitting rotation about three orthogonal axes without translation [12]. Such models are particularly useful in contexts such as motion tracking, posture analysis, and rehabilitation, where the primary objective is to capture head orientation rather than detailed vertebral motion [14–18].

1.1.4 Summary

This section has provided a detailed anatomical and kinematic framework of the upper limb and neck, translating complex biological structures into quantifiable mechanical degrees of freedom. These representations underpin the modelling and control strategies explored in later sections and serve as a normative baseline for evaluating functional impairment. In the next section, the thesis transitions from structure to scale, examining the global epidemiology and burden of upper-limb dysfunction. By situating rehabilitation challenges within their demographic and clinical context, the discussion lays the groundwork for assessing the need and urgency for innovative assistive solutions.

1.2 Epidemiology and Global Burden of Upper-Limb Impairment

While the preceding section outlined the anatomical and mechanical principles that define normal upper-limb function, it is equally important to understand the contexts in which that function is lost. Only by quantifying the scale and causes of upper-limb impairment can the urgency and scope of the rehabilitation challenge be appreciated. This section therefore shifts from structure to statistics, quantifying the global burden of upper-limb functional impairment across musculoskeletal, peripheral nerve, and central nervous system aetiologies.

1.2.1 Musculoskeletal causes

Traumatic amputation

Upper-limb amputation represents the most dramatic form of functional loss of the arm and hand. Aetiologically, it can be divided into traumatic and non-traumatic causes, with the former accounting for the large majority of cases in high-income settings. The Global Burden of Disease (GBD) 2021 dataset provides country- and region-level estimates for traumatic upper-limb loss. Figure 1.1 (derived from GBD 2021 [19]) shows that both incidence and prevalence remain clinically relevant across all Socio-Demographic Index (SDI) regions [20]. In the high-income SDI super-region, the incidence is 2.04 per 100,000 (95% Uncertainty Interval (UI) 1.3-3.4) for unilateral and 1.88 per 100,000 (95% UI 1.2-3.2) for bilateral amputations. A study by Yuan et al. provides additional insights from the GBD study [21]. Global estimates for major, trauma-related upper-limb loss (GBD-2015) suggest a near-equal split between unilateral and bilateral cases, although most national and clinical series show unilateral amputations to be far more common (approximately 5-20 times as frequent). The GBD figure is influenced by methodological choices and by conflict-related blast injuries that disproportionately produce bilateral loss [22, 23].

National studies present similar results: hospital discharge data from the United States in 1996 reported 3.8 per 100,000 trauma-related upper-limb amputations [24, 25], while the French national database recorded 3 per 100,000 traumatic

amputations between 2004 and 2013 [26]. These two studies estimate the percentage of traumatic amputations among total amputations at 74% ± 1%, while a Norwegian population study attributes 84% of cases to trauma [27]. The anatomical level of removal also varies: a large US cohort placed amputations through the humerus at 35%, forearm at 30%, and hand at 14% of all major upper-extremity losses [28].

In summary, these sources place the incidence of traumatic upper-limb amputation in the high-income SDI super-region, or in countries that are part of it, between 3 and 4 cases per 100,000 people. The percentage of traumatic amputations out of the total is estimated between 74% and 84%. Given that the incidence of traumatic amputations according to the GBD report is similar between the high-income super-region and other regions, and considering that vascular diseases are less common [19], it is possible to estimate that the global incidence is similar to that observed in the high-income super-region. This yields an estimated annual global incidence of traumatic upper-limb amputation between 240,000 and 320,000 cases, assuming a global population of 8 billion people.

Non-traumatic amputation

Non-traumatic upper-limb amputation is far less common and is driven mainly by vascular disease, malignancy, and severe infection [27]. Since the GBD report does not quantify these, information must be derived from the same clinical epidemiological studies cited above. This leads to an estimated ratio of non-traumatic to all amputations of between 26% and 16%. Using the previously mentioned incidence values and similar extrapolation across regions, the estimated global incidence ranges from 45,000 to 112,000 new cases annually. The aetiological pattern differs markedly from that of the lower extremity, where incidence is considerably higher (3-5 times greater), and non-traumatic vascular disease predominates [20, 29].

Summary

In summary, upper-limb amputation remains an uncommon but clinically significant event. Trauma is responsible for the vast majority of cases, whereas vascular, malignant, and infectious causes together contribute fewer than one in four amputations.

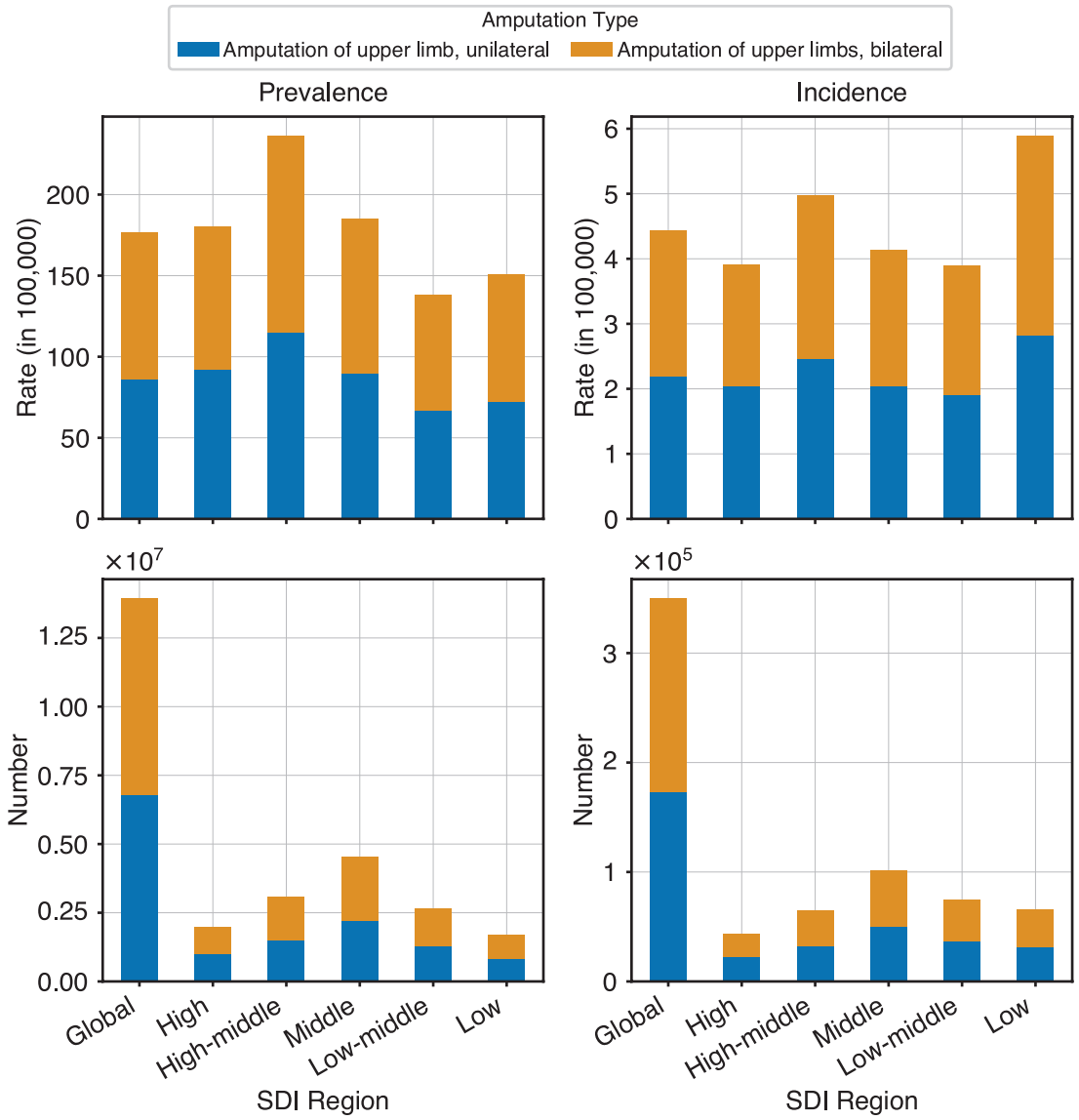

Figure 1.1: Incidence of traumatic upper-limb amputations: per 100,000 of the population, stratified by Socio-Demographic Index (SDI) regions: data from GBD 2021 [19].

1.2.2 Nervous System

Upper-limb impairment often results from lesions or degeneration of the Central Nervous System (CNS) or the Peripheral Nervous System (PNS), especially following stroke and cervical Spinal Cord Injury (SCI).

Stroke

Global stroke incidence is 151 per 100,000 population. Stroke-specific reviews indicate that 40-50% of survivors have persistent upper-extremity paresis at six months [30–32]. Hence, approximately 60-75 individuals per 100,000 develop chronic arm-hand impairment each year, about 5-6 million people globally.

Cervical spinal-cord injury

The worldwide incidence of traumatic cervical SCI ranges from 1 to 4 per 100,000 [33]. In a multicentre cohort of 167 cervical SCI cases, one in four to one in three patients with motor-complete injuries (circa 25-30%) failed to regain even a single functional motor level in the upper limb, and about one in ten with incomplete injuries (circa 10%) showed no recovery. At the C6 level specifically, 15% of complete and 10% of incomplete lesions never recovered functional triceps strength, underscoring that a substantial minority of tetraplegic patients remain without meaningful grasp-related improvement despite two years of natural recovery [34]. A longitudinal cohort study showed that within a year of cervical SCI, roughly 75% of patients whose injuries were incomplete at presentation, and only about 10% of those who were initially motor-complete, regained clinically meaningful upper-limb motor function [35]. Combining this information, the effective incidence of long-term tetraplegia-related upper-limb disability is approximately 0.2-0.6 new severely disabling cases per 100,000 population per year worldwide (with an upper bound of 1 per 100,000 in the worst-case scenario), resulting in 15,000 to 80,000 new cases annually. Most CNS figures come from hospital registries, whereas peripheral nerve and orthopaedic data often derive from surgical cohorts that over-represent severe disease. Self-reported surveys may underestimate subtle dexterity loss. Heterogeneous outcome metrics further complicate cross-study comparisons.

Neurodegenerative diseases

Most studies place the incidence of Multiple sclerosis (MS) in Europe between 0.3 and 18 cases per 100,000 population, and that of Parkinson's Disease (PD)

Aetiology	Annual Incidence (per 100,000)	Key source
Traumatic Amputation	3.0-4.0	[24, 26, 27]
Non-Traumatic Amputation	0.5-1.4	[24, 26, 27]
Stroke	60.0-75.0	[30]
Cervical SCI	0.2-0.6	[33]
Adult BPI	0.1-0.8	[42]
MS + PD	4.0-32.0	[36, 37]
Total	∼67.8-∼113.8	[19]

Table 1.3: Estimated annual incidence of chronic upper-limb impairment (per 100,000). The total value assumes the listed conditions are mutually exclusive and may therefore overestimate the true incidence.

between 5 and 25 cases per 100,000 adults [19, 36, 37]. Consistent with this, the global incidence reported by the GBD is 16.9 per 100,000 (95% UI 15.2-18.8) for PD, and 0.8 per 100,000 (95% UI 0.7-0.9) for MS. Hand-function studies report disabling upper-limb involvement in 65% of MS cases [38, 39] and in 75-80% of PD cases. Multiplying incidence by impairment rates yields an estimated combined incidence of upper-limb impairment in Europe ranging from 4 to 31.7 cases per 100,000 population per year. If these figures were consistent globally, this would correspond to 0.3 to 2.5 million new impairing cases annually, or around 1 million based on the GBD-derived estimates [40, 41].

Adult traumatic Brachial Plexus Injury

In contrast to CNS disorders, damage to the PNS, particularly to the brachial plexus, can also lead to long-term upper-limb dysfunction, although such cases are less common. Incidence varies from 0.17 per 100,000 in Japan to 1.6 per 100,000 in the United States [42]. Clinical series are skewed towards severe cases: total plexus palsy accounts for 33-50% of referrals [43–45]. Assuming 50% of Brachial Plexus Injury (BPI) cases result in long-term functional loss, the annual burden is up to 0.8 cases per 100,000, or about 60,000 new cases globally, with a lower limit of 6,000.

1.2.3 Summary

Table 1.3 summarises annual new cases of chronic upper-limb impairment. Stroke remains the dominant single contributor. While the conditions reported here are not exhaustive, the objective is to provide an overview of the most common causes to communicate the gravity and urgency of upper-limb functional loss. Collectively, the conditions considered generate more than one hundred new cases of lasting upper-limb disability per 100,000 population each year, according to worst-case estimates. This represents a substantial burden of lost independence and underscores the importance of targeted rehabilitation strategies and assistive technology innovation.

Although the focus was kept on the high-impact conditions for which robust, cross-national data exist, several other aetiologies contribute meaningfully to arm-hand disability but remain difficult to quantify. Congenital limb-reduction defects, chronic inflammatory and degenerative joint diseases such as rheumatoid arthritis and severe osteoarthritis, complex regional pain syndrome, and occupational overuse syndromes (e.g. carpal tunnel or tendon rupture) each generate long-term loss of dexterity but are seldom captured in global surveillance studies. Extensive burns with contractures, malignancy-related resections that spare the limb yet impair function, and iatrogenic or civilian gunshot injuries likewise add to the burden. Finally, lifelong motor deficits arising from cerebral palsy, especially spastic hemiplegia, represent a notable paediatric source of upper-limb dysfunction, yet their incidence and prevalence are usually reported for cerebral palsy as a whole rather than stratified by limb-specific impairment, making global quantification difficult. The exclusion of these conditions means that the incidence figures reported here should be regarded as conservative lower bounds rather than exhaustive tallies. While these epidemiological figures quantify the scale of upper-limb disability, they do not reveal how the loss of function shapes daily life. The following section therefore shifts from epidemiological statistics to experiential realities, exploring how users experience upper-limb impairment and what functional goals should guide the design of rehabilitative technologies.

1.3 Needs of Upper Limb Rehabilitation Device Users and Impact on Quality of Life

Having examined the prevalence and causes of upper-limb impairment, focus now shifts to its consequences, specifically, how it affects quality of life and what individuals expect from assistive technology. The section begins with amputees and then extends to neurological populations with comparable motor deficits. An overview of rehabilitation solutions is included in the following sections.

1.3.1 Amputation

Impact on Quality of Life

The loss of one or more limbs following amputation significantly impacts quality of life. The Veterans RAND 12 Item Health Survey (VR-12®) is a brief, generic, multi-use, self-administered health survey composed of 12 items. These items are summarised into two scores: a Physical Health Summary Measure, Physical Component Score (PCS) and a Mental Health Summary Measure, Mental Component Score (MCS) [46]. Together, these scores provide an important distinction between physical and psychological health status.

A 2019 study reported that VR-12 PCS scores for individuals with unilateral and bilateral upper limb amputations (45.1, Standard Deviation (SD) = 8.7 and 44.6, SD = 9.7, respectively) were lower than the population norm (48.6) [47, 48]. However, no statistically significant differences were observed between unilateral and bilateral amputees. In contrast, VR-12 MCS values showed no significant differences between amputees and non-amputees, suggesting that mental health outcomes may be relatively preserved after limb loss. Although mean VR-12 MCS scores approximate population norms, other studies report elevated prevalence of specific mental-health disorders, such as depression or Post-Traumatic Stress Disorder (PTSD), suggesting that generic summary statistics may underestimate individual psychological burden [49].

Similar findings were observed for the QuickDASH, a short, reliable, and validated measure of physical function and symptoms related to upper-limb musculoskeletal disorders [50]. Bilateral amputees demonstrated greater disability, as reflected by higher QuickDASH scores (mean 49.5, SD = 20.7) compared to unilateral amputees (mean 34.7, SD = 22.0). Both groups reported substantially higher QuickDASH scores than the normative population value (15.1), albeit the reference comes from a different cohort [47, 51]. Beyond generic Health-Related Quality of Life (HRQoL) indices, upper-limb loss is associated with high rates of phantom-limb pain, depressive symptoms, reduced employment, and substantial economic costs [52–54].

Further studies support the conclusion that amputation is extremely burdensome: amputees score significantly lower on life satisfaction than control groups and notable differences exist between specific subgroups [55, 56]. These outcomes underscore the importance of tailoring prosthetic technologies to the real-world challenges amputees face. Understanding what users actually want from their devices is therefore essential, both for improving function and minimising abandonment.

Upper Limb Prosthetic User Needs

Given the clear burden on the lives of those affected by amputation, considerable effort has gone into the understanding of what amputees look for in a prosthetic device or other type of replacement technology. Cordella et al. published a review study assessing the functional, cosmetic, and commercial requirements of upper limb amputees [57]. These requirements are drawn from seven independent studies performed previously, all assessing needs of upper limb amputees [22, 58–63]. The study defines a list of user requirements:

1. Execute basic Activities of Daily Living (ADL) grasps (power, pinch, lateral, pointing) for eating / dressing tasks
2. Provide sensory feedback
3. Reliable batteries + electrodes
4. Deliver strong, controllable grip force
5. Enable coordinated use with minimal visual attention

6. Look and feel anthropomorphic (size, weight, shape, colour)
7. Maintain stable, slip-free grasps
8. Allow object re-orientation and in-hand manipulation
9. Offer independent finger motion, especially thumb-index-middle
10. Handle small objects with precision
11. Improve heat dissipation
12. Run quietly (motor noise)
13. Include wrist flexion/extension (more than 1 passive DoF)
14. Supply durable, versatile gloves (flexible, tough, touchscreen-friendly)
15. Start from a natural open hand pose
16. Achieve long device lifespan (circa 150k cycles/year)

While this list is not necessarily complete, it provides a solid and recent foundation to understand the needs of upper limb prosthetic users.

Upper Limb Prosthetic User Satisfaction

Having defined the key functional and ergonomic expectations of prosthetic users, it is essential to evaluate the extent to which existing technologies satisfy these demands in practice. A series of published works about this reveal a complex framework of addressed needs. A similar type of study addresses the reasons for prosthetic device abandonment, a major indicator of user satisfaction.

A first study estimates the rejection rate in the years between 1980 and 2007 at 20% for individuals with upper limb deficiency [64]. A study by the same research group identifies critical factors in device abandonment [65]. The study divides factors into predisposing characteristics, established need, and enabling resources.

1. Predisposing characteristics: Higher rejection rates are associated with very distal or very proximal limb absence; congenital limb absence (especially low/high levels and bilateral) compared to acquired; females with high-level acquired limb loss compared to males; and specific age groups (4-10 years and 24-35 years). Phantom limb pain, residual limb pain, and skin issues are more

common among prosthesis users but are not decisive for rejection. Residuum length and dominant-hand loss are not associated with prosthesis rejection.

2. Established need: Prosthesis rejection is more likely with a lower perceived need for a device and among students compared to full-time workers. Self-reported activity levels are not associated with prosthesis rejection.
3. Enabling resources: Late initial fitting (either in childhood or after amputation), low user involvement in prosthesis selection, dissatisfaction with overall healthcare, and poor prosthetic technology performance are all strongly associated with higher rates of prosthesis rejection.

Another study identified common points of dissatisfaction among users [66].

1. Socket/harness discomfort; weight-induced arm-shoulder-back fatigue
2. Sound-side overuse: pain (tendinitis, arthritis, carpal tunnel)
3. Desire for a sense of "wholeness" in daily, family, and social roles
4. Poor fine-motor control for tasks like typing, eating, buttoning
5. Work-related strain (e.g., typing) causing sound-limb overuse
6. Recent bilateral amputees: high daily assistance needs, low activity, social isolation

Comfort and function remain key factors in upper limb prosthetic abandonment, as identified by another recent study [67].

Another type of study focuses on the important query of whether recent technological advancements contribute significantly to improve subject reception of devices. A first study identifies that most Electromyography (EMG) pattern-classification schemes still lack four features that matter for real-world prostheses: (1) simultaneous, proportional control; (2) integrated sensory feedback; (3) on-line adaptation to signal changes; and (4) fusion with other sensors for complex actions. Academic work has prioritised incremental gains in classification accuracy and, as a result, has drifted away from the practical needs of industry and clinics. Closing this gap requires research that targets intuitive control and system robustness, not just better classifiers, three of the four missing capabilities can in fact be built within the current classification framework if they are made a priority [68]. Similar

results are reported in another study. While many technological enhancements (lighter batteries, advanced control, cosmetic improvements) are now commercially available, they have not reduced abandonment, because they do not adequately address comfort, weight, functional dexterity, or sensory feedback, the features amputees continue to prioritise. Invasive solutions and high-quality, tailored training show promise, but have yet to reach enough users to shift the overall picture [69]. Finally, another study offers a slightly different perspective. Using any active prosthesis improves daily life compared with no prosthesis, but recent high-tech multi-DoF hands have yet to show clear functional advantages. Training quality, multiple-device ownership, and long-term adaptation drive better outcomes [70].

In summary, multiple studies agree that the absence of simultaneous and proportional control, integrated sensory feedback, and adequate comfort are key factors contributing to user dissatisfaction and device abandonment. Importantly, these are also areas with significant potential for improvement.

While much of the literature on assistive technology focuses on prosthetic users, similar challenges are experienced by individuals with neurological injury. These populations face equivalent motor deficits, and often more complex psychosocial consequences.

1.3.2 Non-amputation loss of function

While Section 1.3.1 detailed what amputees seek from upper-limb prostheses, people who retain the limb yet lose its function after stroke or cervical SCI confront a parallel, though distinct, set of challenges. The next pages therefore examine how non-amputation motor deficits shape quality of life, inform device requirements, and ultimately determine user satisfaction.

Impact on quality of life

Stroke survivors experience lasting quality-of-life losses. A 12-month Hong Kong cohort (n = 303) reported World Health Organization Quality of Life - BREF version (WHOQOL-BREF) domain scores of just 56-69% at three months, with further

decline in social-interaction and environment domains by one year; depression, far more than basic-ADL status, drove poorer scores [71]. A synthesis of 39 international studies confirmed Quality of Life (QoL) well below age-matched norms (43-83% reductions) and showed that depression, upper-extremity function, and social/leisure activity together explain up to 73% of QoL variance [72]. Consistent patterns appeared in a Canadian community sample 1-3 years post-stroke (n = 50): Ferrans and Powers' overall QoL was only moderate (circa 18.5/30), and clinical depression (32% prevalence) was the strongest predictor, followed by marital status, perceived social support, and Instrumental Activities of Daily Living (ADL) ability [73]. Taken together, these studies show that stroke imposes a persistent QoL burden, with psychosocial factors and arm-hand function often outweighing general physical disability in their impact. The importance of upper-limb motor impairment and its impact on disability and health is highlighted in many studies, emphasizing the urgency of improving outcomes to enhance the QoL of patients [72, 74–77].

Quality-of-life studies in high tetraplegia present a consistent but nuanced picture. A decade-long cohort follow-up reported uniformly high self-esteem and life satisfaction ($> 94\%$), while showing that day-to-day participation declines with age and is only marginally affected by environmental aids such as lifts or adapted vans; equipment ownership improves perceived QoL even when objective activity does not increase [78]. A broad review of quantitative work in C1-C4 injuries likewise found that most respondents were "glad to be alive" (83-92%) and rated their QoL as average or better (70-86%); activity level emerged as the strongest quantitative correlate of both QoL and self-esteem, prompting the authors to recommend qualitative studies to clarify underlying dimensions [79]. Complementing these data, a Polish cross-sectional comparison of tetraplegic and paraplegic adults showed similar overall WHOQOL-BREF scores (3.2/5) but different determinants: in tetraplegia, professional inactivity and loss of gait reduced QoL, and respondents identified restoration of hand function, second only to sexual function, as their top rehabilitation priority [80].

Studies of tetraplegic individuals suggest that while many report meaningful and satisfying lives, quality of life remains shaped by reduced participation, loss of independence, and limited opportunities for activity [78, 79]. Psychosocial factors, rather than physical impairment alone, appear central to long-term adjustment. Critically, among those with cervical injuries, recovery of hand function is consistently identified as a primary rehabilitation goal and a key determinant of perceived quality of life [80]. Studies show that restoring upper-limb function is rated among the highest priorities for individuals with cervical SCIs [81–83].

Upper Limb Rehabilitation Device User Needs

Motor deficits after stroke or cervical spinal cord injury (tetraplegia) have driven intensive research into user-centred rehabilitation and assistive devices. Li et al. reviewed 42 design requirements for home-use upper-limb robots for stroke survivors [84]. Forbrigger et al. interviewed stroke survivors and therapists about at-home robots, while Kobbelgaard & Kanstrup explored exoskeleton wishes of adults with tetraplegia [85, 86]. A clinician survey on robot uptake and systematic reviews of SCI technologies and hand-exoskeleton design corroborate a common set of priorities [87–89]. The following is a synthesis of needs expressed across the literature.

1. Deliver intensive, task-specific ADL practice (reaching, grasping, self-feeding, grooming) with adjustable assistance/resistance.
2. Provide intuitive, multi-modal control (voice, joystick, sip-and-puff, touch) that minimises setup time and visual attention.
3. Be lightweight, compact, and quickly donned/doffed; portable for home use or wheelchair mounting.
4. Ensure comfort & ergonomics: low weight on joints, no sharp edges, smooth & quiet actuation.
5. Adapt to different limb lengths, hand sizes, tone levels, and progression of recovery.
6. Include motivating feedback/gamified software with clear performance tracking and adjustable difficulty.

7. Guarantee safe, compliant motion with emergency stop and certified limits.
8. Remain affordable, reliable, and low-maintenance; batteries must last a typical day and not drain wheelchair power.
9. Fit into real home environments: small footprint, stowable, and usable from common seating or bed positions.
10. Support a wide range of independent ADLs most valued by users (eating snacks, drinking, scratching, page-turning, oral hygiene).
11. Offer an aesthetic, non-stigmatising appearance to encourage social participation in public spaces.

While not exhaustive, this list synthesises three decades of user-needs research and serves as a current benchmark for designers of non-prosthetic upper-limb rehabilitation technologies.

Upper limb rehabilitation device User Satisfaction

Understanding why some devices succeed in daily life while others are abandoned is essential. Mixed-methods studies of stroke and tetraplegia users identify recurring causes of dissatisfaction and abandonment [85, 87, 90, 91]:

1. Bulk/heavy hardware: inducing shoulder or trunk fatigue, or limiting wheelchair manoeuvrability.
2. Lengthy or complex donning/doffing: that requires caregiver assistance or disrupts routines.
3. Poor adaptability: to the specific impairment level of the user, hand size, or preferred tasks.
4. Jerky, noisy or unnatural motion: that feels unsafe or draws unwanted attention.
5. Discomfort or skin issues: from straps, cuffs, or heat build-up during prolonged wear.
6. High cost or lack of reimbursement: plus recurring maintenance expenses.
7. Technical unreliability: (frequent faults, software crashes) demanding expert support.

8. Insufficient battery life: or excessive drain on wheelchair batteries, limiting community use.
9. Incomplete functional coverage: (e.g., no hand/wrist assistance) so key ADLs remain impossible.
10. Demotivating training: repetitive, non-engaging tasks that fail to show clear progress.
11. Aesthetic or stigma concerns: about wearing a visibly robotic device in social settings.
12. Most critically, a lack of perceived functional gain: if daily independence does not improve, users abandon the device.

Like prosthetic users, individuals with neurological injury ultimately weigh comfort, usability, and real-world function above technical novelty. Devices that are bulky, complex, or deliver little everyday benefit are quickly set aside, regardless of clinical efficacy. Closing this satisfaction gap requires iterative, user-driven design that balances performance with the practical realities of home and community life.

1.3.3 Summary

In synthesis, recovery of lost upper-limb function is of paramount importance for patients who lost it following amputation, and for those who lost it due to neurological or other causes. Although individual needs vary, the user-centred insights summarised here reflect consistently reported priorities across multiple studies and populations. These findings set representative design targets for future technologies: comfort, intuitive multi-DoF control, and reliable sensory feedback. Accordingly, the next section surveys the current landscape of upper-limb prosthetic devices and neurorehabilitation devices (e.g., exoskeletons, orthoses, FES systems), evaluating how existing hardware and control strategies meet, or fall short of, these articulated needs.

1.4 Upper Limb Prosthetic Devices

Building on the user-centred priorities identified in the previous section, such as comfort, intuitive multi-degree-of-freedom control, and reliable sensory feedback, this section examines how current prosthetic devices aim to meet these needs.

The loss of upper-limb function has long motivated the development of replacement technologies, with efforts documented as far back as ancient civilisations. In the modern era, advances in materials, robotics, and control theory have accelerated progress significantly. Contemporary prosthetic devices can be broadly categorised according to both the level of amputation and the source of control. The anatomical level of amputation fundamentally influences the design constraints and functional expectations of a prosthesis. Common classifications include:

- Forequarter
- Shoulder Disarticulation
- Transhumeral
- Elbow Disarticulation
- Transradial
- Wrist Disarticulation
- Fingers

In terms of control strategies, prosthetic devices are typically grouped into three main categories:

- Passive (Cosmetic) Prostheses
- Body-powered prostheses
- Externally powered (active) prostheses

These two categorisations are rarely independent, with some types of prosthetic devices being more suitable to certain levels of amputation. This section outlines all three categories of prosthetic devices and then offers a deeper analysis of the current solutions available for active prostheses, as this is the field where research is the most active. Active prostheses represent the most promising method of replicating human hand functionality because of their potential to provide all of the Degrees of Freedom (DoFs) of a human hand in an intuitive manner without any

power input from the user [92]. These devices potentially offer the most versatile, natural, and power-efficient replacement for amputated hands and may represent a preferred long-term solution for patients [93].

1.4.1 Passive (Cosmetic) Upper Limb Prosthetic Devices

Passive prosthetic devices prioritise aesthetics and simplicity. Though they lack active control, they continue to serve important roles for cosmetic purposes, light support, and cost-sensitive contexts. These devices can be broadly categorised into 4 classes [94]:

- Static Prosthetic Hand
- Adjustable Prosthetic Hand
- Static Prosthetic Tool
- Adjustable Prosthetic Tool

Prosthetic hands offer a lifelike appearance and are used for a variety of activities [95]. Prosthetic tools have a mechanical appearance and are mostly designed for one specific activity which needs to be performed two-handedly [96]. Both passive prosthetic types can either be static or adjustable. Static prostheses cannot be moved at all [97]. Adjustable prostheses feature an adjustable grasping mechanism or parts of the prosthesis can be adjusted to multiple orientations (not taking into account the orientation of the wrist). Adjustment is performed by the sound hand or by pushing the prosthesis against the environment [98]. There are many reasons that an amputee may opt for a passive prosthesis rather than a body-powered or myoelectric one. Although passive partial hand prostheses lack active movement, such as a grip or release, they still do provide support for pushing, pulling, or holding objects. In addition, they can improve the function of the remaining fingers by providing them with a surface against which to manipulate objects. Furthermore, passive prosthetic devices are also much cheaper than their active counterparts [99, 100]. Despite their clear utility, passive prostheses fall short of providing a considerable functional benefit to amputees [100]. For a more detailed review of passive upper limb prosthetic devices, the reader is referred to review papers [94, 99].

1.4.2 Body-Powered Prosthetic Devices

Body-powered devices offer an intermediate solution between passive and active systems. They transmit user-generated motion mechanically and remain in widespread use due to their simplicity, robustness, and low cost. This definition includes all those devices that harness the movement of preserved parts of the body (usually the shoulder or the elbow) to control, through a system of cables, an upper-limb prosthetic device [99]. Body-powered mechanical hooks, mainly with one-DoF control, are popular solutions thanks to their low price, light weight, and easy maintenance. This type of prosthesis is also well suited for high-intensity work due to the control robustness. Also, because the subject must move their shoulder to open and close the hook, these systems have inherent proprioceptive feedback [101]. However, one of the major limitations of the hook solution is the low level of dexterity and non-anthropomorphic appearance. Body-powered hands have solved the anthropomorphic aspect while keeping the robustness of body-powered solutions [93, 102]. Activity-specific passive and body-powered prostheses can provide significant advantages to prosthesis users and are typically lower cost than alternatives. Body-powered prostheses have been shown to have advantages in durability; training time; and frequency of adjustment, maintenance, and feedback [103]. For further insights on the advantages and disadvantages of body-powered upper-limb prosthetic devices, the reader is referred to review papers on the subject [93, 99, 103].

1.4.3 Active Prosthetic Devices

Active prostheses constitute the most technologically advanced class, using motors and embedded electronics to restore lost function. As previously stated, active prostheses represent the most promising frontier in the complete restoration of lost functionality [92, 93, 104]. In this section of the thesis, an overview of available solutions from a hardware perspective is provided, with analysis of control strategies deferred to a subsequent section. For a deeper look into the available hardware

solutions for active upper limb prosthetics, the reader is referred to deep literature reviews on the subject [92, 93, 104, 105].

The review paper by Damerla et al., from 2021, provides a categorisation of externally powered upper limb prosthetic devices in four types: based on where actuators driving DoFs of the hand are placed: 1. Actuators housed in the digits, 2. Actuators housed in the palm, 3. Actuators housed in both the digits and palm, and 4. Actuators housed in the forearm. Examples with sources of these types of solutions are provided [92].

- Architecture 1; Actuators Housed in the Digits: This configuration is particularly suitable in design scenarios that prioritise anthropomorphic dimensions and independent digit control, though it often involves trade-offs in peak force and actuation speed. Examples include:
    1. i-Limb Quantum: Commercial multi-size hand with a motor-per-digit worm-gear layout that trades human-like power for many programmable, even waterproof, grasp patterns [93, 106].
    2. VINCENTevolution3: Similar motor-in-digit scheme (thumb single-phalange) that stays under human-hand mass while offering optional wrist modules and a wide library of grasps [93, 107].
    3. Research Hand: Small Brushless DC motors (BLDC) in each finger leaves palm real estate free for three hefty Alternating Current (AC) motors that drive thumb opposition and a powered two-DoF wrist [93, 108].
- Architecture 2; Actuators Housed in the Palm: This layout gives designers a big mechanical space in the palm, allowing them to optimise either dexterity, strength, speed, or cost while keeping size and inertia user-friendly, a versatility that explains why the majority of modern prosthetic hands adopt this layout. This architecture can be divided into 3 functional categories, each reported with an example.
    1. MultiGrasp-type; SmartHand Transradial Prosthesis: This device incorporates a high number of joints, a hybrid actuation scheme (independent

and under-actuated), and integrated sensors, on-board sensing and an anthropomorphic look while keeping weight near a biological hand [109].

2. Research Institute of Chicago (RIC)-type (one large motor for the four fingers); RIC Hand (Center for Bionic Medicine, Chicago): This design demonstrates the speed- and strength-oriented performance trade-offs characteristic of the RIC concept: two carefully sized palm motors deliver robust grip and fast closure while keeping the device compact enough to accept a powered wrist [110].
3. Greifer-type (single motor, 2-3 digits); Ottobock System Electric Greifer (8E34): This device achieves high grip strength and task reliability through a mechanically simple, rugged design, and is widely used in commercial settings [111].

- Architecture 3; Actuators Housed in Both the Digits and Palm: Hybrid hands split their mechanical layout, embedding larger motors or pumps in the palm for power-hungry tasks while tucking smaller drives or fluidic actuators inside the digits for fine motion.
    1. Fluidhand III: A palm-housed micro-hydraulic pump drives water through on-digit fluidic actuators via palm valves, achieving human-level fingertip forces and sub-second closing times in a hand weighing only slightly more than a biological one, although the digit actuators are constrained to synchronous flexion or extension at any given time [112].
- Architecture 4; Actuators Housed in the Forearm: The trade-off is anatomical: only amputees with sufficiently long residual limbs can accept forearm-based hardware. Where that constraint is met, Architecture 4 offers the most room for power-dense actuation and the closest mass distribution to a physiological arm, making it a promising platform for high-performance, multifunctional prostheses, particularly when anatomical length permits forearm integration.
    1. CyberHand: Five Direct Current (DC)-motor/planetary-gear drives in the forearm pull tendons to each digit, plus one palm motor for thumb opposition; achieves grasp forces above the clinical minimum

while keeping total limb mass below a natural male hand + forearm, giving an anatomically plausible inertia distribution [113].

2. Nickel-Titanium Shape Memory Alloy (NiTi-SMA) forearm hand: Six shape-memory-alloy bundle actuators in the forearm drive coupled finger flexion/extension; the very low actuator mass yields a limb well under the biological hand-forearm weight, though cooling-time limits restrain bandwidth [114].
3. Hydrogen-peroxide pneumatic arm (17-DoF): A monopropellant hydrogen peroxide gas-generator in the forearm powers five pneumatic cylinders that route tendons to the hand, wrist and elbow, promising higher force density than electromagnetic drives in a 2 kg system [115].

The above examples represent one of the many possible categorisations for upper limb prosthetic devices. Due to its completeness and clarity, the review by Damerla et al. provides a useful framework, but other authors provide different classifications [93]. An overview of possible control solutions for such devices is included in a later part of this thesis.

1.4.4 Summary

In summary, the landscape of active upper-limb prosthetic devices reveals a wide spectrum of mechanical architectures, each optimising distinct trade-offs among power, dexterity, size, and user comfort. While these technologies have advanced considerably, they are designed primarily for individuals with limb loss. However, many individuals with upper-limb impairments retain their limb but experience substantial motor dysfunction. For these users, alternative rehabilitation solutions, distinct from prosthetic replacement, have emerged. The following section explores these non-amputation interventions, examining mechanical assistive devices and electrophysiological techniques developed to restore function in patients with intact but impaired limbs.

1.5 Non-amputation rehabilitation solutions

While the previous section examined prosthetic options for individuals with limb loss, many patients retain their limb but suffer substantial motor impairment. For these users, a different set of rehabilitative technologies has emerged. These approaches fall into two broad categories: mechanical assistive devices (such as exoskeletons and robotic trainers) and electrophysiological interventions (including functional electrical stimulation, neuroprostheses, and brain-computer interfaces). This section provides a structured overview of both classes, highlighting key mechanisms, classifications, and therapeutic applications.

1.5.1 Mechanical Assistive Devices

Exoskeletons

Exoskeletons aim to restore motor function by applying external mechanical support to assist or guide limb movement. This type of solution is mostly used to help the recovery of functionality in stroke victims [116]. Depending on the level of impairment, solutions exist to drive the arm as a whole or independent digits. The former category is of wide interest and deeply dealt with in the relevant academic literature. For further information, the reader is referred to review papers on the subject [117–119]. In this brief section, the focus is on a subset of these technologies: exoskeletons for the rehabilitation of the hand and fingers.

The paper by Haarman et al. divides assistive hand exoskeletons designed to restore finger extension in stroke rehabilitation into three portable, ADL-oriented design families [116]:

1. Cable-driven systems route tendons along the dorsum of the fingers inside a glove framework [120–123]. Advantages: compact actuation and good torque transmission. Limitations: glove donning is difficult without help [124]; cable routing generates unwanted axial forces that can irritate joints and soft tissue.
2. Pneumatic soft exoskeletons inflate air bladders or bellows to straighten the digits [125, 126]. Advantages: inherently compliant, reducing shear. Limitations: lack of rigid guidance can cause misalignment, discomfort,

or secondary injury; achieving therapeutic torque requires bulky, heavy compressors, which curtails portability [127].

3. Spring-operated devices (e.g., SaeboFlex and SaeboGlove) rely on extension springs or elastic bands to open the hand [128]. Advantages: simple, lightweight, and fully passive. Limitations: patients must generate high voluntary flexion torque to overcome spring stiffness when grasping; if flexion strength is insufficient, functional benefit during activities of daily living is minimal.

Across all three approaches, designers must balance ease of donning, alignment accuracy, actuator weight, and user-generated flexion effort to deliver practical, everyday assistance for stroke survivors. This paper provides a good overview of the hand exoskeleton landscape, but other authors suggest different categorisations and provide further examples. Sun et al. propose a distinction between soft-glove-based and linkage-type exoskeletons, posing that, compared with the linkage-type exoskeletons, the soft gloves are difficult to ensure enough force for rehabilitation training [121, 129–131]. Conversely, Li et al. provide a distinction based on the actuator system [132]. It is also important to state how, while these solutions are mostly applied for therapeutic purposes, it is also common to use them as permanent solutions, thus restoring functionality with a permanent external assistive device. For further information, the reader is referred to the original studies mentioned above and to a further literature review on the subject [127].

Robotic approaches

A related solution to exoskeletons is represented by robotic assistance in rehabilitation. Much like the previous section, these solutions are mostly applied on stroke patients. Rehabilitation robots harness neuroplasticity to restore motor function through repetitive, quantitative training [133–136]. Different studies provide different classifications for these solutions. A review by Qassim et al. divides them along two axes:

- Treatment approach

  - Continuous Passive Movement (CPM): robot drives the limb without patient effort, lowering tone and activating sensorimotor cortex [137, 138].
  - Active-assisted movement: robot executes motion only after a patient-generated cue (e.g., EMG) and yields greater motor gains than CPM. Current research favours this mode [137, 139, 140].
- Mechanical structure
  - End-effector robots: single distal handle; adaptable trajectories but limited rotation; now used for bilateral mirroring therapy [141, 142].
  - Exoskeleton robots: joint-aligned braces delivering precise torques in compact workspaces; unsuitable for bilateral use and costly to duplicate for both limbs [143, 144].

Other studies, such as the review by Rehmat et al., study the robotic systems used for upper limb rehabilitation based on their mechanical structure, control system, and clinical applications [117]. For further insights, the reader is referred to the review studies mentioned above, and to additional ones [145, 146].

1.5.2 Electrophysiological Interventions

FES

Functional Electrical Stimulation (FES) is the application of electrical pulses to peripheral nerves or muscles synchronously with the voluntary movement of the patient, so that the resulting muscle contractions enhance or complete the intended action and thereby promote activity-dependent neuroplasticity [147, 148]. FES shows promise as a rehabilitation strategy after stroke, with a review by Eraifej et al. identifying a statistically significant improvement in ADL when applied within 2 months post-stroke. However, the currently available evidence prevents firm conclusions regarding its effectiveness or optimal timing. High-quality, large-scale randomised control trials are needed to clarify the therapeutic value of upper limb FES [149]. FES for upper limb applications can be broadly categorised, according to Khan et al., in three types [150]:

1. Open-loop FES : Therapist-programmed stimulation patterns run without patient-derived feedback [151].
2. Closed-loop Brain-Computer Interface (BCI)-FES (Electroencephalography (EEG)-FES): BCI converts motor-imagery EEG signals into real-time stimulation commands [152–154].
3. Closed-loop EMG-controlled FES : Muscle-activity feedback (EMG) modulates stimulation amplitude and timing in real-time.

FES is gaining traction, especially in its closed-loop application, as a solution to improve the recovery of patients affected by upper-limb impairment, doing so while not increasing their dependence on healthcare professionals and the health system [150]. FES applications in tetraplegia were also investigated consistently in the academic literature [155]. These solutions, much like exoskeletons, can also be permanent. For further insights, the reader is directed to the two reviews mentioned above [149, 150].

Neuroprostheses and BCIs

A neuroprosthesis is an engineered device that interfaces directly with the nervous system, peripheral or central, to restore, supplement, or modulate lost sensory-motor or autonomic functions [156]. Neural interfaces, which include BCIs and myoelectric interfaces, allow control of neuroprostheses or FES and enable patients with little or no residual limb functions to mobilise the paralysed limb through imagined or attempted movements. Importantly, neural interfaces also allow closed-loop, functionally contingent proprioceptive feedback [157]. In practice, neuroprostheses can be used to control the body of a subject through brain signals, bypassing natural control pathways that can be damaged or missing.

The usefulness of neuroprostheses in rehabilitation has been investigated in many review studies, most concluding that the use of BCIs and motor neuroprostheses in stroke neurorehabilitation shows promise in restoring lost function, although challenges remain [157]. Another review study, by Shokur et al., frames upper-limb

neuroprostheses as modular systems built from three functional blocks: (1) motor-intention decoding, (2) movement actuation, and (3) sensory feedback acquisition and delivery. Each block consists of interchangeable technological modules that can be selected and combined independently. By cataloguing the state-of-the-art for every module and illustrating how research teams assemble them in human demonstrations, the authors show that progress in neuroprostheses stems either from improvements within a single module or from innovative recombinations of existing ones. Continued gains in reliability at the module level are expected to yield unforeseen neuroprosthesis configurations capable of addressing a wider range of motor disorders and moving neuroprostheses from laboratory or clinical prototypes towards everyday applications [158]. Finally, a third review considered for this thesis, by Hoehler et al., concludes that hybrid neuroprostheses have a positive effect on Upper Limb (UL) recovery after stroke [159].

1.5.3 Summary

In summary, non-amputation rehabilitation technologies span a broad spectrum, from mechanically driven exoskeletons to advanced neural interfaces, each offering unique advantages and trade-offs in terms of portability, usability, and therapeutic efficacy. While mechanical assistive devices focus on restoring movement through external structure and guided repetition, electrophysiological solutions aim to activate or bypass damaged neural pathways directly. Together, these technologies reflect a growing commitment to personalised, functionally meaningful rehabilitation. However, their clinical effectiveness, particularly in unsupervised, everyday settings, remains an active area of investigation.

The effectiveness of both prosthetic and non-amputation rehabilitation devices ultimately depends on their ability to interpret user intent and deliver appropriate movement or feedback. Whether actuating a myoelectric hand or coordinating an exoskeleton during stroke recovery, these systems require reliable control interfaces. The following section surveys the core biosignal sources, neural and muscular, that

enable such interaction, and examines the technologies used to acquire, interpret, and apply them in real-world rehabilitation.

1.6 Biosignal Interfaces for Intent Detection in Upper-Limb Devices

Biosignal interfaces play a foundational role in translating user intent into actionable commands for upper-limb rehabilitation devices. These signals span a continuum from non-invasive brain recordings to peripheral nerve interfaces, each offering distinct trade-offs in invasiveness, signal quality, and clinical feasibility. This section surveys these signal sources, organised by decreasing anatomical proximity to the cortex, focusing on central and peripheral nervous system signals, excluding myoelectric signals which are addressed separately in Section 1.9. In both domains, research is converging on bidirectional pathways that pair motor intention with sensory feedback, aiming to restore more natural, intuitive control. Critically, the ability to reliably extract usable information from these signals, despite noise, biological variability, or hardware limitations, is what enables their transformation into functional control channels for assistive technologies.

These neural interfaces underpin the device families introduced in the previous two chapters. Section 1.4 covered active upper-limb prostheses, while Section 1.5 explored rehabilitation tools such as exoskeletons, robotic trainers, and neuroprostheses. All rely on the ability to access user intent through the biosignal sources described here.

1.6.1 Central Nervous System Signals

BCIs designed for upper-limb rehabilitation device control can be grouped into non-invasive and invasive approaches, each exploiting distinct CNS measurement modalities. Non-invasive sensors avoid surgery but must contend with signal attenuation through the scalp and skull, whereas invasive grids provide higher fidelity at the cost of neurosurgical risk and long-term biocompatibility challenges [160–162]. The following sections first cover non-invasive techniques, EEG and

Functional Near-Infrared Spectroscopy (fNIRS), before turning to the invasive Electrocorticography (ECoG). Comprehensive surveys on CNS control solutions for prosthetics and neurorehabilitation can be found in relevant review papers [160–168].

Non-invasive CNS Interfaces

EEG dominates academic BCI research owing to its millisecond-scale temporal resolution, low hardware cost, and complete non-invasiveness [164, 165, 169]. For amputees who lack functional residual musculature, EEG-based BCIs bypass the need for myoelectric signals and can decode a wider repertoire of grasp and wrist intentions, e.g., pincer versus power grasp, using only inexpensive scalp electrodes [170–174]. Recent work has demonstrated real-time classification of up to ten individual grasp patterns with information-transfer rates competitive with surface EMG [175].

Despite these advantages, three obstacles still block everyday deployment: (1) hardware burden: wet electrodes, wiring, and cap donning remain cumbersome [160, 176, 177]; (2) information-rate trade-offs caused by low signal-to-noise ratio through the skull [178, 179]; and (3) algorithmic maturity: state-of-the-art decoders require user-specific calibration and substantial training data [180–182]. Ongoing efforts focus on dry-electrode technology and miniaturised headsets [183–185], hybrid sensing (see below), and self-calibrating machine-learning pipelines to ease clinical translation [186, 187].

Optical BCIs measure haemodynamic changes associated with neural activity. fNIRS is intrinsically immune to electromagnetic interference and motion-induced cable artefacts, making it attractive for real-world use where EEG suffers [163]. Lightweight scalp-mounted optodes provide a safe, comfortable interface for long-term wear, particularly valuable when residual muscle activity is minimal or stable electrode anchoring is impossible [188]. The 700-1000 nm optical window enables robust monitoring of cortical oxygenation with low instrumental noise that can be further attenuated via low-pass filtering and standardised pipelines [189–191].

Hybrid EEG-fNIRS strategies exploit complementary temporal EEG and spatial/metabolic fNIRS information to mitigate the weaknesses of each modality, yielding improved decoding accuracy in noisy environments [192, 193]. Such hybrids have shown particular promise for high-level amputees experiencing elevated cognitive load and unstable electrode contact [175].

Invasive CNS Interface: ECoG

ECoG records field potentials directly from the cortical surface via implanted subdural grids, offering higher spatial resolution and broader bandwidth than scalp EEG while remaining safer and more stable than penetrating microelectrodes [194, 195]. Classification accuracies of 68-84% for individual finger movements have been reported [196–198], and fast ECoG-BCIs are approaching clinical viability for restoring communication and robotic-arm control in amyotrophic lateral sclerosis and tetraplegia [168].

Nonetheless, unresolved issues in long-term signal stability, hermetic packaging, power delivery, and ethical consent currently preclude commercial adoption [160]. For prosthetic hands, outstanding challenges include miniaturising implantable electronics, developing bi-directional (motor and sensory) interfaces, and establishing surgical risk-benefit balance for otherwise healthy amputees.

1.6.2 Peripheral Nervous System Signals

While CNS-based control provides the most direct route to the brain, many clinical systems instead leverage the PNS, where signals can be accessed with less surgical risk, more stable interfaces, and broader clinical precedent. These interfaces span a calibrated trade-space: the closer the electrode approaches individual axons, the greater the selectivity, and the higher the surgical and biocompatibility burden. Comprehensive discussions of surgical technique, device evolution and clinical outcomes can be found in relevant review papers [199, 200].

Extraneural Cuff Interfaces

Epineurally positioned cuffs circumferentially wrap the nerve, providing a direct electrical contact without penetrating the parenchyma. Helical, spiral and flat-interface (FINE/C-FINE) variants now deliver decade-scale, somatotopically selective stimulation or recording in humans; lead fatigue and low-grade infections at percutaneous exits remain the principal long-term hazards [201–204].

Inter-fascicular electrodes

By inserting thin blades between fascicles, inter-fascicular devices such as SPINE and multigroove electrodes achieve higher selectivity than cuffs while preserving fascicular integrity. Demonstrations are largely confined to acute or short-term animal models, and questions of chronic micromotion and encapsulation are unresolved [205–208].

Intra-fascicular Arrays

Longitudinal (LIFE), transverse (TIME) and high-density (USEA) intra-fascicular arrays pierce one or more fascicles, enabling axon-level stimulation and recording. Early human trials report finger-specific motor control and graded tactile feedback, counterbalanced by elevated risks of insertion trauma, lead failure and early functional decline [209–212].

Regenerative Interfaces

Regenerative sieves, scaffolds and micro-channel electrodes position microelectrodes within conduits through which severed axons are encouraged to regrow, promising near-single-axon resolution. Despite impressive selectivity, these constructs face ongoing challenges related to optimal channel porosity, compressive axonopathy and long-term mechanical durability [213–218].

Clinical Outlook

Hybrid control paradigms, pairing a stable muscle or cuff channel for gross motion with a limited number of intra- or regenerative contacts for fine motor and sensory

feedback, represent the most credible near-term pathway. Demonstrating infection-free longevity and stable electrode-nerve coupling over multi-year horizons remains the decisive translational hurdle.

1.6.3 Summary

Having surveyed cortical and peripheral nerve interfaces, attention is now shifted to the most widely used biosignal in upper-limb rehabilitation: electromyography (EMG). The following section introduces the physiological basis and signal properties of EMG, laying the groundwork for its later analysis as a control modality.

1.7 Electromyography (EMG): Principles and Instrumentation

EMG refers to the measurement of electrical potentials generated by muscle fibres during contraction, typically recorded via electrodes placed on or within the skin. It provides a practical and widely adopted method for accessing efferent motor commands in residual musculature, offering a favourable trade-off between performance, invasiveness, and usability. Among its various forms, sEMG has become the dominant modality for upper-limb rehabilitation and prosthetic control systems, owing to its complete non-invasiveness, ease of deployment, and relatively high signal-to-noise ratio. sEMG captures the summated motor-unit action potentials that propagate through superficial musculature, with both amplitude and dominant frequency scaling with contraction force, making it a reliable proxy for volitional effort [219, 220]. Since its initial demonstrations in the 1940s and the introduction of the first commercial myoelectric prosthesis in 1960, sEMG has remained the default control interface due to its low latency and minimal cognitive demand [221–223].

Nevertheless, sEMG is not without limitations. It remains sensitive to motion artefacts and suffers from variability related to the skin-electrode interface across sessions and users [224–226]. To address these shortcomings, alternative EMG modalities have been developed. Epimysial and intramuscular EMG (iEMG) offer improved signal fidelity and long-term stability, albeit at the cost of minimally

invasive surgical procedures and potential hardware-related complications [227–232]. More recently, targeted muscle reinnervation (TMR) and regenerative peripheral nerve interfaces (RPNIs) have emerged as surgical bioamplification techniques that increase control bandwidth while simultaneously reducing neuroma-related pain [233–237].

This section provides a focused overview of the physiological basis of the EMG signal, biophysical properties, and acquisition technologies. These foundational insights are essential for understanding how EMG can be harnessed to enable intuitive and reliable human-machine interfaces. For comprehensive reviews of EMG-based interfaces and decoding strategies, the reader is referred to relevant articles and academic texts [93, 223, 238].

1.7.1 Muscle and Motor-Unit Physiology

A motor unit is defined as a single α-motoneuron together with the muscle fibres innervated by its axon. The conduction velocity of action potentials along these fibres depends primarily on fibre diameter, typically ranging from 2 to 6 m/s [239, 240]. Muscle fibres are commonly classified into three phenotypes: type I (slow oxidative), which support low-force, fatigue-resistant activity; type IIa (fast oxidative-glycolytic), which combine moderate speed and endurance; and type IIx (fast glycolytic), which produce high force but fatigue rapidly [241].

Voluntary muscle force is modulated by two central mechanisms. First, motor units are recruited in a fixed order according to Henneman's size principle: smaller, fatigue-resistant units are activated before larger, fast-fatiguing ones [242]. Second, the central nervous system adjusts the discharge rates of active units, increasing their firing frequencies from around 4 Hz at threshold to over 30 Hz during maximal voluntary effort [243]. With sustained contraction and fatigue, the electrical and metabolic properties of the fibres change, resulting in broader action potentials, reduced median spectral frequency, and increased root-mean-square amplitude [244].

1.7.2 Origin of the Electromyographic Signal

When a nerve impulse reaches the neuromuscular junction, the muscle fibre membrane depolarises and an intracellular action potential propagates bidirectionally along the fibre. The line-source cable model describes the fibre as a distributed conductor with intracellular and extracellular resistances and membrane capacitances [245]. The superposition of all fibre currents from a single motor unit generates a Motor Unit Action Potential (MUAP). The EMG signal detected at an electrode represents the algebraic sum of all MUAPs generated by fibres within the detection volume of the electrode, shaped by spatial filtering and attenuation through the intervening tissue.

1.7.3 Recording Modalities

Intramuscular and Implanted EMG

Intramuscular Electromyography (iEMG) involves the insertion of fine-wire or needle electrodes directly into the muscle tissue to sample the activity of individual motor units or small motor-unit pools. These signals typically reach amplitudes of 10-15 mV and contain frequency components up to 1.5 kHz, making them particularly valuable in neuromuscular diagnostics and basic physiological research [246]. For long-term use, chronically implanted electrodes can be anchored within or onto muscle surfaces. Epimysial and intramuscular leads eliminate the need for daily placement, offering improved signal-to-noise ratio and enhanced long-term stability [227, 247]. Although the surgical procedures carry inherent risks, such as lead migration, tissue encapsulation, or wire fracture, longitudinal take-home studies have demonstrated the feasibility and durability of implanted EMG systems in real-world control tasks [230].

Surface EMG

sEMG is acquired using disposable silver-silver-chloride electrodes placed on prepared skin overlying the target muscle. The recorded signal represents the superposition of activity from dozens of simultaneously active motor units, resulting in a

stochastic interference pattern. Its dominant power lies between 20 and 250 Hz, and its peak-to-peak amplitude rarely exceeds 2 mV [239]. Two common electrode configurations are used: monopolar setups, which place a single active electrode over the muscle and reference it to a distant site, capturing high-fidelity signals but also common-mode noise, and bipolar setups, which record the difference between two closely spaced electrodes to suppress power-line and electrocardiographic interference [246].

Conventional sEMG systems typically employ two to four channels and form the basis of most commercial myoelectric prostheses. The technique is entirely non-invasive and supports straightforward proportional control strategies. However, sEMG remains vulnerable to motion artefacts, sweat-induced impedance shifts, and crosstalk between adjacent muscles. These limitations are particularly problematic in high-level amputees, where limited residual musculature reduces the degrees of freedom available for reliable signal mapping [224, 225].

High-Density Surface EMG (HD-sEMG)

High Density surface Electromyography (HD-sEMG) extends the conventional surface approach by using arrays of 32 to over 100 electrodes, typically less than 3 mm in diameter and spaced at 10 mm or less [248]. This dense spatial sampling provides several key advantages. The small pick-up area and short inter-electrode distance reduce crosstalk from neighbouring muscles and improve spatial selectivity. The resulting maps of instantaneous amplitude across the grid can reveal activation heterogeneity, shifting innervation zones, and localised fatigue.

Advanced signal processing techniques, such as blind source separation and convolution-kernel compensation, can be applied to multi-channel HD-sEMG data to extract the discharge timings of individual motor units during natural movements. This enables in vivo investigations of motor-unit recruitment and rate coding. Furthermore, tracking the temporal shift of the same motor-unit action potential across adjacent electrodes allows for the estimation of conduction velocity, which has diagnostic utility in assessing myopathies and channelopathies.

Beyond research applications, HD-sEMG has been shown to improve robustness against electrode displacement, an important consideration for clinical control systems [249]. However, the technique also involves trade-offs: bulkier hardware, increased data throughput, and longer calibration procedures are often required.

1.7.4 Signal Properties and Interference

During maximal voluntary contraction, the root-mean-square amplitude of the sEMG signal rarely exceeds 1 mV, although electrically evoked responses can reach peak values of 5-6 mV. The composite spectrum is shaped by the low-pass filtering effects of skin, subcutaneous fat, and electrode area, with median frequencies typically ranging from 60 to 100 Hz under high-force conditions. Principal sources of noise include intrinsic electronic noise from amplifiers and converters, common-mode interference from power lines and electrocardiographic fields, motion artefacts caused by electrode-skin displacement, and crosstalk from adjacent muscles with similar fibre orientations [250–252]. These issues can be mitigated through high common-mode rejection ratios, careful shielding, digital notch or spectral interpolation filters, rigid electrode fixation, high-pass filtering above 20 Hz, and appropriate electrode size and spacing.

1.7.5 Electrode Technologies and Interface Models

Biopotential electrodes are transducers that convert ionic currents within biological tissue into electronic currents suitable for measurement and amplification. They enable the recording of low-amplitude signals such as the electrocardiogram (ECG), electroencephalogram (EEG), and particularly the electromyogram (EMG), which span from microvolts to millivolts and arise from ionic exchanges across cell membranes [253, 254]. An effective electrode interface requires low impedance, chemical and mechanical stability, and minimal sensitivity to motion artefacts [255].

Electrode-Tissue Interface and Equivalent Circuit

At the metal-electrolyte junction, electrochemical reactions establish a double-layer interface and generate a half-cell potential (E_{hc}), which depends on the reactivity of the electrode material. More reactive metals tend to acquire more negative potentials. The complete electrode-skin interface can be modelled as a half-cell voltage source in series with an electrolyte resistance (R_{s}) and a parallel combination of resistance (R_{d}) and capacitance (C_{d}), representing faradaic and displacement currents, respectively. At low frequencies, the system is dominated by R_{d}, while C_{d} becomes more influential at higher frequencies. Additional impedance arises from the skin itself, particularly the stratum corneum.

Motion Artefact and Mitigation

Motion artefacts primarily result from disturbances in the electrode-electrolyte double layer, which induce fluctuations in E_{hc} and introduce low-frequency noise into the signal [256]. Strategies to mitigate these artefacts include abrading or cleaning the skin to reduce impedance, rigid electrode fixation, and the use of non-polarizable electrode materials. When necessary, high-pass filtering below 20 Hz may be applied, though this risks attenuating physiological signal components [246].

Electrode Materials

Silver-silver chloride (Ag/AgCl) remains the clinical and research standard due to its low impedance, good biocompatibility, and near-non-polarizable behaviour. This is achieved through chloride exchange that stabilises surface charge. Alternatives such as platinum, gold, and carbon are more polarizable and therefore less effective for low-noise biopotential recording [256].

Non-Invasive Electrode Designs

Conventional sEMG commonly employs paired Ag/AgCl disc electrodes placed over relevant muscle bellies. Electrode configurations may be monopolar, offering high signal fidelity but greater susceptibility to common-mode interference, or bipolar,

which suppresses noise by subtracting signals from two closely spaced sites [239, 246]. Clinically, Ag/AgCl and KCl gel electrodes remain the standard because the chloride electrolyte provides a stable and reproducible half-cell potential, while the gel maintains low and consistent skin-electrode impedance, ensuring high signal quality and reducing motion artefacts during extended recordings. Variants include suction electrodes that adhere without straps, floating electrodes recessed in gel to stabilise the interface, and flexible or textile-based dry electrodes that improve comfort and day-long wearability but tend to exhibit higher impedance [257–261].

High-Density and Miniaturised Arrays

As discussed earlier in the context of recording modalities, HD-sEMG arrays also present distinct considerations in terms of electrode design and spatial resolution. HD-sEMG arrays comprise 8 to 128 miniaturised electrodes (typically <3 mm in diameter) arranged in tight grids. Given the small surface area of the electrodes, conductive gel is usually employed to reduce the impedance of the skin-electrode interface. These configurations allow for detailed spatial mapping of muscle activity and the decomposition of motor-unit action potentials [248]. Smaller electrode areas and closer spacing reduce crosstalk between adjacent muscles, while integrated preamplifiers mounted directly on the skin help preserve signal quality and suppress noise [250, 252].

Invasive Electrodes

Invasive electrodes, including fine-wire and needle designs, penetrate the muscle tissue and offer high spatial selectivity and bandwidth (up to 1.5 kHz), enabling the isolation of single-fibre or motor-unit action potentials. These electrodes are indispensable in motor-unit physiology studies but are generally unsuitable for routine or long-term clinical monitoring due to their invasiveness [256].

1.7.6 Summary

Electromyography provides a non-invasive or minimally invasive window into neuromuscular activity by detecting the electrical potentials generated by contracting

muscle fibres. Intramuscular electrodes offer fine spatial selectivity, conventional surface electrodes enable global monitoring, and high-density surface arrays combine spatial resolution with convenience. Reliable EMG acquisition demands careful consideration of tissue filtering, electrode design, and interference suppression.

Yet capturing high-quality signals represents only the foundational stage. The translation of these electrical patterns into meaningful human intent critically depends on advanced decoding algorithms, as discussed in detail in the next section.

1.8 Developments in Machine Learning

This chapter introduces the foundations of modern machine learning in order to motivate the algorithms later applied to EMG data. After outlining the role of artificial neural networks, the text summarises learning principles, optimisation techniques, and specialised architectures that exploit spatial, temporal, and contextual structure.

Artificial Intelligence refers to systems designed to perform tasks that normally require human intelligence, such as perception, reasoning, and decision-making. Within this field, machine learning enables algorithms to discover patterns directly from data rather than relying on hand-crafted rules [262].

1.8.1 Neural Networks

A particularly influential subset of machine learning is deep learning, which employs multilayered structures called artificial neural networks. These networks are loosely inspired by the brain and learn complex input-output mappings through iterative optimisation. Crucially, they can extract relevant features automatically when sufficient data are available, avoiding manual feature engineering. Deep neural networks now underpin state-of-the-art results in image analysis, natural language processing, biomedical signal understanding, and many other domains [263]. Their layered hierarchy captures progressively abstract representations, rendering them effective for high-dimensional and unstructured data.

Neural networks are not without limitations. They are often criticised for limited interpretability, and their performance depends heavily on data quality

and quantity. Training large models is computationally expensive and requires careful hyper-parameter tuning. Nevertheless, their versatility keeps them central to contemporary research and industrial practice. In this section, an overview of the most notable types of Neural-Network-based solutions, for the scope of control of rehabilitation solutions, is provided. For a more detailed description of the solutions employed, the reader is referred to the defining papers, cited with the relevant passage, or to in-depth texts [263–265]. The work by Alom et al. for an in-depth review of relevant studies is also recommended [266].

Artificial Neurons and Activation Functions

The basic computational element of a neural network is the perceptron. Each perceptron receives a vector of inputs, computes a weighted sum, adds a bias, and applies a non-linear activation function:

$$y_k \;=\; \phi_k\!\left(\sum_{m=1}^{M} w_{km}x_m + b_k\right). \tag{1}$$

Here x_m denotes the m-th input, w_{km} its weight for neuron k, b_k the bias, and ϕ_k the activation [267]. Activation functions introduce non-linearity, which is essential for approximating complex relationships [264]. Common choices include the logistic sigmoid, the hyperbolic tangent, and the Rectified Linear Unit (ReLU). A softmax function is typically used in the final layer when class probabilities are required [265].

Network Architecture: Layers, Depth, and Width

Perceptrons are organised into layers. Within a layer, every perceptron receives the full input vector, yet each is parametrised by its own weights and bias, allowing the layer to extract multiple features simultaneously. If the input has M elements and the layer contains N perceptrons, the layer produces an N-dimensional output vector through N independent transformations. Successively stacking layers forms a network in which the output of one layer serves as the input to the next. Lower layers detect simple patterns, whereas deeper layers combine those patterns into abstract concepts.

The first layer is called the input layer, the final layer the output layer, and those in between the hidden layers. The depth of the model equals the number of hidden layers plus the output layer, while the width of a layer is its number of perceptrons. Depth increases representational power, whereas width increases capacity; both must be chosen to balance expressiveness against overfitting [264].

Learning in Neural Networks

Learning adjusts the weights and biases so that the network realises a desired input-output mapping. For each training example, the input is propagated forward to yield a prediction. The prediction is compared to the ground truth by a loss function such as mean squared error, mean absolute error, or cross-entropy [264]. Gradients of the loss with respect to every parameter are computed efficiently by the back-propagation algorithm. Parameters are then updated, typically with a variant of gradient descent, to reduce the loss. Repeated over many examples and epochs, this process enables the network to generalise to unseen data.

Classification and Regression

Neural networks address two main supervised problem types. In classification, the target output is a discrete label; the final activation of the network often produces class probabilities. In regression, the target is a continuous value, and the network outputs real-valued predictions. The choice of loss function and final activation depends on which type of problem is being solved [268].

Optimisation and Regularisation

Parameter updates are governed by optimisation algorithms. Basic gradient descent uses the steepest descent direction scaled by a learning rate. Practical training usually relies on stochastic or mini-batch variants for efficiency, together with enhancements such as momentum, RMSprop, Adagrad, or Adam, which incorporate adaptive learning rates and accelerate convergence [269]. Optimisation is complicated by issues such as overfitting and unstable gradients. Overfitting is mitigated through regularisation techniques including dropout, weight decay,

and data augmentation. Vanishing or exploding gradients are alleviated with careful weight initialisation, non-saturating activations, gradient clipping, and normalisation layers [269].

Architectural Variants

Standard neural networks, called fully connected networks or multilayer perceptrons, treat input data as simple lists of numbers. This works well for basic tasks, but it ignores important patterns in more complex data like images, time series, or language. Specialised architectures have been developed to make better use of such structure.

Convolutional Neural Networks (CNNs) are especially useful for images and other data arranged in grids. Instead of looking at the whole image at once, CNNs use small filters (or kernels) that slide across the data to detect patterns, like edges, shapes, or textures. Each filter creates a feature map that highlights where that pattern occurs. Stacking multiple filters helps the network understand complex visual information. CNNs also use pooling layers to shrink the feature maps, which makes computation faster and helps the network focus on the most important parts of the image [270].

Recurrent Neural Networks (RNNs) are designed for sequences, like time series or text. They remember past inputs using an internal memory called a hidden state, which helps them recognise patterns over time. However, basic RNNs struggle with long sequences, they tend to forget what happened earlier. Improved versions like Long Short-Term Memory (LSTM) and Gated Recurrent Unit (GRU) include special gates that decide what information to keep or forget, allowing the model to learn longer-term dependencies more effectively [271–273].

Transformer networks are a newer type of model originally designed for language tasks but now used widely in many areas. Unlike RNNs, they do not process data step by step. Instead, they use a mechanism called self-attention, which allows them to focus on the most relevant parts of the input all at once, regardless of position. This makes them much faster to train and better at handling long-range relationships. Since Transformers do not have a built-in sense of order, they use positional

encodings to keep track of where each item is in the sequence. Today, Transformers are used not only in text but also in image, audio, and biological data analysis [274].

While neural-network-based Machine Learning (ML) solutions have received considerable attention in recent years, other solutions have also been of paramount importance both within and without the biological signal processing domain.

1.8.2 Classical Machine Learning Methods

This short section lists non-neural-network-based ML methods, summarising their definitions, advantages, and limitations. As with neural networks, these classical models can be applied to either classification or regression tasks depending on the problem setup. For a more complete description of each solution, the reader is referred to dedicated texts [263, 275].

Support Vector Machines (SVM)

Support Vector Machines are supervised learning models that aim to find the optimal hyperplane separating data into classes with the maximum margin. They are effective in high-dimensional spaces and are particularly robust for small to medium-sized datasets. However, Support Vector Machines (SVMs) can be computationally intensive and are less effective with noisy or overlapping data [276].

Random Forests

Random Forests are ensemble learning methods that aggregate the predictions of multiple decision trees to enhance predictive performance and robustness. A decision tree is a flowchart-like structure where each internal node represents a decision rule on a feature, each branch a possible outcome, and each leaf a predicted class or value. Trees are easy to interpret and fast to train, but individual trees are prone to overfitting and instability. Random Forests address these issues by training many trees on different subsets of the data and features (via bootstrapping and random feature selection), then combining their outputs, typically by majority vote for classification or averaging for regression. This ensemble strategy significantly improves generalisation, reduces variance, and increases resilience to noise and

outliers. However, the cost is reduced interpretability compared to a single decision tree and increased computational overhead. Despite this, Random Forests remain a strong default choice for many structured-data problems [277].

K-Nearest Neighbours (KNN)

K-Nearest Neighbour (KNN) is a simple, non-parametric algorithm that classifies or predicts a data point based on the majority class (or average output) of its k nearest neighbours in the feature space. It requires no training phase and adapts quickly to new data. However, KNN suffers from high memory requirements and sensitivity to the choice of k and feature scaling [278].

Linear Discriminant Analysis (LDA)

Linear Discriminant Analysis (LDA) is a linear classification technique that projects data onto a lower-dimensional space that maximises class separability. It assumes Gaussian distributions with shared covariance among classes, making it computationally efficient and interpretable. Its main limitation lies in its strong assumptions and relatively poor performance with non-linear boundaries [279].

Linear Regression

Linear Regression models the relationship between a dependent variable and one or more independent variables by fitting a linear equation to the observed data. It is simple, fast, and interpretable, making it a fundamental baseline in both regression tasks and statistical modelling. However, standard linear regression is sensitive to multicollinearity and overfitting in high-dimensional settings [275].

1.8.3 Relevance to Electromyography

These algorithms form the foundation for decoding surface EMG signals in upper-limb rehabilitation. Convolutional models leverage the spatial arrangement of high-density electrode arrays to capture localised muscle activity. Recurrent and Transformer networks model temporal dependencies and dynamic muscle activations. Fully connected layers map these learned features to control signals, enabling intent

detection and device actuation. The following section provides an introduction on how these architectures are adapted, trained, and evaluated for robust, real-time myoelectric control in prosthetic and assistive technologies.

1.9 Machine Learning applications in EMG-Based Control of Upper Limb Rehabilitation Devices

This section applies the machine learning techniques discussed previously to the problem of decoding EMG signals for intuitive control of rehabilitation and prosthetic devices. Because voluntary movement originates in muscle contractions, it is intuitive to infer motor intention from the activity of residual musculature in amputees. As muscle cells are excitable like neurons, their activity can be measured through electromyography, which records the electrical currents generated during contraction [224]. EMG was first experimentally used to control a prosthesis in 1948 [221]. Traditional setups use large bipolar electrodes over muscles (sparse multi-channel approach), providing average muscle activation. The advantages of EMG include non-invasive acquisition, absence of high-level cognitive noise (as in EEG), and a rich foundation in existing literature. In the following, the two major control paradigms are reviewed, classification and regression, highlighting classical and recent deep learning-based approaches.

1.9.1 Pattern Recognition

Hands, whether human or prosthetic, are complex kinematic systems with multiple DoFs. The most basic control method links the activation of a single muscle to a single DoF, but this quickly becomes impractical. A major improvement came with Pattern Recognition approaches, using time- or frequency-domain features instead of raw signals. The first Pattern Recognition (PR)-based control schemes arose around the second half of the 1960s [280, 281]. In this configuration, the acquired EMG signals are processed by the controller to determine the action to be performed by the prosthesis. This pipeline typically consists of five stages: pre-processing,

segmentation, feature extraction, classification, and post-processing. A thorough analysis of these steps is presented in Marinelli et al. [104]. Feature sets are typically drawn from both time and frequency domains. Common examples include Mean Absolute Value (MAV), Zero Crossing (ZC), Waveform Length (WL), Root Mean Square (RMS), Slope Sign Changes (SSC), Autoregressive Coefficients (AR), Cepstrum, Short-Time Fourier Transform (STFT), Wavelet Transform (WT), and Wavelet Packet Transform (WPT) [282–284]. The PR-based controllers apply linear and non-linear methods to classify EMG signals into a large number of possible movements. Within pattern recognition, control strategies generally fall into two families: classification and regression [104]. While traditional methods have proven effective for limited, discrete movement control, recent advances in deep learning have significantly expanded the capacity to decode complex, high-dimensional EMG signals with greater generalisability and robustness.

1.9.2 Classification

Classification techniques have been pioneered by the work of Finley et al., Graupe et al., Kelly et al., and Hudgins et al. [280, 285–287]. Different non-neural-network classifiers have been exploited in ULP control, such as Simple Logistic Regression (SLR), Decision Tree (DT), Logistic Model Tree (LMT), SVM, KNN, and Naive Bayes (NB), whereas the gold standard is linear discriminant analysis [104, 281, 288–290]. Among neural networks, the most common architecture is the Multi-Layer Perceptron (MLP) [291, 292]. Recent studies have extensively explored CNNs, RNNs, and Transformers, particularly on HD-sEMG data, which, due to its dense spatial arrangement, can be structured as images or video streams, making it especially suitable for convolutional and attention-based architectures [104, 293–295]. Recent studies report classification accuracies in the high 70s for up to 50 classes [93, 296].

1.9.3 Regression

The pre-eminent alternative to classification methods lies in regression solutions. Classification approaches still limit the type of movements because the speed of the

related DoFs cannot be controlled independently if two functions are activated at the same time. Conversely, natural movements can only be achieved with independent proportional control of the related DoFs [297]. As opposed to classification, regression maps the output continuously across the considered number of degrees of freedom [93, 104]. This distinction is extremely important because a regression-based approach more closely mimics natural human motor control. Work on applications of regression techniques to upper limb prosthetic control has been conducted in the early 2010s, mostly relying on MLPs to achieve proportional, simultaneous, continuous, and independent control of multiple DoFs [268, 297–299]. Since then, different types of regression solutions have been applied to this issue, improving precision and enabling simultaneous control of up to 24 DoFs [93, 104, 300]. The solutions include MLPs, CNNs, RNNs, and transformers [297, 301–303]. However, online deployment of deep learning models, particularly in embedded or wearable systems, remains constrained by latency, memory footprint, and power consumption. Efficient model compression, pruning, and hardware-specific optimisations are increasingly necessary to ensure practical usability in mobile rehabilitation scenarios.

Commercially available EMG control systems

While the preceding sections and the remainder of this thesis focus on cutting-edge developments that are typically too novel for commercial deployment, numerous EMG-based control systems are already available on the market, particularly in prosthetic applications. Most of these employ sparse electrode configurations rather than HD-sEMG arrays. Commercial myoelectric prostheses commonly rely on two-site differential control or, in pattern-recognition systems, on the order of four to eight channels, as this configuration optimises usability, robustness, and cost in routine clinical practice [281, 304]. A lower electrode count reduces donning time, placement variability, and the need for extensive skin preparation, factors known to affect user comfort and long-term adherence [57, 65]. Fewer electrodes also mitigate real-world degradations, such as limb-position effects and electrode shifts, which can otherwise destabilise pattern-recognition systems [305, 306]. Furthermore,

sparse configurations simplify wiring, power management, and data transmission, while shortening calibration and retraining procedures, practical advantages that lower clinical workload and maintenance demands [307]. For these reasons, current commercial pattern-recognition prostheses balance functionality and practicality, often integrating multi-contact cuffs or small electrode arrays that expose a limited number of EMG channels for control.

1.9.4 Current Challenges

Taken together, classification delivers fast, reliable selection of discrete grasp patterns, while regression provides the proportional, simultaneous control needed for natural motion, making the two paradigms complementary pillars of intuitive, versatile prosthetic control. While significant progress has been made in developing algorithms to classify or regressively output EMG signals, implementation in real-life scenarios of the most advanced solutions remains low. Ultimately, a major challenge in applying machine learning to prosthetic control lies in the persistent gap between performance observed in controlled laboratory settings and that achieved in dynamic, real-world environments [104, 308]. To reduce inter-subject and inter-session variability, major contributors to this performance gap, emerging research has focused on transfer learning and subject adaptation techniques, which allow models trained on one user or dataset to generalise better across different conditions and individuals.

Despite recent progress, three interlinked challenges continue to limit real-world adoption. First, the scarcity of large, labelled EMG datasets often necessitates data-augmentation or synthetic-signal strategies; second, day-to-day electrode shifts demand online, few-shot adaptation to maintain performance across users and sessions; and third, most studies still report offline accuracy rather than task-level, online metrics that reflect functional control [93, 104]. These gaps are examined in detail in the course of this thesis. For additional information on the subject, the reader is referred to recent literature reviews [93, 104, 283, 290, 309–312].

1.10 Summary

Collectively, the nine state-of-the-art sections outlined above establish the conceptual and technical groundwork upon which the subsequent chapters, detailing the proposed algorithm, its implementation, and its evaluation, are built.

2 Introduction

This chapter outlines the foundation of the thesis, introducing the motivation for the research and the approach taken. It defines the research objectives and hypotheses, summarises the key contributions, and provides an overview of the thesis structure and data availability for transparency and reproducibility.

2.1 Problem Statement and Identified Gaps

Upper limb impairments, whether due to amputation, neurological injury, or musculoskeletal disorders, pose a significant burden on the QoL of individuals. This burden is well documented across both high- and low-income regions, with incidence estimates reaching up to 100 new cases per 100,000 people annually [19, 24, 27, 30]. Physically, the impact is profound, affecting daily functioning, independence, and social integration. Mentally, however, the literature presents a more complex and sometimes contradictory picture regarding psychological outcomes [47–49, 51–56].

Despite the clear need for intervention, the adoption and sustained use of prosthetic and rehabilitation devices remain limited. Prosthesis abandonment rates have been reported as high as 30% in some studies [64, 65, 69], and similar challenges are observed in the use of non-amputation rehabilitation technologies [72, 74–77].

These figures underscore a fundamental issue: even when assistive devices are available, many users choose to discontinue their use.

A key factor behind this phenomenon lies in the mismatch between user expectations and what current devices can deliver. Numerous studies have identified user requirements for prosthetic systems, consistently emphasising ease and intuitiveness of control as a primary concern [22, 57–63]. Similarly, dissatisfaction reports frequently highlight poor control performance and discomfort as dominant reasons for abandonment [66, 67].

This is compounded by a broader technological imbalance. While prosthetic and rehabilitation hardware has improved markedly in recent decades, advances in control strategies have not kept pace, particularly in commercially available systems [92, 93, 104, 105, 117–119]. In fact, many current solutions continue to rely on classification algorithms and signal acquisition methods developed decades ago. These approaches often fail to reflect the way humans naturally control their limbs and underutilise the rich information embedded in physiological signals [93, 104, 283, 290, 309–312].

Taken together, these observations suggest that current assistive technologies are not adequately aligned with the practical and cognitive needs of users. In line with commentary in the field, it is possible that the lack of innovation in control strategies is one of the primary barriers to wider adoption and sustained use [93, 283, 300]. As a result, individuals who find these technologies unintuitive or difficult to operate are more likely to abandon them, remaining vulnerable to the long-term functional and psychosocial consequences of their impairments.

Motivated by the challenge of reducing the functional burden of upper limb impairments, the core objective of this thesis is to develop prosthetic and rehabilitation technology solutions that are more effective, more acceptable, and more enduring, ultimately improving the quality of life for affected individuals.

2.2 Proposed Approach

2.2.1 Overview

Having identified the lack of appropriate control solutions, in terms of both control quality and simplicity from the point of view of the user, the overarching aim of this thesis is to design, implement, and validate a control solution for upper-limb rehabilitative devices, both prosthetic and non-prosthetic, that satisfies the functional requirements highlighted in the relevant state of the art.

The approach implemented consists of a joint software-hardware solution that spans the entire control pipeline, from signal acquisition to the translation of motor intention into a virtual kinematic state of the hand. The features of both the hardware and software components draw from the relevant literature and are shaped by the requirements and feedback of current rehabilitation device users. This integrated system, referred to as the Recursive Prosthetic Control Network (RPC-Net)/High-Density Electrode Array (HDE-Array) system, forms the central technical contribution of this thesis. The following sections highlight the key features of the system.

2.2.2 Operational Definitions: Online and Real-time

Before describing the approach chosen for this thesis in detail, it is important to clarify the intended meaning of terms frequently used throughout the manuscript. In this thesis, online operation refers to data acquisition and model inference performed concurrently within the same session, with system outputs produced while signals are being recorded. Offline analysis denotes processing performed after acquisition on previously recorded datasets. Real-time operation indicates that acquisition, feature extraction, inference, and command generation are executed with sufficiently low end-to-end latency for control to feel immediate and natural to the user. Following established literature in myoelectric and BCI control, overall delays below approximately 200 ms are typically perceived as real-time, while latencies above 300 ms begin to degrade smoothness of control [281, 304, 313,

314]. It is important to note that these engineering limits are much longer than the pure neural conduction time from the motor cortex to the peripheral muscles, which is approximately 20-30 ms [315]. The 200 ms threshold refers instead to the total time required for the entire sensorimotor feedback loop, which includes the efferent transmission from cortex to muscle (20-30 ms), proprioceptive feedback to the central nervous system (50-100 ms), and visually guided corrections (150-250 ms) [316–318]. For an artificial control interface to be perceived as natural, its own computational and transmission delays must therefore remain well below these biological latencies so that it can operate seamlessly within the natural feedback loop of the user. In practice, this means keeping the processing time of the system, from signal acquisition to actuation, on the order of a few tens of milliseconds. A total processing delay of up to roughly 50 ms is generally considered acceptable for real-time prosthetic control, as it maintains the overall loop below the 200 ms perceptual limit [304, 313]. Throughout this manuscript, "online" emphasises concurrent, closed-loop operation, whereas "real-time" emphasises the timing requirement.

2.2.3 Signal Source: High-Density Surface EMG

On the software side, the overarching aim of the solution developed in this project is to translate physiological signals into the kinematic state of the hand. When designing such a device, the choice was made to rely on sEMG as the source signal due to its non-invasiveness, the considerable body of related research developed in recent years, and its intrinsic connection to muscle activation [93, 104, 246]. More precisely, HD-sEMG is employed, which involves a high number of acquisition channels over a small skin area. In the literature, there is no single universally accepted cut-off for when sEMG becomes high-density, but two operational conventions are commonly used. The first is based on channel count, whereby arrays with more than approximately 32 channels are considered high-density, while traditional low-density systems typically employ between 1 and 16 channels [244, 319]. The second convention is based on spatial sampling, where inter-electrode distances of 10 mm or less arranged in a grid or quasi-grid configuration are taken to constitute

high-density sampling of the muscle surface [246, 319]. Under either convention, the systems used in this thesis qualify as HD-sEMG. This approach was selected because of the inherently high amount of information conveyed by this type of signal and the recent increase in attention it has received in the literature [104, 293, 320]. The recent development of high-density, high-resolution, wireless EMG amplifiers was also a key factor in the decision to opt for the high-density approach, as opposed to the more traditional sparse configuration [321]. Additionally, HD-sEMG signals are naturally acquired as two-dimensional maps, enabling a range of advanced signal processing strategies [93, 294, 295]. Although a standard HD-sEMG system is initially employed, later configurations deviate from strict definitions due to non-uniform inter-electrode spacing. While formal definitions of HD-sEMG vary, the literature increasingly recognises flexible layouts [319, 322]. Although the electrode layout defines spatial resolution, the recording configuration (monopolar or bipolar) also influences signal characteristics. Monopolar recordings, which measure the potential of each electrode relative to a common reference, preserve spatial detail and are therefore well suited for spatial filtering and source localisation, but they are more susceptible to noise and crosstalk. Bipolar recordings, obtained as the potential difference between adjacent electrodes, provide higher signal-to-noise ratios and improved robustness to motion artefacts, yet they partially lose spatial information and can attenuate signals from deeper or overlapping muscle sources [246, 304]. In this work, a monopolar configuration was adopted to retain the full spatial information of the muscle activity maps, which is critical for the signal processing methods developed in subsequent sections.

2.2.4 Neural Architecture: Shallow Regression Networks

Regarding signal processing, the choice was made for shallow, fully connected neural networks. This choice is primarily motivated by the low computational burden of such architectures, which rely on matrix operations and are thus compatible with low-energy, embedded computing platforms, such as those typically found in rehabilitation devices [92, 264, 266]. In the context of embedded prosthetic control,

network complexity is constrained primarily by memory footprint and inference latency. Typical wearable or forearm-mounted embedded systems provide on the order of a few hundred kilobytes to a few megabytes of memory and support only tens of MFLOPs per second without overheating or draining the battery [323, 324]. In practical terms, this limits feasible architectures to models with roughly 10^4-10^6 trainable parameters, corresponding to fewer than about 10 fully connected layers or their computational equivalent. Architectures exceeding this scale generally require GPU acceleration or mains-powered hardware and are therefore unsuitable for continuous, wearable control applications. The network developed in this thesis falls well within this embedded-scale regime. This is in contrast to the current trend in the literature, which favours increasingly complex architectures that rely on cluster computing resources. While such models can be highly accurate, their computational demands often preclude local deployment, thereby undermining usability and user independence [93, 104, 105].

Furthermore, the architectural choices are informed by physiological reasoning. The goal of the model is not to decode abstract movement intention at the premotor or cognitive level, but rather the descending motor command as it is expressed in the peripheral motoneuron pool and subsequently captured via surface EMG. At this level of representation, the transformation from cortical drive to muscle activation passes through only a small number of synapses in the final corticospinal pathway [3, 325]. The physiological translation from EMG activation to endpoint movement likewise involves a small number of functionally low-dimensional transformations, which are locally well-approximated by shallow nonlinear mappings. This motivates the use of a similarly shallow architecture, as the mapping being learned corresponds to the execution-level motor command rather than the upstream planning hierarchy. It is worth noting that the term shallow neural network is used here in contrast to modern architectures that frequently employ tens or even hundreds of layers. While the solution does not use a shallow network in the traditional sense (i.e., a single hidden layer), its use of fewer than ten layers qualifies it as shallow in comparison. This broader interpretation has also been adopted by other recent studies [326, 327].

2.2.5 Control Strategy: Regression over Classification

In addition, a regression model was selected rather than the more commonly used classification models. This decision is based on the fact that regression more closely reflects the way in which the upper limb is controlled physiologically. Given that simplicity and naturalness of control are consistently identified as key requirements, and that their absence is a major cause of abandonment, adopting a continuous and proportional control paradigm can help reverse this trend [57, 66]. More specifically, regression allows for proportional, simultaneous, independent, and continuous control of multiple outputs. The aim is to build a control system for rehabilitation devices that embodies these same features [104, 300]. Recent interest in regression-based control approaches has also provided useful benchmarks for this work [93, 328].

2.2.6 Choice of Output: Kinematic Model

Another defining feature of the selected approach is the choice of output. The choice was made to use the joint angles of the hand and wrist as the target output. This decision is consistent with physiological principles, as muscle activation is approximately proportional to joint flexion, and aligns with the majority of related studies [3, 104, 301–303]. As for the choice of the kinematic model, a wide range of hand kinematic models has been proposed in the literature, differing in the distribution of DoFs across the anatomical joints of the hand and wrist, as described in the previous chapter (Section 1.1) [5–11]. Taken together, these models exhibit a broad consensus in assigning three degrees of freedom to the wrist and recognising the increased joint complexity of the thumb relative to the fingers; however, they also differ substantially in how they allocate degrees of freedom across joints, particularly in modelling finger abduction, axial rotation, and palm dynamics. The diversity of modelling choices underscores the absence of a universal standard and motivates the development of a unified model that aggregates the most functionally relevant features.

For the sake of this research, a unified model that synthesises all degrees of freedom reported across the reviewed literature was developed, thus capturing the

full kinematic complexity of the human hand. Rather than prioritising minimalism or task-specific reductions, the model was designed to be maximally inclusive: every degree of freedom cited in prior work was incorporated, ensuring anatomical and functional completeness. The resulting model comprises a total of 29 internal DoFs, distributed as follows:

- Fingers: each finger includes five DoFs, with three at the MCP joint (flexion/extension, abduction/adduction, and axial rotation) and one at each IP joint (proximal and distal) for flexion/extension
- Thumb: six DoFs, comprising two DoFs each at the TMC, MCP, and IP joints
- Wrist: three DoFs, corresponding to flexion/extension, abduction/adduction, and axial rotation (pronation/supination)

The description of the model excludes the three global positional DoFs (translation along the x, y, and z axes), which are typically associated with the placement of rigid bodies in space. These translational components are not intrinsic to hand biomechanics and are instead related to overall body movement. A schematic depiction of the proposed model, including joint locations and DoF annotations, is shown in Figure 2.1.

2.2.7 Software Development: Temporal Continuity

The algorithm incorporates a recursive element. Since joint positions are highly stable over time, and current joint states are strongly influenced by previous ones, a temporal loop in which prior estimates help refine present predictions is introduced. This temporal continuity improves output stability and enables smoother transitions between postures, both critical for intuitive and naturalistic control. The model was named RPC-Net (Recursive Prosthetic Control Network). Further details on the implementation of RPC-Net are discussed in Chapter 3.

2.2.8 Hardware Innovation: Dry Electrodes

To enhance the versatility of the software solution developed here, focus was also kept on improving the signal acquisition procedure for HD-sEMG signals. The

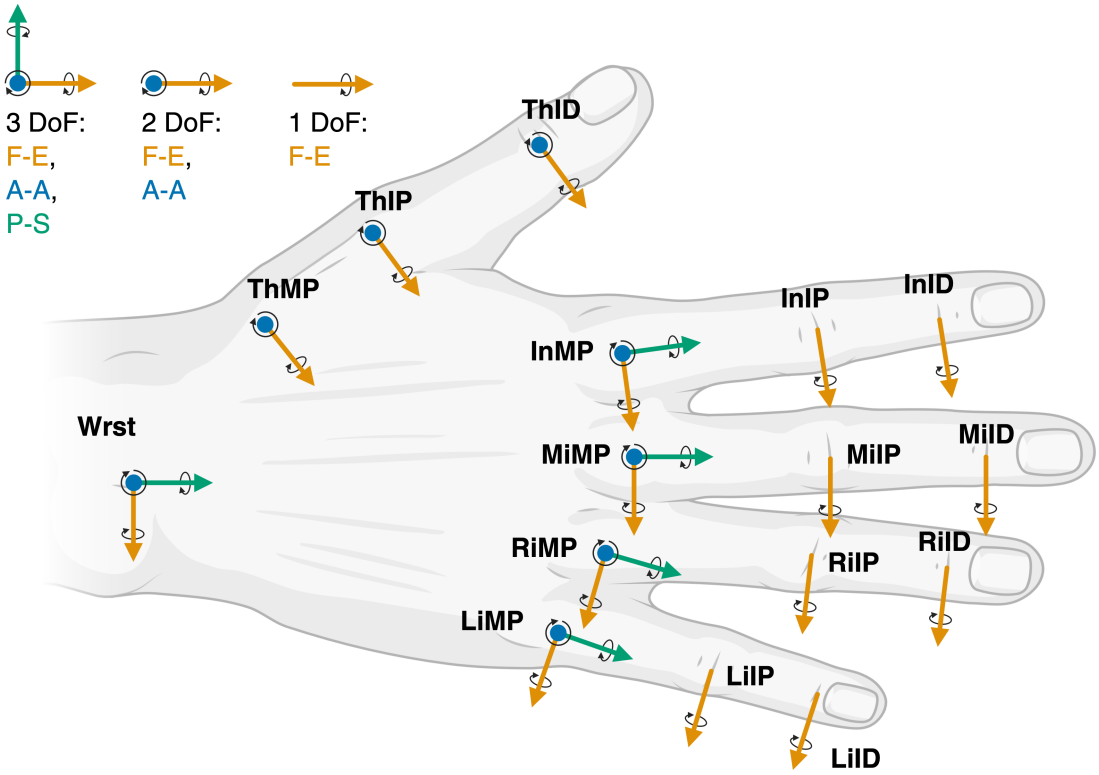

Figure 2.1: Kinematic model: Each joint of the hand has one to three kinematic degrees of freedom. Each degree of freedom can be characterised as flexion-extension (F-E), adduction-abduction (A-A), or pronation-supination (P-S), as shown in the legend (top left). Each joint is given a four-letter code. The arrow indicates the orientation of the axis of rotation. The circle at the origin represents a rotation axis orthogonal to the dorsal surface of the hand.

standard approach involves using arrays of gel-based electrodes (here referring to wet HD-EMG arrays relying on conductive gel to reduce skin-electrode impedance and ensure stable electrical contact) [244]. This method presents two key barriers to widespread usability. First, it requires a time-consuming and precise preparation process, including the application of conductive gel to each electrode. This step often needs to be performed by a trained professional rather than the user, limiting its practicality. Alternative methods exist, but they typically rely on expensive, single-use electrode arrays, which are equally unsuitable for user-operated systems. To ensure comfort and ease of use, an end-user device must be quick and intuitive to apply without expert assistance [329].

Second, traditional HD-sEMG arrays have a fixed inter-electrode distance,

commonly 5, 10, or 15 mm. This fixed pitch poses a problem because anatomical dimensions vary significantly across users. The same distance may span different muscle regions depending on the forearm size of the individual. Furthermore, physiological changes such as weight loss, weight gain, or muscle development may further compromise the consistency of signal acquisition using fixed arrays.

To address these issues, an innovative solution was developed: a dry-electrode bracelet with an adjustable perimeter, named HDE-Array. This wearable device requires no preparation time and can be applied independently by the user. Its electrodes are uniformly distributed around the forearm, promoting consistency in both intra-subject and inter-subject acquisitions. Similar devices have been proposed in recent years, further supporting the relevance and feasibility of this approach [322, 330]. The full definition of HDE-Array is included in Chapter 4.

2.2.9 Integrated Component: EMG Amplifier

To support high-resolution, wearable signal acquisition, the MEACS amplifier was integrated into the system. This device was developed by LISiN and ReC Bioengineering (Turin, Italy) [321]. It was employed as part of the collaborative research framework in which this thesis is embedded. Although the amplifier itself was not developed within the scope of this work, its design, offering wireless transmission and multi-channel acquisition, made it highly compatible with the dry-electrode bracelet. Through this integration, a fully wearable HD-sEMG acquisition platform was assembled that combines cutting-edge hardware with user-centred design principles, enabling practical deployment beyond laboratory environments.

2.2.10 Summary

Taken together, the RPC-Net/HDE-Array system developed in this thesis represents a comprehensive and practical approach to upper limb rehabilitation control. By combining high-density, user-friendly signal acquisition with physiologically informed, computationally efficient control algorithms, the solution aims to bridge the

gap between laboratory-grade control performance and end-user viability. This dual focus, on both performance and usability, defines the central innovation of this work.

2.3 Research Objectives and Hypotheses

Building on the approach outlined above, this thesis aims to rigorously validate the RPC-Net/HDE-Array platform as an efficient, robust, and clinically viable control interface for upper-limb rehabilitation devices by demonstrating its ability to translate high-density surface EMG signals into accurate hand kinematics in real-time.

To achieve this, the thesis is structured around a series of experimental hypotheses, organised into major overarching research questions and corresponding low-level, testable hypotheses. Each overarching question, together with its associated experiments, forms the focus of a dedicated chapter within this thesis.

- **Research Question 1:** Can RPC-Net accurately estimate hand kinematics from HD-sEMG in offline conditions? (Chapter 3)
  - **H1.1**: RPC-Net can generate high-quality hand position estimates from HD-sEMG signals, outperforming current state-of-the-art solutions
  - **H1.2**: RPC-Net is robust against changes in input signal length and the number of electromyographic channels used
  - **H1.3**: Information about previous position can improve estimation performance of RPC-Net
- **Research Question 2:** Can RPC-Net maintain its performance when using dry electrodes (HDE-Array) instead of traditional gel-based electrodes? (Chapter 4)
  - **H2.1**: The estimation accuracy of RPC-Net using the HDE-Array is statistically indistinguishable from that obtained using gel-based electrodes
- **Research Question 3:** Can the kinematic model be effectively reduced to a lower number of DoFs using Principal Component Analysis (PCA)? (Chapter 5)

  - **H3.1**: Five Principal Components (PCs) are sufficient to explain at least 90% of the variance in a representative dataset of natural hand movements
  - **H3.2**: As the number of principal components increases, the decoding performance of the RPC-Net/HDE-Array system approaches that of the full 29-DoF model, achieving at least 90% of full-model accuracy with five or fewer PCs
  - **H3.3**: The decoding performance obtained, in terms of endpoint effector, using five PCs is non-inferior to that of the full 29-DoF kinematic model within a predefined tolerance of 10 mm
- **Research Question 4:** How robust is RPC-Net to electrode repositioning and inter-subject generalisation in offline conditions? (Chapter 6)
  - **H4.1**: The accuracy of the RPC-Net/HDE-Array system decreases when electrode positioning is inconsistent between the training and testing sessions, compared to the baseline case in which electrode positioning remains consistent
  - **H4.2**: When the RPC-Net/HDE-Array system is tested on data from the same session as the training data, its accuracy remains unchanged regardless of whether electrode repositioning is included during training
  - **H4.3**: The performance degradation observed when the system is trained without electrode repositioning and tested on data from a different session can be mitigated by incorporating electrode repositioning during training
  - **H4.4**: Including inter-subject data in the training set improves the overall performance of the system, providing a valid alternative to an increased amount of subject-specific data
- **Research Question 5:** Can subjects use RPC-Net to perform real-time control tasks, and what factors influence their performance during live operation? (Chapter 7)

  - **H5.1**: Subjects can achieve real-time control performance with the RPC-Net/HDE-Array system that mirrors the offline, user-independent accuracy of the system
  - **H5.2**: Generalised training using inter-subject data will yield lower performance compared to training on subject-specific data
  - **H5.3**: The addition of visual feedback during online control will result in better performance of the system
- **Research Question 6:** Can the RPC-Net/HDE-Array system enable intuitive, real-time multi-DoF control using neck muscle activity? (Chapter 8)
  - **H6.1**: Subjects can control a hand kinematic model in real time using neck muscles and the Recursive Functional electrical stimulation Control Network (RFC-Net)/HDE-Array system, achieving task performance comparable to that observed with forearm muscle control
  - **H6.2**: Performance in controlling the hand kinematic model using head and neck muscles, is comparable between tetraplegic and healthy subjects
  - **H6.3**: Subjects can successfully use the RFC-Net/HDE-Array system to control three independent cursors in a task-oriented experiment, with 1 DoF per cursor
  - **H6.4**: Performance in the cursor-based task is comparable between healthy and tetraplegic subjects

Taken together, these research questions and hypotheses define the structure and scope of the experimental investigations carried out in this thesis. Each chapter that follows focuses on one of these questions, presenting the experimental design, methodology, results, and interpretation necessary to evaluate the corresponding hypotheses. In doing so, this thesis aims not only to validate the RPC-Net platform in a range of real-world scenarios, but also to contribute foundational knowledge towards practical, scalable solutions for upper-limb rehabilitation and neuroprosthetic control.

2.3.1 Performance Criteria

Having established the hypotheses to be tested, it is necessary to define the performance criteria against which they are evaluated. In the context of upper-limb rehabilitation, accuracy is meaningful only insofar as the user perceives the device as responding proportionally and without perceptible drift or tremor. Physiologically, fingertip contact spans a deformation range of approximately 1-2 mm during light object manipulation [331], and proprioceptive resolution at the metacarpophalangeal joints is on the order of 1-2° [332]. These values represent the perceptual lower bound of human sensorimotor resolution, and therefore correspond to the level of perfect accuracy from the point of view of the user: below this threshold, artificial and biological movement become indistinguishable. In practical terms, a control system is considered high-quality when its reconstruction error approaches this perceptual floor, that is, when average joint-space error remains within a few degrees, or equivalently within only a few millimetres of end-effector displacement, and without persistent oscillations around the target posture. Throughout this thesis, this physiological benchmark serves as the reference against which control quality is interpreted.

In addition to defining what constitutes a high-quality reconstruction, it is also necessary to establish what qualifies as a meaningful difference between two control strategies. Statistical significance alone is not sufficient, as very small performance differences may reach significance with large sample sizes while remaining imperceptible to the user. For the purposes of this thesis, a difference is considered operationally meaningful only when it exceeds the perceptual and functional threshold of the sensorimotor system. Whereas the 2 mm threshold reflects the level below which deviations are indistinguishable from natural fingertip deformation, differences become behaviourally salient when they exceed the spatial extent of the distal finger-pad contact region. The effective contact area of the volar fingertip spans approximately 8-12 mm, corresponding to the aggregate receptive field organisation of slowly adapting mechanoreceptors [325]. Accordingly, two approaches are considered meaningfully different if their end-effector errors differ

by more than 10 mm, as deviations of this magnitude fall above the perceptual threshold during manipulation. Smaller differences, although potentially statistically significant, are treated as physiologically negligible. This definition provides the minimum effect size used in the interpretation of all subsequent hypothesis testing.

2.4 Contributions

This thesis makes four primary contributions:

- the development of RPC-Net, a physiologically inspired, low-complexity regression model for real-time decoding of hand kinematics from high-density surface EMG signals;
- the design and validation of HDE-Array, a wearable dry-electrode interface for rapid, repeatable, and preparation-free HD-sEMG acquisition;
- the integration of these components into a unified, user-centred control platform, and its evaluation across multiple real-world scenarios, including offline, online, and reduced-channel conditions; and
- the creation of multiple annotated datasets, including a multi-part, high-quality dataset of HD-sEMG and hand kinematics recorded under various conditions with both healthy and tetraplegic participants.

2.5 Thesis Structure

The remainder of this thesis is organised as follows:

- Chapter 3 presents the implementation of the RPC-Net model and its initial validation using offline HD-sEMG data.
- Chapter 4 introduces the HDE-Array system and evaluates its performance relative to traditional gel electrodes.
- Chapter 5 explores dimensionality reduction techniques applied to the kinematic model and examines their influence on system performance.
- Chapter 6 investigates the robustness of the system with respect to electrode repositioning and inter-subject variability.

- Chapter 7 extends the evaluation to online scenarios and assesses performance under different operational conditions.
- Chapter 8 presents the RFC-Net model, a variant of RPC-Net, developed for multi-DoF control using neck muscle signals in both tetraplegic and able-bodied users.
- Chapter 9 provides an integrated assessment of the experimental outcomes and discusses their broader implications.
- Chapter 10 summarises the key findings of the thesis and outlines directions for future research.
- Appendix A contains the co-author permission forms and documentation related to ethics approval procedures.

2.6 Data Availability

All datasets and source code developed in the course of this thesis have been made freely available to support transparency and reproducibility.

The source code is hosted in a publicly accessible Dropbox folder: `https://www.dropbox.com/scl/fo/nkvbse7evo0k8ou1utn7i/AMDh_MOZQJ6gCwDXGPadmZ0?rlkey=ynoix3anpc81v24hogn3fymb4&st=xrqx07q2&dl=0` [333].

The dataset is available via Zenodo: `https://zenodo.org/records/14246378` [334].

Further details about the data structure and acquisition protocols are provided in the relevant chapters.

3

Developing RPC-Net: Leveraging High-Density Electromyography and Machine Learning for Improved Hand Position Estimation

3.1 Introduction

In 2019, the prevalence of upper limb amputations in the United States, United Kingdom, and the European Union was more than 1,000,000 (incidence 40,000), 100,000 (incidence 3,200), and 800,000 (incidence 25,000), respectively [335]. Loss of upper limb functionality has a major impact on quality of life, underscoring the pressing need for effective solutions [56]. Great strides have been made in designing advanced upper limb prostheses and developing control strategies for these devices. Specifically, efforts have been directed towards creating prostheses that replicate the kinematic complexity of the human hand [113, 336–339]. Many types of control solutions for these devices have been explored, with a primary focus on sEMG, currently the most viable option for prosthetic control [68, 340].

Despite the considerable advancements in technology, abandonment rates for prosthetic devices, a good indicator of user satisfaction, are consistently high, and rarely below 30% [67, 69, 341]. Factors contributing to abandonment include

comfort, function, and appearance [67], and it appears that none of those is strongly predominant over the others [58]. In general, users feel that prostheses do not address their needs [22], often find them uncomfortable or painful and feel that control is not natural enough [57, 65]. The definition of control naturalness varies in the literature, encompassing factors such as independent finger movement, force control capability, ease in performing daily tasks, and the inclusion of sensory feedback [67, 341]. Overall, the fact that technical developments have not led to visible improvements in abandonment rates or consumer satisfaction suggests that current approaches do not meet patient needs [69].

An analysis of current control solutions may provide insight into the factors contributing to this trend. ML and its subfield Deep Learning (DL) have been extensively employed in recent years to address prosthetic control. Applications of classification-based algorithms, a subset of ML, have been investigated [93, 282–284, 342]. This type of algorithm predicts categorical outputs by mapping input features to a finite set of classes. For prosthetic control, this entails classifying electromyographic signals as one of several predefined movements, each of which is assumed to be consistent. Research has been focused on developing more complex solutions to improve accuracy in the classification of more and more classes [343, 344]. Classification-based approaches, however, deviate significantly from how humans control their hands, and thus, may not be able to provide users with the natural-feeling control they desire [59].

In contrast to classification approaches, regression-based solutions offer a more natural control mechanism, taking steps towards human-like prosthetic control [328, 345–348]. This type of solution has recently become the focus of growing interest because of its potential [93, 349–351]. Despite the clear improvement that regression-based approaches bring, some problems persist. First, most existing solutions do not control the complete kinematics of the hand, instead focusing solely on either the wrist or the fingers, even if control of many kinematic DoFs independently was identified as an important attribute [67, 68]. Second, some of these solutions require electromyogram signals acquired distally. However, this is incompatible with the

needs of upper limb amputees; only 5% of hand amputees retain distal muscles in their forearms, whereas more than 30% of the same population retain proximal forearm muscles [57]. Third, most of these solutions employ computationally intensive algorithms with substantial computational cost, which may render them less suitable for embedding into devices or application in clinical settings, ultimately hindering their practical applicability [352–356].

It is possible that these limitations are contributing to the observed low satisfaction among prosthesis users. RPC-Net was developed in this study to address the shortcomings observed, and is based on the confidence that accurate hand position estimation is crucial for improving prosthetic device control. This novel, computationally efficient, deep network leverages regression principles to estimate hand position (as a high-DoF kinematic model) from electromyographic activity, and is intended to be implemented as a control solution for articulated hand prostheses. Regression-based control and a high-DoF kinematic model address naturalness of control, a key factor in device abandonment [328, 345–348]. RPC-Net is recursive (making use of previous estimates to refine the current one) and uses 96 HD-sEMG channels from the proximal forearm as source signal, fewer than most control approaches and in accordance with the anatomical needs of amputees [93, 283].

In this chapter, RPC-Net, designed to meet the needs of prosthesis users while being computationally efficient, is introduced and validated to demonstrate the following experimental hypotheses:

1. RPC-Net can generate high-quality hand position estimates from HD-sEMG signals, outperforming current state-of-the-art solutions
2. RPC-Net is robust against changes in input signal length and the number of electromyographic channels used
3. Information about previous position can improve estimation performance of RPC-Net

RPC-Net is evaluated offline on data collected from healthy subjects, focusing on the accuracy of the estimate of position from the EMG signal. For this purpose, electromyographic and hand-position data were collected from twelve

healthy participants, and RPC-Net was used to translate the electromyographic data into hand position. This first evaluation is a stepping stone towards the development of a prosthetic solution implementing RPC-Net that satisfies user needs, is efficient, and conducive to a more natural control experience.

3.2 Materials and Methods

This section describes the instrumentation and software used in this study (Section 3.2.1) and the experimental procedures employed to assess the hypotheses (Section 3.2.2). The experimental procedures adhered to the Declaration of Helsinki and were approved by the local ethics committee (CER-Polito, Prot. No. 107460/2023). All data used in this chapter are available online [334].

3.2.1 Instrumentation

EMG Amplifier

EMG was recorded on the surface of the dominant forearm using the MEACS system, an EMG amplifier developed at LISiN (Politecnico di Torino, Turin, Italy) [321, 357]. The system is made up of multiple Sensor Units (SU), each measuring 34 mm × 30 mm × 15 mm and sampling 32 channels at $f_s = 2.048$ kHz (192 V/V gain, 16-bit resolution, 2.4 V dynamic range). Signals were hardware-filtered by the amplifier with a passband of 10-500 Hz. Three SUs were used, each connected to an anisotropic electrode array (2 rows and 16 columns, with 10 mm and 15 mm inter-electrode distance respectively) for a total of $N = 96$ acquired monopolar electromyographic channels. Each electrode array consisted of 32 Ag/AgCl electrodes mounted on a polyimide (PI) film substrate, manufactured by LISiN (Politecnico di Torino, Turin, Italy). The HD-sEMG arrays relied on conductive gel, applied manually, to reduce skin-electrode impedance and ensure stable electrical contact. The conductive gel used was Ten20 (Weaver and Company, Aurora, CO, USA). To synchronise the EMG and motion tracking data, the MEACS system incorporates a wireless synchronisation unit linked to the Vicon Lock. When motion tracking

starts or stops, this unit emits a digital signal recorded alongside the EMG data, facilitating alignment of the two datasets.

Hand position data

Hand position data were acquired using a motion capture system (Vicon Motus; Vicon Motion Systems, Oxford, UK) sampling at 100 Hz. The setup included 12 infrared cameras (Vero v2.2) and 33 reflective markers.

Acquisition Software

EMG data were acquired using the MEACS system interfaced through BP, a proprietary desktop application. The MEACS system streams raw EMG signals wirelessly to a laboratory desktop computer, where the BP application records, displays, and processes them in real-time. Motion data were recorded with Vicon Nexus (v2.11, Oxford Metrics plc). Subsequent data processing, including filtering and feature extraction, was performed using MATLAB (R2024a, The MathWorks, Inc.), while custom algorithms were implemented in Python with BSD-licensed libraries.

3.2.2 Experimental Approach

The experimental approach utilised a single dataset, labelled DS1 within the larger thesis-wide dataset. The following subsections detail the data acquisition protocol, pre-processing pipeline, network training strategy, testing methodology, and performance evaluation metrics for RPC-Net.

Subjects

Twelve healthy subjects were recruited (S1-S12), seven males and five females (aged 20-26 years, weighing 55-90 kg and 165-195 cm tall). Each participant provided written, informed consent before participation. All subjects were right-handed, had no surgical interventions on their dominant arm, and had a forearm circumference between 20 and 30 cm.

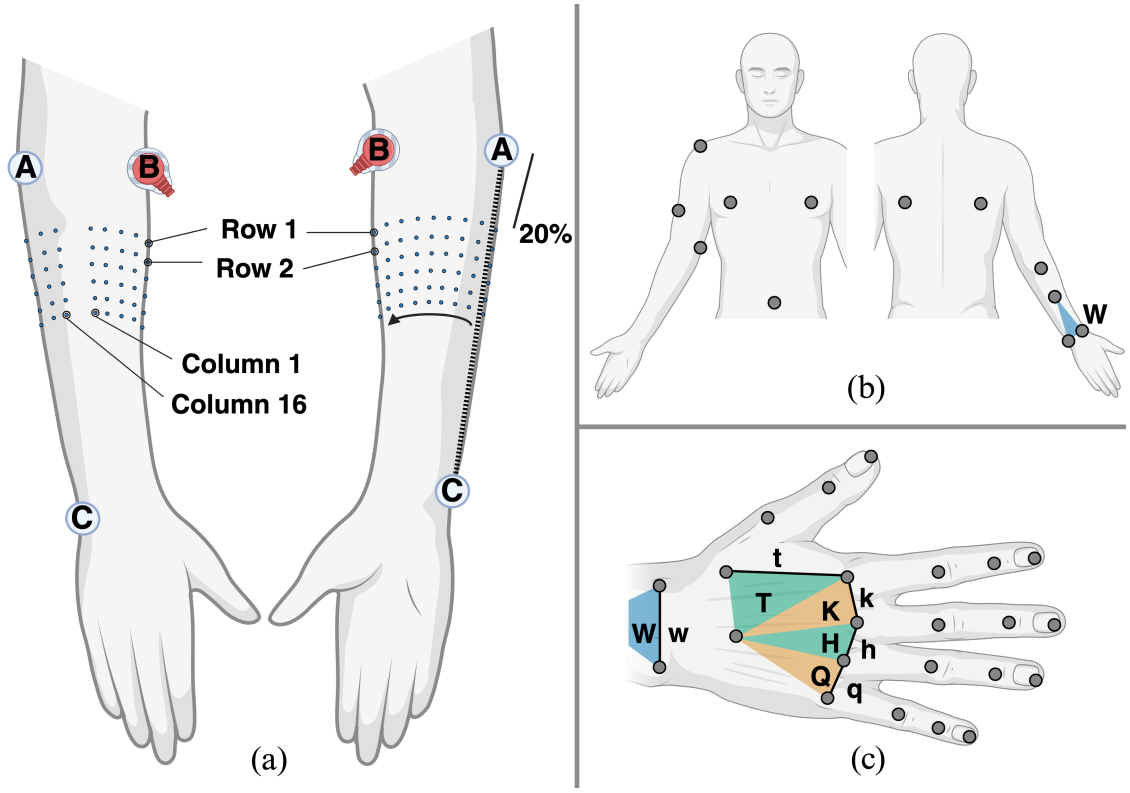

Figure 3.1: Subject setup: (a) Position of electrodes on the forearm of the subject. Ventral (L) and dorsal (R) views (medial epicondyle (A), lateral epicondyle (B), pisiform bone (C)). (b) Placement of 12 infrared markers on the body of the subject. Plane W is highlighted in blue. (c) Placement of 21 infrared markers on the hand (and two forearm markers, also depicted in (b)). Markers are placed proximally to each joint. Planes W, H, Q, K, and T are highlighted in orange, blue, and green, whereas lines w, h, q, k, and t are shown in black.

High-Density surface EMG electrode placement

For EMG acquisition, the EMG amplifier and gel electrodes described in Section 3.2.1 were used. The electrodes were arranged in 6 rows and 16 columns around the circumference of the forearm, covering approximately a third of its length (Figure 3.1 and Figure 3.2). The electrode array was placed so that the most proximal electrode of column 4, as defined in Figure 3.1, lay at 20% of the distance between the medial epicondyle and the pisiform bone. The reference electrode was positioned on the lateral epicondyle. The electromyographic signal was used as input for RPC-Net during the phases of training and testing. The recordings were performed in a monopolar configuration, in which each electrode measures the potential difference relative to a common reference. This configuration facilitates high-density coverage

and straightforward mapping of spatial activation patterns, making it well suited for regression-based approaches such as RPC-Net [246].

Hand position data

Hand position data were acquired using the instrumentation defined in Section 3.2.1. A total of $M_h = 21$ infrared reflective markers (diameter of 6 mm) were positioned on the dominant hand of the subject, embedded in a glove. Additionally, 12 markers were placed on the upper limb and trunk, resulting in $M = 33$ markers in total (Figure 3.1). The hand position data, translated to joint angles using the Inverse Kinematic Algorithm (IKA) defined below, were used both as input and as target value for the training phase of RPC-Net.

Protocol

The acquisition protocol consisted of six trials per subject: five for training and one for testing. The trial to be used for testing was selected randomly. During the trials, high-density EMG and hand position data of the participants were acquired as they transitioned between a set of 16 hand poses. This set comprised:

1. 4 wrist poses: flexion; extension; adduction; abduction;
2. 8 finger poses: index finger metacarpophalangeal flexion; index finger metacarpophalangeal extension; index finger proximal interphalangeal flexion; index finger proximal interphalangeal extension; flexion of the middle, ring, and little fingers; extension of the middle, ring, and little fingers; adduction of the index and middle fingers; abduction of the index and middle fingers
3. 4 thumb poses: flexion; extension; adduction; abduction.

Each trial included 32 poses (16 poses repeated 2 times each). Participants were seated with their dominant forearm positioned on a vertical support at shoulder height. Initially, participants were instructed to relax their hands and wrists. Subsequently, a monitor presented one of the 16 hand poses every 7 seconds. Prompts were in random order to prevent participants from anticipating the sequence. Participants were not instructed to transition at a specific speed. At the end of the trial, the subject was instructed to relax their hands and wrists.

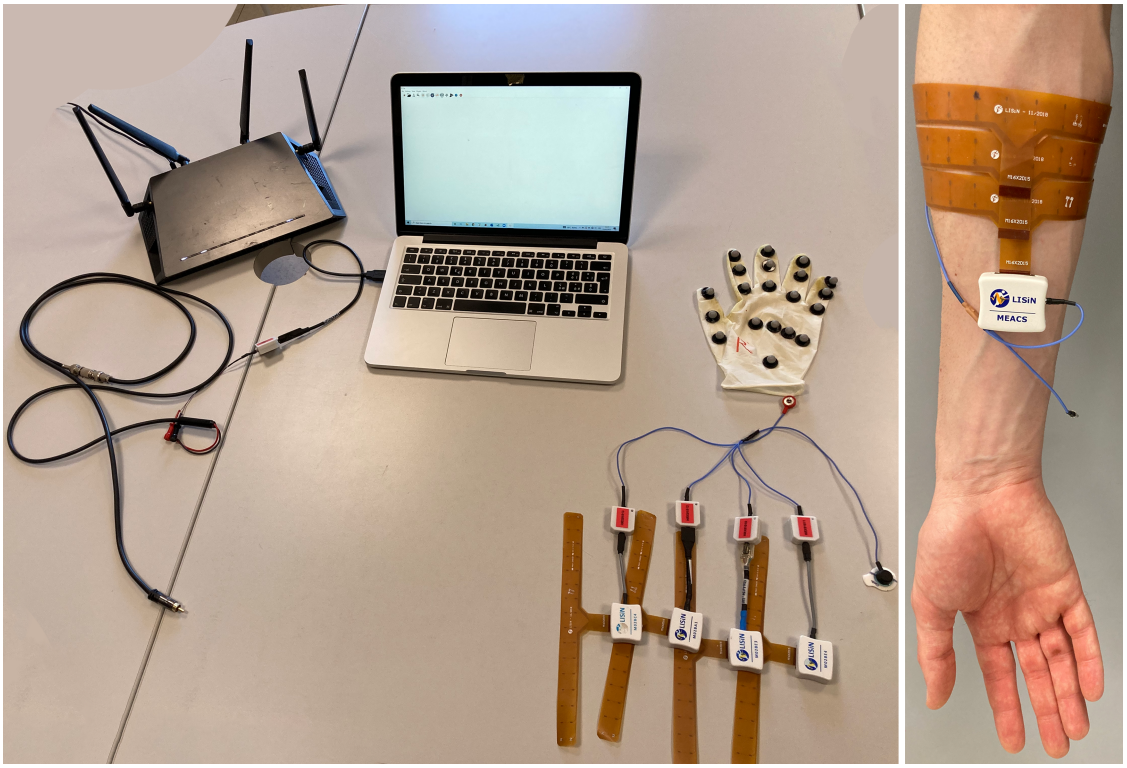

Figure 3.2: Instrumentation and electrode placement: (Left) Instrumentation used for data acquisition (from top left, clockwise): Wi-Fi router, lab laptop, glove with embedded markers, reference cable with reference electrode, four receiving synchronisation units, four MEACS SUs, four electrode arrays (32 electrodes each), transmitting synchronisation unit, cable for connection to the Vicon Lock, and power supply of the transmitting synchronisation unit. (Right) Electrode placement of 96 HD-sEMG electrodes on a subject. For clarity, a single SU is shown instead of three.

Inverse Kinematic Algorithm

RPC-Net requires joint angles as input and returns those in output, so an IKA was developed to translate 3D marker positions, as captured by the motion capture system, into hand joint angles. The selection of joint angles is informed by a 29-DoF kinematic model (Figure 2.1) developed for the sake of this research, and defined in Section 2.2.6. The core of the IKA is the optimisation process designed to identify the 29 joint angles (one per kinematic DoF) that best approximate the marker positions. The process is executed for each frame captured by the Vicon system. The process has three phases:

1. wrist angles (3 DoFs). In phase 1, the three wrist angles represent hand rotations around the x, y, and z axes, starting from a reference position where

the K plane is aligned with the W plane and lines k and w are parallel (Figure 3.1).

2. finger angles (5 DoFs per finger). In phase 2, each finger moves in flexion-extension at the Metacarpo-phalangeal (MP) joint and at the interphalangeal (PIP, DIP) joints. The flexion plane for each finger is defined by two angles, α and β (positive for pronation and radial deviation respectively), optimised using sequential quadratic programming (MATLAB; max evaluations = 500; function tolerance = 10^{-1}; optimality = 10^{-6}) [358]. α and β are zero when the flexion plane is perpendicular to the defining line (k for the middle and index finger, h for the ring, and q for the little). A sigmoid function such that $\alpha_1 = \alpha_0 * \text{sigmoid}(\zeta)$ and $\beta_1 = \beta_0 * \text{sigmoid}(\zeta)$ (where ζ represents the mean distance of the 4 markers from the principal direction of the same markers) refines α and β to prevent excessive motion when the finger is not flexed. Markers are then projected onto the flexion plane, and three additional angles (γ, δ, ϵ), representing the angles between finger segments (MP, PIP, DIP), are computed. The three flexion angles are set to zero when the three finger markers lie on the K (index and middle), H (ring), or Q (little) planes. Flexion of a joint corresponds to a positive angle.
3. thumb angles (6 DoFs). In phase 3, the thumb moves in flexion-extension and adduction-abduction at the MP, PIP, and DIP joints. All thumb angles are set to zero when markers align on the T plane (perpendicular to the t line), and angles are computed by rotating the system to set the proximal joint at zero degrees.

Phases 1 and 3 are error-free, while phase 2 introduces minor discrepancies between actual and estimated positions. Across all subjects, the average error in marker position was less than 1 mm (mean: 0.35 mm, standard deviation: 0.42 mm over 4,328,075 frames). The IKA projects from a 3D space to a J-dimensional joint angle space ($J = 29$, number of joints). This model is crucial, because RPC-Net was designed to take as input and return as output the joint angles of the hand rather than the 3D positions of the markers. This choice is motivated by the fact

that muscle activation is proportional to joint angles rather than to finger endpoint position. A Forward Kinematic Algorithm (FKA) to translate angles to marker position, based on the same kinematic model, was developed as well.

Data Pre-processing

The objective of the pre-processing procedure is to transform the data acquired into suitable inputs for RPC-Net. Raw EMG signals were first converted from bits to volts, then offset-corrected, rectified, and transformed into RMS values using a sliding window of $w_l = 200$ samples (97.7 ms). The choice of RMS as a feature was due by three reasons:

1. Preliminary pilot work, which identified it as the descriptor yielding the best performance.
2. The MEACS amplifier software interface includes a built-in TCP/IP module capable of streaming RMS values in real time, making RMS the ideal choice for future online developments.
3. The RMS is widely used in EMG signal processing due to its well-established relationship with muscle activation intensity.

The window length was selected based on practical considerations of real-time compatibility: the MEACS TCP/IP module is limited to a transmission rate of approximately 13 Hz, corresponding to a 75 ms RMS window. To ensure compatibility with this interface for future online applications, the RMS window was set to approximately 100 ms, providing a small tolerance margin while maintaining a temporal resolution suitable for smooth control. The window step w_s was 29 samples. For each computation, the RMS was calculated over a window of 200 consecutive samples, defined for sample x_i as the interval $[x_i, x_{i+199}]$, inclusive. The window then advanced by 29 samples for each subsequent computation (e.g., samples 0-199, 29-228, 58-257, and so on) until the upper bound exceeded the total number of samples in the recording. Given an electromyographic signal that is L seconds long and N-dimensional, the output of the pre-processing procedure is $l = floor(\frac{L*f_s - w_l}{w_s}) + 1$ samples long and N-dimensional. This procedure effectively subsamples the signal

from $f_s = 2.048$ kHz to $\frac{f_s}{w_s} = 70.6$ Hz through the computation of RMS. The resulting RMS values were divided by 10^{-4} to bring the data into a standardised range suitable for RPC-Net training, yielding unit variance. Vicon marker positions were processed using a moving average filter with a window length of 20 samples and subsequently mapped into a 29-dimensional joint-angle space using the IKA. To prepare the joint-angle data for network training, rest angles were subtracted, and the resulting values were normalised by dividing by 45 degrees, centring the data at zero and producing unit variance. Finally, linear interpolation was applied to align the sampling rates of the EMG and joint-angle data, ensuring synchronised, time-matched input-output pairs for RPC-Net training. Given an L-second-long signal, the output of the pre-processing procedure is $l = floor(\frac{L*f_s - w_l}{w_s}) + 1$ samples long and J-dimensional.

RPC-Net

RPC-Net, a neural network intended to convert multimodal input into sample-wise predictions of the 29 hand joint angles, was devised for this research. The architecture includes 29 individual sub-networks, each assigned to one joint. All sub-networks share the same input for each iteration and generate outputs that collectively represent the complete kinematic state of the hand. Each sub-network consists of a two-branched neural network, where one branch processes the electromyogram (EMG branch), and the other analyses past joint angles (angle branch). These two branches converge into a root that returns an estimate for a single joint angle. Each sub-network excludes from the kinematic input the angle which it is estimating, to avoid overfitting issues. The outputs from the 29 sub-networks are combined to create a full set of 29 joint angles, which also serve as input for the subsequent estimates, creating a recursive loop. Both input signals consist of multiple time points. The EMG input consists of a 0.9 s segment of the electromyographic signal preceding the instant at which the joint angle estimate is calculated. Of the 64 samples in this segment (given a sampling frequency of 70.6 Hz), only every fourth sample is processed for efficiency. This action effectively reduces the sampling frequency to 17.7 Hz. Consequently, the EMG branch input size becomes $I_E = 16$

(samples) × 96 (channels), that is, 1536 inputs. The joint angle input incorporates the kinematic state for the 3.6 s interval leading up to the time point of the predicted position. Every thirty-second sample (i.e., one in 32) is chosen (diminishing the sampling rate to 2.2 Hz), and the signal encompasses $J = 29$ channels. This results in an input size of $I_A = 8$ (samples) × 29 (joints) or 232 inputs for the angle branch input (reduced to 224 for each individual subnetwork). The output of the network is the sample-wise approximation of the 29 joint angles of the hand, determined at a frequency of 70.6 Hz. For myoelectrical control systems, delay is defined as the time difference between motion intention and system output. While the input signal covers a 0.9 s window, this does not introduce any delay in the prediction process in addition to the Inference Time (IT) of the network. This is because RPC-Net performs the estimate of the sample immediately following the most recent EMG reading, corresponding to the onset of motor intention; earlier EMG values within the 0.9 s window improve prediction by providing previous context. The initial 0.9 s of a session may not be used for training or testing of the network due to the absence of sufficient earlier data. In its full configuration, RPC-Net has almost $2.6 \cdot 10^7$ parameters (25915879).

During the testing phase, joint angles produced by the RPC-Net undergo processing via a fourth-order low-pass Butterworth filter (with a cut-off frequency $f_c = 1$ Hz) to eliminate high-frequency fluctuations and are subsequently mapped back into 3D space using the FKA. The structure of each branch is detailed in Figure 3.3. The network was trained with the Adam optimiser (in its PyTorch implementation), learning rate = 10^{-5}; $\varepsilon = 10^{-12}$; $\beta_1 = 0.9$; $\beta_2 = 0.99$; batch size = 2000; loss criterion = MSELoss. The model was trained for 200 epochs. During the training of RPC-Net, the joint angle input data were taken from the recordings, and the recursion loop was disabled.

Development of RPC-Net

The development of RPC-Net was preceded by a series of pilot studies aimed at identifying a neural architecture capable of translating electromyographic activity

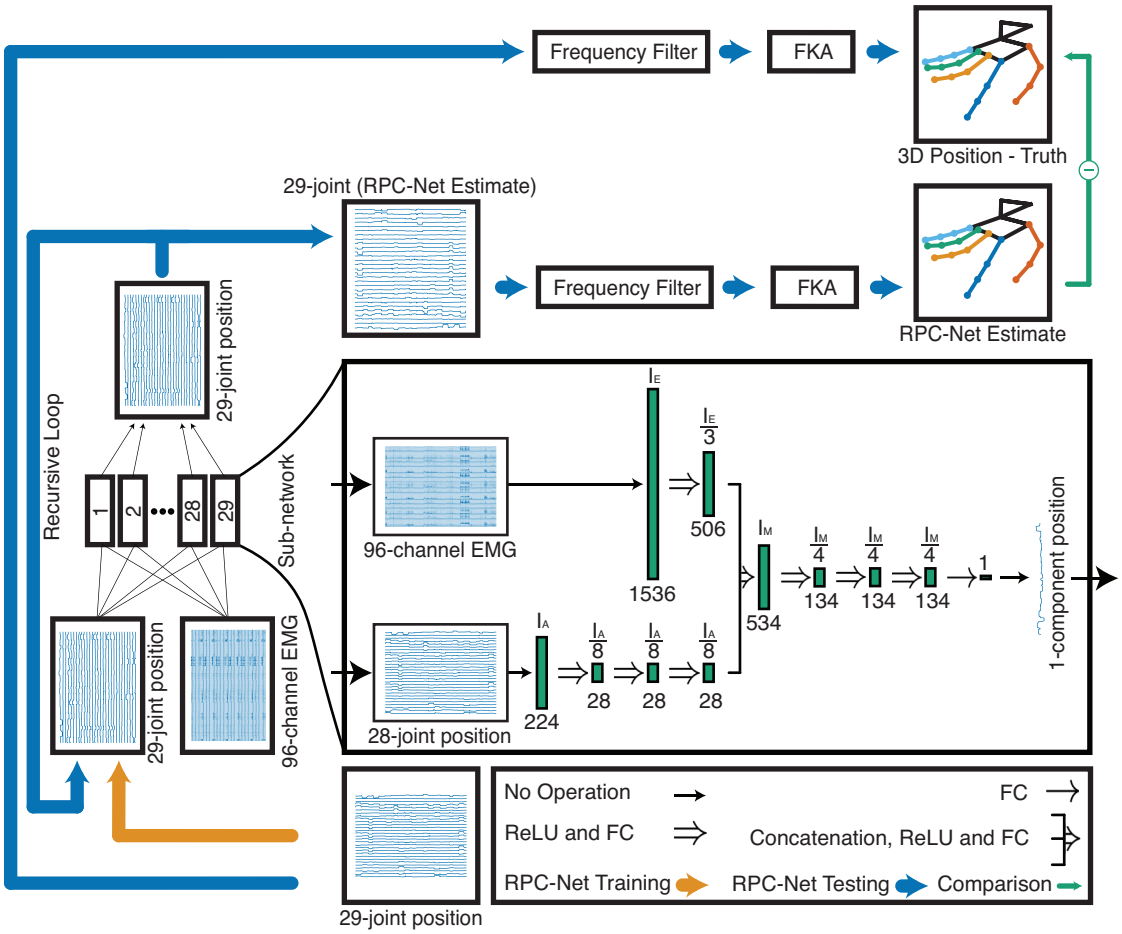

Figure 3.3: RPC-Net architecture: The whole network is made up of 29 individual sub-networks, each trained to regress one of the 29 hand joints. The arrow on the left highlights how the output of RPC-Net is used as input for the subsequent iteration. A detailed view of one sub-network is shown on the right-hand side of the figure. E refers to the EMG branch and A refers to the angle branch. I_E and I_A represent the width of the EMG (1536 units) and angle (224 units) inputs respectively. $I_M = I_E + I_A$ is the width of the merged outputs of the two branches (534 units). Values above the green layers indicate the width of the corresponding layer as a function of I_x, the input size of that branch, expressed numerically beneath each layer. The kinematic input of each of the sub-networks is made up of 28 angles, because the one in output is excluded from the input. The top left part of the figure displays the filtering and 3-D conversion performed outside the network loop. Orange and blue arrows represent the data path followed for the training and testing phase, and the green arrow the comparison performed to assess the accuracy of the algorithm.

into continuous joint angle predictions. Initial experiments were conducted with a single subject performing 16 distinct motor tasks. The first prototype was a regression-modified version of ResNet-18 [359], which was optimised to predict the trajectory of a single joint. Although this approach yielded accurate results,

its computational cost and architectural complexity rendered it unsuitable for embedded applications. Consequently, the design process pivoted away from the ResNet-based framework towards a fundamentally simpler fully connected architecture. Development restarted from a minimal configuration with two hidden layers and eight neurons per layer, which was then systematically expanded in depth and width until performance improvements reached a plateau. Following this optimisation, the 29 single-joint models were merged into a unified multi-branch structure, enabling the simultaneous estimation of all hand joints. Finally, a position-feedback mechanism was introduced to incorporate temporal context and stabilise predictions across successive time steps.

Performance Indicators

The performance of RPC-Net was assessed as its ability to estimate the position of the hand from the electromyogram. The performance was measured, independently for each subject, with two indicators: Mean Distance (MD) and Mean Pearson Correlation Coefficient (MPCC), both computed for the test trial only. MPCC is the mean of the individual Pearson Correlation Coefficient (PCC) obtained from comparing the actual and predicted joint angle value for each of the 29 DoFs considered, over the whole test trial. The median, first and third quartiles of the PCC were also computed along with the mean. MD is the mean, over the whole test trial, of the Weighted Fingertip Distance (WFD). For each time point estimated, WFD is defined as the average of: the distance between the position of the tip of the index finger (as recorded through Vicon) and its estimate (computed by RPC-Net), the distance between the position of the tip of the middle finger and its estimate, and the distance between the position of the tip of the thumb and its estimate. The median, first quartile and third quartile of the WFD over time were computed. A schematic representation of this process is included in Figure 3.4. Computational efficiency was evaluated using IT, defined as the average time required by the trained model to produce a single output prediction from an input sample. Computational efficiency, in this context, refers to the ability of the model

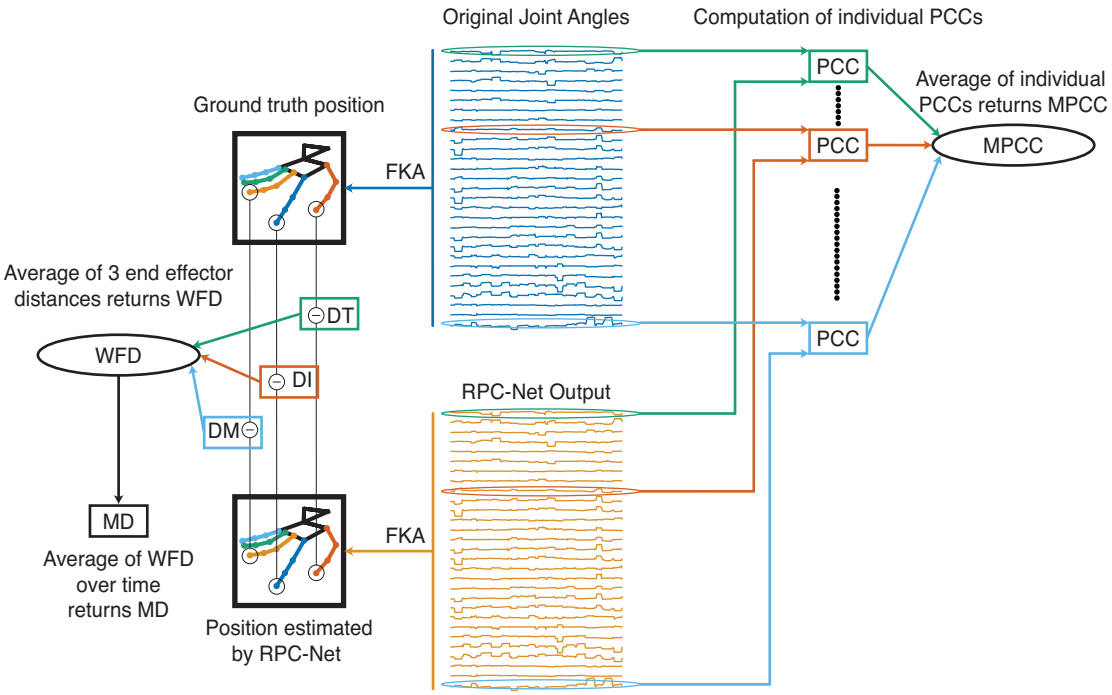

Figure 3.4: Schematic definition of MD and MPCC: The scheme represents the way in which the original joint angles and the estimate from RPC-Net are used to compute both MD and MPCC. PCC: Pearson Correlation Coefficient; MPCC: Mean Pearson Correlation Coefficient; FKA: Forward Kinematic Algorithm; DT: Distance of Thumb; DM: Distance of Middle finger; DI: Distance of Index finger; WFD: Weighted Fingertip Distance; MD: Mean Distance.

to generate output predictions rapidly and with minimal processing load, which is critical for real-time myoelectric control. It was quantified as the average inference time per sample during the test trial. The operations in RPC-Net do not benefit from using a Graphics Processing Unit (GPU) during the prediction phase (forward passes), and the PyTorch library does not improve performance in this context. Thus, although GPU usage can accelerate the training phase, performing matrix operations with the NumPy library, rather than PyTorch, on a Central Processing Unit (CPU) yielded the best performance during testing. IT was calculated as the average time, over 10^5 iterations, required by the NumPy implementation of the network to perform a forward pass. Computation was performed on an Intel(R) Xeon(R) Platinum 8268 CPU (2.90 GHz).

3.2.3 Comparison with State of the Art Solutions

Other state-of-the-art solutions for hand-position estimation were tested on the present dataset and their performance compared with that of RPC-Net. For each solution, a modified version was implemented to have a similar IT to RPC-Net (ensuring a fairer comparison), to fit the input (96-channel HD-sEMG, 16 samples) and to have the same output as RPC-Net (29 joint angles). The solutions (identified with a code) considered are:

1. the CNN proposed in Olsson et al. [293]. The original implementation has 4 convolutional layers with 128, 64, 64, 64 output channels and 4 fully connected layers with 512, 512, 128 and 16 units respectively. The modified version used in this study (CNN-Ols) has 4 convolutional layers with 128, 192, 192, 192 output channels and 5 fully connected layers with 1536, 1536, 384 and 29 units respectively.
2. The RNN proposed in Quivira et al., originally with hidden size of 50, 6 layers and 10 outputs, modified to have hidden size of 248, 8 layers and 29 outputs (RNN-Qui) [360].
3. The transformer architecture introduced in Putro et al. [361]. The original implementation has 1024 as dimension of model, 4 transformer layers and 22 outputs. The modified implementation used here (TRF-Put) has 96 as dimension of model, 15 transformer layers and 29 outputs. In the present implementation, the ReLU function after the last fully connected layer in the regression block was omitted.

The EMG input for RNN-Qui and TRF-Put was reshaped to a 16 (samples) $\times$ 96 (EMG channels) 2D array. For CNN-Ols, it was reshaped to a 16 (samples) $\times$ 6 (EMG electrode rows) $\times$ 16 (EMG electrode columns) 3D array. To compare the performance of RPC-Net with these alternative solutions, a one-sided paired t-test between the performance of RPC-Net and that of TRF-Put, RNN-Qui, and CNN-Ols, across all subjects, was performed for both MD and MPCC. The choice of the paired t-test was justified by the fact that it exhibits higher statistical power, under the assumption of normally distributed data, if compared to non-parametric

tests. This test is widely regarded as a robust method for assessing differences in two paired populations [362]. The one-sided version was chosen because superiority of RPC-Net in relation to other models was assessed. The condition of normality was verified with a Shapiro-Wilk test.

No correction for multiple comparisons was applied, as each comparison was pre-specified and corresponded to an independent model architecture tested under the same conditions. The analyses were therefore not exploratory or post hoc, and the resulting p-values were interpreted independently with due consideration for potential Type I error. This approach is consistent with recommendations for confirmatory analyses in which each hypothesis addresses an independent theoretical construct rather than a single family of related outcomes [363].

3.2.4 Variations of RPC-Net

Additional simulations were run to assess the effect of computational-cost-related parameters on the performance of the network by means of different statistical tools. The effect of the inclusion of information about the previous joint state was assessed with one-sided paired t-tests (see Section 3.2.4), and so was the effect of using a single or multiple networks for each joint (Section 3.2.4). The choice of this statistical tool is justified in Section 3.2.3. The condition of normality was verified with a Shapiro-Wilk test. For selected experimental conditions (Section 3.2.4, Section 3.2.4, Section 3.2.4), the results observed with RPC-Net and RPC-Net-B (defined in Section 3.2.4) were compared. Since, in this case, data distribution normality could not be guaranteed, the one-sided Wilcoxon signed-rank test, a non-parametric alternative to the paired t-test, was used [362]. The one-sided version was used because the superior performance of RPC-Net in relation to RPC-Net-B is assessed.

Inclusion or exclusion of previous joint state as input to RPC-Net

To evaluate if information about previous joint state could enhance performance, a comparison was performed between the performance of the original RPC-Net architecture with that of a similar architecture that does not make use of information

about previous kinematic state: RPC-Net-B (i.e., RPC-Net without the angle branch). The comparison was performed by means of a one-sided paired t-test between the results observed for RPC-Net and RPC-Net-B across all subjects, for both MD and MPCC.

Length of input signal

The length of the two signals given as input to RPC-Net was varied, keeping the sampling frequency unvaried, and thus modifying the number of samples in input. A different number of sampling points in input implied a change in network architecture, so that layer width was still a function of the number of input channels I_E and I_A, as shown in Figure 3.3. The EMG signal lengths were (rounded to the closest hundredth of second) 0.9 s (original length), 0.79 s, 0.68 s, 0.56 s, 0.45 s, 0.34 s, 0.22 s, and 0.11 s. The angle signal lengths were 3.60 s (original length), 3.15 s, 2.70 s, 2.25 s, 1.80 s, 1.35 s, 0.90 s and 0.45 s. Linear regression analysis, effective in quantifying the strength and direction of a linear relationship, was used to analyse the effect on performance of the length of input signals. The hypothesis that an increase in signal length correlates with an improvement in performance was tested [362]. The same assessment was performed on RPC-Net-B and the results compared through a Wilcoxon signed-rank test (96 coupled observations, 8 per subject, one each for RPC-Net and RPC-Net-B).

Width of neural network

The width of the neural layer of the EMG branch of RPC-Net was varied. Six widths were considered (in addition to the original one). The widths tested were: 1536 (original width), 1152 (E1), 921 (E2), 256 (E3), 768 (E4) and 576 (E5) units, each identified by a code (En). The assessment was performed both on RPC-Net and RPC-Net-B and the results compared using a Wilcoxon signed-rank test (72 coupled observations, 6 per subject, one each for RPC-Net and RPC-Net-B).

Table 3.1: Input electrode subsets

Code	Rows	Code	Rows	Code	Columns
A1	1-4	C1	1	D1	Even
A2	1,2,5,6	C2	2	D2	Odd
A3	3-6	C3	3	F1	1-5-9-13
B1	1-2	C4	4	F2	2-6-10-14
B2	3-4	C5	5	F3	3-7-11-15
B3	5-6	C6	6	F4	4-8-12-16

Definition of subsets of electrode rows and columns.

Number of electrodes used as input

The performance of RPC-Net using a subset of EMG channels as input was assessed. Subsets were defined either on the proximo-distal axis or on the circumferential axis. This implied a change in network architecture so that the width of the layers was still a function of the number of input channels, as shown in Figure 3.3. The 12 combinations of row subsets and the 6 combinations of column subsets reported in Table 3.1 were tested in addition to the original solution, which includes all rows and all columns.

Single network for multiple joints or separate networks for each joint

Two variations of RPC-Net (RPC-Net-W and RPC-Net-I) were developed that, instead of 29 independent sub-networks (each corresponding to a joint angle), are made up of a single unit that takes the same inputs and returns 29 joint angles. In RPC-Net-I, the structure of the network is identical to that of a single branch in RPC-Net (see Figure 3.3). RPC-Net-W is similar to RPC-Net-I, but the width of the layers was multiplied by a constant factor of 5 to match the IT of RPC-Net, thus ensuring a more appropriate comparison in performance. The performance of these alternative architectures was assessed and compared with that of the original RPC-Net, by means of a one-sided paired t-test across all subjects, for both MD and MPCC. The assessment was performed both on RPC-Net and RPC-Net-B, for which

analogous RPC-Net-I-B and RPC-Net-W-B were developed (i.e., RPC-Net-I-B is RPC-Net-I without joint angle input and RPC-Net-W-B is RPC-Net-W without joint angle input) and the results compared using a Wilcoxon signed-rank test (36 coupled observations, 3 per subject) with one observation each for RPC-Net (RPC-Net-W and RPC-Net-I) and RPC-Net-B (RPC-Net-W-B and RPC-Net-I-B).

3.3 Results

3.3.1 Performance of RPC-Net

Figure 3.5 shows the trend of WFD values over time, highlighting the discrepancy between RPC-Net estimates and actual data. A similar measure, the Unweighted Mean Distance (UMD), is also reported; it is computed using all hand markers rather than only the index, middle, and thumb. Table 3.2 reports the MPCC and MD for all subjects. Figure 3.6 shows the overlap between RPC-Net estimates and the actual joint angles, with joint codes defined in Figure 2.1. The results shown correspond to a one-minute interval from the test trial acquired for S11. These results indicate that the estimates are consistently good across all joints. The best results in terms of PCC are observed for the flexion/extension of the wrist joint and the metacarpophalangeal joint of the four fingers. The inference time of RPC-Net is 10.1 ms, with a standard deviation of 0.4 ms.

3.3.2 Variations of RPC-Net and Comparison with Other Solutions

Figure 3.7 to Figure 3.14 show RPC-Net performance when compared with other DL solutions and its own variants, measured by the previously defined indicators: MD, MPCC, and IT. Markers indicate mean values, intervals highlight the first and third quartiles, and a dot symbolises the median. Relevant statistical measures are provided in each caption. For the one-sided paired t-test, the t statistic and the corresponding p-value were included in the caption. For regression analyses, the caption includes $\hat{\beta}_1$, SE, t, p, R^2 and adjusted R^2. In Figure 3.8, Figure 3.10 and Figure 3.13 the left and right plot columns indicate architectures with

Table 3.2: Performance indicators for RPC-Net across subjects

Subject	MD (Q1, Med, Q3) (mm)	MPCC (Q1, Med, Q3) (%)
S1	25.5 (16.5, 23.5, 33.6)	60.4 (48.6, 62.8, 79.3)
S2	23.2 (16.9, 22.4, 28.4)	78.0 (73.0, 86.8, 91.9)
S3	21.9 (14.5, 20.0, 26.9)	81.2 (79.0, 86.7, 90.1)
S4	26.0 (14.9, 23.5, 34.0)	70.6 (56.0, 77.3, 92.8)
S5	30.4 (19.2, 26.9, 40.1)	68.3 (58.3, 73.8, 83.5)
S6	30.1 (19.4, 28.2, 38.0)	72.6 (65.8, 76.5, 87.5)
S7	30.2 (18.3, 25.2, 37.0)	75.0 (62.2, 77.7, 87.2)
S8	25.3 (15.3, 21.3, 32.2)	83.7 (79.7, 85.7, 91.0)
S9	25.4 (15.9, 23.5, 32.9)	70.1 (60.1, 72.5, 83.1)
S10	26.6 (16.6, 24.5, 32.6)	76.1 (66.5, 79.5, 85.0)
S11	19.4 (12.4, 17.4, 24.5)	84.6 (77.0, 87.8, 91.7)
S12	20.6 (13.9, 18.4, 25.2)	79.0 (73.5, 79.3, 90.7)

Performance of RPC-Net for the twelve subjects considered in the study. The mean, first quartile (Q1), third quartile (Q3), and median (Med) are shown for each subject and for both performance indicators.

or without information about previous position, respectively, while Figure 3.9, Figure 3.11 and Figure 3.14 compare the two conditions, using y-values from the left and right columns to determine the position of a marker. Values on the y-axis in the left columns of the first group of figures are the x-axis in the second (comparison) group of figures, and values on the y-axis in the right plot column are the y-axis. Bland-Altman plots are also included. For the Wilcoxon signed-rank test the statistic W (sum of the ranks of positive differences) and the p-value were reported in the caption. Figure 3.7 compares the performance of RPC-Net, RPC-Net-B, TRF-Put, RNN-Qui, and CNN-Ols, referring to the experiments in Section 3.2.3 and Section 3.2.4. Statistical tests confirm the superior performance of RPC-Net over the other solutions. Another analysis (right column of plots) studies the impact of angle branch input signal length, revealing no significant influence on performance. Figure 3.8 and Figure 3.9 depict performance trends

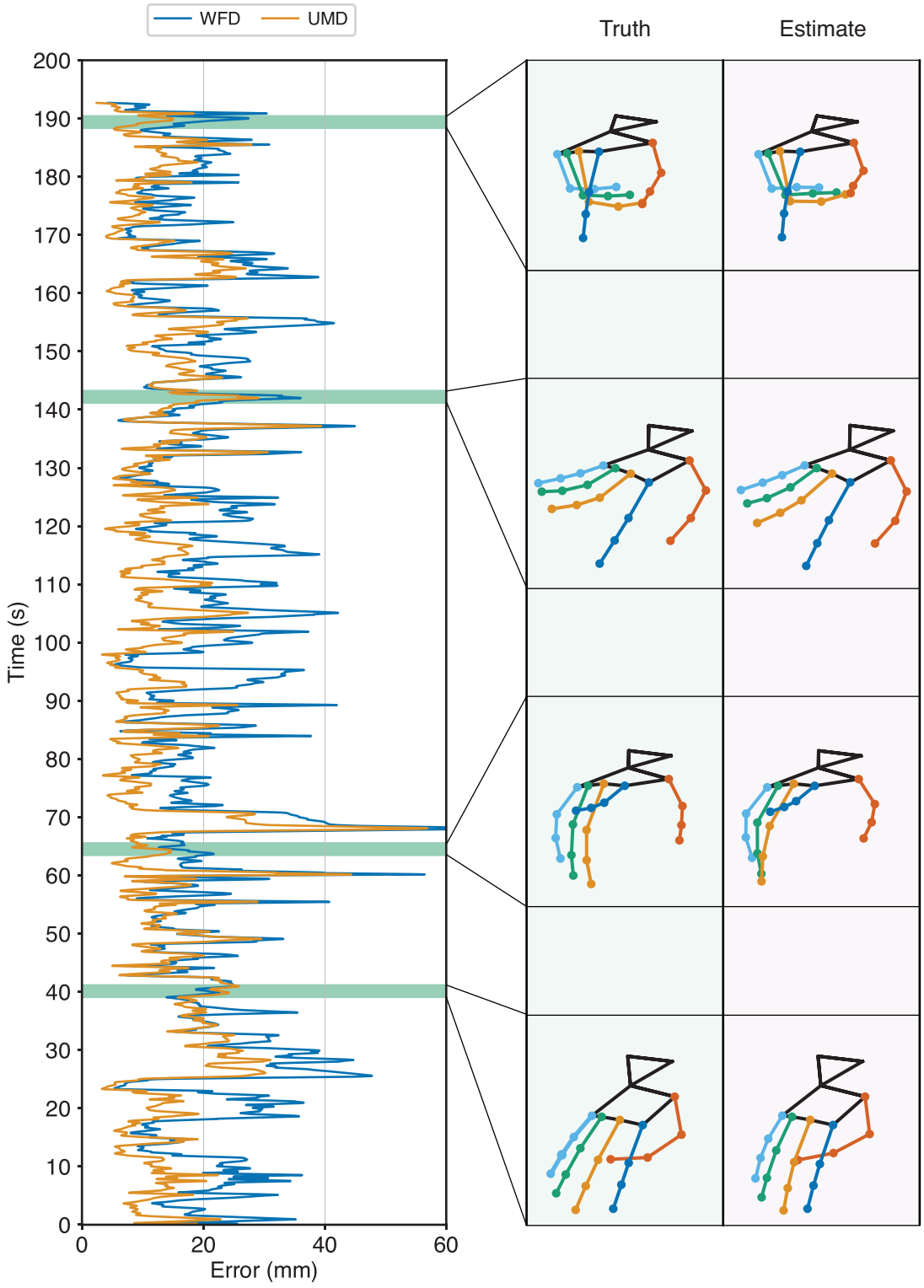

Figure 3.5: Estimation error of RPC-Net: The two lines show UMD and WFD over the S11 test trial. For selected time points, the estimated position (right) and the actual one (left) are shown on the side.

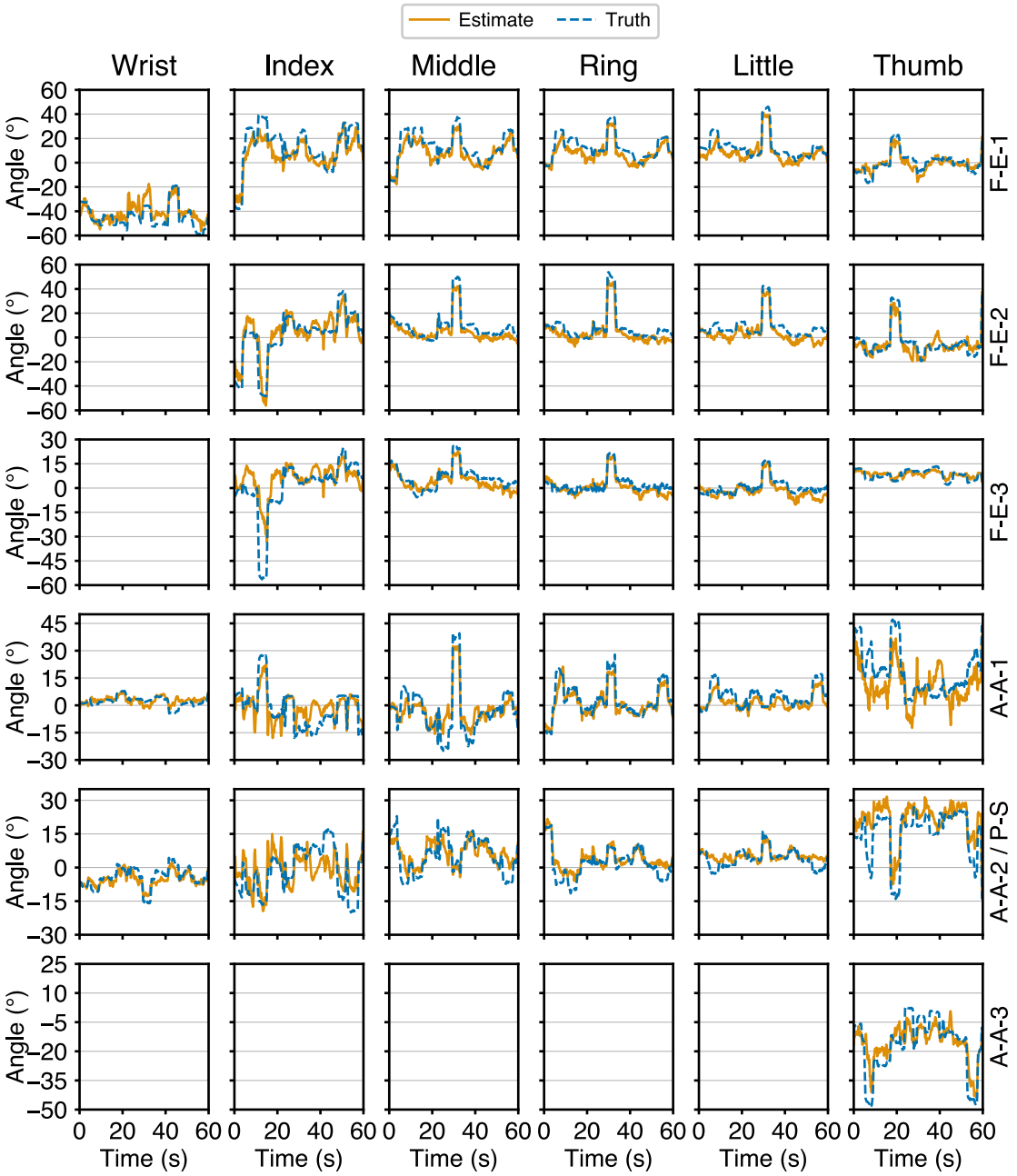

Figure 3.6: Comparison between RPC-Net estimates and target values: The 29 joints considered are shown. The columns represent the anatomical region to which each angle belongs, while the rows represent the type of DoF considered, as defined in Figure 2.1. DoFs of the same type (e.g., F-E) are numbered from proximal to distal. The results refer to a one-minute interval in the test recording from S11. This subject was selected not for representativeness of overall accuracy, but for the clarity of flexion and extension activity.

based on EMG branch input signal length for RPC-Net and RPC-Net-B, as detailed in Section 3.2.4. Longer signals predictably enhance performance. Figure 3.10 and

Figure 3.11 examine the influence of the EMG branch layer width on performance for RPC-Net and RPC-Net-B, as defined in Section 3.2.4. Visually, wider layers improve performance, though computational cost escalates more quickly. Figure 3.12 evaluates RPC-Net variants using a subset of electrodes, defined in Section 3.2.4. Fewer electrodes predictably lower performance. However, computational cost decreases significantly with fewer electrodes. Lastly, Figure 3.13 and Figure 3.14 contrast the performances of RPC-Net, RPC-Net-W, RPC-Net-I, and their RPC-Net-B counterparts, as described in Section 3.2.4. RPC-Net outperforms RPC-Net-I (with a considerable difference in computational cost), but not RPC-Net-W. The results, as seen in Figure 3.9, Figure 3.11, and Figure 3.14, indicate that prior kinematic state information consistently improves performance.

3.4 Discussion

The most important consideration that can be inferred from the results is that RPC-Net is capable of translating electromyographic activity into hand position with high accuracy.

The first hypothesis assessed in this study was that RPC-Net can generate high-quality hand position estimates from HD-sEMG signals and that it can outperform current state-of-the-art solutions. The results support this hypothesis. RPC-Net achieved a mean endpoint error (MD) of 25.4 mm across subjects. As outlined in Section 2.3.1, control can be considered functionally perfect when the endpoint error approaches 2 mm, essentially indistinguishable from true movement. Although the performance achieved by RPC-Net does not reach this theoretical optimum, an error of roughly 25 mm still represents high-quality control (Section 2.3.1), in line with or exceeding results reported in comparable studies [93, 346]. From a practical perspective, this magnitude of deviation corresponds to subtle spatial discrepancies that do not compromise the recognisability or intention of the movement. In prosthetic or rehabilitation contexts, where users typically employ continuous visual and proprioceptive feedback to guide motion, such an error would still enable intuitive and functional interaction. Indeed, several prior works have identified

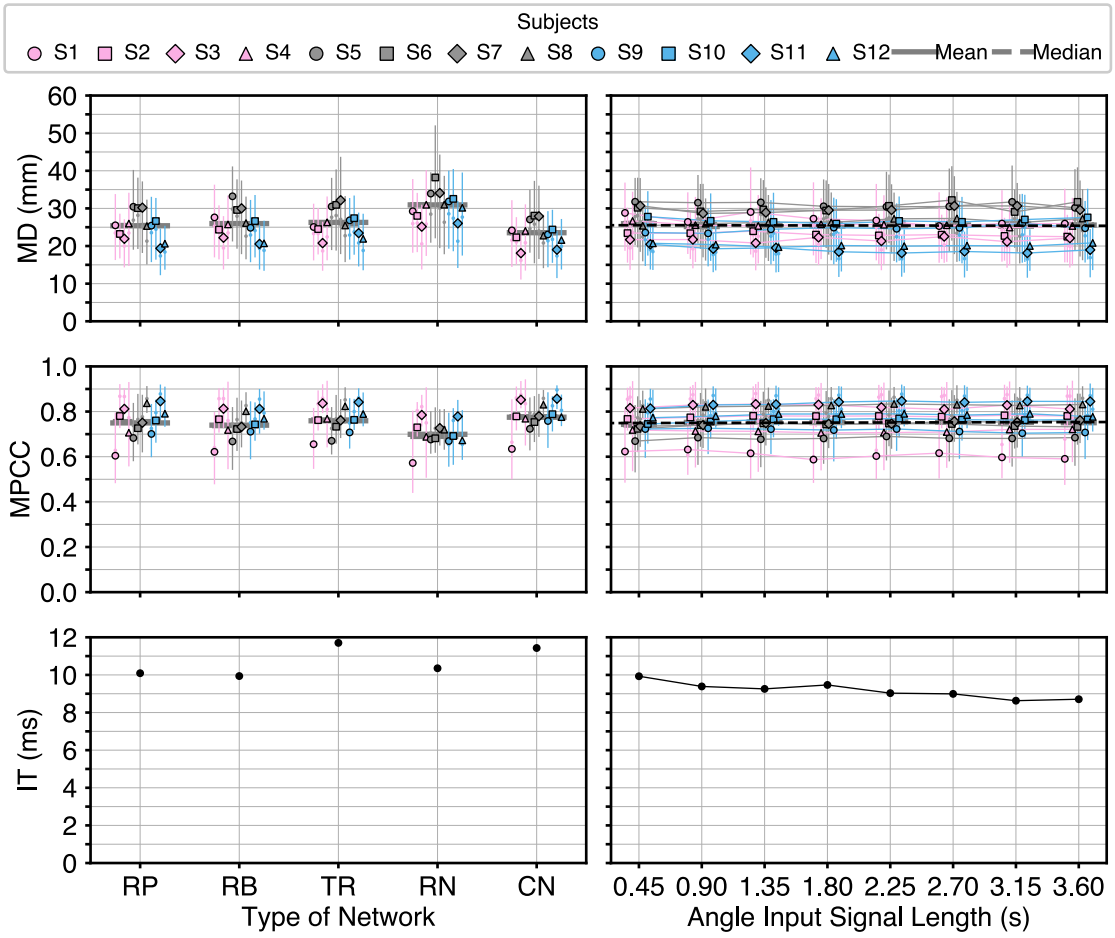

Figure 3.7: Performance of RPC-Net (comparison with state of the art): (Left) Comparison of the performance between RPC-Net, RPC-Net-B, TRF-Put, RNN-Qui, and CNN-Ols. The figure reflects the experimental conditions outlined in Section 3.2.3 and Section 3.2.4. Markers indicate the mean, with IQR shown. Median is shown as a smaller marker. One-sided paired t-test results for MD (H_0: RPC-Net $\geq$ RPC-Net-B): $t(11)$ = -1.89 $p = 4.2{\cdot}10^{-2}$, (H_0: RPC-Net $\geq$ TRF-Put): $t(11)$ = -2.32 $p = 2.0{\cdot}10^{-2}$, (H_0: RPC-Net $\geq$ RNN-Qui): $t(11)$ = -9.99 $p = 4.1{\cdot}10^{-7}$, (H_0: RPC-Net $\geq$ CNN-Ols): $t(11)$ = 4.93 $p = 1$. One-sided paired t-test results for MPCC (H_0: RPC-Net $\leq$ RPC-Net-B): $t(11)$ = 1.99 $p = 3.6{\cdot}10^{-2}$, (H_0: RPC-Net $\leq$ TRF-Put): $t(11)$ = -1.32 $p = 8.9{\cdot}10^{-1}$, (H_0: RPC-Net $\leq$ RNN-Qui): $t(11)$ = 4.80 $p = 2.8{\cdot}10^{-4}$, (H_0: RPC-Net $\leq$ CNN-Ols): $t(11)$ = -3.6 $p = 1.0$. (Right) Performance as a function of angle branch input signal length, as described in Section 3.2.4. Regression analysis results for MD (H_0: $\beta_1 = 0$ mm/s): $\hat{\beta}_1$ = $-4.1{\cdot}10^{-2}$ mm/s, $SE = 3.8{\cdot}10^{-1}$, $t = -1.1{\cdot}10^{-1}$, $p = 9.1{\cdot}10^{-1}$, $R^2 = 1.2{\cdot}10^{-4}$, adjusted R^2 = $-1.1{\cdot}10^{-2}$. Regression analysis results for MPCC (H_0: $\beta_1 = 0$ 1/s): $\hat{\beta}_1 = 1.3{\cdot}10^{-3}$ 1/s, $SE = 6.4{\cdot}10^{-3}$, $t = 2.1{\cdot}10^{-1}$, $p = 8.4{\cdot}10^{-1}$, $R^2 = 4.6{\cdot}10^{-4}$, adjusted R^2 = $-1.0{\cdot}10^{-2}$.

endpoint errors of up to 50 mm as the approximate upper limit for functionally acceptable control of end-effectors. Within this framework, RPC-Net therefore achieves high-quality performance well within the range of practical usability.

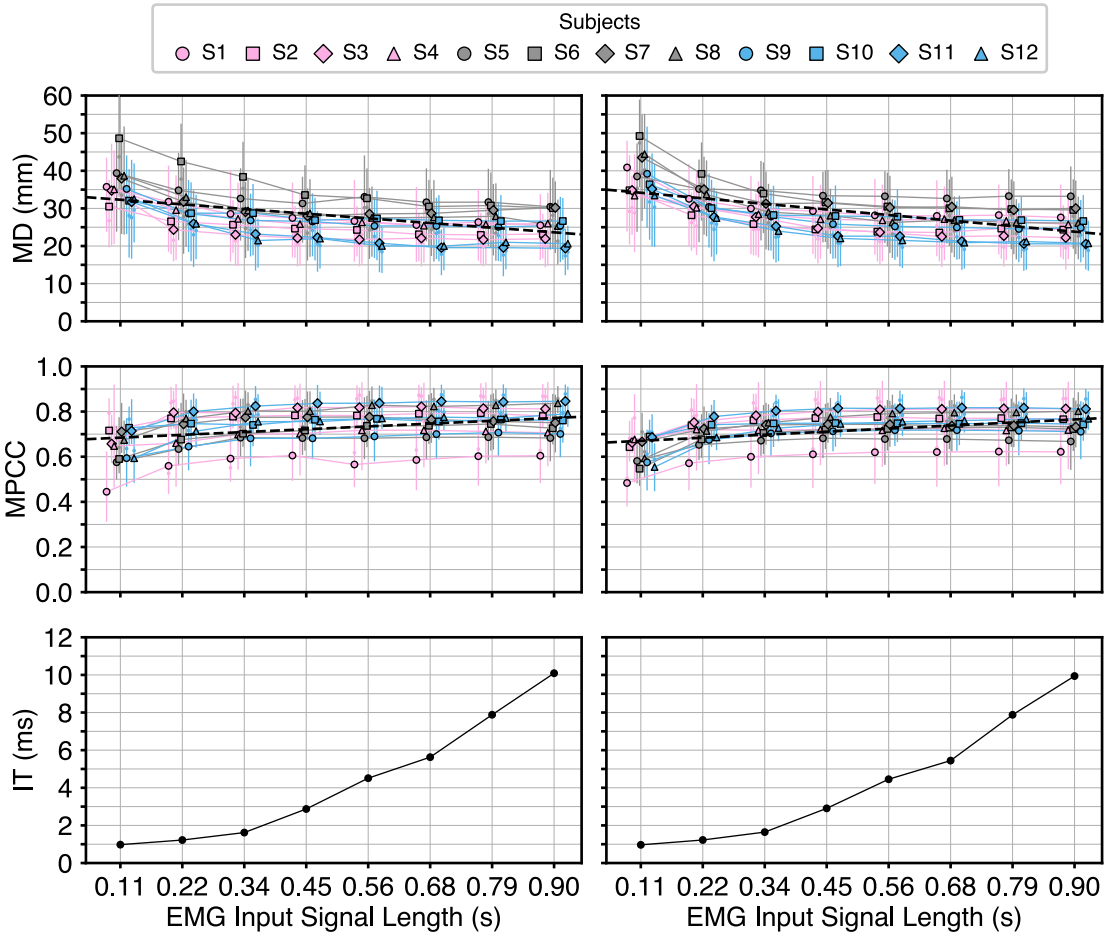

Figure 3.8: Performance of RPC-Net as a function of EMG input signal length: Results for RPC-Net and RPC-Net-B are presented, as defined in Section 3.2.4. Markers indicate the mean, with IQR shown. Median is shown as a smaller marker. (Left) RPC-Net. Regression analysis results for MD (H_0: $\beta_1 = 0$): $\hat{\beta}_1$ = -1.1·10^{1} mm/s, SE = 1.8·10^{0}, t = -6.2·10^{0}, p = 1.5·10^{-8}, R^2 = 2.9·10^{-1}, adjusted R^2 = 2.8·10^{-1}. Regression analysis results for MPCC (H_0: $\beta_1 = 0$): $\hat{\beta}_1$ = 1.1·10^{-1} 1/s, SE = 2.9·10^{-2}, t = 3.8·10^{0}, p = 2.5·10^{-4}, R^2 = 1.3·10^{-1}, adjusted R^2 = 1.2·10^{-1}. (Right) RPC-Net-B. Regression analysis results for MD (H_0: $\beta_1 = 0$): $\hat{\beta}_1$ = -1.3·10^{1} mm/s, SE = 1.7·10^{0}, t = -7.7·10^{0}, p = 1.4·10^{-11}, R^2 = 3.9·10^{-1}, adjusted R^2 = 3.8·10^{-1}. Regression analysis results for MPCC (H_0: $\beta_1 = 0$): $\hat{\beta}_1$ = 1.2·10^{-1} 1/s, SE = 2.4·10^{-2}, t = 4.9·10^{0}, p = 3.8·10^{-6}, R^2 = 2.0·10^{-1}, adjusted R^2 = 2.0·10^{-1}.

In terms of robustness, it is worth mentioning that the current implementation of the algorithm includes a fourth-order low-pass Butterworth filter (cut-off frequency $f_c = 1$ Hz) applied to the estimated joint angles prior to conversion into marker positions. The purpose of this filtering step was to suppress high-frequency components associated with natural hand tremor and noise-related fluctuations in

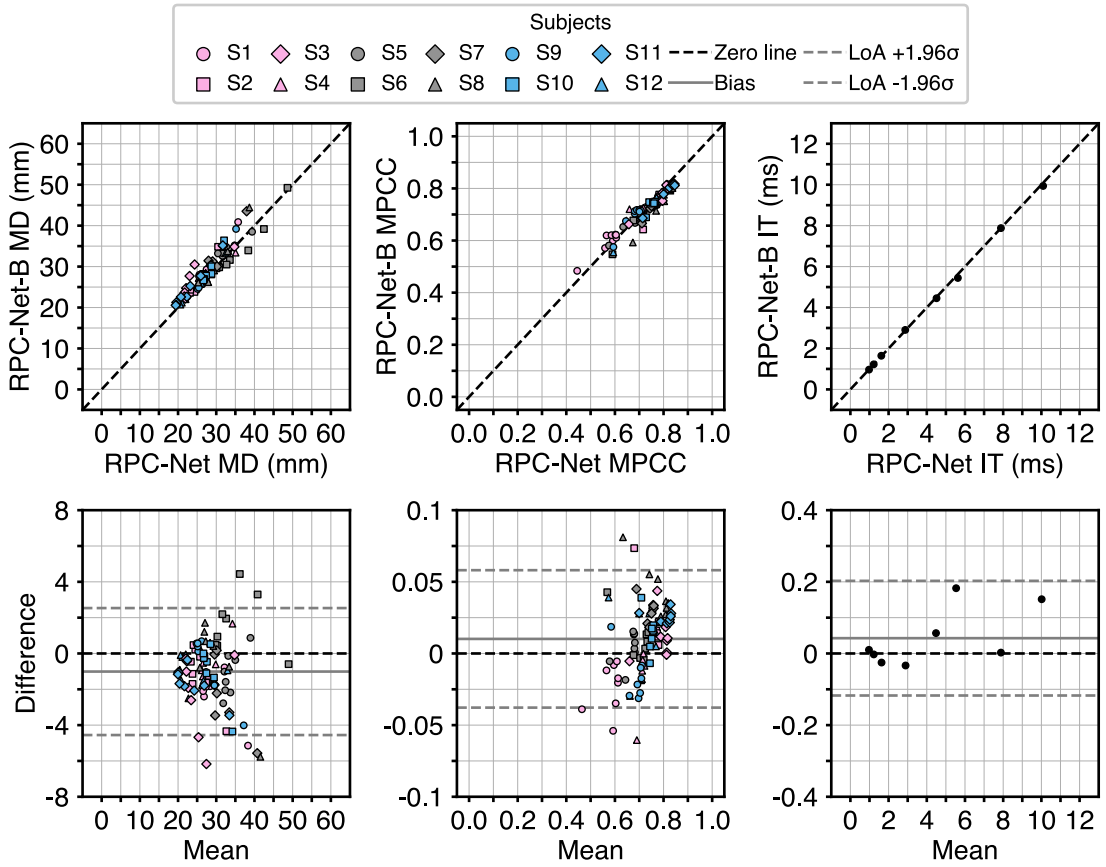

Figure 3.9: Comparative analysis (EMG input signal length): Results for RPC-Net and RPC-Net-B, as defined in Section 3.2.4. A comparative analysis between the two models is presented. (Top:) Subject-by-subject and case-by-case comparison of MD, MPCC, and IT values obtained with RPC-Net and RPC-Net-B. (Bottom:) Bland-Altman plots showing agreement between the two models. Each point represents an individual subject-element pair, plotted as the difference between models against their mean. The solid grey line indicates the mean bias, the dashed grey lines denote the 95% limits of agreement (bias ± 1.96 SD), and the dashed black line marks zero difference. Wilcoxon signed-rank test results for MD (H_0: median RPC-Net $\geq$ median RPC-Net-B): $W = 908$, $p = 1.1{\cdot}10^{-7}$. Wilcoxon signed-rank test results for MPCC (H_0: median RPC-Net $\leq$ median RPC-Net-B): $W = 3425$, $p = 3.1{\cdot}10^{-5}$.

the predicted trajectories, thereby improving the smoothness of the reconstructed movements. This post-processing step effectively mitigated artefacts arising from continual movement and reduced apparent shaking in the generated motion profiles.

While other ML approaches yield results comparable to those reported here in EMG-based prosthetic control, these either control a limited number of DoFs [301, 328], rely on electrodes positioned too distally [346], or employ algorithms that demand substantial computational resources [364, 365]. As for the second

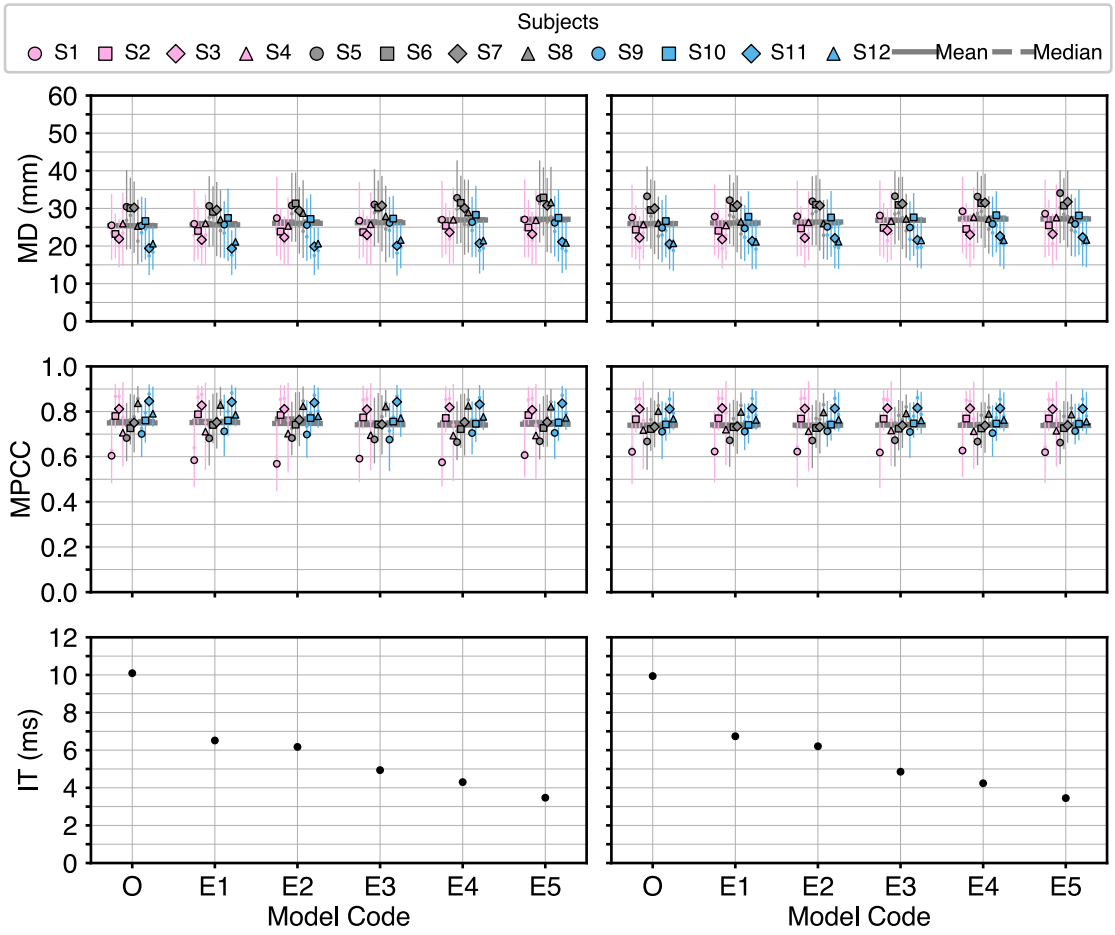

Figure 3.10: Performance of RPC-Net as a function of EMG layer width: Results for RPC-Net and RPC-Net-B. The x-axis shows the layer-width codes defined in Section 3.2.4. The original configuration (O) is also reported. Markers indicate the mean, with IQR shown. Median is shown as a smaller marker. (Left) RPC-Net. (Right) RPC-Net-B.

point, the use of electrodes positioned too distally (on the wrist or thumb) poses a challenge in applications, as many amputees lack these parts of the limb [57]. The results indicate that all the necessary information to determine the current kinematic state of the hand can be derived from the electromyographic activity in the proximal portion of the forearm, even for joints with distal or intrinsic actuators. Although the adequacy of forearm electromyogram for prosthetic control has been demonstrated [93], no study has yet demonstrated the feasibility of all-DoF control using electromyographic activity acquired solely from the proximal forearm. On the computational front, algorithms that demand extensive resources necessitate

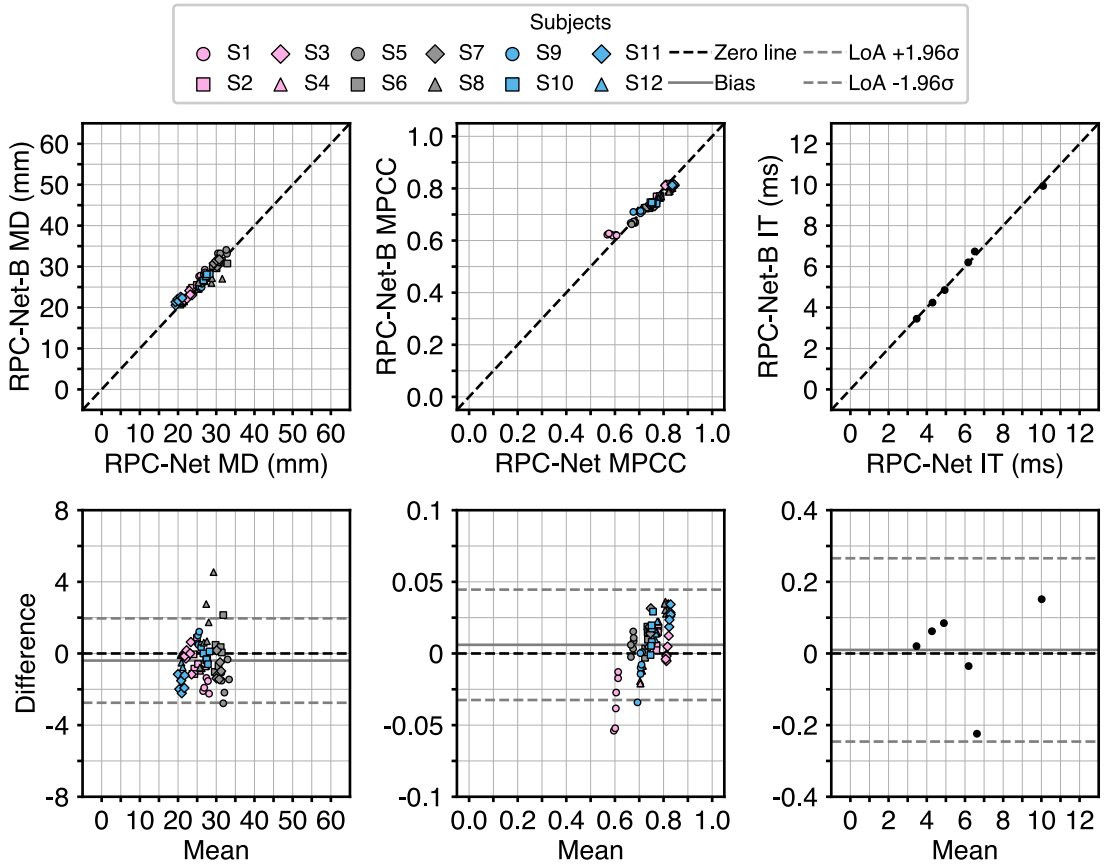

Figure 3.11: Comparative analysis (EMG layer width): Results for RPC-Net and RPC-Net-B (Section 3.2.4). A comparative analysis between the two models is presented. (Top:) Subject-by-subject and case-by-case comparison of MD, MPCC, and IT values obtained with RPC-Net and RPC-Net-B. (Bottom:) Bland-Altman plots showing agreement between the two models. Each point represents an individual subject-element pair, plotted as the difference between models against their mean. The solid grey line indicates the mean bias, the dashed grey lines denote the 95% limits of agreement (bias $\pm$ 1.96 SD), and the dashed black line marks zero difference. Wilcoxon signed-rank test results for MD (H_0: median RPC-Net $\geq$ median RPC-Net-B): $W = 717$, $p = 4.0{\cdot}10^{-4}$. Wilcoxon signed-rank test results for MPCC (H_0: median RPC-Net $\leq$ median RPC-Net-B): $W = 1856$, $p = 1.2{\cdot}10^{-3}$.

advanced hardware like GPUs, which are impractical to embed into a prosthetic device, thereby limiting their applicability in clinical settings.

In this regard, the results point to another novel finding: high-quality regression can be achieved using simple fully-connected neural architectures, rather than complex convolutional structures, a result demonstrated by the performance of RPC-Net when compared with an implementation of the solutions proposed by Quivira et al. [360], Olsson et al. [293], and Putro et al. [361]. The comparison

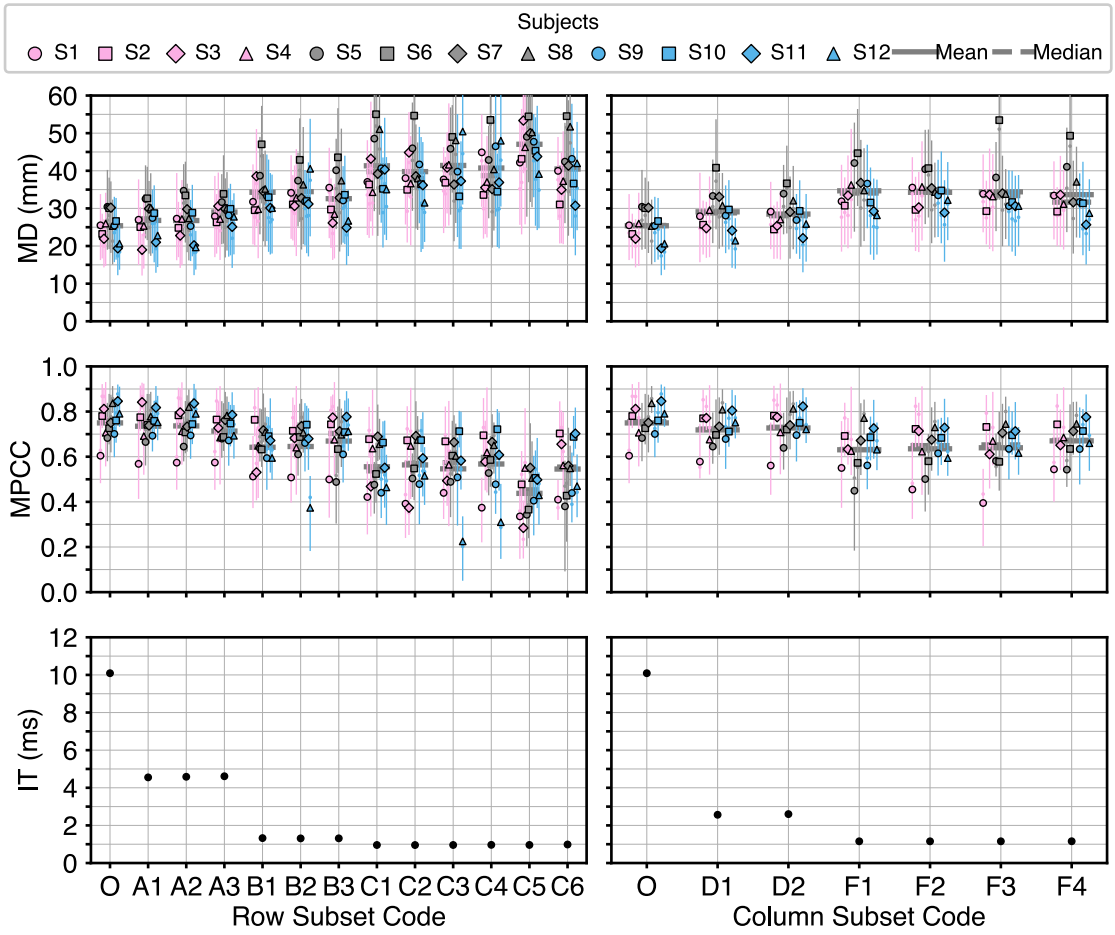

Figure 3.12: Performance of RPC-Net as a function of the subset of electrodes used: The original configuration (O) is also reported. Protocol described in Section 3.2.4. Markers indicate the mean, with IQR shown. Median is shown as a smaller marker. (Left) Row subsets. (Right) Column subsets.

performed in this chapter demonstrates that, for approximately equal computational cost, RPC-Net clearly outperforms the RNN architecture proposed by Quivira et al. This is supported by the p-values observed in the one-sided t-test ($4.1{\cdot}10^{-7}$ for MD and $2.8{\cdot}10^{-4}$ for MPCC). Specifically, RPC-Net achieved an improvement of over 5 mm in MD (25.4 mm vs 30.9 mm) and more than 5 percentage points in MPCC (75.0% vs 69.9%). When compared to the transformer architecture proposed by Putro et al., the results are more nuanced: RPC-Net showed better performance in MD (25.4 mm vs 26.3 mm, $p = 2.0{\cdot}10^{-2}$), whereas the transformer architecture performed slightly better in MPCC (75.0% vs 75.9%, $p = 8.9{\cdot}10^{-1}$). In contrast, the CNN developed by Olsson et al. outperformed RPC-Net on both metrics (MD:

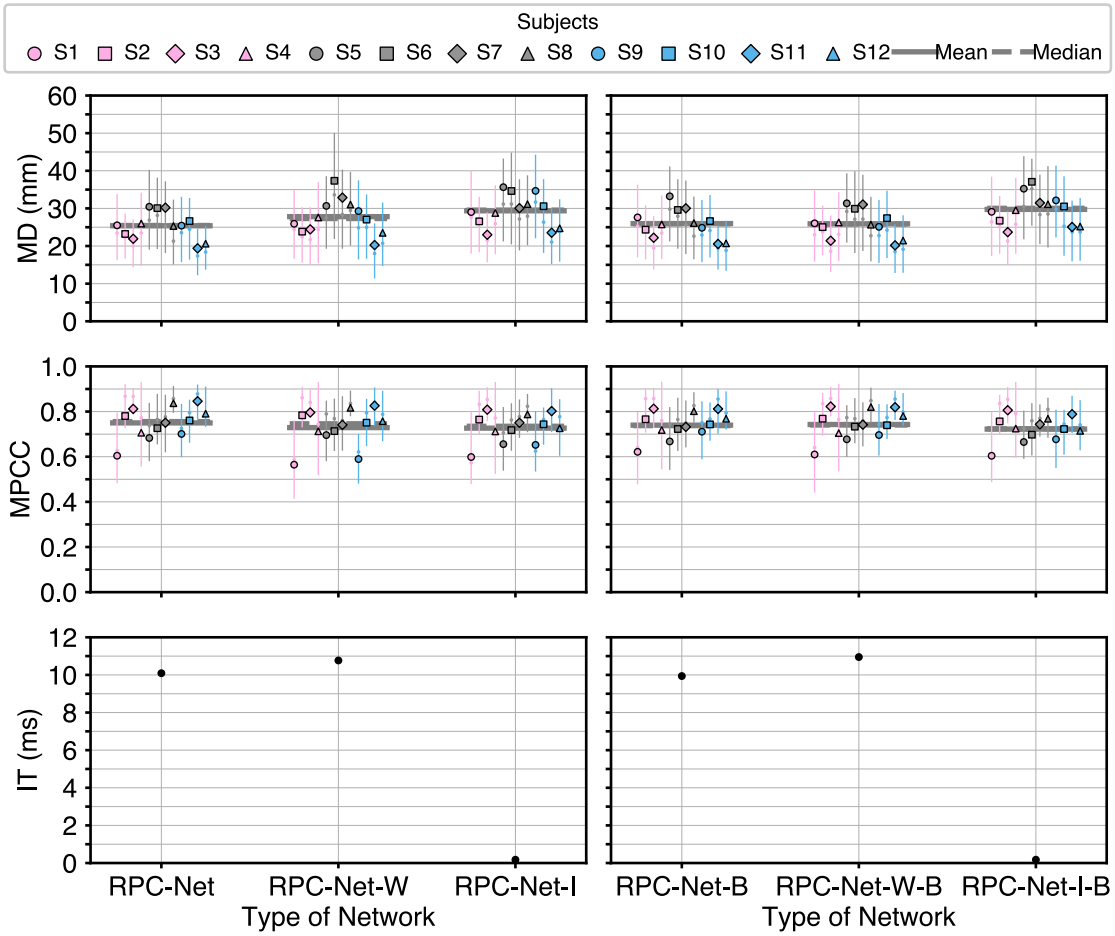

Figure 3.13: Performance of RPC-Net-I, RPC-Net-W, and RPC-Net: Protocol described in Section 3.2.4. Markers indicate the mean, with IQR shown. Median is shown as a smaller marker. (Left) RPC-Net. One-sided paired t-test results for MD(H_0: RPC-Net $\geq$ RPC-Net-W): $t(11)$ = -3.7, $p = 1.7{\cdot}10^{-3}$, (H_0: RPC-Net $\geq$ RPC-Net-I): $t(11)$ = -5.9, $p = 5.4{\cdot}10^{-5}$. One-sided paired t-test results for MPCC (H_0: RPC-Net $\leq$ RPC-Net-W): $t(11) = 2.2$, $p = 2.4{\cdot}10^{-2}$, (H_0: RPC-Net $\leq$ RPC-Net-I): $t(11) = 3.5$, $p = 2.6{\cdot}10^{-3}$. (Right) RPC-Net-B. One-sided paired t-test results for MD (H_0: RPC-Net-B $\geq$ RPC-Net-W-B): $t(11) = 0.22$, $p = 5.9{\cdot}10^{-1}$, (H_0: RPC-Net-B $\geq$ RPC-Net-I-B): $t(11)$ = -6.2, $p = 3.6{\cdot}10^{-5}$. One-sided paired t-test results for MPCC (H_0: RPC-Net-B $\leq$ RPC-Net-W-B): $t(11)$ = -0.93, $p = 8.1{\cdot}10^{-1}$, (H_0: RPC-Net-B $\leq$ RPC-Net-I-B): $t(11) = 3.3$, $p = 3.7{\cdot}10^{-3}$.

23.5 mm vs 25.4 mm, $p = 1$; MPCC: 77.5% vs 75.0%, $p = 1$). Although RPC-Net did not outperform all compared solutions, it consistently delivered results within a reasonable margin of the best-performing models, specifically, remaining within 2 mm of the top MD value. Importantly, the extremely lightweight design of RPC-Net makes it a strong candidate for deployment on microprocessors within

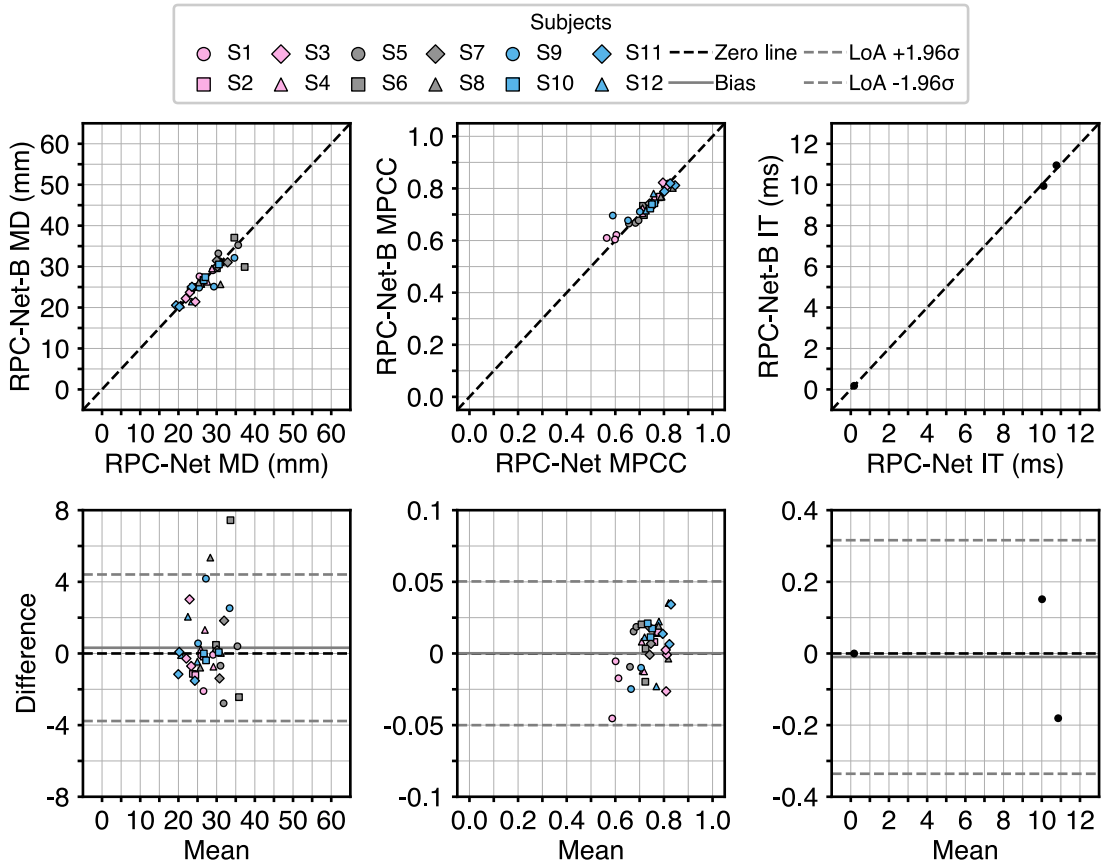

Figure 3.14: Comparative analysis (RPC-Net-W, RPC-Net-I, and RPC-Net): Protocol described in Section 3.2.4. Results for RPC-Net and RPC-Net-B. A comparative analysis between the two models is presented. (Top:) Subject-by-subject and case-by-case comparison of MD, MPCC, and IT values obtained with RPC-Net and RPC-Net-B. (Bottom:) Bland-Altman plots showing agreement between the two models. Each point represents an individual subject-element pair, plotted as the difference between models against their mean. The solid grey line indicates the mean bias, the dashed grey lines denote the 95% limits of agreement (bias $\pm$ 1.96 SD), and the dashed black line marks zero difference. Wilcoxon signed-rank test results for MD (H_0: median RPC-Net $\geq$ median RPC-Net-B): $W = 321$, $p = 4.3{\cdot}10^{-1}$. Wilcoxon signed-rank test results for MPCC (H_0: median RPC-Net $\leq$ median RPC-Net-B): $W = 387$, $p = 2.0{\cdot}10^{-1}$.

rehabilitation devices, a level of hardware efficiency that would be more difficult to achieve with CNNs or RNNs.

In quantitative terms, the full version of RPC-Net comprises approximately $2.6{\cdot}10^7$ trainable parameters and requires about $5.1{\cdot}10^7$ floating-point operations per inference cycle (corresponding to roughly $5.1{\cdot}10^8$ per second). These values place the network outside the functional constraints identified in Section 2.2.4 by at least an order of magnitude. However, as discussed in the remainder of this

section, RPC-Net exhibits substantial robustness to reductions in both electrode count and layer width. Because the number of parameters and the associated computational cost scale quadratically with layer width, even modest reductions in these dimensions lead to large decreases in memory and processing requirements. Consequently, with minor architectural adjustments, whose performance impact is quantified later in this chapter, RPC-Net can be brought within the computational limits required for deployment on embedded hardware.

Second, the results illustrate the resilience of RPC-Net against reductions in EMG electrode numbers, shorter input signals, and other conditions that could lower computational cost. The findings indicate that while additional input data typically enhances estimation quality, the improvement does not correspond proportionally to computational cost. For instance, reducing the number of electrodes from 96 to 32 only increased fingertip distance by less than 10 mm and reduced MPCC by 10%, yet resulted in an 85% reduction in computation time. Hence, a control solution based on RPC-Net could offer substantial flexibility and could be implemented with fewer electrodes or a shorter input signal, implying that the computational cost of the solution could be further minimised with minimal performance loss, making it highly adaptable to clinical practice. Previous studies have explored the adequacy of fewer electrodes for control, but none for this number of DoFs [366, 367].

It is noteworthy that the reduction in electrode count affected participants differently: for some, such as S11, performance remained largely stable, whereas others, such as S6, experienced a substantial drop in accuracy. Several factors could explain this inter-subject variability. First, the quality of the recorded electromyographic signal is strongly influenced by individual physiological characteristics, including skin impedance, subcutaneous fat thickness, and muscle volume, all of which vary with body composition and can alter the spatial reach of the detected potentials. In subjects with stronger or more superficial musculature, each electrode can capture activity from a wider region, rendering the system less sensitive to reductions in channel count. Second, small variations in electrode placement can have a pronounced effect, particularly for muscles with limited superficial exposure.

Some intrinsic or distal finger muscles, for instance, may be accessible on the skin surface for only a few millimetres; a minor shift in electrode position can therefore cause these signals to be missed entirely. This limitation is accentuated by the fixed inter-electrode spacing of the array, which restricts the flexibility to compensate for anatomical variability across subjects. Finally, when the number of electrodes is reduced, noisy or low-quality channels exert a greater relative influence on the input representation, potentially degrading performance in individuals with less favourable recording conditions. Together, these factors likely account for the subject-dependent impact of electrode reduction observed.

As for the third and final hypothesis assessed in this chapter, incorporating information about the previous kinematic state significantly improves performance in every condition tested. The improvement provided by the inclusion of previous-state information is consistent across subjects and across experimental conditions. Although these improvements are statistically significant, the resulting reduction in endpoint error typically remains below the operational threshold of 10-12 mm defined in Section 2.3.1, and therefore does not constitute a behaviourally meaningful difference in absolute accuracy. In real-life situations, however, this feature could offer a stabilising mechanism to counteract the stochastic nature of electromyographic signals.

In synthesis, this chapter demonstrated that RPC-Net is capable of translating electromyographic activity into hand position with high accuracy, withstanding a comparison with recent state of the art techniques and demonstrating robustness to changes in input structure. This finding is of vital importance, as it demonstrates that a solution addressing user needs and allowing natural-feeling control while remaining computationally efficient can achieve high performance, and it opens new opportunities for the implementation of such solutions in a clinical setting. The experiments described in this work were conducted entirely offline and on healthy subjects. For RPC-Net to be properly validated for controlling upper limb prostheses, its performance must be demonstrated in conditions more closely resembling

the actual target case. To achieve this, the next chapters include the online implementation of RPC-Net and its application to a real rehabilitation scenario.

3.5 Conclusion

In this chapter, RPC-Net, a method for translating electromyographic activity to hand position using a computationally efficient neural network architecture, was introduced and extensively evaluated. The results of the study demonstrated that RPC-Net performs better than state-of-the-art methods with a similar computational cost and without requiring advanced computational resources. This signifies a crucial development, making the system more adaptable and potentially more accessible in clinical settings. A key feature that substantially contributes to system performance is the incorporation of information about the previous kinematic state. Furthermore, robustness was demonstrated against changes in input signal length and the number of EMG channels used, reinforcing flexibility and adaptability. The development and success of RPC-Net have significant implications for biomedical research and practical applications. It offers a new avenue for prosthetic control that is more natural-feeling, computationally efficient, and flexibly adaptable to different clinical settings and patient needs. This progress has the potential to improve the quality of life for individuals with limb loss, advancing biomedical research and its clinical applications.

4

HDE-Array: Development and Validation of a New Dry Electrode Array Design to Acquire HD-sEMG for Hand Position Estimation

4.1 Introduction

As discussed in Chapter 3, the high burden and prevalence of upper-limb amputations and cervical spinal cord injuries highlight the continued need for effective upper-limb rehabilitation technologies [21, 33, 56, 368–371]. While advances in prosthetic design and FES have been substantial, with sEMG emerging as the leading control source, device abandonment remains high, often exceeding 30%, due to limitations in comfort, functionality, and control naturalness [22, 57, 58, 65, 67, 69, 93, 104, 336–338, 341, 372–376].

In the previous chapter, these issues were addressed with RPC-Net, which estimates hand position using HD-sEMG from the forearm. RPC-Net surpasses the performance of existing state-of-the-art control solutions and effectively addresses some of the factors that have historically hindered user acceptance and comfort, particularly the naturalness of control. However, during the validation process, it became apparent that traditional gel electrodes (here referring to HD-sEMG arrays

relying on conductive gel to reduce skin-electrode impedance and ensure stable electrical contact), though effective at capturing EMG signals, have significant practical drawbacks. The need for adhesive pads and conductive gel makes them cumbersome to apply, time-consuming to clean, and unsuitable for daily or home-based use, thereby complicating the acquisition setup and limiting user acceptance. Building on the success of RPC-Net, a new solution was developed to address these issues: the HDE-Array. HDE-Array consists of two rings of 32 dry electrodes each, eliminating the need for adhesive pads and conductive gel required by gel arrays. This makes it more cost-effective, comfortable, and faster for users, improving accessibility for daily use and addressing a key factor in device acceptance. The growing preference for dry electrodes is reflected in recent literature [357, 377–379]. Additionally, the HDE-Array includes more electrodes per ring than any current dry-electrode solution [104, 300], providing unprecedented spatial resolution crucial for capturing detailed EMG signals and aligning with the anatomy of the forearm [380]. This higher spatial resolution aims to improve signal quality, enhancing control accuracy. However, while the RPC-Net/HDE-Array system is expected to improve comfort and usability of a rehabilitation device, the new hardware may introduce drawbacks, such as lower proximo-distal coverage and higher skin-electrode impedance compared with gel electrodes, which must be evaluated, especially in the way they affect the performance of RPC-Net.

The objective of the study presented in this chapter is to assess how these potential drawbacks affect the performance of RPC-Net when using HD-sEMG signals acquired with HDE-Array, rather than with traditional gel electrode arrays. To do this, a single hypothesis is tested:

1. The estimation accuracy of RPC-Net using the HDE-Array is statistically indistinguishable from that obtained using gel-based electrodes

The goal is to show that RPC-Net can operate effectively with the HDE-Array, expanding its usability in rehabilitation solutions. Additionally, skin-electrode impedance was characterised and compared with EMG-amplifier input impedance and with skin-electrode impedance for gel electrodes. Signal variance was then

analysed across rows and columns (to confirm that the proximo-distal coverage is sufficient), and the performance of RPC-Net was evaluated using a single row of electrodes. To conduct these experiments, two datasets were used (each including HD-sEMG and hand position): one using dry electrodes (newly acquired) and one using gel electrodes (used in Chapter 3). The gel-electrode dataset was used to assess changes in proximo-distal variance, whereas both datasets were used together to test overall performance.

4.2 Materials and Methods

This section describes the instrumentation and software used (Section 4.2.1) and then details the experimental approach employed in the three parts that make up this study (Section 4.2.2, Section 4.2.3 and Section 4.2.4). The experimental procedures adhered to the Declaration of Helsinki and were approved by the local ethics committee (CER-Polito, Prot. No. 107460/2023). All data used in this study are available online [334].

4.2.1 Instrumentation

The MEACS amplifier, Vicon motion tracking system and software defined in the previous chapter (Section 3.2.1) were used for this chapter as well.

HDE-Array

The HDE-Array is a Two-Dimensional (2D) polyimide array assembled using elastic bands (Figure 4.1). The unassembled array measures 632 mm × 48 mm, featuring 32 resin stiffeners spaced 20 mm apart. Two electrodes, 10 mm apart, are soldered on each stiffener, resulting in 64 electrodes arranged in 2 rows and 32 columns. The silver disc electrodes (99.999% purity silver, Ag) have a 4 mm diameter (12.57 mm^2 area). When assembled, the HDE-Array perimeter is 200 mm (unstretched). No visible corrosion or degradation was observed over the four-year life of the manufactured HDE-Array.

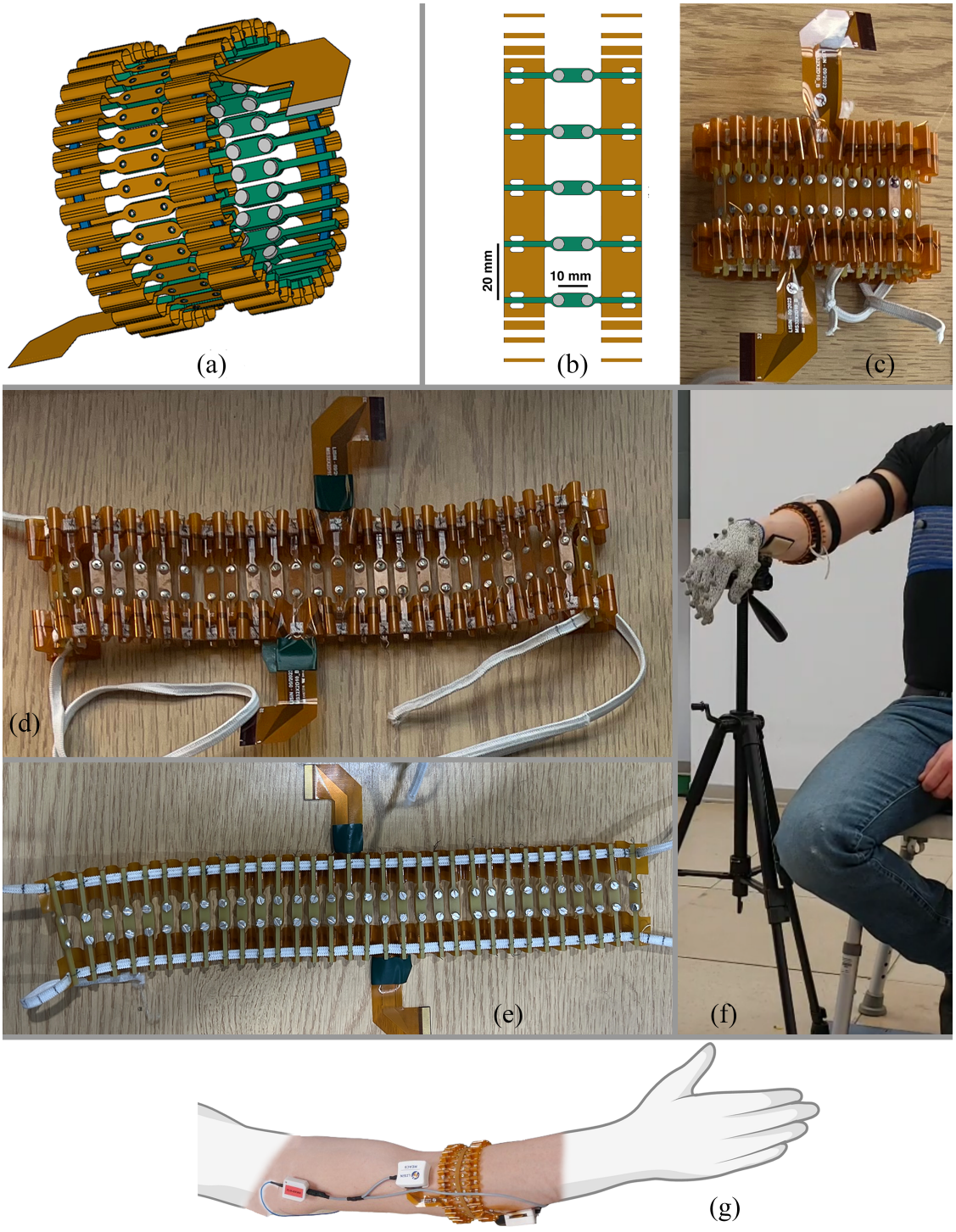

Figure 4.1: HDE-Array: (a) 3D rendering of the array in its assembled form. Polyimide is shown in orange, stiffeners in green, elastic bands in blue, and electrodes in silver. (b) Schematic of the repeating unit of the array (unassembled), including dimensions. (c) Assembled array. (d-e) Unassembled array viewed from different angles. (f) Subject wearing the HDE-Array and the glove with embedded motion tracking markers. (g) HDE-Array worn by the subject.

4.2.2 RPC-Net Performance: HDE-Array and Gel Electrodes

This part of the study tested the main hypothesis by comparing RPC-Net performance using HD-sEMG signals from gel electrodes and the HDE-Array, verifying whether the HDE-Array is suitable for position estimation. This was done using data from two datasets: DS2.s1 (HDE-Array) and DS1 (gel electrodes). EMG data were pre-processed, used to train RPC-Net, and then used by RPC-Net to return a position estimate. The accuracy of this estimate when compared with ground truth, measured by the metrics mentioned in Section 4.2.2, defined performance. The following subsections detail the data acquisition protocol, pre-processing pipeline, network training strategy, testing methodology, and performance evaluation metrics for RPC-Net.

Data

For this part of the study, two HD-sEMG and hand-kinematics recording datasets were used, labelled as DS1 and DS2.s1 within the larger thesis-wide dataset. The acquisition procedure followed for the two datasets was similar and diverged mainly in the type of electrode used for acquisition. Gel electrodes were used for DS1 and dry electrodes (HDE-Array) for DS2.s1. In this instance, DS1 was modified to match the number of channels in DS2.s1. DS1 was also used as a dataset in the previous chapter (Section 3.2.2). For the sake of synthesis, the acquisition protocol of DS2.s1 alone is described, indicating the differences with DS1, and referring the reader to the previous chapter for a full description of the acquisition protocol of DS1.

DS2.s1: Dry Electrodes Data

DS2.s1 is part of a larger dataset labelled DS2 within the thesis-wide dataset, which also includes DS2.s2 [334]. While only DS2.s1 is used for this study, the acquisition procedure observed for DS2.s2 is also reported for completeness.

Data were collected at the Laboratory of Motion Analysis (Politecnico di Torino, Turin, Italy), between November and December 2023. Sixteen right-handed healthy

volunteers, reporting no surgical interventions on their dominant arm, participated in the study (S13-S28; 8 males, 8 females, age: 20-26; weight: 55-90 kg; height: 165-195 cm, forearm circumferences: 20-32 cm). Written informed consent was obtained from all participants. Each session involved eight trials (divided into two sessions: six trials in s1 and two trials in s2) where HD-sEMG and hand position data were collected as subjects performed 16 hand poses:

1. 4 wrist poses: flexion, extension, adduction, abduction
2. 8 finger poses: index finger metacarpophalangeal flexion and extension; index finger proximal interphalangeal flexion and extension; flexion and extension of the middle, ring, and little fingers; adduction and abduction of the index and middle fingers
3. 4 thumb poses: flexion, extension, adduction, abduction

Before each session, skin was scrubbed with an abrasive gel to lower skin-electrode impedance, and electrodes and markers were placed. Twenty-one reflective markers were positioned on the dominant hand (embedded in a glove), and 12 more on the upper limb and trunk, for a total of 33 markers (Figure 4.2). EMG was acquired using two Sensor Units (SUs) connected to HDE-Array with dry electrodes arranged in 2 rows and 32 columns around the forearm, for a total of $N = 64$ monopolar EMG channels (Figure 4.2). An additional elastic band around HDE-Array secured it and improved skin contact. HDE-Array was positioned so that the most proximal electrode of column 1, as defined in Figure 4.2, was located at 30% of the distance between the lateral epicondyle and pisiform bone. The reference electrode was placed on the lateral epicondyle. A 10-second recording was performed to calibrate the Vicon system by instructing wrist movements. Each trial consisted of 32 movements (16 poses repeated two times). Participants were seated with their dominant forearm on a vertical support at shoulder height. A monitor prompted poses in random order every 6-8 seconds. The interval between prompts was adjusted by the participants for comfort, without a specified transition speed. Each trial lasted 200 to 260 s, depending on the length of the interval between prompts. After the completion of the six trials making up s1, a break of several

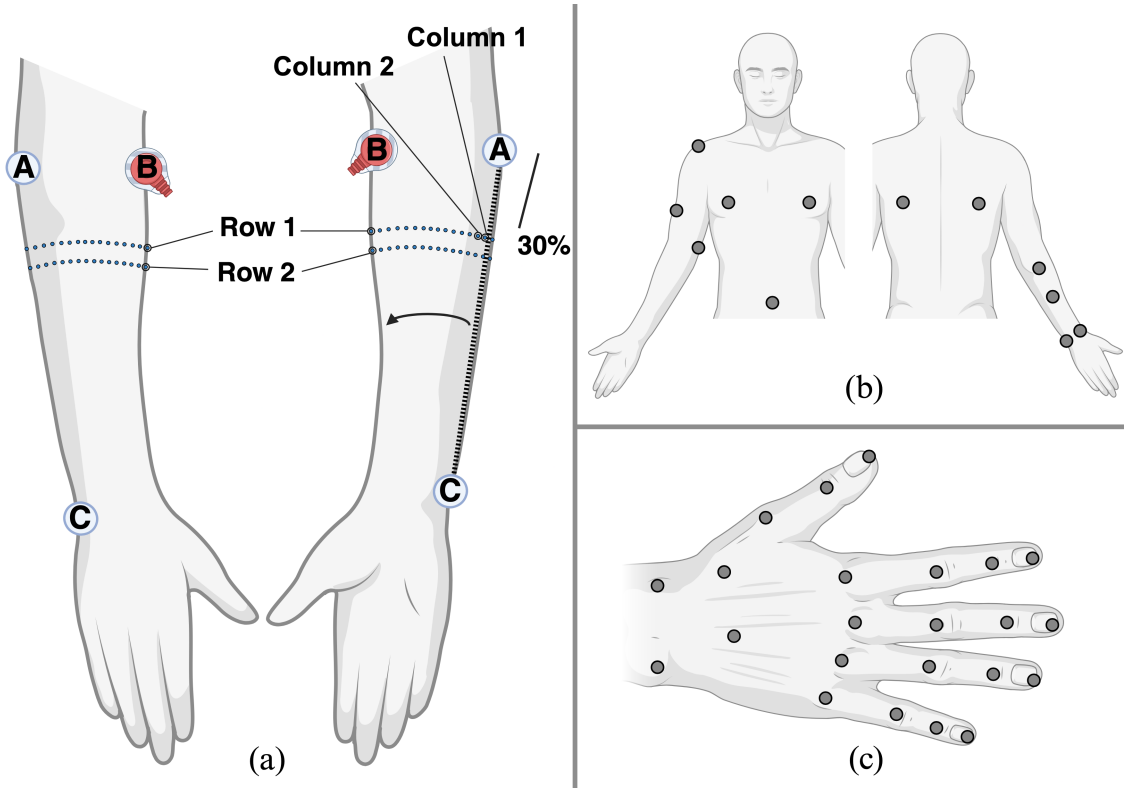

Figure 4.2: Subject setup: (a) HDE-Array placement on the front and back of the arm. Light blue dots indicate electrodes. Thirty per cent of the distance is shown. (b) Placement of 12 infrared markers on the body of the subject. (c) Placement of 21 infrared markers on the hand (and two forearm markers, also depicted in (b)). Markers are placed proximally to each joint.

hours to two days was observed depending on subject availability. After the break, the whole procedure was performed for two additional trials, making up s2. After each use, the electrodes were briefly polished with a soft abrasive cloth and stored dry to minimise corrosion and preserve stable electrode-skin characteristics across sessions. Only DS2.s1, corresponding to the first six trials, was used in this study.

DS1: Gel Electrode Data

DS1 was collected at the Laboratory of Motion Analysis (Politecnico di Torino) between February and March 2023. Twelve right-handed healthy volunteers, reporting no surgical interventions on their dominant arm, participated in the study (7 males, 5 females, age: 20-26; weight: 55-90 kg; height: 165-195 cm, forearm circumferences: 21-32 cm). Written informed consent was obtained from all

participants. The protocol mirrored DS2.s1, with one change: EMG was acquired using three SUs connected to anisotropic gel electrode arrays (2 rows, 16 columns, with 10 mm and 15 mm inter-electrode distances) for a total of $N = 96$ monopolar EMG channels. Electrode placement followed the protocol outlined in the previous chapter (Section 3.2.2), with electrodes arranged in 6 rows and 16 columns around the circumference of the forearm, covering approximately a third of its length.

Pre-processing

The objective of the pre-processing procedure is to transform the data acquired into suitable inputs for RPC-Net. Raw EMG signals were first converted from bits to volts, then offset-corrected, rectified, and transformed into RMS values using a sliding window of $w_l = 200$ samples (97.7 ms). The window step w_s was adjusted based on prompt duration, as defined in Section 4.2.2: 25 samples for 8 seconds, 29 for 7 seconds, and 33 for 6 seconds, ensuring consistency in sample number across subjects. Given an electromyographic signal that is L seconds long and N-dimensional, the output of the pre-processing procedure is $l = floor(\frac{L*f_s - w_l}{w_s}) + 1$ samples long and N-dimensional. The resulting RMS values were divided by 10^{-4} to bring the data into a standardised range suitable for RPC-Net training, resulting in unit variance.

Vicon marker positions were processed using a moving average filter with a window length of 20 samples and subsequently mapped into a 29-dimensional joint-angle space using the IKA (Section 3.2.2). To prepare the joint-angle data for network training, rest angles were subtracted, and the resulting values were normalised by dividing by 45 degrees, centring the data at zero and producing unit variance. Finally, linear interpolation was applied to align the sampling rates of the EMG and joint-angle data, ensuring synchronised, time-matched input-output pairs for RPC-Net training. Given an L-second-long signal, the output of the pre-processing procedure is $l = floor(\frac{L*f_s - w_l}{w_s}) + 1$ samples long and J-dimensional. No difference in pre-processing was present between DS2.s1 and DS1.

RPC-Net Training and post-processing

RPC-Net, as defined in the previous chapter (Section 3.2.2) is a neural network that estimates hand position from HD-sEMG signals acquired on the proximal forearm, refining estimates recursively based on prior values (Section 3.2.2). The version of RPC-Net used in this study processes inputs from 64 EMG channels and 29 joint angles. Each sub-network, responsible for a specific joint angle, excludes its corresponding input channel, using the remaining 28 angles instead. This setup creates a robust recursive loop between EMG signals and past angles. During training, actual joint angles replace past estimates. During the testing phase, joint angles produced by the RPC-Net undergo processing via a fourth-order low-pass Butterworth filter (with a cutoff frequency $f_c = 1$ Hz) to eliminate high-frequency fluctuations and are subsequently mapped back into 3D space using the FKA. The network was trained with the Adam optimiser (in its PyTorch implementation), learning rate = 10^{-5}; $\varepsilon = 10^{-12}$; $\beta_1 = 0.9$; $\beta_2 = 0.99$; batch size = 2000; loss criterion = MSELoss. The model was trained for 200 epochs. During the training of RPC-Net, the joint angle input data were derived from the recording, and the recursion loop was not used. IT is 4.2 ms (standard deviation 0.2 ms) over 10^5 iterations on an Intel(R) Xeon(R) Platinum 8268 CPU (2.90 GHz).

Statistical Parametric Mapping

One-dimensional 1D Statistical Parametric Mapping (SPM) was also employed. It is designed to detect differences in pairs of time-varying signals [381]. Given the difference between the estimate of a signal and its value, the one-sample t-test computes a t-statistic at each time point, creating a test-statistic map that is compared with a critical threshold derived from random-field theory to determine statistical significance. The input is an $n \times k$ signal-difference matrix, where n is the number of time points and k the number of trials; the output is an $n \times 1$ t-statistic series. The one-sample t-test (spm1d Python toolbox) was used to assess whether the distance between actual and estimated joint angles differed significantly from zero [382]. Starting with 28 pairs (estimate and value) of test recordings (12

from DS1 and 16 from DS2.s1), the differences for 29 joint angles were computed, yielding 28 29×p matrices A, where p is the number of samples. These were split into 16 subrecordings (the 16 movements, each 8 s), producing 16 datasets B with 28 n×29 matrices each. Dataset B was then separated into gel (C1) and dry (C2) electrode groups. C1 was rearranged into 29 n×12 matrices D1 and C2 into 29 n×16 matrices D2, where 12 and 16 are the subject counts for gel and dry electrodes, respectively. A one-sample t-test was performed on each of the 29 matrices in D1, producing 29 t-statistic series E1; the same was done for D2, yielding E2. Each test also returned a critical threshold ($\alpha = 0.05$). Subtracting every element of E1 and E2 from their respective thresholds produced F1 and F2. Averaging the 29 signals in F1 and computing their Inter-Quartile Range (IQR) gave G1, an n×1 representation of cross-joint variability, termed the Cross-Joint Derivative (CJD). The same procedure on F2 produced G2 for the dry-electrode data. Thus, two CJD traces (G1 and G2) were obtained for each movement. Finally, the RMS difference between the gel and dry CJD traces was computed for each movement, obtaining a single value H per movement. Averaging these 16 H values yielded an overall Cross-Movement Cross-Joint Difference (CMCJD) that quantifies the performance gap between position estimates from dry and gel electrodes.

In 1D SPM, the multiple comparisons problem is addressed intrinsically through Random Field Theory (RFT). Instead of testing each time point independently, RFT models the smoothness and temporal correlation of the data to estimate the expected behaviour of random fields under the null hypothesis. The resulting critical threshold is therefore adjusted to maintain the overall family-wise error rate at the pre-specified α level (here 0.05) across the entire time domain, ensuring that the probability of a false positive cluster anywhere in the signal remains controlled [381, 382].

Performance Assessment

The performance of RPC-Net was assessed as its ability to estimate the position of the hand from the EMG. The performance was measured, independently for each subject, with two indicators: MPCC and MD, both computed for the test

trial only. MPCC is the mean of the individual PCC obtained from comparing the actual and predicted joint angle values for each of the 29 DoFs considered, over the whole test trial. MD is the mean, over the whole test trial, of the distances between index, middle, and thumb tips and their estimates. A thorough definition of MD and MPCC is included in the previous chapter (Section 3.2.2).

To test the hypothesis (i.e., the accuracy of hand position estimates when the signal is acquired with gel or dry electrodes is equal), two comparative analyses were performed: 1) a comparison between the performance of RPC-Net (MD and MPCC) using signals from HDE-Array (32×2 electrodes) and its performance with gel electrodes (16×4 electrodes). 2) The performance of RPC-Net with a subset of HDE-Array channels (16×2 configuration using alternate columns) was compared with the same subset from the gel array to evaluate dry and gel electrodes independently of their configuration. A one-tailed t-test was used to compare these conditions, testing the null hypothesis that the performance of RPC-Net with the HDE-Array is less than or equal to that with gel electrodes. MD and MPCC distributions were normal, as confirmed by a Shapiro-Wilk test.

The performance of RPC-Net using EMG data from a single ring of HDE-Array was also assessed, testing individual rows and the full setup using three two-tailed t-tests. The null hypotheses were:

- performance with both rows is equal to performance with the proximal row only,
- performance with both rows is equal to performance with the distal row only,
- performance with the proximal row is equal to performance with the distal row.

Lastly, the CJD was used to visualise the difference in accuracy between estimates performed with HD-sEMG acquired with gel and dry electrodes. For each of the 16 movements considered, the CJD for the dry and gel group (along with the IQR) were plotted for a visual comparison. The CMCJD was also reported as an overall measure of difference.

4.2.3 Variance Analysis Across Columns and Rows for Gel Electrodes

Data

For this part of the study, DS1 was used.

Experimental Approach

The HDE-Array has increased circumferential electrode concentration, reducing the number of rows compared to typical configurations [330]. To determine if this reduces information, a variance analysis on DS1 was performed, following these steps for each subject:

1. Aggregate the six EMG recordings into a single 20-minute signal ($n\times96$).
2. Compute the RMS using a sliding 200-sample window to obtain signal B.
3. Normalise B by dividing by the channel-wise mean over time.
4. Reshape B into an $n\times16\times6$ signal C (6 rows and 16 columns).
5. Calculate variance across columns (proximo-distal) and rows (circumferential) for each time point of signal C, to obtain an $n\times16$ signal D1 and an $n\times6$ signal D2.
6. Average D1 and D2 over time to get a 1×16 array E1 and a 1×6 array E2.

Proximo-distal Normalised Dimensional Variance (NDV) is defined as each of the values in E1 and circumferential NDV as each of the values in E2. This yields 264 data points: 192 proximo-distal and 72 circumferential (considering 12 subjects). A Shapiro-Wilk test assessed distribution non-normality, followed by a one-tailed Mann-Whitney U test to evaluate the null hypothesis that median proximo-distal NDV is greater than or equal to median circumferential NDV. Rejection of this null hypothesis would indicate higher NDV across the circumferential direction [383, 384]. A higher NDV across the circumference would imply that a reduction in the number of rows results in a smaller loss of information content than an equivalent reduction in the number of columns, successfully addressing, along with the results in Section 3.3.2, concerns of insufficient proximo-distal coverage.

4.2.4 Skin-Electrode Impedance Characterisation

Data

Data used in this part of the study are labelled as AD1 in the thesis-wide dataset. The electrode-skin impedance (Z_E) (Figure 4.3) was characterised within the sEMG bandwidth. This is important, especially around power-line frequency (and harmonics), because the interaction between the amplifier input stage and the electrode-skin system can cause signal distortion and attenuation due to the voltage divider effect and power-line interference [251, 256, 385–388]. Following a previous protocol, impedance and noise were measured using a multi-channel impedance meter from LISiN (Politecnico di Torino) [357]. For dry-contact silver electrodes, the electrode-skin contact can be modelled as a parallel R-C network. Within the sEMG bandwidth (10 Hz - 500 Hz), this network is predominantly non-polarisable and the impedance magnitude is primarily due to the resistive component and is less influenced by the reactive, frequency-dependent components [256, 385, 389]. Measurements were taken between two identical electrodes, assuming comparable skin properties and negligible tissue impedance (Z_T) [390]. A schematic of the model circuit is shown in Figure 4.3.

Experimental Approach

Impedance measurements were performed using a multi-channel automatic impedance meter developed at LISiN (Politecnico di Torino, Turin, Italy), which injects a sinusoidal current through the impedance under test and measures the resulting voltage drop [357]. The system operates in current-drive mode, generating a 1 μA rms sinusoidal excitation with adjustable frequency. The input and output voltages were simultaneously acquired using a NI-DAQ USB-6210 acquisition board (National Instruments, Texas, USA; 16-bit resolution, 10 kHz sampling rate). The instrument was battery-powered and electrically floating relative to ground to minimise artefacts at power-line frequencies.

To characterise Z_E, two analyses were conducted:

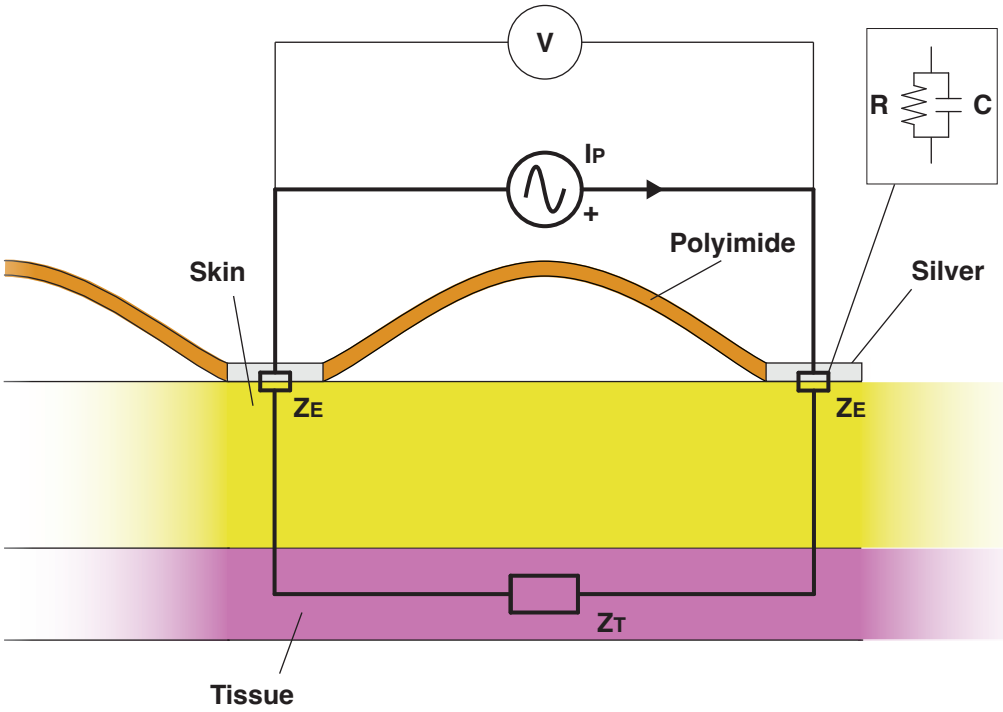

Figure 4.3: Electrical model of the skin-electrode interface: Skin in yellow, electrode array in orange, electrodes in silver, and underlying tissue in pink. Z_T is assumed to be much smaller than Z_E. The R-C parallel model is represented as a single impedance element Z. The current I_P is injected, and the voltage difference V is measured.

1. Impedance magnitude ($|Z_E|$) at 50 Hz was measured on 28 adjacent electrode pairs on the proximal ring of the HDE-Array for 5 subjects, totalling 140 measurements. For comparison, 28 measurements were also done on one subject using a gel electrode array (4×8, 10 mm inter-electrode distance, used for EMG acquisition in [391]). Median and IQR were calculated.
2. For one subject, impedance magnitude and phase were measured across 50 frequencies (1 Hz to 10 kHz, 12.3 points per decade) using 32 pairs of adjacent electrodes on the HDE-Array first and on a gel array (4×8, 10 mm spacing) then. A Bode plot was generated using the median phase and magnitude, with IQRs, for both conditions.

These procedures aim to assess the reliability of the dry-electrode-skin interface for EMG acquisition, addressing concerns about high impedance of the HDE-Array. To further compare impedance differences, EMG was recorded during a

bilateral isometric task. The subject lifted a 30 kg barbell for 12 seconds, while HD-sEMG was recorded from the right biceps (gel array, described above) and from the left biceps (HDE-Array). Spectrograms and RMS signals were computed for the channel on each arm corresponding to electrodes positioned on the midpoint between the acromion and biceps insertion [392]. The error for the RMS signals (Root Mean Square Error (RMSE), mV) and for the spectrograms (RMSE, dB) was then calculated to quantify differences between the two signals.

4.3 Results

This section presents the findings from the variance analysis (Section 4.2.3), impedance validation (Section 4.2.4), and RPC-Net performance (Section 4.2.2).

4.3.1 Variance Analysis

Figure 4.4 shows the distribution of circumferential and proximo-distal NDV for EMG signals in DS1 without applying subject-wise distinctions. Each data point represents an NDV measurement from individual sessions over time. The median proximo-distal NDV was 0.086 (IQR: 0.047), while the median circumferential NDV was 0.167 (IQR: 0.098). The Mann-Whitney U test results ($U = 1549$, $n = 264$, $p = 1.4{\cdot}10^{-22}$) indicate rejection of the null hypothesis (i.e., median proximo-distal NDV $\geq$ median circumferential NDV).

4.3.2 Impedance Characterisation

Figure 4.5 shows impedance results (Section 4.2.4). The figure displays the impedance values for both dry and gel electrodes at 50 Hz. The median impedance amplitude observed at 50 Hz for dry electrodes is 661 kΩ (IQR: 604 kΩ), which is almost three times higher than that for gel electrodes (214 kΩ, IQR: 84 kΩ). For a single subject, the Bode plot for the frequency range of 1 Hz to 10 kHz is shown. Figure 4.6 shows comparable EMG signal frequency content and amplitude for both dry and gel electrodes. The raw signal traces in the top row show similar RMS profiles over the 12-second task, with overlapping RMS values, and an RMSE of

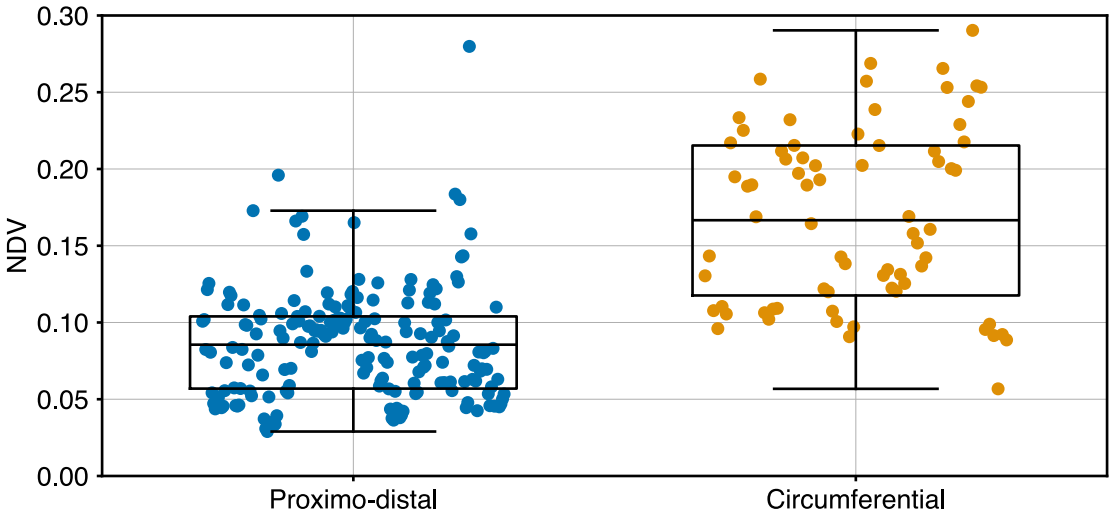

Figure 4.4: Variance analysis results: Distribution of proximo-distal and circumferential NDV, as outlined in Section 4.2.3. Mann-Whitney U test results (H_0: median proximo-distal NDV $\geq$ median circumferential NDV): $U = 1549$, $n = 264$, $p = 1.4{\cdot}10^{-22}$.

0.21 mV between the RMS traces, confirming consistent signal power. The bottom row spectrograms indicate similar frequency distributions for both electrode types, with an RMSE of 8.2 dB between the spectrograms.

4.3.3 RPC-Net Performance

This subsection compares the performance of the RPC-Net/HDE-Array setup with a traditional gel-based electrode setup and assesses the performance of single rings of HDE-Array electrodes (Section 4.2.2). Figure 4.7 depicts the subject-wise performance, measured as MD and MPCC. The caption includes statistical test results performed to assess the experimental hypotheses. Table 4.1 presents the averages of MD and MPCC across subjects for each tested condition.

For the comparison between the 2×32 dry-electrode setup and the 4×16 gel-electrode setup, the mean MPCC was 0.74 for the dry electrodes and 0.72 for the gel electrodes, while the mean MD was 27.0 mm and 28.2 mm, respectively. The t-test results were as follows: MD: $t(26) = -0.70$, $p = 2.5{\cdot}10^{-1}$; MPCC: $t(26) = 0.81$, $p = 2.1{\cdot}10^{-1}$. For the simplified setup (2×16 electrodes), the mean MD was 30.3 mm for dry electrodes and 33.9 mm for gel electrodes ($t(26) = -1.87$, $p = 3.6{\cdot}10^{-2}$),

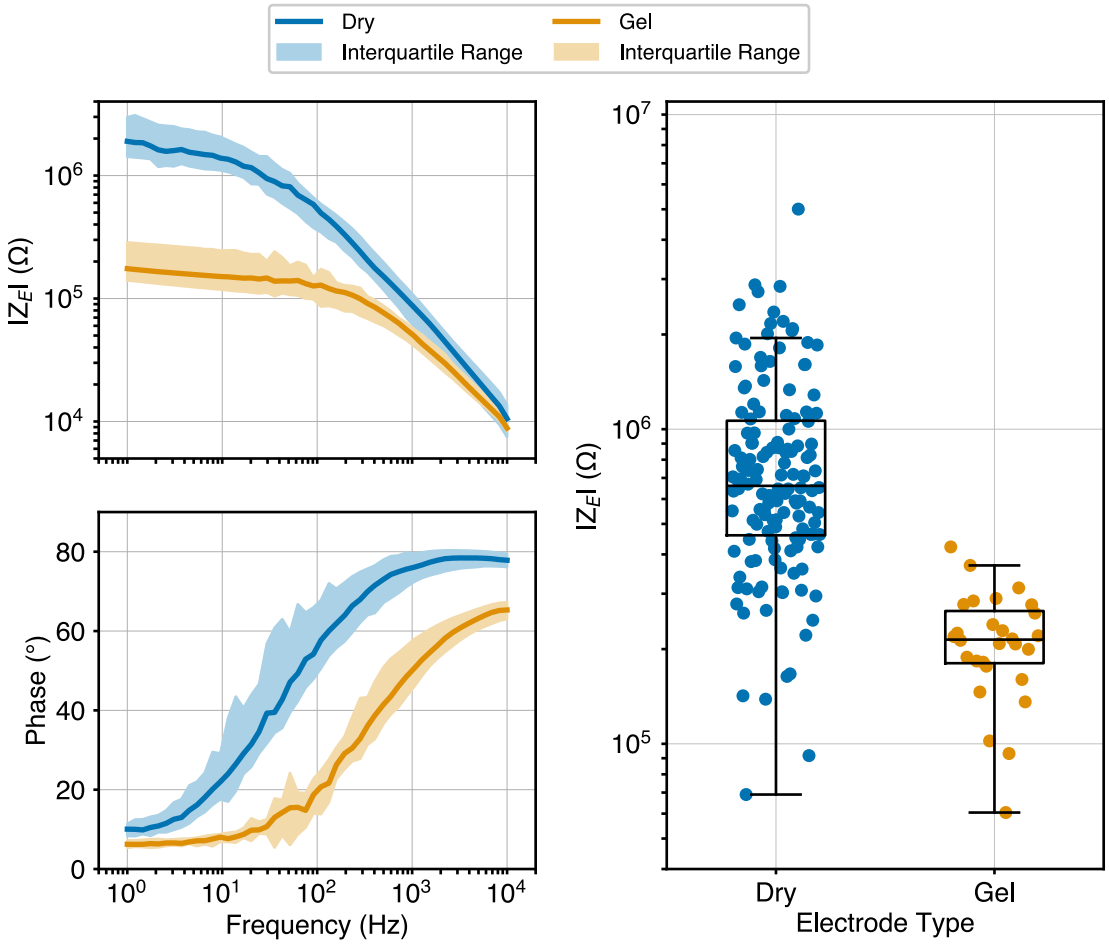

Figure 4.5: Impedance characterisation results: The figure reflects the experimental conditions outlined in Section 4.2.4. (Left) Bode plot in the 1 Hz to 10 kHz range. For each frequency tested, the line represents the median across 32 measurements, and the shaded area shows the corresponding IQR. (Right) Impedance values at 50 Hz. The y-axis indicates $|Z_e|$, the magnitude of the impedance at 50 Hz (power line frequency). The x-axis indicates the type of electrodes with which the measurement was taken. Measurements relating to the two conditions and the corresponding box plots are shown. Dry-electrode median = 661 kΩ (n = 140; first quartile: 460 kΩ, third quartile: 1064 kΩ). Gel-electrode median = 214 kΩ (n = 28; first quartile: 180 kΩ, third quartile: 264 kΩ).

and the mean MPCC was 0.71 for dry electrodes and 0.64 for gel electrodes ($t(26)$ = 2.45, $p = 1.1{\cdot}10^{-2}$). The t-tests in both cases evaluated the null hypothesis that the performance of RPC-Net using data acquired with gel electrodes is equal to or superior to the performance using data acquired with dry electrodes. Finally, when analysing data from a single ring of electrodes, the t-tests showed differences between the full setup and the proximal ring setup. The mean MD was 27.0 mm for the full setup and 31.5 mm for the proximal ring ($t(15)$ = -6.10, $p = 2.1{\cdot}10^{-5}$), and

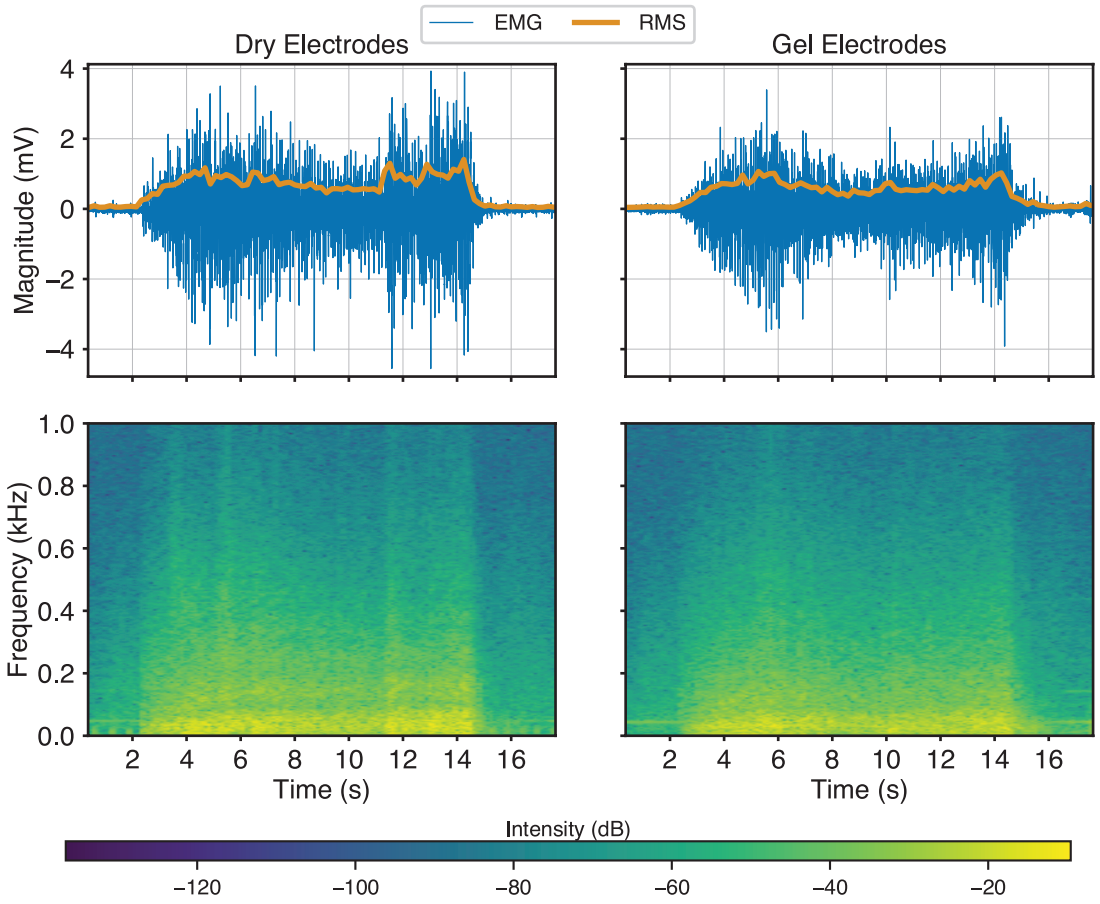

Figure 4.6: Direct signal comparison: EMG signals acquired from dry electrodes (left) and gel electrodes (right) during the same isometric task. The top row shows the raw EMG traces with the RMS values overlaid, while the bottom row presents the corresponding spectrograms for each condition.

the mean MPCC was 0.74 for the full setup and 0.69 for the proximal ring ($t(15) = 7.41$, $p = 2.2{\cdot}10^{-6}$). Similarly, for the distal ring setup, the mean MD was 27.0 mm for the full setup and 31.6 mm for the distal ring ($t(15) = -5.09$, $p = 1.3{\cdot}10^{-4}$), and the mean MPCC was 0.74 for the full setup and 0.70 for the distal ring ($t(15) = 5.96$, $p = 2.6{\cdot}10^{-5}$). In this case, the two-tailed t-test assessed the null hypothesis of equality of performance of RPC-Net when using data acquired with two rings and with a single ring. Figure 4.8 compares joint angle estimation accuracy across movements, showing the computed CJD for all movements. A higher CJD indicates a smaller difference between the estimate and the actual position, and zero is the threshold for statistical significance. Gel electrodes showed higher accuracy, though

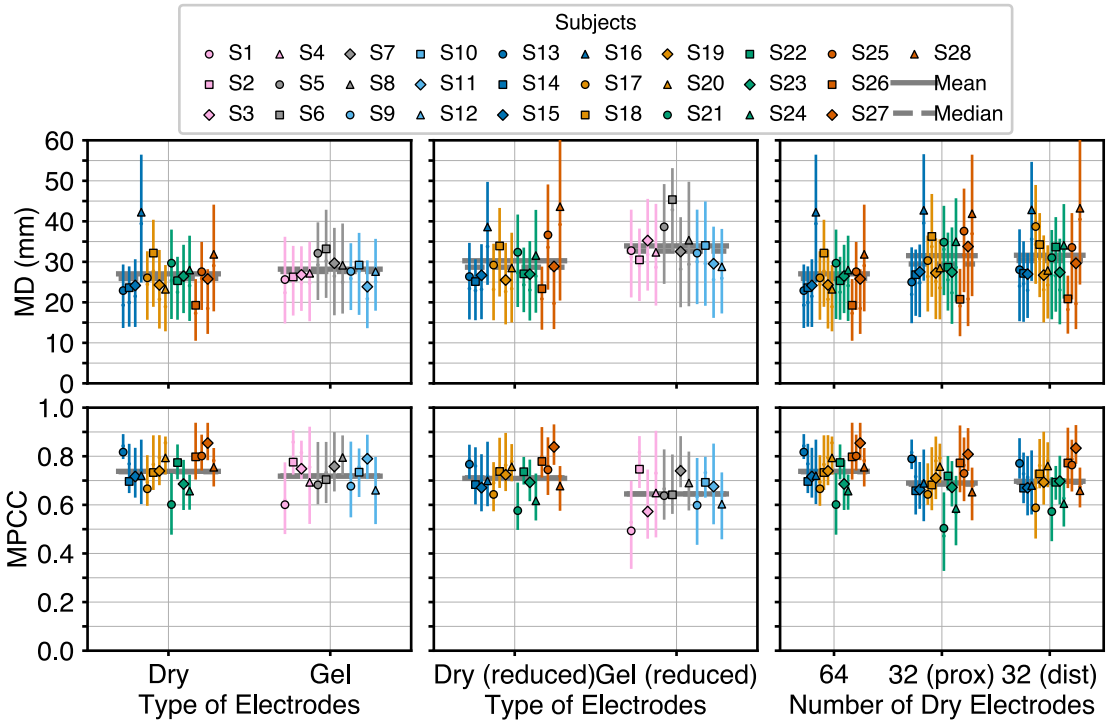

Figure 4.7: RPC-Net performance results (dry vs gel electrodes): The figure reflects the experimental conditions outlined in Section 4.2.2. Markers indicate the mean, with IQR shown. Median is shown as a smaller marker. (Left) Performance indicators for RPC-Net across all subjects. One-sided paired t-test results for MD (H_0: gel-electrode $\leq$ dry-electrode): $t(26)$ = -0.7, $p = 2.4{\cdot}10^{-1}$. One-sided paired t-test results for MPCC (H_0: gel-electrode $\geq$ dry-electrode): $t(26) = 0.8$, $p = 2.1{\cdot}10^{-1}$. (Middle) Performance indicators for RPC-Net across all subjects, with a reduced number of electrodes for a more accurate comparison. One-sided paired t-test results for MD (H_0: gel-electrode $\leq$ dry-electrode): $t(26)$ = -1.8, $p = 3.6{\cdot}10^{-2}$. One-sided paired t-test results for MPCC (H_0: gel-electrode $\geq$ dry-electrode): $t(26) = 2.5$, $p = 1.1{\cdot}10^{-2}$. (Right) Performance indicators for RPC-Net for dry electrodes only, comparing the full setup to one ring at a time. Two-sided paired t-test results for MD (H_0: Full setup = Proximal Ring): $t(15)$ = -6.1, $p = 2.1{\cdot}10^{-5}$, (H_0: Full setup = Distal Ring): $t(15)$ = -5.1, $p = 1.3{\cdot}10^{-4}$, (H_0: Proximal Ring = Distal Ring): $t(15)$ = -0.1, $p = 9.0{\cdot}10^{-1}$. Two-sided paired t-test results for MPCC (H_0: Full setup = Proximal Ring): $t(15) = 7.4$, $p = 2.2{\cdot}10^{-6}$, (H_0: Full setup = Distal Ring): $t(15) = 6.0$, $p = 2.6{\cdot}10^{-5}$, (H_0: Proximal Ring = Distal Ring): $t(15)$ = -1.0, $p = 3.4{\cdot}10^{-1}$.

values are consistently greater than zero for both signals. The CMCJD was 0.62.

4.4 Discussion

The HDE-Array is a viable device for acquiring HD-sEMG data for accurate hand position estimation through RPC-Net.

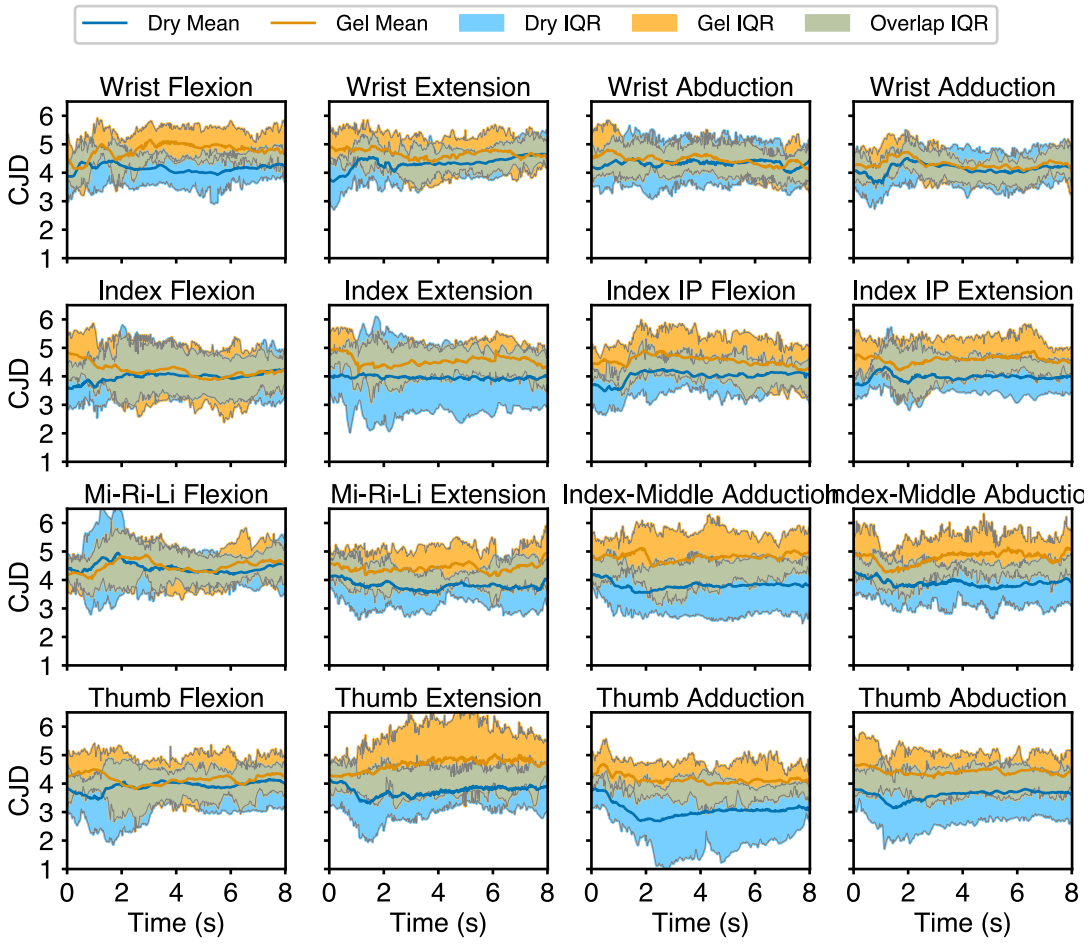

Figure 4.8: SPM analysis results: The figure reflects the conditions outlined in Section 4.2.2. Comparison of CJD and corresponding IQR for the 16 movements considered, for position estimates obtained from data acquired with dry electrodes and gel electrodes. Critical t-value was computed for a significance level of 0.05. A higher CJD indicates a smaller difference between the value and the estimate.

In the first part of the chapter, variance analysis of EMG signals from the 16×6 setup showed greater variability around the forearm circumference than along the proximo-distal axis, confirmed by the results of the Mann-Whitney U test. This result aligns with the longitudinal structure of forearm muscles, and it suggests that reducing rows to increase circumferential electrodes does not significantly compromise information [380]. The HDE-Array achieves double the circumferential resolution of similar devices and four times that of the Myo armband [330, 393]. HDE-Array also allows for increased proximo-distal channels by adding another array (32×4 electrodes).

Table 4.1: RPC-Net performance

Condition	MD (mm, Range)	MPCC (Range)
Dry - 32×2	27.0 (19.3-42.2)	0.74 (0.60-0.85)
Gel - 16×4	28.2 (23.9-33.2)	0.72 (0.60-0.79)
Dry - 16×2	30.3 (23.3-43.6)	0.71 (0.58-0.84)
Gel - 16×2	33.9 (28.8-45.4)	0.64 (0.49-0.75)
Dry - 32×1 (proximal)	31.5 (20.8-42.7)	0.69 (0.50-0.81)
Dry - 32×1 (distal)	31.6 (20.9-43.2)	0.70 (0.57-0.83)

Performance of RPC-Net. The mean and range of MD and MPCC (across subjects) are shown.

Second, the skin-electrode impedance of the dry electrodes was characterised. At 50 Hz, the impedance (661 kΩ, IQR: 604 kΩ) was higher than that of gel electrodes (214 kΩ, IQR: 84 kΩ) but still well below the input impedance of the amplifier at the same frequency (80 MΩ) [321]. The normalised impedance (median 83 kΩ cm^2) aligns with the theoretical estimate of 58.50 ± 64.16 kΩ cm^2 from [377]. The Bode plots (Figure 4.5) confirm that the skin-electrode impedance can be modelled as a parallel R-C network, with no significant non-linearities at significant EMG frequencies (10-500 Hz) for either dry or gel electrodes. The shape, phase, and overall trend of the Bode plots are consistent with those reported in the relevant literature, after accounting for differences in electrode area. A first study reported a normalised impedance of 7.8 Ω·m^2 at 0 Hz, compared with 25 Ω·m^2 in the present work; while different, these values are within the same order of magnitude and likely reflect the use of a different electrode material or different skin conditions [394]. Similarly, another study reported comparable high-frequency values (0.07 Ω·m^2) to those observed here (0.12 Ω·m^2), supporting the validity of the measured impedance characteristics [184]. The higher IQR observed for the dry electrodes suggests variability due to differences in contact pressure or other factors, indicating variable impedance at the skin-electrode interface. The spectrograms and raw signal traces (Figure 4.6) show that the quality of EMG signals remains comparable to gel

electrodes, as demonstrated by the low overall error between the traces and between spectrograms. Overall, the dry electrodes, although exhibiting higher impedance across the frequency spectrum, have electrical properties suitable for HD-sEMG acquisition, consistently with similar studies [357, 395].

Results in the left-hand part of Figure 4.7 and in Section 4.3.3 show that RPC-Net with dry electrodes performs at least as well as, if not better than, with gel electrodes in terms of MPCC and MD, when both solutions are considered with the full range of electrodes. One-tailed t-tests give p-values around 0.2, suggesting failure to reject the null hypothesis, with a slight trend towards higher performance for dry electrodes. Although the dry electrodes exhibit substantially higher impedance than gel electrodes, it appears that this does not adversely affect signal quality or model performance. The sEMG contractions analysed are high in amplitude and dominated by low frequencies, and the 80 MΩ input impedance of the amplifier minimises any voltage-divider effects. As a result, the higher electrode impedance has negligible practical influence on the performance of RPC-Net. Furthermore, Figure 4.7 shows that RPC-Net performs better with dry electrodes even when the electrode arrangement of the two types of electrode is the same (2×16), with p-values below 0.05. These results demonstrate that the performance of RPC-Net, when disregarding the configuration of the electrodes, is higher with dry electrodes. This finding also helps rule out the possibility that the superior performance observed with the HDE-Array arises solely from its higher circumferential resolution, rather than from intrinsic advantages of the dry electrodes themselves.

Results from single rings (proximal or distal) are significantly worse but comparable to the full setup, as indicated by t-tests with p-values below 0.001. Although there is a clear rejection of equal performance, MPCC and MD remain within acceptable limits for single-ring setups, and the difference is below the operational threshold of 10-12 mm defined in Section 2.3.1. This result is important as it allows for a 75% reduction in inference time (to 1.2 ms) and a simpler, cheaper setup using a single MEACS SU. Figure 4.8 and Section 4.3.3 indicate that the performance of RPC-Net with dry electrodes is comparable to that with gel electrodes. Indeed, for

both gel and dry electrodes, the CJD remained strictly positive for all 16 movements, indicating that, on average across the 29 joints, the error did not reach the random-field-theory threshold; hence the difference between actual and estimated positions was not statistically significant at any time point. The low CMCJD (0.62) further confirms the similarity in behaviour between the two setups.

All results support the experimental hypothesis that the outcomes previously obtained with RPC-Net and gel electrodes can be replicated using the newly developed HDE-Array. Moreover, the complete HDE-Array/RPC-Net setup matched or outperformed all comparable solutions reported in the academic literature in terms of offline performance [300, 330, 346]. Although user comfort and usability were not directly assessed in this study, the array was explicitly designed to enhance both aspects. First, it offers clear practical advantages over conventional signal acquisition systems by eliminating lengthy setup procedures, removing the need for skin preparation, and avoiding the discomfort associated with gel-based electrodes. These features are expected to improve user comfort, acceptance, and overall usability. Second, the open and flexible structure of the HDE-Array supports stable skin contact and effective ventilation, thereby reducing the influence of physiological factors such as sweating, skin hydration, and keratinisation on electrode impedance. This design promotes consistent performance even during prolonged or high-intensity use. Third, the electrodes demonstrated excellent long-term robustness and reliability: over four years of experimental operation, no visible corrosion or degradation of the silver contacts was observed, and signal quality remained stable across repeated sessions. Taken together, these short- and long-term observations highlight the robustness of the system under realistic conditions. Nonetheless, future work should systematically evaluate user comfort and usability to confirm these anticipated advantages and to further validate the suitability of the HDE-Array for long-term experimental and clinical use. With comparable control performance, the added value of the RPC-Net/HDE-Array system would lie in its enhanced comfort, acceptance, and usability, achieved without compromising control accuracy.

4.5 Conclusion

This chapter introduced a novel HDE-Array for HD-sEMG acquisition using dry electrodes. It was demonstrated that this setup performs comparably to traditional gel-electrode setups when data acquired with it were used for position estimation through RPC-Net. The electrical properties of dry electrodes were also assessed and found suitable for EMG acquisition. These findings suggest that the HDE-Array, combined with RPC-Net, offers a viable alternative to traditional gel-based setups, potentially improving the practicality and comfort of HD-sEMG acquisition for prosthetic control and other applications in rehabilitation technologies. The improved usability brought by dry electrodes makes the technology more accessible for daily use, reducing the preparation time and discomfort associated with gel electrodes. In conclusion, the combination of HDE-Array and RPC-Net represents a significant advancement in the field of HD-sEMG acquisition, and promises an enhanced user experience and broad applicability in biomedical engineering.

5

Synergy-Based Dimensionality Reduction for Hand Kinematic Control: A PCA Study Using the RPC-Net/HDE-Array System

5.1 Introduction

As discussed in the previous chapters, intuitive and precise control of assistive and rehabilitation devices remains a central challenge in neural engineering [57, 69, 93, 341, 374]. Recent progress in Brain Machine Interfaces (BMIs) has been driven by advances in decoding biological signals, particularly sEMG, and machine learning approaches, especially neural networks, have become fundamental to translating these signals into control commands [93, 104, 312, 373, 374]. In particular, regression-based approaches, as opposed to classification-based ones, have gained prominence for enabling proportional, continuous, independent, and simultaneous control, key features for natural and dexterous movement [59, 93, 328, 345–351].

Yet controlling the human hand remains a daunting task. With 27 bones and over 35 muscles, the full kinematic description of the hand can encompass up to 30 DoFs, depending on the kinematic model considered [5, 6]. This complexity poses challenges not only for decoding, but also for designing devices that can replicate

or interact with natural hand motion [150, 238]. As a result, many efforts have focused on simplifying hand kinematics through the study of synergies, coordinated patterns of movement that reduce the dimensionality of control [396–399]. PCA is commonly used to extract these synergies by identifying the dominant axes of variability across movement data [400, 401]. While results vary across studies, a consistent finding is that a small number of PCs, often fewer than five, can capture the majority of variance in natural hand motion [402].

Despite their potential, synergies are rarely incorporated into regression-based EMG control systems [150, 238, 300, 403]. This represents a missed opportunity, as integrating synergies could offer several advantages. First, reducing the number of output DoFs leads to lower computational complexity and faster inference times, which are key requirements for embedding control systems into low-power, real-time hardware like microcontrollers. Second, most rehabilitation and prosthetic devices are physically limited in the number of actuators or stimulation channels they can support. Designing control schemes around synergies could therefore enable more effective and realistic device behaviour within these hardware constraints [336–338, 372]. Finally, PCA inherently acts as a denoising mechanism, which could increase the robustness of the learning process by filtering out low-variance, noisy components [404].

In the previous chapters, the RPC-Net/HDE-Array system, a combined hardware and software platform for the acquisition of HD-sEMG signals and their translation into hand kinematics, was defined. This system was initially validated using a full 29-DoF kinematic model, defined in Section 2.2.6. However, to explore whether dimensionality reduction could optimise system performance, the impact of incorporating into the system a synergy-based approach via PCA is now investigated. Specifically, it is assessed whether the kinematic model can be successfully reduced to a lower number of DoFs through PCA, and both the potential benefits and the possible drawbacks of integrating PCA in terms of decoding accuracy and overall usability of the RPC-Net/HDE-Array system.

To achieve this, the following three hypotheses were tested:

1. Five PCs are sufficient to explain at least 90% of the variance in a representative dataset of natural hand movements
2. As the number of principal components increases, the decoding performance of the RPC-Net/HDE-Array system approaches that of the full 29-DoF model, achieving at least 90% of full-model accuracy with five or fewer PCs
3. The decoding performance obtained, in terms of endpoint effector, using five PCs is non-inferior to that of the full 29-DoF kinematic model within a predefined tolerance of 10 mm

To evaluate these hypotheses, data acquired in previous studies were re-processed, PCA was applied to derive synergy-based kinematic representations, and the performance of the system was benchmarked across a range of dimensionalities. In the next sections, the data collection protocol, the analytical pipeline, and the evaluation metrics are detailed.

5.2 Materials and Methods

This section describes the instrumentation and software used in this study (Section 5.2.1), as well as the experimental procedures employed to assess the hypotheses (Section 5.2.2). The experimental procedures adhered to the Declaration of Helsinki and were approved by the local ethics committee (CER-Polito, Prot. No. 107460/2023). All data used in this study are available online [334].

5.2.1 Instrumentation

The MEACS amplifier, Vicon motion tracking system, and software defined in Chapter 3 (Section 3.2.1) were used for this chapter, along with the HDE-Array defined in the previous chapter (Section 4.2.1).

5.2.2 Experimental Protocol

The objective of the experiments was to assess the hypotheses defined in Section 5.1 and, more broadly, to evaluate how PCA can affect the performance of the RPC-Net/HDE-Array system.

Data Acquisition

The dataset used for this study was acquired during the original study validating the HDE-Array, described in Chapter 4, and is labelled as DS2.s1 within the larger thesis-wide dataset [334]. For a more thorough description of the procedures involved, readers are referred to the relevant chapter. Data were collected at the Laboratory of Motion Analysis (Politecnico di Torino, Turin, Italy), between November and December 2023. Sixteen right-handed healthy volunteers, with no history of surgery on the dominant arm, participated in the study (S13-S28; 8 males, 8 females, age: 20-26; weight: 55-90 kg; height: 165-195 cm, forearm circumferences: 20-32 cm). Written informed consent was obtained from all participants. Each session comprised six trials in which high-density EMG and hand-position data were collected while 16 hand poses were performed, as follows:

1. 4 wrist poses: flexion, extension, adduction, abduction
2. 8 finger poses: index finger metacarpophalangeal flexion and extension; index finger proximal interphalangeal flexion and extension; flexion and extension of the middle, ring, and little fingers; adduction and abduction of the index and middle fingers
3. 4 thumb poses: flexion, extension, adduction, abduction

Before each session, skin was scrubbed with an abrasive gel to lower skin-electrode impedance, and electrodes and markers were placed. Twenty-one reflective markers were positioned on the dominant hand (embedded in a glove), and 12 more on the upper limb and trunk, for a total of 33 markers (Figure 5.1). EMG was acquired using two SUs connected to HDE-Array with dry electrodes arranged in 2 rows and 32 columns around the forearm, for a total of $N = 64$ monopolar EMG channels (Figure 5.1). An additional elastic band around the HDE-Array secured it and improved skin contact. HDE-Array was positioned so that the proximal electrode of column 1, as defined in Figure 5.1, lay at 30% of the distance between the lateral epicondyle and pisiform bone. The reference electrode was placed on the lateral epicondyle. A 10 s recording was made for Vicon calibration during which wrist movements were executed. Each trial consisted of 32 movements (16

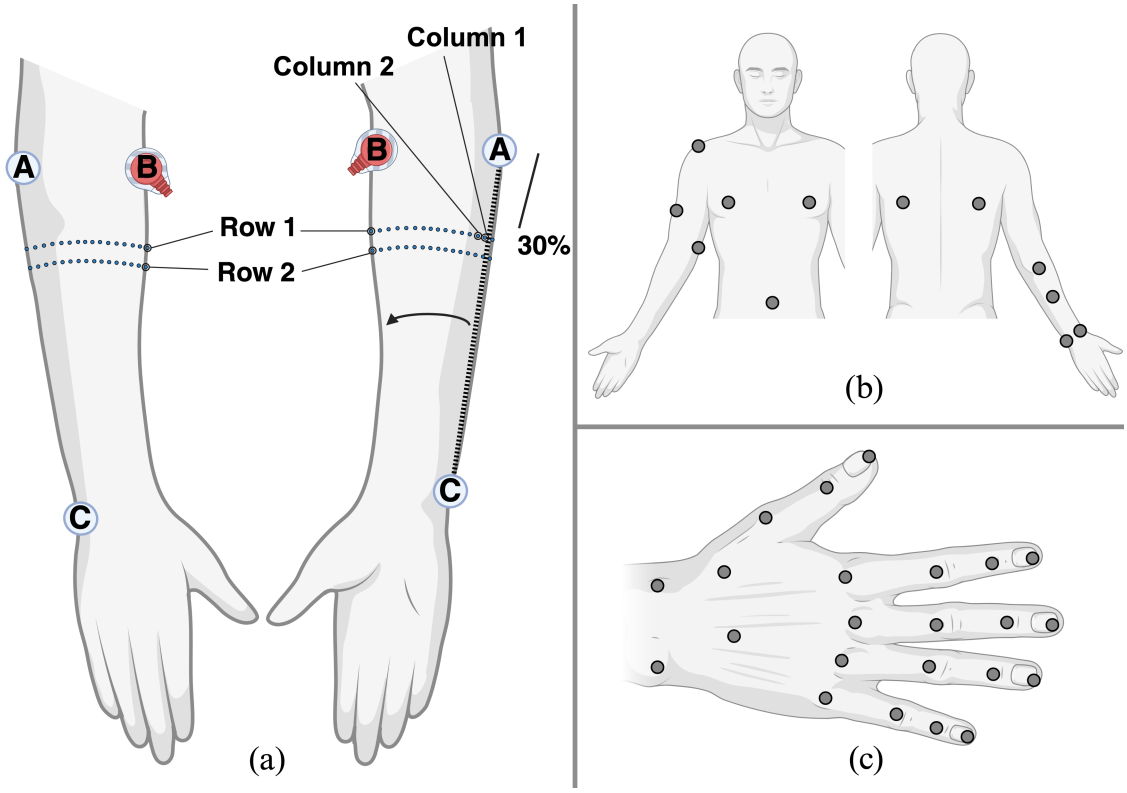

Figure 5.1: Subject setup: (a) HDE-Array placement on the front and back of the arm. Light blue dots indicate electrodes. 30% landmark along the lateral-epicondyle-pisiform axis is shown. (b) Placement of 12 infrared markers on the torso and upper limb. (c) Placement of 21 infrared markers on the hand and two additional markers on the forearm (also visible in (b)). Markers were placed proximally to each joint.

poses repeated two times). Participants were seated with their dominant forearm on a vertical support at shoulder height. A monitor prompted poses in random order every 6-8 seconds. Participants adjusted the interval between prompts for comfort; no transition speed was prescribed. Each trial lasted 200-260 seconds, depending on the length of the interval between prompts.

Pre-processing: HD-sEMG and Kinematic Data

The pre-processing procedure was designed to transform the data acquired into suitable inputs for RPC-Net. Raw EMG signals were first converted from bits to volts, then offset-corrected, rectified, and transformed into RMS values using a sliding window of $w_l = 200$ samples (97.7 ms). The window step w_s was adjusted based on prompt duration, as defined in Section 5.2.2: 25 samples for 8 seconds, 29 for 7

seconds, and 33 for 6 seconds, ensuring consistency in sample number across subjects. Given an electromyographic signal that is L seconds long and N-dimensional, the output of the pre-processing procedure is $l = floor(\frac{L*f_s - w_l}{w_s}) + 1$ samples long and N-dimensional. The resulting RMS values were divided by 10^{-4} to bring the data into a standardised range suitable for RPC-Net training, resulting in unit variance.

Vicon marker positions were processed using a moving average filter with a window length of 20 samples and subsequently mapped into a 29-dimensional joint-angle space using the IKA (Section 3.2.2). To prepare the joint-angle data for network training, rest angles were subtracted, and the resulting values were normalised by dividing by 45 degrees, centring the data at zero and producing unit variance. Finally, linear interpolation was applied to align the sampling rates of the EMG and joint-angle data, ensuring synchronised, time-matched input-output pairs for RPC-Net training. Given an L-second signal, the output of the pre-processing procedure is $l = floor(\frac{L*f_s - w_l}{w_s}) + 1$ samples long and J-dimensional.

Computation of PCA

To assess how PCA influences the performance of the system, a 29-DoF kinematic representation of the hand for each subject (see Section 5.2.2) was first obtained. The kinematic data from all 16 participants were then combined, resulting in approximately 2.2 million data points. Using the pooled dataset, a single global mean (μ) was computed and removed from every sample, ensuring a consistent zero-centring across all subjects. Next, the standard PCA routine from the scikit-learn library in Python was applied to the mean-centred data, recording both the PCA coefficients and the fraction of total variance explained by each component. The resulting PCs, derived from the global covariance structure, were then used to transform kinematic data of each subject by subtracting the same global mean μ and multiplying by the PCA coefficient matrix P. The influence of different numbers of retained PCs on RPC-Net regression performance was then evaluated, as detailed later in this chapter.

RPC-Net Training and Post-processing

RPC-Net, as defined in Chapter 3 (Section 3.2.2), is a neural network that estimates hand position from HD-sEMG signals acquired on the proximal forearm. Estimates are refined recursively on the basis of previous values. For this study, RPC-Net was modified to handle a flexible number of kinematic inputs (from 1 to 29) so that PCA can be applied to the 29-DoF input signal. This version of RPC-Net processed inputs from 64 EMG channels and a variable number of PCs in place of joint angles (n). Each sub-network, responsible for a specific PC, excludes its corresponding input channel, using the remaining $n-1$ PCs instead. This setup creates a robust recursive loop between EMG signals and past PC values. During training, actual ground truth values replace prior estimates. Let:

- A_0: the original 29-DoF joint-angle input.
- $A_n = PCA(A_0)$: The n-dimensional representation obtained via PCA (with n ranging from 1 to 29).
- $A_1 = PCA^{-1}(PCA(A_0))$: Approximate 29-DoF signal. Applying the inverse PCA transform to A_n does not reproduce A_0 exactly because dimensionality reduction introduces reconstruction error.
- B_n: The n-dimensional output of RPC-Net at inference time.
- $B_0 = PCA^{-1}(B_n)$: The reconstructed 29-DoF output obtained by applying the inverse PCA transform to B_n.

During training, A_n was used as input to RPC-Net in place of the full 29-DoF vector A_0. The output B_n was then compared to A_n to train the network. In the testing phase, the n-dimensional output of the network B_n is fed back into RPC-Net for subsequent time steps, as part of the recursive loop. B_n was also transformed back to 29 dimensions (B_0) for downstream processing and comparison to ground truth. Both A_0 (or A_1) and B_0 could be mapped to 3D marker positions via the IKA or the FKA, enabling spatial comparison with the ground truth. A diagram of this updated RPC-Net/HDE-Array pipeline is provided in Figure 5.2.

RPC-Net was trained and tested independently for each subject-PC combination, using a 5-to-1 train-test ratio. During the testing phase, joint angles produced by

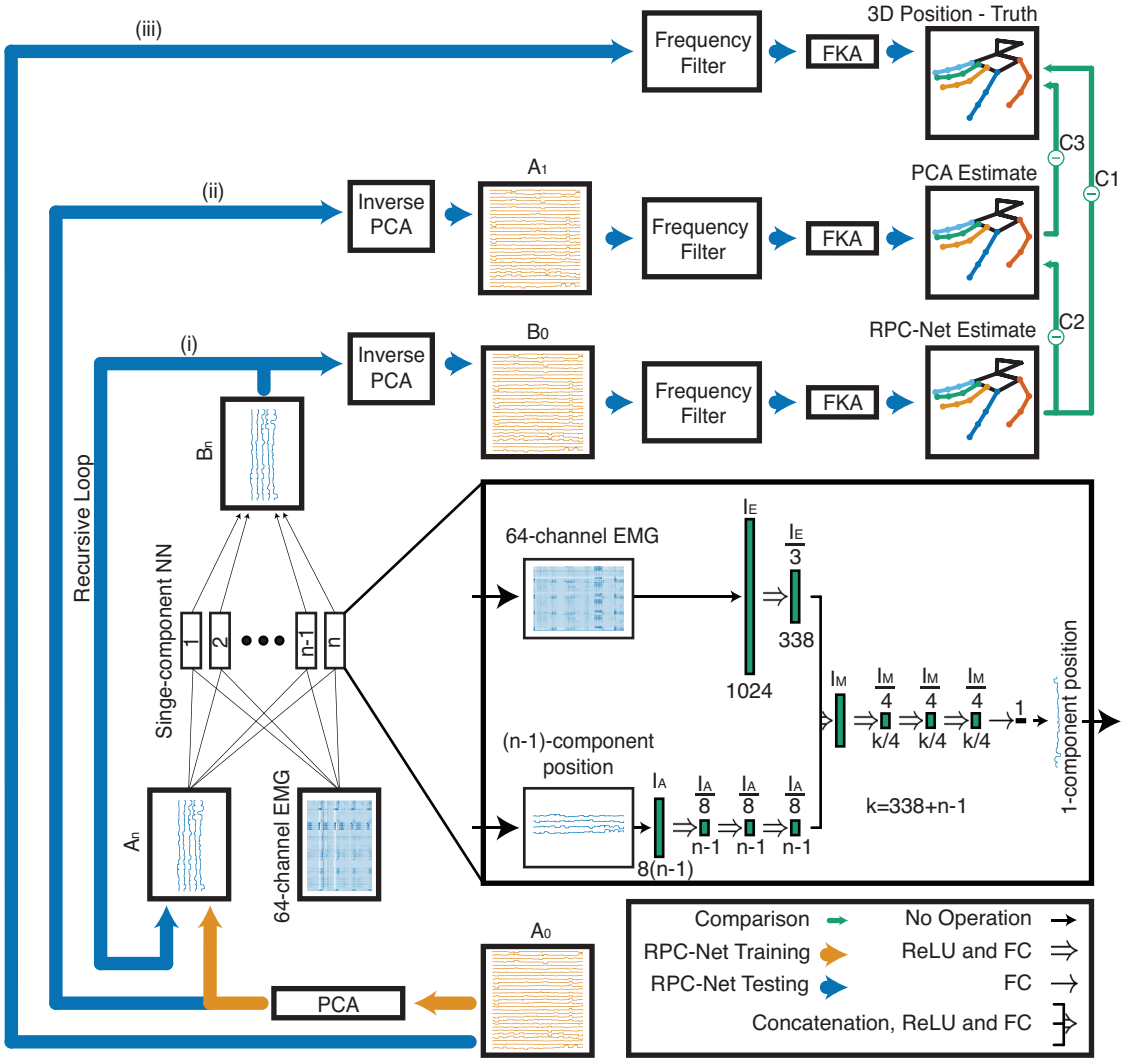

Figure 5.2: RPC-Net and PCA implementation: A_0=29-joint position; A_n=n-component position; A_1=29-joint PCA estimate; B_n=n-component position; B_0=29-joint RPC-Net estimate. RPC-Net comprises n regression sub-networks, one per PC. The right panel details a single sub-network, with two branches: the EMG (E) and the angle branch (A). Layer widths are shown above the blocks. Each sub-network receives $n-1$ PCs (all but the target PC) together with the EMG features and returns the position of the target joint in PC space. Orange arrows mark the training data flow: ground-truth joint positions captured by the motion-capture system are first projected onto the PC basis and then fed to the network. Blue arrows denote the inference paths: (i) the network output is fed back recursively to replace the kinematic input at the next time step, representing the RPC-Net prediction proper; (ii) ground-truth data are projected into PC space and then reconstructed, yielding an output used for performance assessment that depends only on the PCA coefficients and is independent of RPC-Net; (iii) the outermost path applies frequency filtering and forward-kinematic conversion to the ground-truth, providing another baseline used for performance assessment. The top right inset depicts these filtering and FKA operations and the evaluation pairings.

RPC-Net were processed with a fourth-order low-pass Butterworth filter (cut-off frequency $f_c = 1$ Hz) to eliminate high-frequency fluctuations and are subsequently mapped back into 3D space using the FKA. The network was trained with the Adam optimiser (in its PyTorch implementation), learning rate = 10^{-5}; $\varepsilon = 10^{-12}$; $\beta_1 = 0.9$; $\beta_2 = 0.99$; batch size = 2000; loss criterion = MSELoss. The model was trained for 200 epochs. IT is 4.2 ms (standard deviation 0.2 ms) over 10^5 iterations on an Intel(R) Xeon(R) Platinum 8268 CPU (2.90 GHz) using the full 29-DoF input; this inference time decreased linearly as the dimensionality was reduced by PCA.

Performance Assessment

The performance of RPC-Net was assessed as its ability to estimate the position of the hand from the electromyogram. The performance was measured, independently for each subject, with two indicators: MPCC and MD, both computed for the test trial only. MPCC is the mean of the individual PCC obtained from comparing the actual and predicted joint angle value for each of the 29 DoFs considered, over the whole test trial. MD is the mean, over the whole test trial, of the distances between index, middle finger and thumb tips and their estimates. Thorough definitions of MD and MPCC are provided in Chapter 3 (Section 3.2.2). In order to examine how the number of PCs affects system performance, MPCC and MD were computed in the following three cases:

1. Case 1 (C1): MD and MPCC are computed using A_0 and B_0. This represents the capability of the system to control the full 29-DoF hand model when PCA-based dimensionality reduction is used during the computation of the output, then inverted. It measures how closely the PCA-based system can reconstruct the original 29-DoF motion.
2. Case 2 (C2): MD and MPCC are computed using A_1 and B_0. Here, both the ground-truth signal (A_1) and the predicted signal (B_0) have been passed through the PCA pipeline, which only retains n components. For instance, if $n = 2$, the system only reconstructs two principal components rather than all 29 DoFs. This scenario evaluates the performance of the system when

controlling a limited number of DoFs, potentially simplifying the learning task.

3. Case 3 (C3): MD and MPCC are computed using A_1 and A_0. This assesses how much information is lost by reducing the dimensionality. By comparing A_0 (the original 29-DoF signal) to A_1 (the inverse PCA reconstruction), the extent of distortion introduced by the PCA transform was quantified.

Analysing these three cases provides a comprehensive view of how PCA influences the accuracy of the system and its capacity for full- or reduced-DoF control.

Hypothesis Testing

1. Five PCs are sufficient to explain at least 90% of the variance in a representative dataset of natural hand movements : To test this hypothesis, the cumulative variance explained as a function of the number of retained PCs was examined. Specifically, when computing the PCA coefficients via scikit-learn, it was recorded how many PCs were required for the cumulative variance to exceed 90%. The cut-off point at which the curve surpassed 90% variance was then used to determine whether five PCs were sufficient. Furthermore, PCA was also run on data from each subject individually; the resulting variance coefficients were averaged across subjects to determine whether a subject-wise computation yielded better results.
2. As the number of principal components increases, the decoding performance of the RPC-Net/HDE-Array system approaches that of the full 29-DoF model, achieving at least 90% of full-model accuracy with five or fewer PCs : The analysis focused on MD and MPCC from Case 1 (Section 5.2.2), for all 16 subjects and for each possible number of PCs (up to 29). The results were grouped by the number of PCs and the performance trend was modelled using the function $y = a + b \cdot e^{cx}$ where x is the number of PCs. Ninety per cent of the asymptotic performance of the fitted curve was calculated to test whether five or fewer PCs reached this threshold. Spearman rank test assessed whether performance showed a positive monotonic trend as the number of

PCs increased. Additionally, the trends in Case 2 and Case 3 were visually examined to gain further insights into the behaviour of the system under different dimensionalities.

3. The decoding performance obtained, in terms of endpoint effector, using five PCs is non-inferior to that of the full 29-DoF kinematic model within a predefined tolerance of 10 mm : To test this final hypothesis, a paired one-sided non-inferiority t-test was conducted comparing the decoding performance (Case 1) of the system using five principal components (5-PC model) with that of the full 29-DoF model (no PCA). The null hypothesis (H_0) stated that the mean performance with five components was more than a predefined tolerance ($\delta = 10$ mm for MD, $\delta = 10$ percentage points for MPCC) worse than the full model ($\mu_{5\text{PC}} - \mu_{\text{All PCs}} \geq \delta$ for MD and $\mu_{5\text{PC}} - \mu_{\text{All PCs}} \leq -\delta$ for MPCC), whereas the alternative hypothesis (H_1) specified that the reduced model was non-inferior ($\mu_{5\text{PC}} - \mu_{\text{All PCs}} < \delta$ for MD and $\mu_{5\text{PC}} - \mu_{\text{All PCs}} > -\delta$ for MPCC). The test was conducted at a one-sided significance level of $\alpha = 0.05$ with target power 1-$\beta = 0.80$. Normality of the paired differences was verified using the Shapiro-Wilk test prior to applying the t-test. The same analysis was repeated for twelve principal components (12-PC model) to assess whether additional components provided significant improvement beyond five.

5.3 Results

This section presents the findings from the assessments described in Section 5.2.2, focusing on how PCA affects the RPC-Net/HDE-Array system.

5.3.1 Analysis of Variance Explained by Different PCs

Our first hypothesis posited that five or fewer PCs were expected to capture at least 90% of the variance in the 29-DoF hand kinematic model used in this study. This hypothesis refers to PCA computed with data from all subjects pooled together. Figure 5.3 illustrates the individual variance contributed by each PC

and the cumulative variance of the first n PCs, for PCA computed on pooled data and on individual subjects. Notably, in the former case, the first principal component alone accounts for 32.9% of the total variance, and the sum of the first five PCs reaches 73.2%. Therefore, five PCs fall short of the 90% threshold targeted by the hypothesis. Instead, 90% variance is surpassed at 12 PCs (90.1%). An additional observation indicates that each of the first five components explains more than 5% variance individually, while subsequent components contribute less. Nevertheless, the collective variance explained by five components remains below the desired 90%, indicating that the initial hypothesis is not supported by these results. For additional context, a similar experiment was performed in which PCA was computed separately for each subject. The variance explained at each PC count was calculated per subject and then averaged across subjects; the results are also plotted in Figure 5.3. Under this subject-wise PCA, the 90% threshold was surpassed at 8 PCs. Figure 5.4 depicts the movements resulting from activation of the first three principal components. A heatmap illustrating the loading coefficients of the 29 PCs and the corresponding contribution and direction of each kinematic DoF to a given component is shown in Figure 5.5.

5.3.2 Performance of RPC-Net with PCA

The second hypothesis stated that, as the number of PCs increased, the performance of the RPC-Net/HDE-Array system approaches that of the full 29-DoF model, reaching at least 90% of full-model performance with five or fewer PCs. The results of this analysis are summarised in Figure 5.6, which reports the outcome of Case 1, the direct comparison between RPC-Net output and the original 29-DoF joint-angle trajectories (i.e., without applying an inverse PCA transform to the ground truth). This represents the ability of the system to reconstruct full kinematics after training on reduced-dimensional input. As shown in Figure 5.6, performance improves consistently with the number of PCs. Spearman's rank tests confirmed the trend (MD: decreasing, $p = 6.5 \cdot 10^{-97}$; MPCC: increasing, $p = 2.8 \cdot 10^{-125}$). An exponential model, $y = a + b \cdot e^{cx}$, was fitted, where y represents either MD or MPCC and x is the

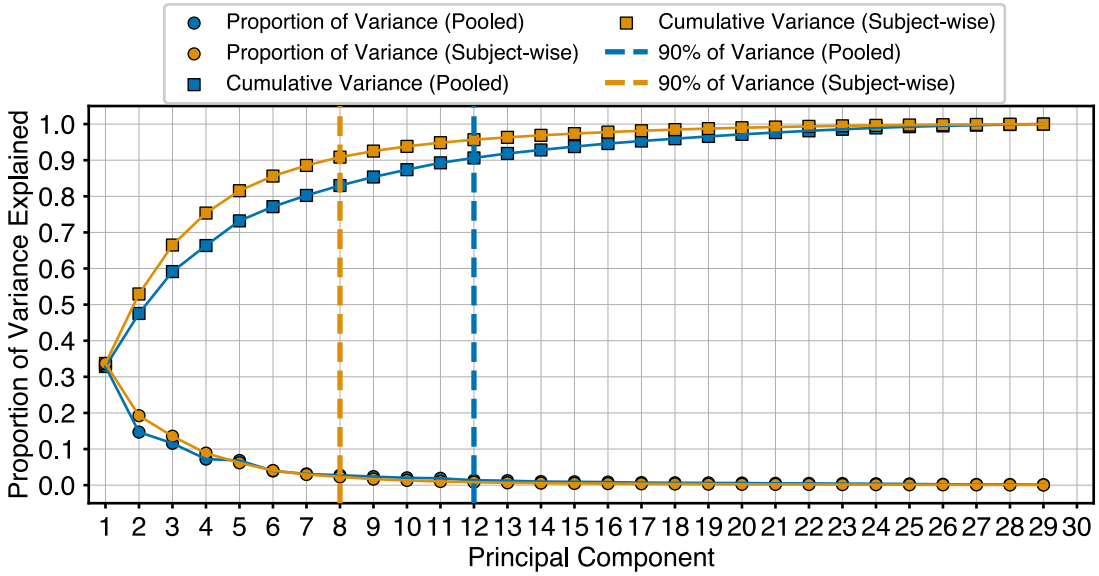

Figure 5.3: Variance explained by principal components: The figure reports both the individual and cumulative variance captured by successive principal components, contrasting the coefficient matrix P_{pool} (pooled data) with P_{subj} (subject-specific data); dashed vertical lines mark, for each curve, the lowest-order component at which the cumulative explained variance exceeds 90%.

number of PCs. The fitted parameters are listed in Table 5.1. According to the fitted curves, the system reaches 90% of its asymptotic performance at 5 PCs (for MD) and at 11 PCs (for MPCC). These findings support the first part of the hypothesis, confirming that performance increases as the number of PCs rises. However, the second part of the hypothesis, stating that 90% performance is reached with five or fewer PCs, is only partially supported, holding for MD but not for MPCC.

To complement this analysis, performance was also evaluated for Case 2 and Case 3, with results shown in Figure 5.7 and Figure 5.8, respectively. In Case 2, both the predicted and ground-truth signals are projected into PCA space and reconstructed via inverse PCA. This scenario is relevant for assessing the performance of the system when controlling a low-dimensional output. Here, the performance trend is inverted compared to Case 1: as the number of PCs increases, performance decreases. Spearman's rank tests confirmed this inversion (MD: increasing, $p = 7.6{\cdot}10^{-24}$; MPCC: decreasing, $p = 2.9{\cdot}10^{-65}$). The model parameters for Case 2 are also included in Table 5.1. In Case 3, the information loss due solely to PCA was evaluated by comparing the original 29-DoF signal (A_0) to its reconstructed

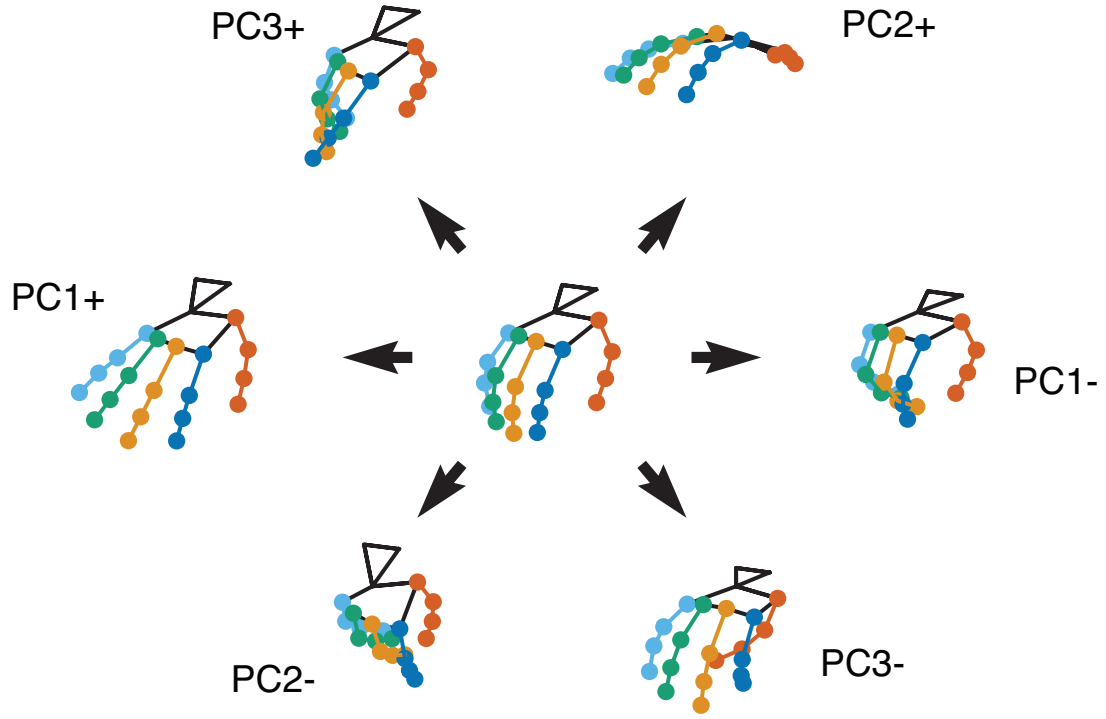

Figure 5.4: Visual representation of movements corresponding to the main principal components computed through PCA. The plus and minus signs indicate increases or decreases from the rest position. The first principal component (PC1) is dominated by flexion-extension of the middle, ring, and little fingers. PC2 primarily corresponds to wrist flexion-extension combined with simultaneous finger movement. PC3 mainly represents coordinated flexion-extension of the index finger and thumb, accompanied by simultaneous wrist adduction-abduction.

version (A_1) after dimensionality reduction and inverse PCA. As expected, the loss decreases with the number of PCs. Spearman's rank tests returned $p = 0$ for both MD and MPCC, indicating perfectly monotonic trends.

5.3.3 Performance Comparison of 5 PCs vs Full Model

The final hypothesis examined whether the decoding performance obtained with five principal components (5-PC model) was statistically non-inferior to that of the full 29-DoF kinematic model. A paired one-sided non-inferiority t-test was applied separately to the mean decoding error (MD) and the mean Pearson correlation coefficient (MPCC), using the non-inferiority margins of $\delta = 10$ mm for MD and

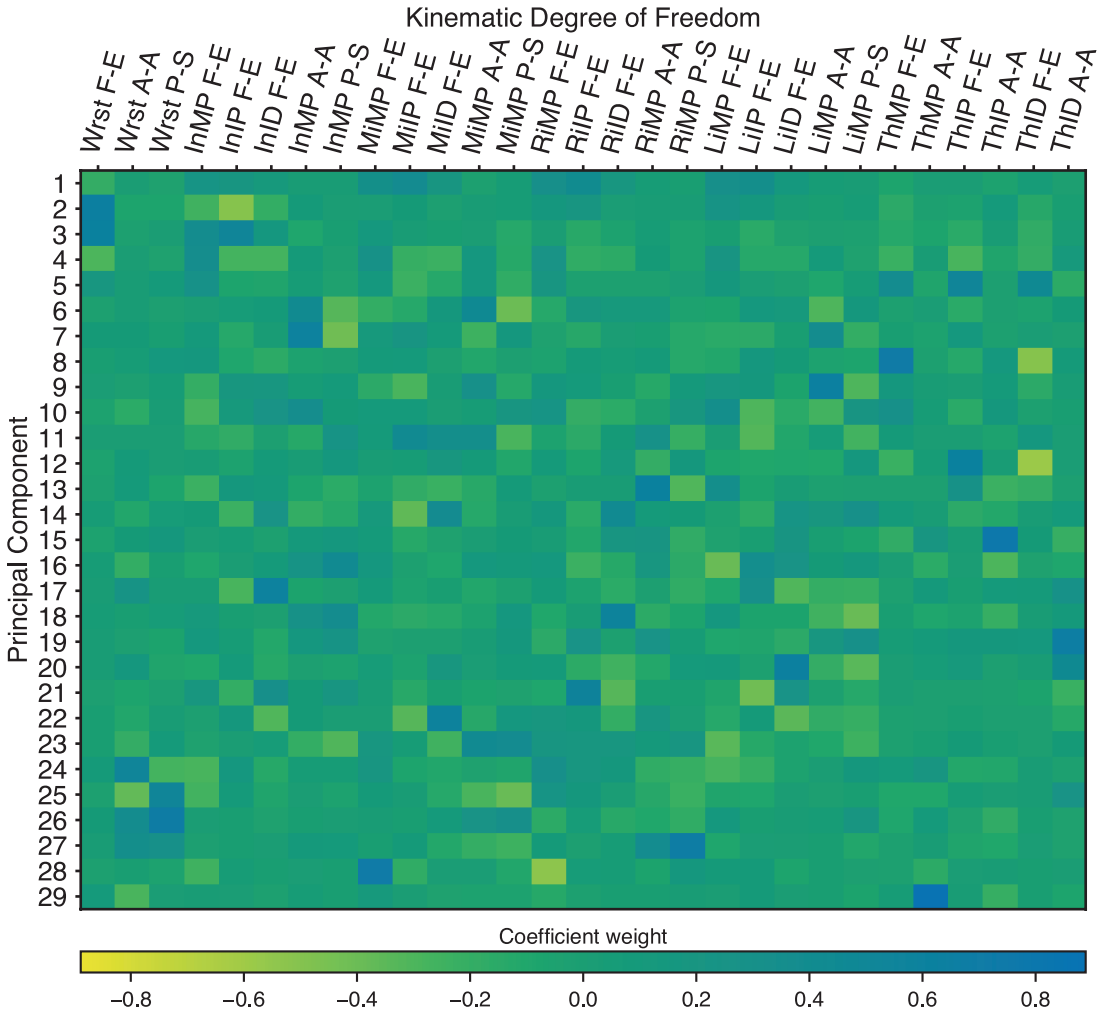

Figure 5.5: Heatmap illustrating the loading coefficients of the 29 PCs computed with PCA. Each column represents a specific kinematic DoF of the wrist and fingers (with labels defined in Section 2.2.6), while each row corresponds to a principal component. Positive and negative coefficient weights (shown by the colour scale) indicate the relative contribution and direction of each DoF to a given component. This representation highlights the dominant motion synergies captured by the PCA, revealing correlated joint patterns underlying hand and wrist movements.

$\delta = 0.1$ for MPCC. The tests were conducted at a one-sided significance level of $\alpha = 0.05$ with target power $1 - \beta = 0.8$.

For MD, performance with five PCs (mean = 35.0 mm) was worse than that of the full model (26.7 mm). The paired mean difference ($\mu_{5\text{PC}} - \mu_0$) was 8.3 mm, with a one-sided 95% upper confidence bound of $U = 9.9$ mm. Because this bound lies below the non-inferiority margin ($\delta = 10$ mm), the five-PC configuration

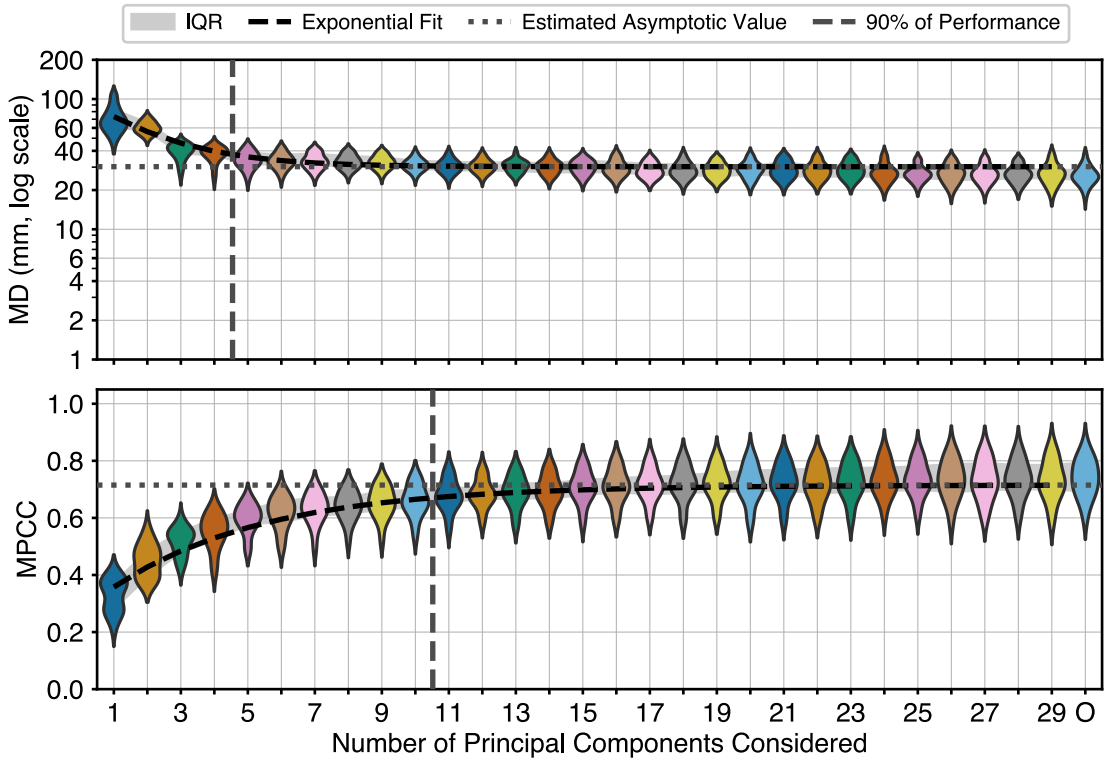

Figure 5.6: Case 1. Performance as a function of PCs considered: (Top): MD: 90% of performance is achieved at: 5 PCs; Regression parameters: $a + b \cdot e^{cx}$: a = $3.02{\cdot}10^{1} \pm 4.46{\cdot}10^{-1}$; b = $7.14{\cdot}10^{1} \pm 5.30{\cdot}10^{0}$; c = $-5.07{\cdot}10^{-1} \pm 4.38{\cdot}10^{-2}$; R^2 = 0.74; Mean difference between regression and mean: $1.66{\cdot}10^{0}$. Spearman's rank test, p-value: $6.5{\cdot}10^{-97}$. (Bottom): MPCC: 90% of performance is achieved at: 11 PCs; Regression parameters: $a + b \cdot e^{cx}$: a = $7.15{\cdot}10^{-1} \pm 6.23{\cdot}10^{-3}$; b = $-4.44{\cdot}10^{-1} \pm 2.48{\cdot}10^{-2}$; c = $-2.19{\cdot}10^{-1} \pm 2.04{\cdot}10^{-2}$; R^2 = 0.73; Mean difference between regression and mean: $1.34{\cdot}10^{-2}$; Spearman's rank test, p-value: $2.8{\cdot}10^{-125}$.

was deemed non-inferior to the full model ($t_{15} = 1.90$, $p = 3.8{\cdot}10^{-2}$). In contrast, for MPCC, performance with five PCs (0.60) fell below that of the full model (0.74) by 0.14, and the corresponding lower confidence bound ($L = -0.16$) did not exceed the margin ($-\delta = -0.10$). Thus, non-inferiority was not established for this metric ($t_{15} = -3.74$, $p = 9.9{\cdot}10^{-1}$).

For completeness, the same analysis was performed for the 12-PC model. In this case, both metrics satisfied the non-inferiority criterion: for MD, the mean difference was 4.21 mm ($U = 5.23$ mm, $t_{15} = 9.90$, $p = 2.8{\cdot}10^{-8}$), and for MPCC, the mean difference was -0.053 (L = -0.068, $t_{15} = 5.32$, $p = 4.3{\cdot}10^{-5}$). These results indicate that, while a five-PC model achieves decoding errors comparable to the full 29-DoF representation, a slight degradation in correlation performance remains,

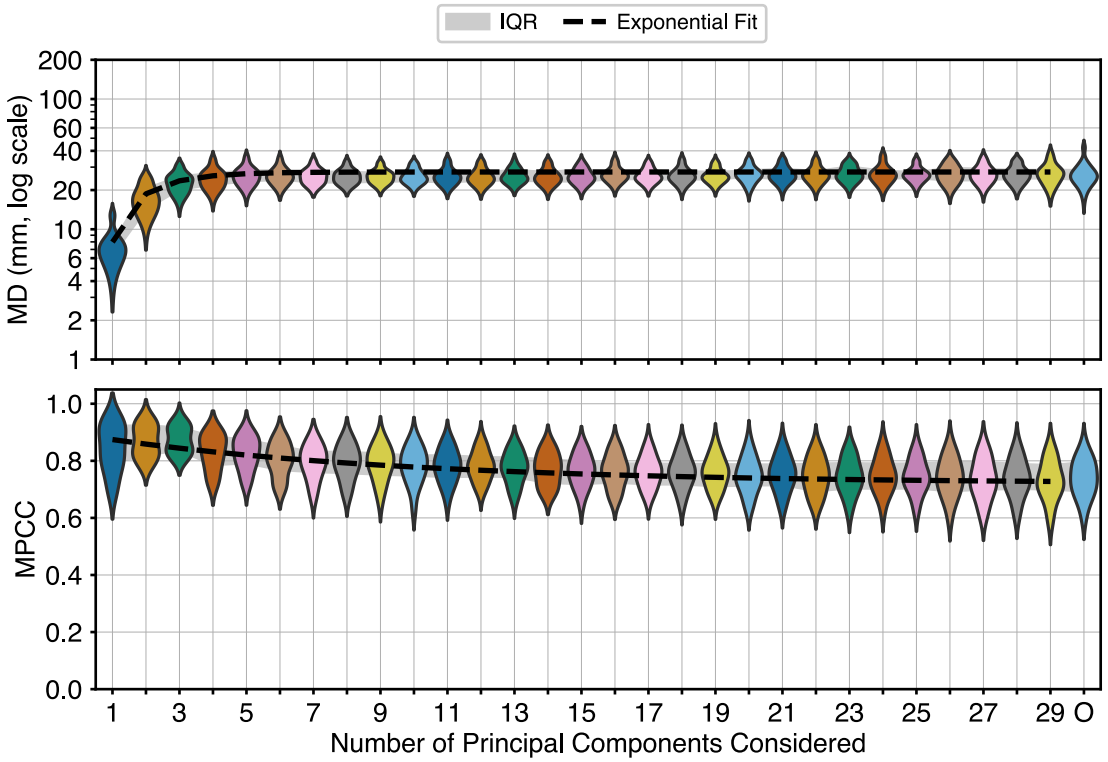

Figure 5.7: Case 2. Performance as a function of PCs considered: (Top): MD: Regression parameters: $a + b \cdot e^{cx}$: a = $2.75{\cdot}10^{1} \pm 2.73{\cdot}10^{-1}$; b = $-4.34{\cdot}10^{1} \pm 6.5{\cdot}10^{-1}$; c = $-7.97{\cdot}10^{-1} \pm 1.13{\cdot}10^{-1}$; $R^2 = 0.54$; Mean difference between regression and mean: $9.56{\cdot}10^{-1}$; Spearman's rank test, p-value: $7.6{\cdot}10^{-24}$. (Bottom): MPCC: Regression parameters: $a + b \cdot e^{cx}$: a = $7.20{\cdot}10^{-1} \pm 1.34{\cdot}10^{-2}$; b = $1.72{\cdot}10^{-1} \pm 1.59{\cdot}10^{-2}$; c = $-1.09{\cdot}10^{-1} \pm 3.03{\cdot}10^{-2}$; $R^2 = 0.36$; Mean difference between regression and mean: $1.02{\cdot}10^{-2}$; Spearman's rank test, p-value: $2.9{\cdot}10^{-65}$.

which is mitigated when twelve PCs are used.

5.4 Discussion

The results presented in the previous section indicate that applying PCA within the RPC-Net/HDE-Array control system can substantially reduce the complexity of the original 29-DoF kinematic model, while preserving high performance.

However, the initial hypothesis, that five or fewer PCs would capture 90% of the total variance, was not confirmed because the first five PCs explained only about 73% of the variance. Twelve PCs were required to exceed the 90% threshold, which still represents a major simplification compared to the full model. Notably, each of the first five PCs explained more than 5% of the variance individually,

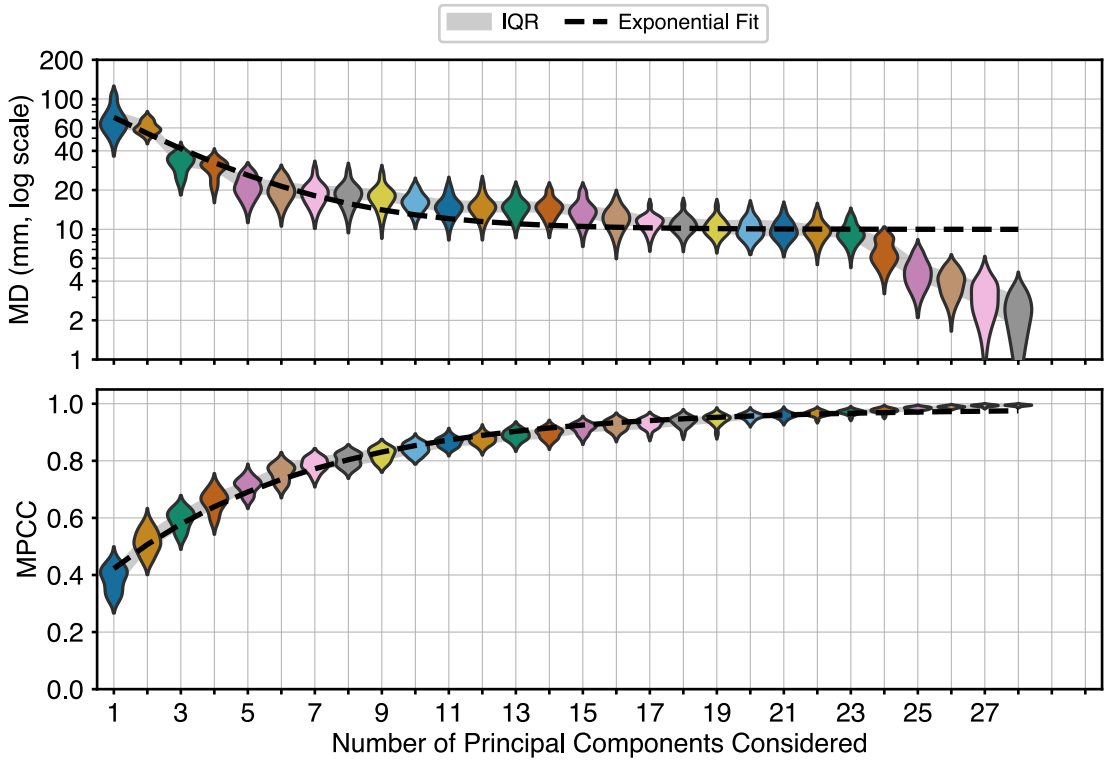

Figure 5.8: Case 3. Performance as a function of PCs considered: (Top): MD: Regression parameters: $a + b \cdot e^{cx}$: a = $9.98{\cdot}10^{0} \pm 6.95{\cdot}10^{-1}$; b = $8.77{\cdot}10^{1} \pm 4.80{\cdot}10^{0}$; c = $-3.40{\cdot}10^{-1} \pm 2.55{\cdot}10^{-2}$; $R^2 = 0.87$; Mean difference between regression and mean: $3.23{\cdot}10^{0}$; Spearman's rank test, p-value: 0.0. (Bottom): MPCC: Regression parameters: $a + b \cdot e^{cx}$: a = $9.82{\cdot}10^{-1} \pm 5.06{\cdot}10^{-3}$; b = $-6.59{\cdot}10^{-1} \pm 1.20{\cdot}10^{-2}$; c = $-1.64{\cdot}10^{-1} \pm 6.30{\cdot}10^{-3}$; R^2 = 0.97; Mean difference between regression and mean: $1.25{\cdot}10^{-2}$; Spearman's rank test, p-value: 0.0.

yet additional smaller contributions from PCs 6 through 12 collectively added the remaining 17% needed to surpass 90%. Interestingly, these 12 PCs could be mapped approximately to anatomical groupings (e.g., three primary DoFs each for the wrist, index finger, thumb, and a combined set of the middle, ring, and little fingers). However, this mapping should be treated with caution because PCA axes often span multiple joints rather than aligning in a one-to-one manner. The discrepancy between these findings and older reports suggesting fewer PCs might suffice may be due to the increased complexity of the hand movements studied here [398, 400, 405, 406]. It was also observed that PCA computed on a per-subject basis yielded a steeper variance-explained curve and reached 90% at about eight PC. Nevertheless, computing PCA coefficients individually for each user demands

Table 5.1: Fitted parameters of the exponential performance model

	MD (mm)		
Coefficient	Case 1	Case 2	Case 3
a	30.2 ± 0.5	27.5 ± 0.3	10.0 ± 0.7
b	71.4 ± 5.3	-43.4 ± 6.5	87.7 ± 4.8
c	-0.51 ± 0.04	-0.80 ± 0.11	-0.34 ± 0.03
	MPCC		
a	0.72 ± 0.01	0.72 ± 0.01	0.98 ± 0.01
b	-0.44 ± 0.02	0.17 ± 0.02	-0.66 ± 0.01
c	-0.22 ± 0.02	-0.11 ± 0.03	-0.17 ± 0.01

Fitted parameters for the exponential model $y = a + b \cdot e^{cx}$, where x is the number of PCs considered and y is the performance metric (MD or MPCC). 95% CIs are included.

additional kinematic tracking and calibration, complicating real-world adoption. Pooling data from all 16 subjects produced a universal set of principal components but required more PCs to reach the same variance threshold.

An interesting alternative to the approach adopted in this chapter would be to compute PCA directly on the spatial trajectories of the reflective markers rather than on joint angles. This representation would comprise 63 signals (21 markers, each with three spatial coordinates) and might capture inter-marker covariation patterns that are partially lost during the inverse-kinematics reconstruction of joint angles. From a dimensionality-reduction perspective, the resulting variance-explained curve would likely exhibit a similar initial steepness to that observed for the joint-angle data, reflecting the underlying coordination of hand motion, but would be expected to plateau earlier, indicating a diminishing contribution of higher-order components. In practical terms, the first 29 PCs derived from the marker-space data would likely convey a level of information comparable to that conveyed by the 29-DoF joint model, as both ultimately describe the same physical phenomenon. Adopting a marker-space representation would, however, require substantial modifications to the network architecture, since RPC-Net is

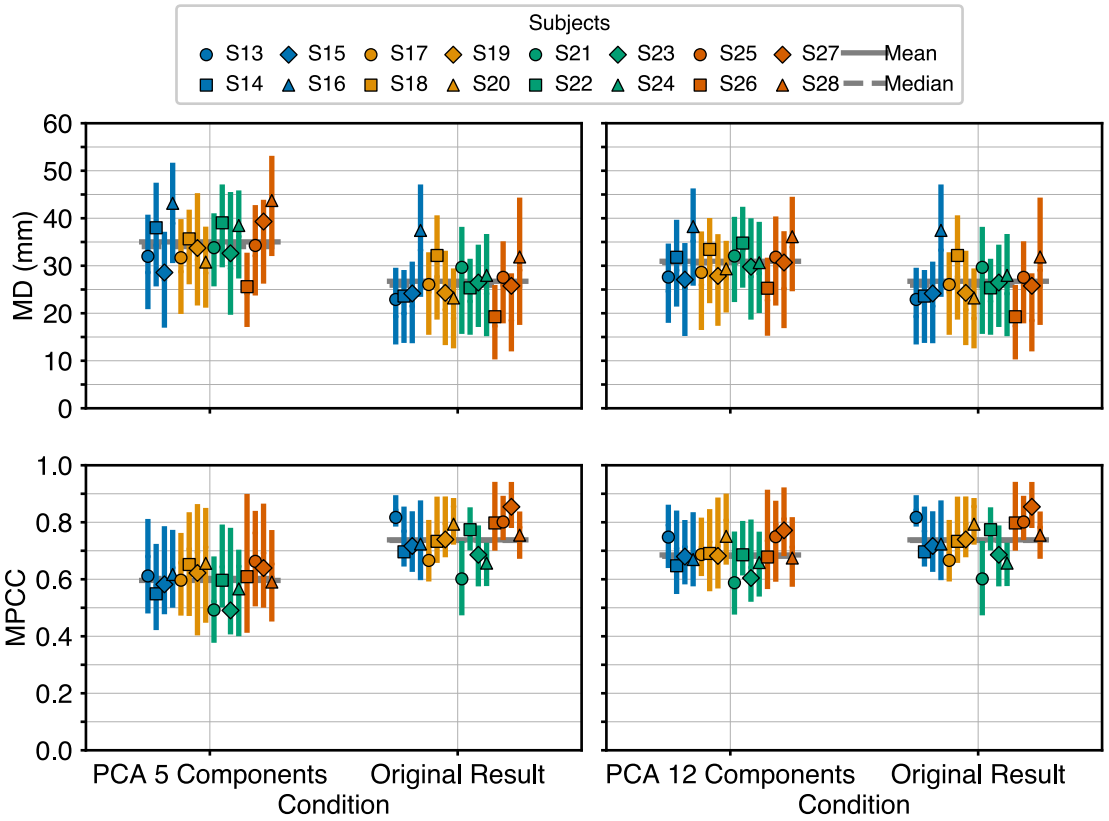

Figure 5.9: Direct comparison between full and reduced models: Markers indicate the mean, with IQR shown. Paired one-sided non-inferiority t-test results for 5 PCs: MD (H_0: $\mu_{5\text{PC}} - \mu_{\text{All PCs}} \geq \delta$): $t(15) = 1.9$, $p = 3.8{\cdot}10^{-2}$; MPCC (H_0: $\mu_{5\text{PC}} - \mu_{\text{All PCs}} \leq -\delta$): $t(15) = \text{-}3.7$, $p = 9.9{\cdot}10^{-1}$. Paired one-sided non-inferiority t-test results for 12 PCs: MD (H_0: $\mu_{12\text{PC}} - \mu_{\text{All PCs}} \geq \delta$): $t(15) = 9.9$, $p = 2.8{\cdot}10^{-8}$; MPCC (H_0: $\mu_{12\text{PC}} - \mu_{\text{All PCs}} \leq -\delta$): $t(15) = 5.4$, $p = 4.3{\cdot}10^{-5}$.

designed to operate on joint-based kinematic inputs. Nevertheless, implementing PCA closer to the output layer of such a restructured model could potentially enhance noise suppression and reduce error propagation through the processing pipeline, thereby improving overall stability. Exploring this approach, either as an alternative or complementary dimensionality-reduction strategy, could represent a valuable direction for future research.

The second hypothesis stated that, as the number of PCs increased, the performance of the RPC-Net/HDE-Array system would approach that of the full 29-DoF model, reaching at least 90% of full-model performance with five or fewer PCs. The results indicate that this hypothesis was only partially supported. Performance improved consistently as PCs increased; however, the 90% threshold

(relative to the asymptote of the fitted curve) was reached at five PCs for MD only. For MPCC, 11 PCs were required to reach the same relative performance. Although this outcome did not fully validate the hypothesis, several implications emerge. Reducing the number of input PCs from 29 to 11 resulted in a measured IT reduction of approximately 60%, and up to 80% when using just five PCs. These reductions, recorded on a standard CPU platform (see Section 5.2.2), suggest that lower-dimensional input can significantly improve the ease of online deployment of RPC-Net. A lighter architecture enables integration into smaller and cheaper hardware components, which is especially relevant for embedded systems in assistive or rehabilitation devices. Moreover, using a reduced number of PCs is more compatible with the physical constraints of prosthetic devices and FES systems, which typically support only a limited number of actuators or stimulation channels. Directly mapping individual PCs to actuators remains possible in principle, but would require the PCs to maintain stable, interpretable structure across users and contexts. Nonetheless, the observed trade-off between dimensionality and decoding accuracy highlights an important design space for tuning the system to practical constraints. In summary, although the second hypothesis was not fully confirmed, the results underscore the potential of PCA-based dimensionality reduction to streamline inference and facilitate hardware integration in real-world deployments of RPC-Net.

Finally, the third hypothesis proposed that performance with five PCs would not differ significantly from that of the full 29-DoF model. The results partially supported this claim. Paired one-sided non-inferiority t-tests returned p-values below the significance threshold and demonstrated non-inferiority for the mean decoding error (MD) within a margin of 10 mm (threshold discussed in Section 2.3.1). The same could not be said for MPCC, where the observed difference exceeded 10 percentage points. These findings indicate that reducing the number of control channels to five does not substantially compromise spatial accuracy, although some temporal correlation is inevitably lost. This outcome aligns with the design rationale behind using PCA on joint angles rather than on muscle activity. The approach was intentionally chosen to improve compatibility with low-DoF, underactuated

prosthetic devices, where each principal component can be interpreted as a control channel driving a coordinated multi-joint movement. In this sense, a prosthesis equipped with only five actuators, one per principal component, could reproduce the main functional synergies of the hand, capturing around 75% of kinematic variance and achieving over 90% of full-model accuracy in terms of MD, according to the results of the present study. These results suggest that PCA-based dimensionality reduction provides a principled route to simplifying control while preserving natural motion performance in low-DoF prosthetic designs, thereby supporting the potential clinical applicability of the RPC-Net/HDE-Array system in real-life rehabilitation. Using twelve PCs, corresponding to roughly 90% variance coverage, reduced these discrepancies to 4 mm for MD and 0.05 for MPCC. In this case, the null hypothesis of inferiority was rejected for both metrics, confirming that the 12-PC configuration was statistically non-inferior to the full model, with the given margin. This smaller gap may be acceptable in many prosthetic or rehabilitation applications, where an endpoint error below 5 mm lies within functional tolerances, as explained in Section 2.3.1. Nevertheless, statistically significant differences remain, indicating that, although twelve PCs did not fully replicate the performance of the full 29-DoF model, they provide a favourable balance between accuracy, computational efficiency, and synergy-based control.

5.5 Conclusion

This chapter assessed the extent to which PCA can simplify hand kinematic control within the RPC-Net/HDE-Array framework, without substantially compromising performance. It was hypothesised that five PCs would capture 90% of the variance in the 29-DoF hand model, that system performance would approach the full-model baseline with increasing PCs, and that using five PCs would be statistically indistinguishable from the full model.

Although five PCs did not reach 90% variance explained, 12 PCs did, representing a meaningful reduction from the original 29 DoFs. Performance analyses indicated that a smaller number of PCs significantly decreased inference time,

thereby improving computational efficiency and feasibility for online or embedded applications. A strong monotonic increase in performance was observed as the number of PCs rose; the 90% performance threshold was met at five PCs only for MD, whereas 11 PCs were required for MPCC. Paired one-sided non-inferiority t-tests indicated that performance with five PCs was non-inferior to the full 29-DoF model for decoding error, but not for correlation. When twelve PCs were used, both metrics satisfied the non-inferiority criterion, highlighting a practical trade-off between accuracy and model complexity. In conclusion, PCA-based dimensionality reduction offers notable benefits for hand motion decoding, particularly in scenarios with hardware or computational constraints.

6

Artificial Neural Networks for HD-sEMG-Based Hand Position Estimation: Addressing Inter- and Intra-Subject Variability

6.1 Introduction

As discussed in previous chapters (Chapter 3-Chapter 5), despite significant advances in prosthetic design and control strategies, abandonment rates remain high due to limitations in comfort, functionality, intuitiveness, and aesthetics, with user feedback suggesting that progress in control strategies is critical for improving device adoption [22, 57, 58, 65, 67, 69, 93, 104, 330, 339, 341, 342, 373, 375, 376, 402, 407–409].

In Chapter 3 and Chapter 4, two components, designed to address current limitations in the control of rehabilitation devices, were developed and validated. First, a shallow neural network, RPC-Net, that maps HD-sEMG signals from the proximal forearm to hand kinematics was introduced (Chapter 3). Second, traditional gel electrodes were replaced with the HDE-Array and the effectiveness of the HDE-Array in combination with RPC-Net was demonstrated (Chapter 4). While preliminary results are encouraging, further validation is essential to confirm real-world applicability. A critical issue concerns electrode repositioning. In

earlier work, as in most similar studies, training and testing datasets were recorded within the same session, typically by splitting a single large dataset. This ensures identical electrode placement during training and testing. However, for practical deployment, users must be able to don and doff the device across sessions, possibly days apart, without sacrificing control accuracy. This implies that the system should maintain robust performance even when trained and tested on data from different sessions, where electrode positions, despite anatomical landmark consistency, may differ. Changes in the skin condition likewise affect HD-sEMG signals. Recent research has explored these challenges [410–412]. This line of inquiry naturally extends to the broader question of how acquisition-related variability compares in significance to that caused by inter-subject anatomical differences. Far from being a theoretical concern, this issue is highly relevant in practical settings. Constructing a multi-subject training dataset that can later be refined for individual users could significantly enhance training efficiency [413, 414]. In this context, transfer learning has emerged as a promising approach [415, 416].

Given the importance of robustness to electrode shifts and skin condition changes, as well as the potential of multi-subject training, this work evaluates the RPC-Net/HDE-Array system along these dimensions. Specifically, robustness is assessed by comparing system performance under two conditions: training without repositioning and training with repositioning incorporated. Additionally, the effect of inter-subject training was evaluated by measuring performance when the system was trained on data from multiple users. Four experimental hypotheses regarding the RPC-Net/HDE-Array system were tested:

1. The accuracy of the RPC-Net/HDE-Array system decreases when electrode positioning is inconsistent between the training and testing sessions, compared to the baseline case in which electrode positioning remains consistent
2. When the RPC-Net/HDE-Array system is tested on data from the same session as the training data, its accuracy remains unchanged regardless of whether electrode repositioning is included during training

3. The performance degradation observed when the system is trained without electrode repositioning and tested on data from a different session can be mitigated by incorporating electrode repositioning during training
4. Including inter-subject data in the training set improves the overall performance of the system, providing a valid alternative to an increased amount of subject-specific data

To test these hypotheses, a new dataset of HD-sEMG and hand-position recordings was acquired, incorporating electrode repositioning during training, and was complemented with previously acquired datasets for comparative analysis.

6.2 Materials and Methods

This section describes the instrumentation and software used in this study (Section 6.2.1) and the experimental procedures employed to assess the hypotheses (Section 6.2.2). All procedures followed the Declaration of Helsinki and received approval from the local ethics committee (CEP Unicamp, Approval Reference: 34583120.2.0000.5404). All data used in this study are available online [334].

6.2.1 Instrumentation

The MEACS amplifier, Vicon motion tracking system, and software defined in Chapter 3 (Section 3.2.1) were used for this chapter, along with the HDE-Array defined in Chapter 4 (Section 4.2.1).

6.2.2 Experimental Protocol

The objective of the experiments was to assess the hypotheses defined in Section 6.1. The following subsections detail the data acquisition protocol, pre-processing pipeline, network training strategy, testing methodology, and performance evaluation metrics for RPC-Net.

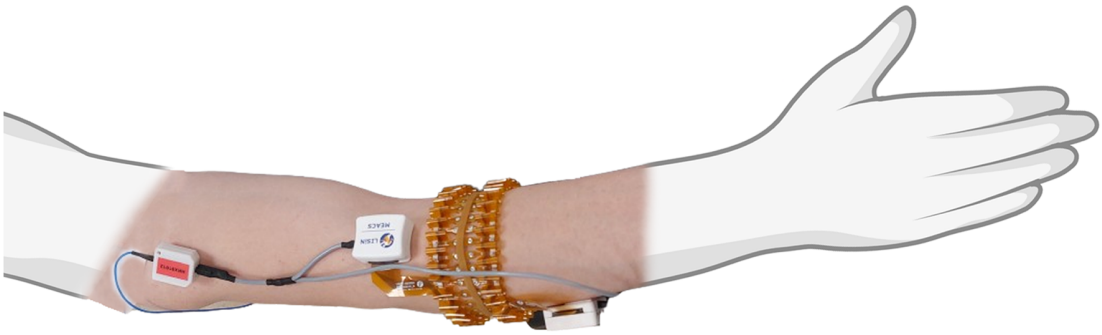

Figure 6.1: HDE-Array configuration: The array is shown wrapped around the forearm of the participant.

Data

Two datasets were used in this study, labelled as DS2 and DS3 within the larger thesis-wide dataset, which are structurally similar but differ in several key aspects [334]. DS2 was acquired for the study described in Chapter 4 and also used for the study reported in Chapter 5 of this thesis, while DS3 was acquired specifically for this study. For clarity and conciseness, the data collection and processing procedures used for DS3 are described and its differences from DS2 are highlighted. For a more thorough description of the procedures involved in the acquisition of DS2, readers are referred to the relevant chapter.

DS3.a: Joint EMG and Kinematic Data with Electrode Repositioning

DS3 comprises two subsets, DS3.a and DS3.b, but only DS3.a was used in the present study. As such, only the procedures relevant to DS3.a are reported. DS3.a comprises data acquired at the Department of Orthopaedics, Rheumatology, and Traumatology, State University of Campinas (SP, Brazil), between July and August 2024. Four right-handed healthy volunteers, reporting no surgical interventions on their dominant arm, participated in the study (S29-S32; age: 21 to 28 years; weight: 75 to 90 kg; height: 180 to 195 cm; forearm circumference: 22 to 30 cm). Written informed consent was obtained from all participants. Each subject completed two sessions of simultaneous HD-sEMG and hand kinematic data collection, both

performed on the right arm. During the first session (DS3.a.s1), each subject completed six trials; in the second session (DS3.a.s2), they completed two additional trials, for a total of eight trials. During each trial, subjects performed 16 hand poses:

1. 4 wrist poses: flexion, extension, adduction, abduction
2. 8 finger poses: index finger metacarpophalangeal flexion and extension; index finger proximal interphalangeal flexion and extension; flexion and extension of the middle, ring, and little fingers; adduction and abduction of the index and middle fingers
3. 4 thumb poses: flexion, extension, adduction, abduction

Before the start of the first session, electrodes and markers were placed. Twenty-one reflective markers were positioned on the dominant hand (embedded in a glove), and 12 more on the upper limb and trunk, for a total of 33 markers (Figure 6.2). EMG was acquired using one SU connected to the proximal row of HDE-Array. This resulted in 32 dry electrodes arranged in a single row around the forearm, for a total of $N = 32$ monopolar EMG channels. An additional elastic band around the HDE-Array secured the array and improved skin contact. HDE-Array was positioned so that the proximal electrode of column 1, as defined in Figure 6.2, was located at 30% of the distance between the lateral epicondyle and pisiform bone. The reference electrode was placed on the lateral epicondyle. A 10-second recording was performed to calibrate the Vicon system by instructing wrist movements. Each trial consisted of 32 movements (16 poses repeated two times). Participants were seated with their dominant forearm on a vertical support at shoulder height. A monitor prompted poses in random order every 6 to 8 seconds. The interval between prompts was adjusted by the participants for comfort, without a specified transition speed. Each trial lasted 200 to 260 seconds, depending on the length of the interval between prompts. To introduce variability in electrode positioning, the HDE-Array was removed and repositioned (following the same anatomical landmarks) between each trial. In the current chapter and throughout the rest of this thesis, the term "reposition", when referring to the HDE-Array, denotes the complete removal of the device from the forearm of the subject followed by its reapplication according

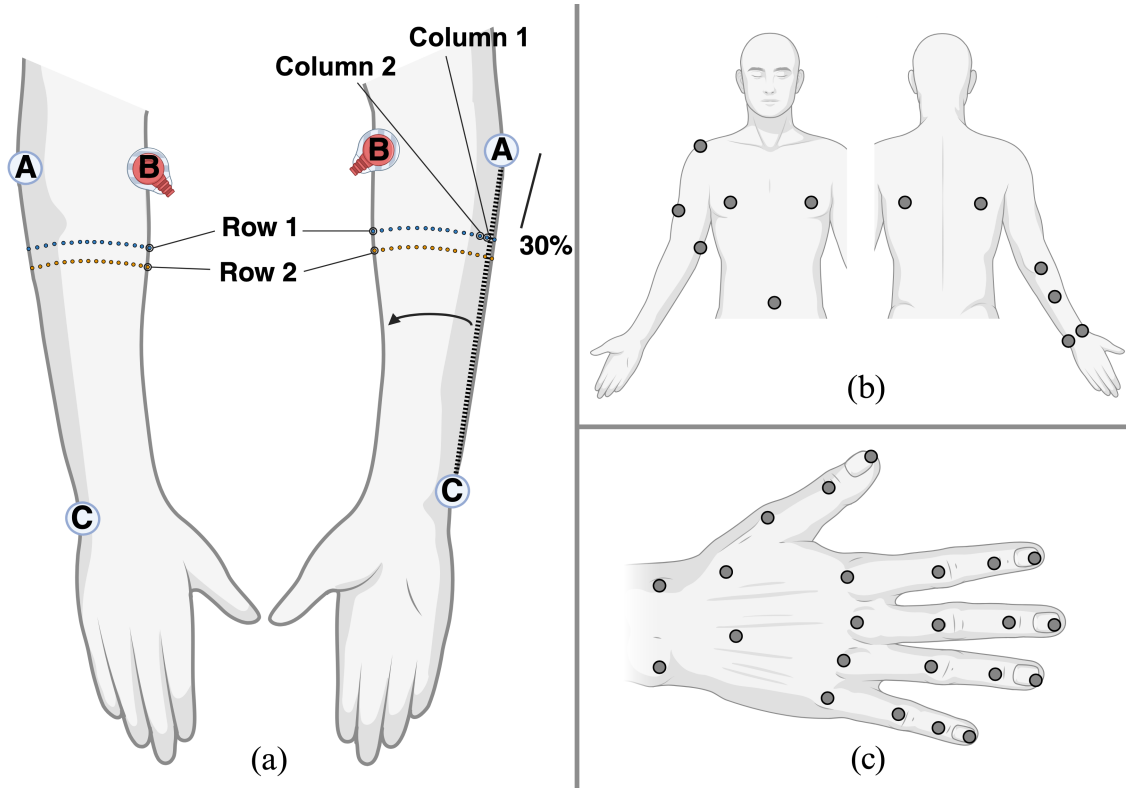

Figure 6.2: Subject setup: (a) HDE-Array placement around the forearm, showing the front and back views. Light blue and orange dots represent electrode locations. The array is positioned with electrode 1 at 30% of the distance between the lateral epicondyle and the pisiform bone. (b) Placement of 12 infrared markers on the body of the subject. (c) Placement of 21 infrared markers on the hand and two on the forearm, with each marker positioned proximally to a joint.

to the same procedure defined above, using the same anatomical landmark for alignment. Additionally, to introduce variability in skin conditions, an abrasive gel was applied between trials 4 and 5 to reduce skin impedance. Trials 1 to 6 constitute the first session. After a break of less than thirty minutes, participants completed two more trials, making up the second session, following the same experimental protocol. Electrodes were again repositioned between trials, though no further skin preparation was performed. These latter two trials constitute DS3.a.s2 as referenced throughout the rest of this manuscript.

DS2: Joint EMG and Kinematic Data without Electrode Repositioning

DS2 was acquired as the primary dataset for Chapter 4. The acquisition procedure is similar to that of DS3.a, with the following key differences:

1. Data were collected at the Laboratory of Motion Analysis (Politecnico di Torino) between November and December 2023. Sixteen healthy right-handed volunteers (S13-S28; 8 males, 8 females; age: 20 to 26 years; weight: 55 to 90 kg; height: 165 to 195 cm) participated.
2. EMG data were acquired using two MEACS SUs connected to both the proximal and distal rows of the HDE-Array, yielding 64 dry electrodes arranged in two circumferential rows around the forearm. When compared with data from DS3.a, only the 32 proximal electrodes are considered.
3. No electrode repositioning was performed during the first session.
4. Skin preparation was carried out before the start of both sessions.
5. The interval between sessions ranged from several hours to two days.
6. In the second session, no electrode repositioning was performed between the two trials.

The first six trials, making up session 1, will be referenced as DS2.s1, and the final two (session 2) as DS2.s2.

Pre-processing

The pre-processing procedure is intended to transform the acquired data into suitable inputs for RPC-Net. Raw EMG signals were first converted from bits to volts, then offset-corrected, rectified, and transformed into RMS values using a sliding window of $w_l = 200$ samples (97.7 ms). The window step w_s was adjusted based on prompt duration, as defined in Section 6.2.2: 25 samples for 8 seconds, 29 for 7 seconds, and 33 for 6 seconds, ensuring consistency in sample number across subjects. Given an electromyographic signal that is L seconds long and N-dimensional, the output of the pre-processing procedure is $l = floor(\frac{L*f_s - w_l}{w_s}) + 1$ samples long and N-dimensional. The resulting RMS values were divided by 10^{-4} to bring the data into a standardised range suitable for RPC-Net training, resulting in unit variance.

Vicon marker positions were processed using a moving average filter with a window length of 20 samples and subsequently mapped into a 29-dimensional joint-angle space using the IKA (Section 3.2.2). To prepare the joint-angle data

for network training, rest angles were subtracted, and the resulting values were normalised by dividing by 45 degrees, centring the data at zero and resulting in unit variance. Finally, linear interpolation was applied to align the sampling rates of the EMG and joint-angle data, ensuring synchronised, time-matched input-output pairs for RPC-Net training. Given an L-second-long signal, the output of the pre-processing procedure is $l = floor(\frac{L*f_s - w_l}{w_s}) + 1$ samples long and J-dimensional. Pre-processing was identical for DS2 and DS3.a.

RPC-Net Training and Post-processing

RPC-Net, as defined in Chapter 3 (Section 3.2.2), is a neural network that estimates hand position from HD-sEMG signals acquired on the proximal forearm, refining estimates recursively based on prior values. The version of RPC-Net used in this study processes inputs from 64 (or 32) EMG channels and 29 joint angles. Each sub-network, responsible for a specific joint angle, excludes its corresponding input channel, using the remaining 28 angles instead. This setup creates a robust recursive loop between EMG signals and past angles. During training, actual joint angles replace past estimates. During the testing phase, joint angles produced by the RPC-Net undergo processing via a fourth-order low-pass Butterworth filter (with a cutoff frequency $f_c = 1$ Hz) to eliminate high-frequency fluctuations and are subsequently mapped back into 3D space using the FKA.

In this study, two versions of RPC-Net were used: RPC-Net-32, which uses 32 EMG channels as input, and RPC-Net-64, which processes 64 channels. RPC-Net-32 is used in the part of the study evaluating the robustness of the system to electrode displacement and skin condition variability, while RPC-Net-64 is used in the second part, which assesses the impact of multi-subject training. Both versions were implemented in PyTorch. On an Intel(R) Xeon(R) Platinum 8268 CPU at 2.90 GHz, RPC-Net-32 achieves an average IT of 1.3 ms (standard deviation: 0.2 ms) across 10^5 iterations. The network was trained with the Adam optimiser (in its PyTorch implementation), learning rate = 10^{-5}; $\varepsilon = 10^{-12}$; $\beta_1 = 0.9$; $\beta_2 = 0.99$; batch size = 2000; loss criterion = MSELoss. The model was trained for 200 epochs.

During the training of RPC-Net, the joint angle input data were taken from the recording, and the recursion loop was not used. RPC-Net-64 achieved an average IT of 4.2 ms (standard deviation: 0.2 ms). Given the larger input size and dataset used for the second part of the study, a batch size of 10000 was adopted for training.

Performance Assessment

The performance of RPC-Net was assessed as its ability to estimate the position of the hand from the electromyogram. The performance was measured with two indicators: MPCC and MD, both computed for the test trial only. MPCC is the mean of the individual PCC obtained from comparing the actual and predicted joint angle values for each of the 29 DoFs considered, over the whole test trial. MD is the mean, over the whole test trial, of the distances between index, middle, and thumb tips and their estimates. A thorough definition of MD and MPCC is included in Chapter 3 (Section 3.2.2).

Assessment of Robustness to Electrode Shifts and Skin Conditions

To evaluate Hypotheses 1 to 3, the performance of the RPC-Net-32/HDE-Array system under different training and testing conditions was compared. Specifically, two factors were varied

1. whether electrode repositioning was introduced during training, and
2. whether the system was tested on data from the same session or from a separate session.

Two main assessment configurations are defined:

1. Intra-session assessment: RPC-Net-32 was trained on 5 out of the 6 trials (a 5:1 train-test split) within the same session, namely DS3.a.s1 or DS2.s1, and tested on the remaining trial from that session.
2. Extra-session assessment: RPC-Net-32 was trained on the same 5 trials from DS3.a.s1 or DS2.s1 but tested on one of the two trials from DS3.a.s2 or DS2.s2, respectively. In this case, the same subset of 5 trials used for the Intra-session assessment was used, without adding the sixth one to the training data.

Because DS3.a included electrode repositioning and DS2 did not, these two assessment types yield four distinct cases, defined with a two-letter abbreviation:

1. Intra-session with repositioning (DS3.a): IR.
2. Extra-session with repositioning (DS3.a): ER.
3. Intra-session without repositioning (DS2): IN.
4. Extra-session without repositioning (DS2): EN.

Comparing system performance across these four cases addresses Hypotheses 1 to 3. Additionally, to explore how the amount of training data affects performance (Hypothesis 2), intra-session performance of the system (with and without repositioning) was assessed using subsets of 1, 2, 3, 4, and all 5 training trials, while holding the same test trial fixed. An average was then performed across all possible trial combinations to minimise selection bias.

Assessment of Generalised Training via Inter-Subject Data

This experiment was conducted exclusively using DS2. Since no direct comparison with DS3.a was required, all 64 HD-sEMG channels recorded from the forearm were used. Only intra-session data were considered (6 trials per subject). The goal was to evaluate the generalisation capability of RPC-Net-64 when trained on data from multiple subjects. The dataset was split into groups of 2, 4, 8, or 16 subjects. For group sizes of 2, 4, and 8, subjects were randomly selected into non-exhaustive groupings. Specifically, eight random groups of two subjects, four groups of four subjects, and two groups of eight subjects were evaluated, for a total of 64 groups (considering each group existed in as many versions as needed to have each subject as test subject at least once).

Four training conditions (0, 1, 3, and 5) were defined, differing in the amount of data from the test subject included during training. In conditions 1, 3, and 5, the training protocol consisted of using all data from the training subjects in a group to train RPC-Net-64, plus one, three, or five additional training trials from the test subject, respectively. These never included the test trial of the test subject, which remained the same across all conditions and was used exclusively in the testing

phase to assess performance. Regardless of group size, simulations were run such that each subject served as the test subject once per group size. This meant that, for each group size considered, 16 versions of RPC-Net-64 were trained and that, for each condition, 64 versions of RPC-Net-64 were trained (four group sizes × 16 subjects). Results were averaged across group sizes (16 data points per size). To contextualise performance, a within-subject baseline in which RPC-Net was trained exclusively on data from the test subject using the same number of trials (i.e., 1, 3, or 5, depending on the condition) was also evaluated.

The objective of this assessment is to evaluate if data from other subjects can effectively substitute, during training, data from the test subject. The aim was to evaluate if, for example, the performance observed when training the system on 5 trials from the test subject can be replicated by training on just one trial, and supplementing with data from different subjects. For condition 0, no data from the test subject were included in training. This condition represents a boundary case, and aims to determine how well the system can perform when trained on data from other subjects only. As per conditions 1, 3, and 5, regardless of group size, simulations were run such that each subject served as the test subject once per group size. This meant that, for each group size considered, 16 versions of RPC-Net-64 were trained. Results were averaged across group sizes (16 data points per size).

Hypothesis Testing

Four hypotheses to evaluate the performance of the RPC-Net/HDE-Array system under varying experimental conditions were tested:

1. The accuracy of the RPC-Net/HDE-Array system decreases when electrode positioning is inconsistent between the training and testing sessions, compared to the baseline case in which electrode positioning remains consistent : To test this hypothesis, system performance in the IN and EN conditions, as defined in Section 6.2.2 was compared. A one-sided paired t-test was used to assess whether the mean performance across subjects differed significantly between conditions, using both MD and MPCC as evaluation metrics. The

null hypothesis assumed equality between conditions, while the alternative hypothesis reflected the expectation that intra-session performance would be superior. Specifically, the hypotheses tested were $H_0 : \mu_{IN} \geq \mu_{EN}$ vs. $H_1 : \mu_{IN} < \mu_{EN}$ for MD, and $H_0 : \mu_{IN} \leq \mu_{EN}$ vs. $H_1 : \mu_{IN} > \mu_{EN}$ for MPCC. This reflects the fact that lower MD and higher MPCC indicate better performance. Normality of the distributions was verified with a Shapiro-Wilk test.

2. When the RPC-Net/HDE-Array system is tested on data from the same session as the training data, its accuracy remains unchanged regardless of whether electrode repositioning is included during training : To test this hypothesis, the performance of the system under IN and IR conditions was analysed, across increasing numbers of training trials. For each condition, performance curves were constructed by fitting a non-linear regression model of the form $y = a + b \cdot e^{(cx)}$, where x is the number of training trials and y is the corresponding performance metric (MD and MPCC). Each curve was fitted using 80 data points (16 subjects $\times$ 5 training trial counts). Parameter estimates are reported, and the coefficient of determination (R^2) was used to assess goodness of fit. To assess whether the IN performance curve generalised to the IR condition, the fitted model was applied to the repositioning data and the distributions of residuals were compared using Levene's test. A non-significant result was interpreted as evidence that the variability in model fit was consistent across conditions, supporting generalisability. As a formal test of performance comparability at full training exposure, a one-sided unpaired t-test on the 5-trial condition was conducted. The alternative hypothesis assumed that performance without repositioning would be superior. Specifically, hypotheses tested were: $H_0 : \mu_{IN} \geq \mu_{IR}$ and $H_1 : \mu_{IN} < \mu_{IR}$ for MD; $H_0 : \mu_{IN} \leq \mu_{IR}$ and $H_1 : \mu_{IN} > \mu_{IR}$ for MPCC. Normality was verified with a Shapiro-Wilk test.

3. The performance degradation observed when the system is trained without electrode repositioning and tested on data from a different session can be mitigated by incorporating electrode repositioning during training : To evaluate this hypothesis, a one-sided paired t-test comparing IR and ER performance was performed. The alternative hypothesis was that IR performance would be superior, reflecting a degradation in performance when transitioning across sessions. Specifically, the hypotheses tested were: $H_0 : \mu_{IR} \geq \mu_{ER}$ and $H_1 : \mu_{IR} < \mu_{ER}$ for MD; $H_0 : \mu_{IR} \leq \mu_{ER}$ and $H_1 : \mu_{IR} > \mu_{ER}$ for MPCC. To assess whether repositioning-aware training mitigates this degradation, the results of this test were compared to the corresponding no-repositioning case. Additionally, a one-sided unpaired t-test to directly compare ER and EN was performed. The alternative hypothesis was that training with repositioning would result in better generalisation across sessions. Specifically, the hypotheses tested were: $H_0 : \mu_{ER} \geq \mu_{EN}$ and $H_1 : \mu_{ER} < \mu_{EN}$ for MD; $H_0 : \mu_{ER} \leq \mu_{EN}$ and $H_1 : \mu_{ER} > \mu_{EN}$ for MPCC. Together, these analyses test whether training with electrode repositioning improves the robustness of the system to session-to-session variability. Normality of the distributions was verified with a Shapiro-Wilk test.
4. Including inter-subject data in the training set improves the overall performance of the system, providing a valid alternative to an increased amount of subject-specific data : To evaluate this hypothesis, Spearman's rank correlation test was performed to assess whether system performance exhibited a monotonic trend with respect to the number of training subjects. This analysis was conducted separately for each of the four experimental conditions (conditions 0, 1, 3, and 5), defined by the number of additional training trials from the test subject. For all conditions, the hypothesis tested was $H_0 : \rho = 0$ and $H_1 : \rho \neq 0$. The result was then interpreted to assess whether the monotonic trend was increasing or decreasing. To support the interpretation of monotonic trends, linear regression models of the form $y = ax + b$ were also fit for each condition, where x represents the number of training subjects

and y the performance metric. The choice of a linear model was supported by preliminary analyses indicating that, within the interval considered, the relationship between variables was approximately linear and that linear fitting yielded the most consistent results. Exponential fitting was also evaluated but exhibited poor extrapolation behaviour and was therefore deemed unsuitable for this analysis. Finally, to provide a direct comparison of the effects of generalised training, the results observed for condition 5 with 15 additional subjects and with no additional subjects were compared. A two-sided paired t-test: $H_0 : \mu_{15} = \mu_1$ and $H_1 : \mu_{15} \neq \mu_1$ was used for both MD and MPCC. Normality of the distributions was verified with a Shapiro-Wilk test.

6.3 Results

This section presents the results of the experimental evaluations outlined in Section 6.2.2. Specifically, it examines the impact of electrode repositioning and skin-condition variability on system performance, as well as the effectiveness of incorporating such variability during training. Additionally, the section assesses the influence of inter-subject training on the generalisation capabilities of the RPC-Net/HDE-Array system.

6.3.1 Robustness of RPC-Net Against Electrode Repositioning

To evaluate whether the performance of RPC-Net decreases when electrode repositioning is included in the testing phase, as posited in Hypothesis 1, IN and EN results were compared. Figure 6.3 displays performance for four experimental configurations: intra-session and extra-session testing, both with and without electrode repositioning during training. The comparison between intra- and extra-session results without repositioning reveals a substantial deterioration in performance. The MD increased from 31.5 mm to 65.1 mm, while the MPCC dropped from 0.69 to 0.34. Both differences were statistically significant, as confirmed by one-tailed paired t-tests (MD: H1: $\mu_{IN} \leq \mu_{EN}$, $p = 4.1{\cdot}10^{-6}$; MPCC: H1: $\mu_{IN} \geq \mu_{EN}$, $p = 1.5{\cdot}10^{-6}$).

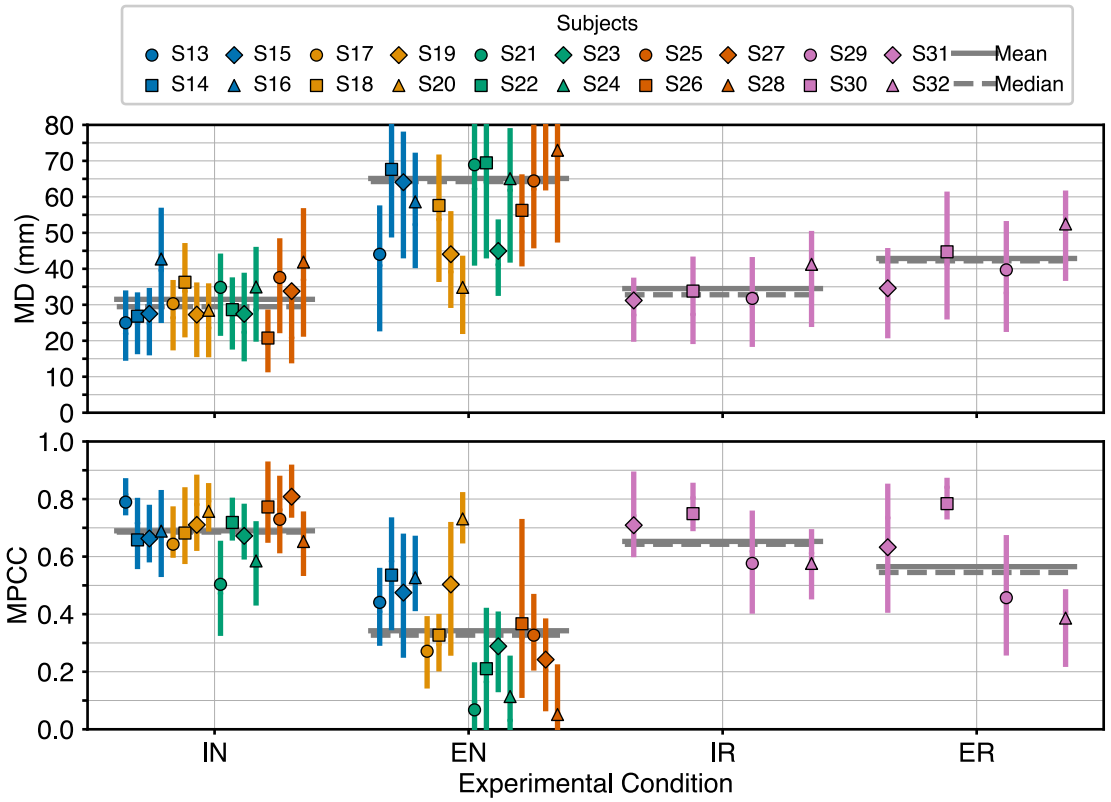

Figure 6.3: Comparison of RPC-Net performance under different conditions: The figure shows the performance of the RPC-Net/HDE-Array system with and without electrode repositioning and across intra- and extra-session scenarios for all subjects. Interquartile ranges, means, and medians are shown. t-test results for MD: IN vs. EN: $H_0 : \mu_{IN} \geq \mu_{EN}$; $H_1 : \mu_{IN} < \mu_{EN}$: $t(15) = -6.62$, $p = 4.1{\cdot}10^{-6}$; IN vs. IR: $H_0 : \mu_{IN} \geq \mu_{IR}$; $H_1 : \mu_{IN} < \mu_{IR}$: $t(18) = -0.90$, $p = 1.9{\cdot}10^{-1}$; IR vs. ER: $H_0 : \mu_{IR} \geq \mu_{ER}$; $H_1 : \mu_{IR} < \mu_{ER}$: $t(3) = -4.61$, $p = 9.6{\cdot}10^{-3}$; ER vs. EN: $H_0 : \mu_{ER} \geq \mu_{EN}$; $H_1 : \mu_{ER} < \mu_{EN}$: $t(18) = -1.89$, $p = 3.8{\cdot}10^{-2}$. t-test results for MPCC: IN vs. EN: $H_0 : \mu_{IN} \leq \mu_{EN}$; $H_1 : \mu_{IN} > \mu_{EN}$: $t(15) = 7.21$, $p = 1.5{\cdot}10^{-6}$; IN vs. IR: $H_0 : \mu_{IN} \leq \mu_{IR}$; $H_1 : \mu_{IN} > \mu_{IR}$: $t(18) = 0.83$, $p = 2.1{\cdot}10^{-1}$; IR vs. ER: $H_0 : \mu_{IR} \leq \mu_{ER}$; $H_1 : \mu_{IR} > \mu_{ER}$: $t(3) = 1.86$, $p = 8.0{\cdot}10^{-2}$; ER vs. EN: $H_0 : \mu_{ER} \leq \mu_{EN}$; $H_1 : \mu_{ER} > \mu_{EN}$: $t(18) = 2.15$, $p = 2.3{\cdot}10^{-2}$.

As a result, Hypothesis 1 is supported: RPC-Net does not maintain consistent performance across sessions in the absence of repositioning-aware training. Summary values for all conditions are provided in Table 6.1.

6.3.2 Effect of Repositioning on Intra-Session Learning

Including electrode repositioning during training was evaluated for its influence on learning dynamics of RPC-Net under intra-session conditions. Specifically, it was assessed whether performance trends as a function of training set size differ in

Table 6.1: Effect of session variability on RPC-Net performance

Condition	MD (mm, Range)	MPCC (Range)
Repositioning, Intra-Session (IR)	34.5 (31.2-41.2)	0.65 (0.58-0.75)
No Repositioning, Intra-Session (IN)	31.5 (20.8-42.7)	0.69 (0.50-0.81)
Repositioning, Extra-Session (ER)	42.9 (34.6-52.5)	0.57 (0.39-0.78)
No Repositioning, Extra-Session (EN)	65.1 (34.8-129.9)	0.34 (0.05-0.73)

MD: Mean Distance. MPCC: Mean Pearson Correlation Coefficient. Lower MD and higher MPCC indicate better performance. Mean and range across subjects are shown for each condition considered.

IR and IN. Figure 6.4 illustrates system performance across increasing numbers of training trials, reported in terms of MD and MPCC. In both the no-repositioning and repositioning conditions, performance improves consistently with additional training data. A relatively stable performance gap is observed across all training set sizes; approximately 5 mm in MD and 0.05 in MPCC, with the no-repositioning condition achieving slightly better absolute values. However, both trends appear to follow similar trajectories in shape. To quantify these trends, the performance data were fitted with a non-linear exponential model of the form $y = a + b \cdot e^{(cx)}$, where x denotes the number of training trials and y the performance metric. For all conditions and metrics, the R^2 goodness of fit values were computed (MD, no-repositioning: $R^2 = 0.27$; MPCC, no-repositioning: $R^2 = 0.21$; MD, repositioning: $R^2 = 0.44$; MPCC, repositioning: $R^2 = 0.29$) and Spearman's rank correlation test gave: MD, no-repositioning: $p = 7.5{\cdot}10^{-33}$; MPCC, no-repositioning: $p = 6.9{\cdot}10^{-22}$; MD, repositioning: $p = 4.5{\cdot}10^{-16}$; MPCC, repositioning: $p = 6.5{\cdot}10^{-9}$. These results confirm the presence of a statistically significant learning trend with increasing data.

To assess whether the performance model from the no-repositioning condition could generalise to the repositioning data, the fitted no-repositioning model was applied to the repositioning data and the resulting residuals were compared using Levene's test. This analysis evaluates whether the variability (i.e., spread) of residuals differs significantly across conditions, which would indicate model misfit. Levene's test revealed no significant differences in residual variance for either

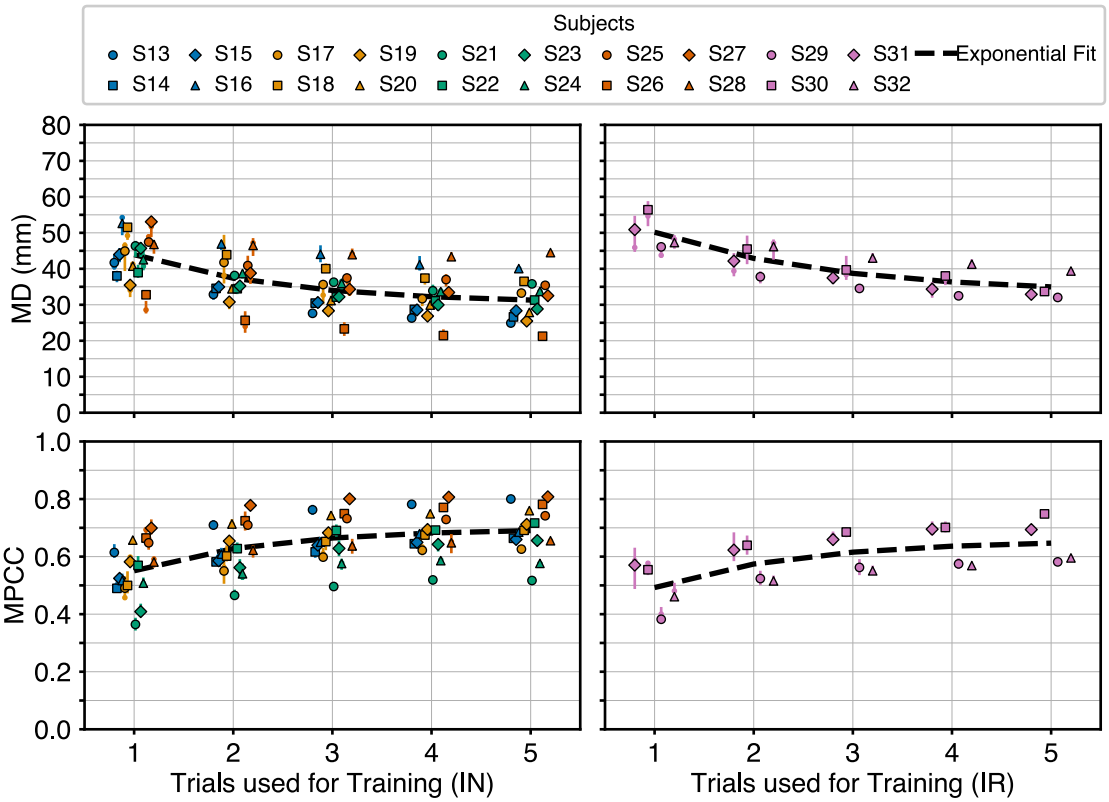

Figure 6.4: Intra-session performance with and without electrode repositioning: System performance (MD and MPCC) across all subjects as a function of the number of training trials. Interquartile ranges are shown. Dashed lines represent the best-fit exponential curves ($y = a + b \cdot e^{(cx)}$); estimated coefficients are reported in Table 6.2. For MD-IN: $R^2 = 0.27$; MD-IR: $R^2 = 0.44$. For MPCC-IN: $R^2 = 0.21$; MPCC-IR: $R^2 = 0.29$. Spearman's rank test results: MD-IN: ρ = -0.50, $p = 7.5{\cdot}10^{-33}$; MD-IR: ρ = -0.65, $p = 4.5{\cdot}10^{-16}$; MPCC-IN: ρ = -0.41, $p = 6.9{\cdot}10^{-22}$; MPCC-IR: ρ = 0.49, $p = 6.5{\cdot}10^{-9}$. Mean differences between mean values and exponential estimate: MD-IN: 0.1 mm; MD-IR: 0.2 mm; MPCC-IN: 0.001; MPCC-IR: 0.002. Levene's test results: for MD, Levene's statistic = 3.31, $p = 6.9{\cdot}10^{-2}$; for MPCC, Levene's statistic = 0.30, $p = 5.8{\cdot}10^{-1}$.

performance metric (MD: statistic = 3.31, $p = 6.9{\cdot}10^{-2}$; MPCC: statistic = 0.30, $p = 5.8{\cdot}10^{-1}$), suggesting that the underlying model structure is applicable to both conditions. The fitted regression parameters for each curve are reported in Table 6.2. According to these models, approximately 90% of asymptotic performance was reached between 3 and 5 training trials in both cases. Finally, to directly assess end-point performance, a one-sided unpaired t-test was conducted comparing the five-trial results under both training conditions. No statistically significant differences were observed (MD: $p = 1.9{\cdot}10^{-1}$; MPCC: $p = 2.1{\cdot}10^{-1}$), indicating that repositioning during training does not significantly affect final performance when

Table 6.2: Fitted parameters of the exponential performance model

	No Repositioning (IN)		Repositioning (IR)	
	MD (mm)	MPCC	MD (mm)	MPCC
a	30.3 ± 2.9	0.70 ± 0.03	33.1 ± 6.3	0.66 ± 0.07
b	26.2 ± 5.6	-0.31 ± 0.09	29.7 ± 7.1	-0.33 ± 0.14
c	-0.66 ± 0.32	-0.74 ± 0.40	-0.56 ± 0.42	-0.68 ± 0.63

Fitted parameters of a pooled exponential model, $y = a+b\cdot e^{(cx)}$, across participants, where x denotes the number of training trials and y the performance metric (MD or MPCC). Reported uncertainties represent 95% confidence intervals derived from the non-linear least-squares covariance. Values are shown for intra-session training under both Repositioning and No Repositioning conditions.

sufficient data are available. These findings support Hypothesis 2: RPC-Net achieves comparable intra-session performance regardless of whether electrode repositioning is included in training, particularly when trained on a sufficient number of trials.

6.3.3 Effect of Repositioning on Cross-Session Performance

To assess whether incorporating electrode repositioning during training mitigates performance degradation across sessions, as stated in Hypothesis 3, IR and ER results were compared. As shown in Figure 6.3, the impact of session changes under this condition is notably reduced compared to the no-repositioning case. Although the MD increased from 34.5 mm to 42.9 mm between intra- and extra-session conditions (H_1: $\mu_{IR} \leq \mu_{ER}$; $p = 9.6{\cdot}10^{-3}$), the decline in MPCC from 0.65 to 0.57 was not statistically significant (H_1: $\mu_{IR} \geq \mu_{ER}$; $p = 8.0{\cdot}10^{-2}$). These results suggest that incorporating repositioning during training attenuates the negative impact of session-related variability on system performance. This conclusion is further supported by a direct comparison of ER and EN performance. When repositioning was included, performance improved significantly for both MD (42.9 mm to 65.1 mm; H_1: $\mu_{ER} \leq \mu_{EN}$; $p = 3.8{\cdot}10^{-2}$) and MPCC (0.57 to 0.34; H_1: $\mu_{ER} \geq \mu_{EN}$; $p = 2.3{\cdot}10^{-2}$). Overall, these results confirm Hypothesis 3: training

Table 6.3: Fitted parameters for the linear performance model

	MD			
Condition	0	1	3	5
a	-1.00	1.77	0.71	0.79
CI (a)	± 0.83	± 0.40	± 0.26	± 0.23
b	80.4	31.0	33.0	28.8
CI (b)	± 7.6	± 3.3	± 2.1	± 1.9
	MPCC			
a	0.005	-0.022	-0.013	-0.013
CI (a)	± 0.004	± 0.005	± 0.005	± 0.004
b	0.20	0.71	0.71	0.75
CI (b)	± 0.03	± 0.04	± 0.04	± 0.03

Parameters and 95% CIs of the equation $ax+b$ for different experimental conditions. MD: Mean Distance; MPCC: Mean Pearson Correlation Coefficient.

with electrode repositioning improves the robustness of the system to cross-session variability, reducing performance deterioration in more realistic usage scenarios.

6.3.4 Effect of Inter-Subject Training on System Generalisation

To assess whether including inter-subject data in the training set improves the overall performance of the system, as stated in Hypothesis 4, performance was evaluated across different training conditions that included varying numbers of subjects. The analysis considered four experimental conditions (conditions 0, 1, 3, and 5), defined by the number of trials from the test subject incorporated into the training set: Condition 0: No data from the test subject included; Condition 1: One trial included; Condition 3: Three trials included; Condition 5: Five trials included. Performance trends for each condition are shown in Figure 6.5. Linear regression models of the form $y = a + bx$ were fitted to describe the relationship between the number of training subjects and system performance, measured by MD and MPCC.

The fitted parameters are reported in Table 6.3. The linear regression revealed a significant positive or negative relationship ($p \leq 0.05$) for all conditions. The results reveal that in conditions 1, 3, and 5, performance tends to decline as more subjects are added. These trends are confirmed by the results of Spearman's rank correlation test. For MD, the p-values associated with the test $H_0 : \rho = 0$ were: $1.1{\cdot}10^{-21}$ (Condition 1), $1.4{\cdot}10^{-4}$ (Condition 3), and $1.6{\cdot}10^{-6}$ (Condition 5). For MPCC, the corresponding values were $4.9{\cdot}10^{-20}$, $1.3{\cdot}10^{-5}$, and $7.3{\cdot}10^{-7}$, respectively. The values of ρ were positive for MD (conditions 1, 3 and 5), and negative for MPCC. A paired two-sided t-test comparing performance with one subject versus 16 subjects (with five test-subject trials included in both conditions) revealed a statistically significant drop in accuracy when adding 15 more subjects (MD: $t(15) = -8.57$, $p = 3.7{\cdot}10^{-7}$; MPCC: $t(15) = 8.15$, $p = 6.9{\cdot}10^{-7}$), as illustrated in Figure 6.6. These results do not support Hypothesis 4, as performance does not improve when including data from a larger pool of subjects. For the sake of completeness, the results derived from Condition 0, where no data from the test subject were included in training, are also reported. The results reveal a divergence in behaviour between Condition 0 and the other three conditions, as in the former performance improves with the number of additional subjects, reflecting a positive generalisation effect. These trends are confirmed by the results of Spearman's rank correlation test. For MD, the p-value associated with the test $H_0 : \rho = 0$ was: $1.8{\cdot}10^{-2}$, and $4.5{\cdot}10^{-3}$ for MPCC. The value of ρ was negative for MD and positive for MPCC reinforcing the opposing direction of the performance trend when subject-specific data are present. Only Condition 0 aligns with Hypothesis 4 by demonstrating improved performance with increasing subject diversity in the absence of any overlap with test-subject data.

6.4 Discussion

The results presented in the previous section indicate that the RPC-Net/HDE-Array system is not inherently robust to electrode shifts and skin condition variability when such factors are absent from the training data. However, introducing this variability during training significantly mitigates performance degradation, enhancing the

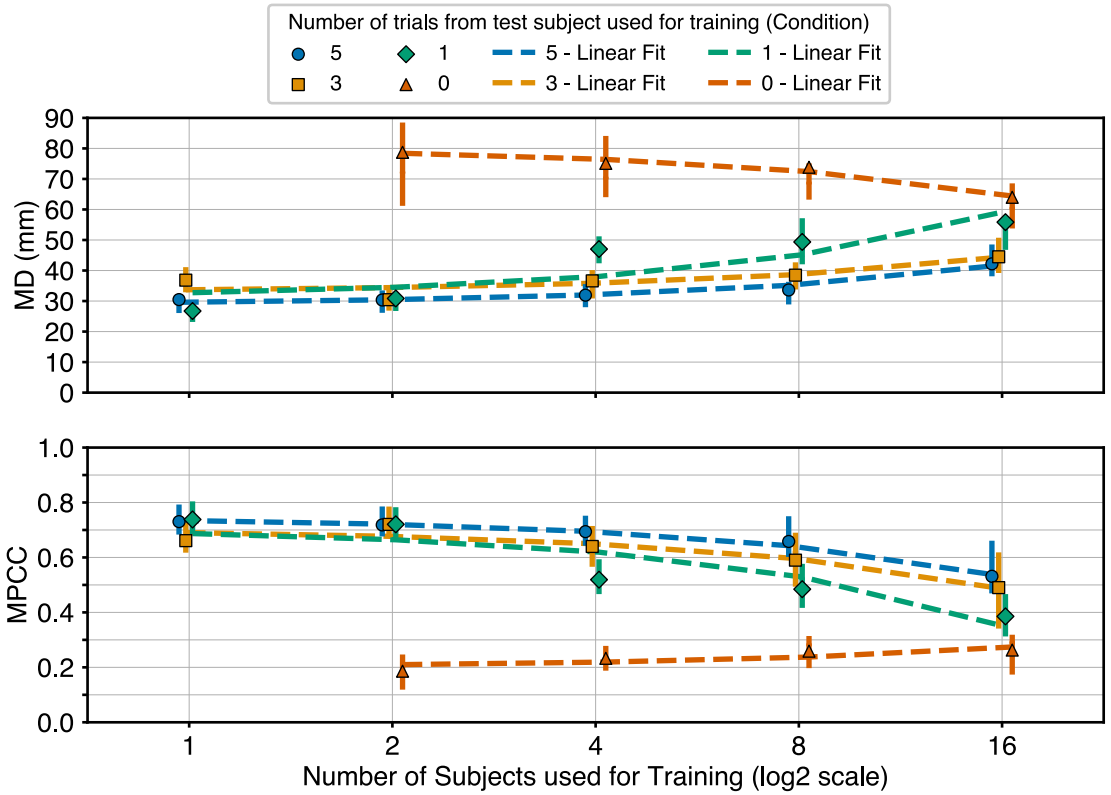

Figure 6.5: Performance as a function of number of training subjects: Performance trends for Conditions 0, 1, 3, and 5 as a function of the number of training subjects. Each marker shows the mean performance across all subjects for the given condition; interquartile ranges are indicated. Dashed lines depict the best-fit linear relationships ($y = ax + b$); computed parameters with confidence intervals are in Table 6.3. The x-axis is plotted on a base-2 logarithmic scale, and the number of subjects used for training includes the test subject. Although the regression is linear, the trend appears exponential due to the logarithmic scaling of the x-axis. Each subject in the training set corresponds to approximately 20 minutes of recorded data (256 s of data per trial, 5 trials per subject). Each trial from the test subject added (1, 3, or 5, depending on the condition considered) corresponds to 4 minutes of data (256 s). Regression results: For MD: Condition 0: $R^2 = 0.09$, $p = 1.9{\cdot}10^{-2}$; Condition 1: $R^2 = 0.50$, $p = 2.6{\cdot}10^{-13}$; Condition 3: $R^2 = 0.27$, $p = 8.5{\cdot}10^{-7}$; Condition 5: $R^2 = 0.38$, $p = 1.4{\cdot}10^{-9}$. For MPCC: Condition 0: $R^2 = 0.10$, $p = 1.3{\cdot}10^{-2}$; Condition 1: $R^2 = 0.56$, $p = 1.9{\cdot}10^{-15}$; Condition 3: $R^2 = 0.31$, $p = 9.7{\cdot}10^{-8}$; Condition 5: $R^2 = 0.36$, $p = 3.4{\cdot}10^{-9}$. Spearman's rank test results: for MD: Condition 0: ρ = -0.30, $p = 1.8{\cdot}10^{-2}$; Condition 1: $\rho = 0.83$, $p = 1.1{\cdot}10^{-21}$; Condition 3: $\rho = 0.41$, $p = 1.4{\cdot}10^{-4}$; Condition 5: $\rho = 0.51$, $p = 1.6{\cdot}10^{-6}$. for MPCC: Condition 0: $\rho = 0.35$, $p = 4.5{\cdot}10^{-3}$; Condition 1: ρ = -0.81, $p = 4.9{\cdot}10^{-20}$; Condition 3: ρ = -0.47, $p = 1.3{\cdot}10^{-5}$; Condition 5: ρ = -0.52, $p = 7.3{\cdot}10^{-7}$.

robustness of the system in more realistic scenarios. In addition, the findings suggest that inter-subject training does not provide an adequate substitute for additional data from the tested subject. This section provides a detailed interpretation of

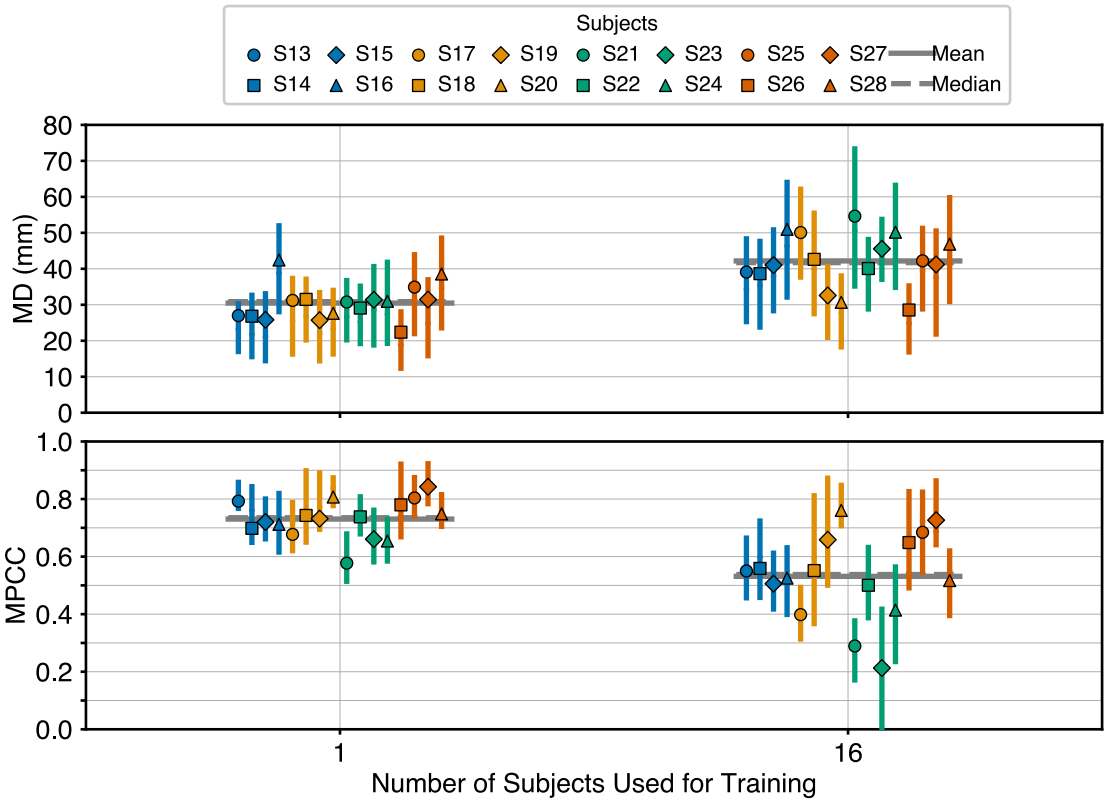

Figure 6.6: RPC-Net performance with one and sixteen training subjects: The figure shows the performance of the RPC-Net/HDE-Array system in Condition 5 when trained with either 15 additional subjects or no additional subjects, across all test subjects considered in this study. The interquartile range is shown, along with the mean and median of each distribution. t-test results for MD: 1 vs. 16: $H_0 : \mu_1 = \mu_{16}$; $H_1 : \mu_1 \neq \mu_{16}$: $t(15)$ = -8.57, $p = 3.7{\cdot}10^{-7}$. t-test results for MPCC: 1 vs. 16: $H_0 : \mu_1 = \mu_{16}$; $H_1 : \mu_1 \neq \mu_{16}$: $t(15) = 8.15$, $p = 6.9{\cdot}10^{-7}$.

these findings in relation to the original hypotheses of the study and positions them within the context of current research in the field.

The first objective of this study, articulated through Hypotheses 1 to 3, was to evaluate the robustness of the RPC-Net/HDE-Array system to electrode repositioning and skin condition variability. The findings presented in Section 6.3.1 clearly show that, under the previously adopted training protocol, where data are acquired within a single session and without repositioning, the system fails to generalise when electrodes are repositioned. In this condition, endpoint errors exceed 65 mm, a substantial increase compared with the typical performance of under 35 mm. Such a level of inaccuracy renders the system unsuitable for reliable control applications (Section 2.3.1). This degradation is also well below the performance reported in

previous work and in other relevant studies, with some subjects exhibiting near-zero correlation between estimated and actual joint angles (Chapter 3, Chapter 4) [300]. These results support the first experimental hypothesis.

However, when variability is intentionally introduced during the training phase, specifically through repeated electrode repositioning and skin preparation, the system becomes substantially more robust, as demonstrated in Section 6.3.3. In this configuration, the performance drop between intra- and extra-session testing is reduced to less than 8 mm, with extra-session MD values falling below 45 mm. This performance level is comparable to prior results and aligns with the broader state of the art. Moreover, the 22 mm improvement in MD between the extra-session conditions with and without repositioning-aware training underscores the effectiveness of this approach, and is well above the operational difference threshold defined in Section 2.3.1. Importantly, the electrode repositioning during data collection was performed by the subjects themselves, not by the researchers. This procedure eliminates potential bias and demonstrates the potential robustness of the system in real-world use cases, where users must independently don the system across multiple sessions. Given these results, it is possible to state that the third hypothesis was successfully demonstrated. Additional support for this conclusion comes from Section 6.3.2, which shows that including repositioning in the training protocol does not significantly impair intra-session performance. The observed difference, approximately 5 mm in MD, and the non-significant p-value, suggest that training protocols incorporating variability can still be suitable for both offline validation and online control scenarios. These results support the second hypothesis of the present study.

From a methodological perspective, two points warrant clarification to properly contextualise these findings. First, the datasets representing training with and without repositioning included different numbers of subjects (4 and 16, respectively). Although the statistical tests applied (paired and unpaired t-tests) account for these differences and the nominal α level remains valid in principle, small sample sizes inherently increase the risk of both Type I and Type II errors. The results

should therefore be interpreted with appropriate caution. Second, the slightly lower performance observed here compared to what is stated in Chapter 4 on the same dataset arises from a methodological difference: in this part of the current study, only a single row of electrodes was used, whereas previous work employed both proximal and distal rows.

The findings presented in this part of the study are particularly important for the development of user-friendly, deployable assistive technologies, where users cannot rely on precise electrode reapplication by trained personnel. In real-life scenarios, individuals must be able to maintain performance over time and operate the device as independently as possible. Ensuring robust performance under self-operated conditions significantly lowers the barrier to adoption in both clinical and home settings, making long-term rehabilitation and daily assistive use more feasible. The results demonstrate that the RPC-Net/HDE-Array system can support this level of robustness, with the appropriate calibration procedures.

The second objective of this study, addressed through Hypothesis 4, was to evaluate whether including data from additional subjects during training could improve the performance of the RPC-Net/HDE-Array system. As shown in Section 6.3.4, such improvement was observed only when no data from the test subject were included in the training set (Condition 0). This finding suggests that the model is highly sensitive to subject-specific patterns in the sEMG data. When personalised data are available, they appear to dominate the learning process; introducing data from other individuals may dilute their influence, thereby reducing overall performance. An exception can be observed in the fact that, when using three trials from the test subject, performance appears to improve when an additional subject is included in the training set. This result, while representing an exception, indicates that, in some cases, the addition of another subject can bring improvements. Conversely, when subject-specific data are unavailable, the addition of inter-subject data likely enables the model to learn more generalisable patterns of activation. In this condition, performance improves with the number of training subjects, likely due to increased exposure to variability across individuals. Still, across all

conditions tested, the inclusion of even a small amount of data from the target subject consistently yielded better results than purely inter-subject training. These findings are consistent with recent literature on sEMG generalisation across users, reinforcing the importance of both personalised calibration and scalable generalisation strategies in muscle-computer interface design [417].

At this stage, it is worth considering a few aspects that influence how these insights should be interpreted. As detailed in Section 4.2.2, the amount of data per recording and per subject is highly consistent across the dataset, allowing a direct comparison between the number of subjects included and the total volume of training data. Each subject contributes approximately 20 minutes of data (five trials of 256 s each), while each additional trial from the test subject adds roughly 4 minutes. Consequently, increases in the number of training subjects correspond to proportional increases in total data. As illustrated in Figure 6.5, performance improves almost linearly with the number of training subjects, suggesting that a sufficiently large training pool could, in principle, allow inter-subject training to match or even surpass combinations that rely on limited subject-specific data. However, this relationship should be interpreted with caution. The linear trend observed is likely a local approximation of a nonlinear (most plausibly exponential) relationship that would prevent prediction errors from decreasing indefinitely. In other words, while additional subjects may continue to improve generalisation, performance gains are expected to plateau beyond a certain dataset size.

This saturation effect naturally raises the question of how to maximise the contribution of limited subject-specific data when refining a general model trained across multiple individuals. A practical solution to this challenge would enable real-world applications in which a pre-trained algorithm is rapidly personalised through short calibration sessions. One approach could involve increasing the weighting of subject-specific data during fine-tuning, ensuring that individual characteristics exert a stronger influence on model adaptation. However, this strategy alone may not fully exploit the complementarity between general and personalised datasets. Reinforcement learning could therefore be employed to refine a pre-trained supervised

model through reward-based feedback, accelerating adaptation while leveraging the strengths of both paradigms. Finally, personalisation might also be improved by transforming HD-sEMG data into circumferential activation representations, aligning general and individual data within a common feature space and further reducing the amount of data required for calibration.

In summary, the findings indicate that the RPC-Net/HDE-Array system still relies heavily on subject-specific data and does not consistently benefit from inter-subject learning when such data are available, thereby only partially confirming the fourth hypothesis of this study. Developing an effective inter-subject training protocol remains a crucial step towards real-time applications, as it could eliminate the need for subject-specific calibration and provide end users with a system ready for immediate use. Future work will pursue this objective by implementing and experimentally validating the strategies outlined above.

6.5 Conclusion

This study validated the performance of the RPC-Net/HDE-Array system under realistic conditions, where assumptions of consistent electrode placement and stable skin conditions no longer hold. The results demonstrate that, while the system is sensitive to such variability when unaccounted for, deliberately introducing it during training significantly enhances robustness. This supports the feasibility of using an initial training phase, based on motion tracking, to enable consistent control in subsequent sessions without retraining. The potential of inter-subject training to improve performance was also evaluated. While promising only in the absence of test-subject data, these results show that RPC-Net can generalise from multi-subject datasets to achieve satisfactory performance. Developing a robust protocol for effective inter-subject training remains an important goal. If achieved, it would reduce the amount of time-consuming subject-specific calibration, providing users with a ready-to-use interface for intuitive and natural control. While these findings represent an important step towards real-world application, several limitations remain. First, the number of subjects, especially for inter-subject analysis, was

limited. A broader and more diverse cohort is required to confirm generalisability. Second, the system has not yet been validated in closed-loop, real-time control settings using functional assistive devices. Third, the current protocol depends on an optical motion tracking system for generating ground-truth kinematics, which limits scalability. Finally, this study focused solely on feed-forward control; future implementations may benefit from integrating sensory feedback. Together, these results demonstrate the feasibility and potential of the RPC-Net/HDE-Array system for practical use in muscle-computer interfaces. By improving robustness, reducing calibration demands, and identifying paths towards full generalisation, this work advances the field towards intuitive, ready-to-use solutions that can meaningfully improve the quality of life for individuals with upper-limb impairments.

7

Real-Time Hand Kinematic Estimation with HD-sEMG and Artificial Neural Networks: Feasibility and Effects of Multi-Subject Training and Visual Feedback

7.1 Introduction

As discussed in previous chapters (Chapter 3-Chapter 6), device abandonment in upper-limb rehabilitation remains high due to persistent limitations in comfort, functionality, intuitiveness, and aesthetics. Growing evidence indicates that further progress depends less on mechanical improvements and more on advanced, adaptive control strategies, with HD-sEMG emerging as a promising non-invasive interface for capturing rich neuromuscular information [22, 57, 58, 65, 67, 69, 93, 104, 330, 341, 342, 373, 375, 376, 402, 407–409].

Two complementary solutions that address key limitations in current control systems were proposed and validated in previous chapters. First, a shallow neural network architecture, RPC-Net, capable of mapping HD-sEMG signals from the proximal forearm to continuous hand kinematics (Chapter 3), was developed. Second, a novel HDE-Array was introduced as an alternative to gel electrodes, and its

effectiveness was demonstrated when used in combination with RPC-Net (Chapter 4). Building on these developments, the robustness of the system under practical conditions was further evaluated, specifically examining its performance when electrode configurations varied between training and testing, and assessing the impact of multi-subject training on generalisation and control accuracy (Chapter 6).

While these results, and those of similar studies, are promising, further validation is essential to ensure applicability in real-world rehabilitation scenarios. A particularly critical and often overlooked aspect is the ability of subjects to use the developed systems for control applications. In much of the current literature, including the solutions described earlier in this manuscript, control solutions are evaluated based on how accurately they estimate output signals compared to ground truth. For example, in regression tests, systems are judged by how much the predicted output differs from the recorded value. Furthermore, training and testing datasets are often collected within the same session or during closely spaced sessions, with offline processing that requires substantial computational resources [418]. Although crucial as an initial benchmark, this offline evaluation overlooks the practical constraints of real-world deployment.

Real-time validation addresses this gap and represents a decisive step towards practical implementation [93, 238]. Validation of this type serves several essential functions. First, it verifies that the control pipeline is computationally efficient enough to operate on standard hardware in real time, without extensive offline processing. Second, it tests whether the training phase can be completed within a time frame compatible with clinical or at-home rehabilitation settings. Third, it directly addresses a fundamental part of real-life control: the dynamic interaction between the subject and the control system. This enables assessment of direct, task-oriented control behaviour rather than relying on post hoc reconstructions of recorded signals. This distinction is crucial, as online performance more accurately reflects how users interact with the device in daily life. In addition to these core advantages, real-time testing offers further benefits. First, it provides a more rigorous framework for assessing system robustness, particularly in the presence

of variations in the skin-electrode interface between training and testing [410–412]. Additionally, it enables evaluation of generalised training across users or recording sessions, addressing a key challenge highlighted in prior work [413, 414]. Finally, by placing the user directly in the control loop, real-time validation allows investigation of the effects of visual feedback on performance, an often overlooked but critical factor for the usability of prosthetic and rehabilitation technologies. Despite its clear usefulness, real-time validation remains rare and thus represents a common limitation in the literature even though, recently, this trend appears to be inverting [299, 300, 328, 418–420].

Building on the insights from the limitations identified in earlier studies, the present study aims to assess the real-time control capability of subjects using the RPC-Net/HDE-Array system, with a focus on three key factors: the relationship between online subject performance and the offline, user-independent accuracy of the system; the impact of generalised (inter-subject) training; and the influence of visual feedback during control. To this end, the following experimental hypotheses are tested:

1. Subjects can achieve real-time control performance with the RPC-Net/HDE-Array system that mirrors the offline, user-independent accuracy of the system
2. Generalised training using inter-subject data will yield lower performance compared to training on subject-specific data
3. The addition of visual feedback during online control will result in better performance of the system

To evaluate these hypotheses, a new dataset comprising HD-sEMG and hand-position data, segmented into training and testing phases, was acquired.

7.2 Materials and Methods

This section describes the instrumentation and software used in this study (Section 7.2.1) and the experimental procedures employed to assess the hypotheses (Section 7.2.2). All procedures followed the Declaration of Helsinki and received

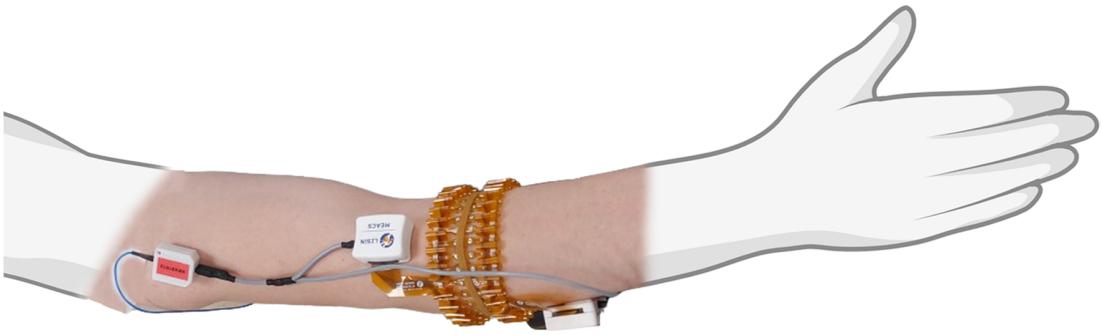

Figure 7.1: HDE-Array configuration: The array is shown wrapped around the forearm of the subject.

approval from the local ethics committee (CEP Unicamp, Approval Reference: 34583120.2.0000.5404). All data used in this study are available online [334].

7.2.1 Instrumentation

The MEACS amplifier, Vicon motion tracking system and software defined in Chapter 3 (Section 3.2.1) were used for this chapter, along with the HDE-Array defined in Chapter 4 (Section 4.2.1).

7.2.2 Experimental Protocol

These experiments aimed to assess the hypotheses defined in Section 7.1. The following subsections detail the data acquisition protocol, pre-processing pipeline, network training strategy, testing methodology, and performance evaluation metrics for RPC-Net.

Data

For this study, a single dataset was used, DS3 within the larger thesis-wide dataset [334]. DS3 comprises two sections: DS3.a, used in this study for training RPC-Net, and DS3.b, consisting of EMG data recorded along with the online hand position estimates produced by RPC-Net, which served the evaluation of real-time subject performance. DS3.a was also used for the study reported in Chapter 6.

DS3.a: Training Phase Data Acquisition

DS3.a comprises data acquired at the Department of Orthopaedics, Rheumatology, and Traumatology, State University of Campinas (SP, Brazil), from July to August 2024. Four right-handed healthy volunteers, reporting no surgical interventions on their dominant arm, participated in the study (S29-S32; age: 21 to 28 years; weight: 75 to 90 kg; height: 180 to 195 cm; forearm circumference: 22 to 30 cm). Written informed consent was obtained from all participants. Each subject completed two sessions of simultaneous HD-sEMG and hand kinematic data collection, both performed on the right arm. During the first session (DS3.a.s1), each subject completed six trials; in the second session (DS3.a.s2), they completed two additional trials, for a total of eight trials. During each trial, subjects performed 16 hand poses:

1. 4 wrist poses: flexion, extension, adduction, abduction
2. 8 finger poses: index finger metacarpophalangeal flexion and extension, index finger proximal interphalangeal flexion and extension, flexion and extension of the middle, ring, and little fingers, adduction and abduction of the index and middle fingers
3. 4 thumb poses: flexion, extension, adduction, abduction

Before the start of the first session, electrodes and markers were placed. Twenty-one reflective markers were positioned on the dominant hand (embedded in a glove), and 12 more on the upper limb and trunk, for a total of 33 markers (Figure 7.2). EMG was acquired using one SU connected to the proximal row of HDE-Array. This resulted in 32 dry electrodes arranged in a single row around the forearm, for a total of $N = 32$ monopolar EMG channels. An elastic band around the HDE-Array secured the device and improved skin contact. HDE-Array was placed so that the proximal electrode of column 1, as defined in Figure 7.2, was positioned at 30% of the distance between the lateral epicondyle and pisiform bone. The reference electrode was placed on the lateral epicondyle. A 10-second recording was performed to calibrate the Vicon system by instructing wrist movements. Each trial comprised 32 movements (16 poses, each repeated twice). Participants were seated with their dominant forearm on a vertical support at shoulder height. A monitor

prompted poses in random order every 8 seconds. Each trial lasted 260 seconds. To introduce variability in electrode positioning, the HDE-Array was removed and repositioned (following the same anatomical landmarks) between each trial. Additionally, to introduce variability in skin conditions, an abrasive gel was applied between trials 4 and 5 to reduce skin impedance. Trials 1 to 6 formed the first session (DS3.a.s1). After a break of less than thirty minutes, participants completed two more trials making up the second session, following the same experimental protocol. Electrodes were again repositioned between trials, though no further skin preparation was performed. These two trials constitute DS3.a.s2 and are referenced as such throughout the manuscript. The distinction between DS3.a.s1 and DS3.a.s2 is not relevant for this study. These trials were used to build the primary dataset (DS3.a) for training RPC-Net, as described in the following sections. Three to five days later, the acquisition of DS3.b took place. Since the acquisition of DS3.b relies heavily on the use of the trained RPC-Net, the training procedure for RPC-Net is first described, followed by the acquisition procedure for DS3.b.

Pre-processing: HD-sEMG and Kinematic Data

The objective of the pre-processing procedure is to transform the data acquired into suitable inputs for RPC-Net. Raw EMG signals were first converted from bits to volts, then offset-corrected, rectified, and transformed into RMS values using a sliding window of $w_l = 152$ samples (74 ms). The window slide w_s was 19 samples. Given an electromyographic signal that is L seconds long and N-dimensional, the output of the pre-processing procedure is $l = floor(\frac{L*f_s - w_l}{w_s}) + 1$ samples long and N-dimensional. The resulting RMS values were scaled by 10^{-4} to bring the data into a standardised range suitable for RPC-Net training, resulting in unit variance.

Vicon marker positions were processed using a moving average filter with a window length of 20 samples and subsequently mapped into a 29-dimensional joint-angle space using the IKA (Section 3.2.2). To prepare the joint-angle data for network training, rest angles were subtracted, and the resulting values were normalised by division by 45°; this centred the data at zero and yielded unit

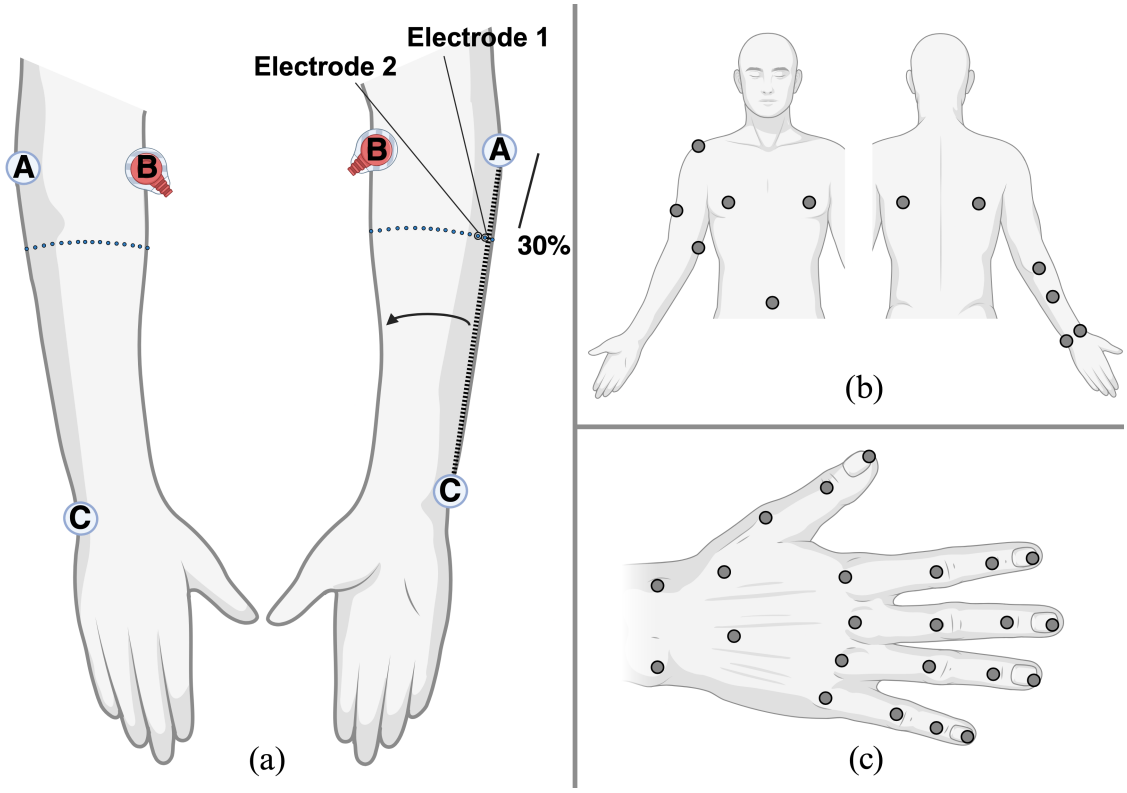

Figure 7.2: Subject setup: (a) HDE-Array placement around the forearm, showing the front and back views. Light blue dots represent electrode locations. The array is positioned at 30% of the distance between the lateral epicondyle and the pisiform bone. (b) Placement of 12 infrared markers on the body of the subject. (c) Placement of 21 infrared markers on the hand and two on the forearm, with each marker positioned proximally to a joint.

variance. Finally, linear interpolation aligned the sampling rates of the EMG and joint-angle data, ensuring synchronised, time-matched input-output pairs for RPC-Net training. Given an L-second-long signal, the output of the pre-processing procedure is $l = floor(\frac{L*f_s - w_l}{w_s}) + 1$ samples long and J-dimensional.

RPC-Net Training and Post-processing

RPC-Net, as defined in Chapter 3 (Section 3.2.2) is a neural network that estimates hand position from HD-sEMG signals acquired on the proximal forearm, refining estimates recursively based on prior values. The version of RPC-Net used in this study processes inputs from 32 EMG channels and 29 joint angles. Each sub-network, responsible for a specific joint angle, excludes its corresponding input channel, using the remaining 28 angles instead. This setup creates a robust recursive loop between

EMG signals and past angles. During training, actual joint angles replace past estimates. All training data were drawn from DS3.a, utilising the entire dataset without a train-test split, as testing was performed in a separate online session. RPC-Net versions were implemented in PyTorch.

On an Intel(R) Xeon(R) Platinum 8268 CPU (2.90 GHz), RPC-Net-32 achieved an average inference time of 1.3 ms (standard deviation: 0.2 ms) across 10^5 iterations. The network was trained with the Adam optimiser (in its PyTorch implementation), learning rate = $5{\cdot}10^{-4}$, $\varepsilon = 10^{-12}$, $\beta_1 = 0.9$, $\beta_2 = 0.99$; batch size = 2000; loss criterion = MSELoss. The model was trained for 50 epochs. For RPC-Net-G, 100 epochs were used for training, to account for more data.

Two versions of RPC-Net were considered:

- RPC-Net-S (RPC-Net-Subject Specific): Trained on data from individual subjects. Four separate instances of RPC-Net-S were created, one for each subject;
- RPC-Net-G (RPC-Net-Generalised): Trained on combined data from all four subjects, with equal weighting of data from each subject.

DS3.b: Testing Phase Data Acquisition

The testing (assessment) phase occurred three to five days after the training session and consisted of three parts, addressing the key components of this study. This phase resulted in the acquisition of DS3.b. The subjects who participated in the testing phase were the same individuals from the training phase. For all three parts, the HDE-Array was applied to the forearm in the same manner as during training, and subjects maintained the same seated position. Participants were prompted to perform seven hand movements: rest (R) and six specific movements (M1 to M6): index extension, three-finger extension, wrist extension, index flexion, three-finger flexion, and wrist flexion. Each prompt was displayed as a 3D hand skeleton (Figure 7.3). The MEACS system streamed HD-sEMG data, which were processed by BP in real time to compute RMS values over a 74 ms window (152 samples) updated every 74 ms. These RMS values were fed into a Python-based

application implementing either RPC-Net-S or RPC-Net-G (depending on the part), along with the FKA. The neural network produced estimates of joint angles, which were mapped into 3D marker positions by the FKA, and subsequently displayed next to the prompt. The setup achieved a refresh rate above 12 frames per second, comparable to similar studies [300]. Subjects were instructed to match the prompt to the network output as closely as possible, advancing to the next prompt at their discretion. On average, subjects spent 10.1 s ± 5.7 s per prompt ($n = 168$ prompts). A total of 14 prompts (7 movements × 2 repetitions) were presented in each part. Crucially, no motion tracking was conducted during testing. Instead, the ground truth for performance evaluation was defined by the hand positions prompted on the monitor. The key differences between the three parts involved the type of neural network employed and whether visual feedback was provided. RPC-Net-S (matched with each subject) was used in Parts 1 and 3, while RPC-Net-G was used in Part 2. In Parts 1 and 2, the real-time neural network output was shown alongside the prompt, whereas in Part 3, although the estimates given by the network were recorded in the background, the only reference provided to the subject was the target skeleton and they could not see RPC-Net-S output. To minimise bias, the study was conducted double-blind, and the order of Parts 1 and 2 was randomised. A representation of the acquisition interface is shown in Figure 7.4.

Online-Offline Comparison

To compare the online control performance of subjects using the RPC-Net/HDE-Array system and the regression accuracy of the system observed offline, data from the four subjects were also used to train and test RPC-Net-S offline. For this application, only data from DS3.a were used, and a five-to-one train/test split was employed. RPC-Net-S was trained using the specifications detailed in Section 7.2.2. For the testing data, target positions were derived from marker data recorded via the motion-tracking system during the corresponding trials. In contrast, estimated positions were computed in post-processing by RPC-Net using HD-sEMG signals acquired during those same trials. The analysis involved

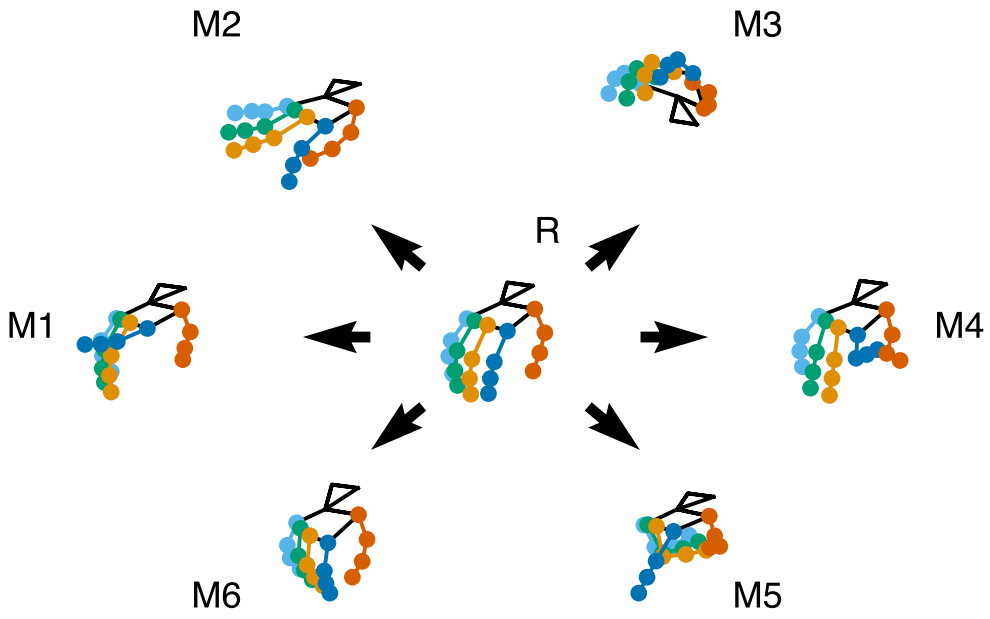

Figure 7.3: Prompted hand positions: Subjects were asked to produce the following poses: M1: index extension; M2: three-finger extension; M3: wrist extension; M4: index flexion; M5: three-finger flexion; M6: wrist flexion. The resting position (R) is shown in the centre.

comparing target positions with network estimates, following the protocol used in Chapter 4. This mirrors the conventional offline-validation paradigm used in prior literature. The set of four target-estimate pairs will be referred to as the Baseline Data throughout the remainder of the chapter.

Performance Assessment

The control performance of each subject was evaluated using two metrics: Mean Angular Distance (MAD) and Mean Global Distance (MGD). MAD evaluates angular accuracy, while MGD assesses spatial reconstruction precision, thereby quantifying how closely the participant could steer the device towards the target. Lower values for both metrics indicate better performance. To compute MAD, the online output of RPC-Net (29 joint angles over time) was extracted and the absolute difference between these estimated angles and the target angles at each time point was calculated. The resulting 29-dimensional time series was averaged into a single time-varying signal, A. A moving average (window 1 s; step 150 ms)

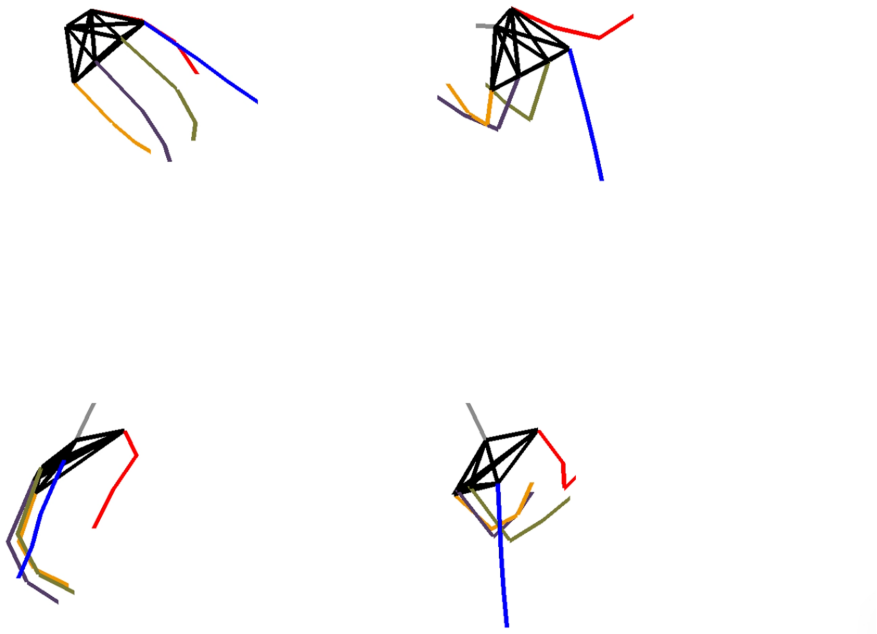

Figure 7.4: Visual interface for real-time testing: Visual feedback presented to the subjects during the testing phase. The two virtual hand skeletons on the right side of the monitor represent the target position, shown twice from different viewing angles to improve spatial clarity. On the left side of the monitor, the live output of the algorithm is displayed, also from two angles to help subjects better perceive its current state. During each trial, subjects were instructed to match the live output on the left to the target pose on the right as closely as possible. When visual feedback was removed, the left side of the monitor was left blank, while the rest of the interface remained identical.

was applied to produce a smoothed signal, B. The minimum value of B for each of the 7 movements was recorded as the MAD for that specific subject-movement-part combination, representing the best alignment achieved during the attempt. MGD was computed similarly. First, the 29 output angles from RPC-Net were converted into 3D marker positions using the FKA. The same conversion was applied to the target joint angles, producing corresponding 3D target marker positions. Distances over time between the estimated and target marker positions were averaged into a time-varying signal, A. A moving average was then applied, yielding a smoothed signal, B. The minimum value of B for each movement was recorded as the MGD for that subject-movement-part combination. For Baseline Data, modifications were made due to its non-task-oriented nature. MAD and MGD were averaged across the entire time-varying signal A (computed as the absolute difference between estimated angles and the target angles at each time point), rather than extracting minima, to

reflect the different experimental design, thus providing a pure regression-accuracy benchmark. In the case of Baseline Data, a single MAD and MGD value was computed for each subject, without a movement-specific breakdown.

It is worth noting that, in previous chapters, the performance of the RPC-Net/HDE-Array system was quantified using MD and MPCC, which capture average spatial and temporal correspondence between estimated and target trajectories, while in the present chapter and the following one, performance is instead expressed through MGD and MAD, which reflect the best performance across a trial. This shift reflects the different nature of the experiments and their objectives, and is justified by three considerations:

1. Metrics based on minimum distance or best task achievement provide a closer correspondence with those commonly reported in related real-time control studies, facilitating direct comparison with the literature [300].
2. Measures such as MGD and MAD, which focus on the best alignment reached during a trial rather than on average similarity across its duration, are better suited to task-oriented protocols like the one employed here.
3. Whereas the earlier chapters primarily assessed the intrinsic accuracy of the algorithm itself, the present and following studies evaluate the ability of subjects to operate the system effectively.

In synthesis, metrics reflecting the ultimate task achievement of the participant offer a more meaningful representation of control performance than those capturing continuous trajectory similarity.

Hypothesis Testing

Three hypotheses were tested to evaluate the performance of subjects using the RPC-Net/HDE-Array system under varying conditions:

1. Subjects can achieve real-time control performance with the RPC-Net/HDE-Array system that mirrors the offline, user-independent accuracy of the system : To test whether real-time performance of subjects matches offline performance, data from Part 1 of the testing phase were compared with Baseline Data.

MGD and MAD values observed in Part 1 of the testing phase were grouped by movement (M1-6 and R), yielding four data points per movement. These were displayed on a plot along with the mean across subjects for each movement. The same values were also grouped by subject and displayed along with the mean across movements. For comparison, the MGD and MAD were computed for each subject in the Baseline Data, and the mean and range of these values were displayed in the same plots. This qualitative evaluation aimed to determine whether subjects, when using RPC-Net in real time, could replicate the offline accuracy benchmark.

2. Generalised training using inter-subject data will yield lower performance compared to training on subject-specific data : It was assessed whether control performance of subjects differs when operating a network trained on their own data (RPC-Net-S) versus a network trained on pooled multi-subject data (RPC-Net-G). Using data from Part 1 and Part 2 of the testing phase, a Wilcoxon signed-rank test was applied to compare the distributions of seven movement-specific MGD values (and similarly MAD values) obtained under both conditions for each subject. The null hypothesis, H_0, states that the difference in MGD and MAD between the paired observations (RPC-Net-S minus RPC-Net-G) is symmetric about $\mu = 0$. The alternative hypothesis, H_1, is that this difference is symmetric about $\mu > 0$. To justify the use of the Wilcoxon signed-rank test, it was assumed that the performance in each of the seven tasks was independent, thereby satisfying the requirement of the test for independent samples. The same statistical comparison was also performed using the mean across all movements for each subject under the two conditions, resulting in a second Wilcoxon signed-rank test conducted on eight total data points (four per condition). A paired t-test was not used due to the small sample size and the absence of normality in some distributions, as confirmed by the Shapiro-Wilk test.
3. The addition of visual feedback during online control will result in better performance of the system : To assess the effect of visual feedback on control

accuracy of subjects, a similar analysis to that described in the previous point was conducted, but compared Part 1 and Part 3 of the testing phase instead. This resulted in a new definition of difference between paired observations (no-feedback minus feedback). Under the alternative hypothesis, H_1, this difference was assumed to be symmetric about $\mu < 0$.

7.3 Results

This section presents the findings from the assessments described in Section 7.2.2. It includes an analysis of the real-time performance of subjects using the RPC-Net/HDE-Array system compared to offline, user-independent performance of the system. It also compares subject-specific (RPC-Net-S) with generalised (RPC-Net-G) training, and evaluates performance with and without visual feedback.

7.3.1 Real-time vs. Offline Performance

Figure 7.5 shows the values of MGD and MAD achieved by the subjects for the six movements considered and rest, using RPC-Net-S with visual feedback. Each data point represents the value for a single subject-movement combination. The subject-wise mean MGD is consistently below 45 mm, and the mean MAD is below 15°. Mean values per movement appear in Table 7.1. The same figure also shows the data grouped by subject, with mean values reported in Table 7.2 (RPC-Net-S column). The mean and range of 4 subject-specific MGD and MAD values observed in the Baseline Data (representing offline, user-independent performance of RPC-Net) are also displayed in both plots: mean MGD equals 25.7 mm (range 4.5 mm) and mean MAD is 8° (range 4°).

7.3.2 Subject-specific vs. Generalised Training

Figure 7.6 shows results of the comparison between the performance of subjects when using RPC-Net trained on a single subject (RPC-Net-S) and when trained on pooled data from all subjects (RPC-Net-G). The respective group-wide means observed were 34.7 mm and 33.0 mm for MGD and 11° and 10° for MAD. The

Table 7.1: Subject performance with RPC-Net-S

Movement	MGD (mm, Range)	MAD (°, Range)
Index Extension	38.7 (29.4-50.7)	12 (7-13)
3-finger Extension	38.8 (22.1-49.6)	12 (9-14)
Wrist Extension	28.9 (12.9-43.6)	12 (9-15)
Index Flexion	48.4 (35.1-60.7)	14 (12-17)
3-finger Flexion	30.7 (17.2-39.2)	13 (7-17)
Wrist Flexion	30.5 (23.3-45.7)	9 (8-10)
Rest	26.7 (17.9-40.1)	7 (6-8)

Mean MGD and MAD across subjects for each movement with RPC-Net-S and visual feedback. Range is included.

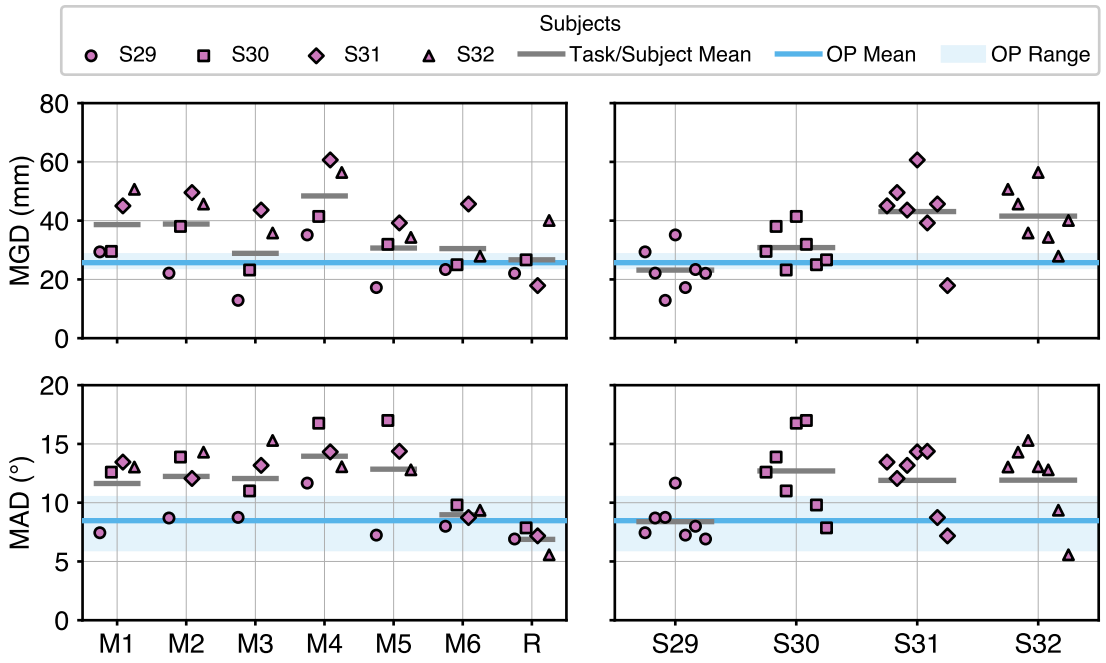

Figure 7.5: Movement-wise real-time performance results: Including comparison with offline results. (Left:) Mean MGD and MAD for each subject across six movements and rest. For comparison, mean and range for the offline user-independent benchmark (OP) are overlaid. (Right:) The same data grouped by subject. Movements retain the left-to-right order within each subject.

Wilcoxon signed-rank test result, where the null hypothesis is that the difference between paired observations (RPC-Net-S minus RPC-Net-G) is symmetrical about $\mu \leq 0$, returned a p-value of 0.31 for MGD and 0.19 for MAD, indicating that the

Table 7.2: Performance comparison between RPC-Net variants

	MGD (mm, Range)		
S	RPC-Net-S	No Feedback	RPC-Net-G
S29	23.2 (12.9-35.1)	22.4 (11.4-42.5)	27.7 (11.7-45.8)
S30	30.8 (23.2-41.4)	39.1 (25.9-54.8)	27.2 (14.5-52.1)
S31	43.1 (17.9-60.7)	42.9 (11.2-70.2)	40.8 (7.6-105.3)
S32	41.5 (27.9-56.4)	37.8 (20-47.5)	36.3 (9-96.1)
All	34.7 (12.9-60.7)	35.6 (11.2-70.2)	33.0 (7.6-105.3)
	MAD (°, Range)		
S	RPC-Net-S	No Feedback	RPC-Net-G
S29	8 (7-12)	8 (5-10)	10 (4-15)
S30	13 (8-17)	14 (10-19)	9 (6-15)
S31	12 (7-14)	12 (6-16)	11 (4-16)
S32	12 (6-15)	11 (4-14)	11 (5-15)
All	11 (6-17)	11 (4-19)	10 (4-16)

Performance of subjects using RPC-Net-S and RPC-Net-G, with and without feedback. Mean and range across subjects are included.

null hypothesis could not be rejected for either metric. For subject-wise tests, the p-values for the same hypothesis were 0.85, 0.11, 0.15 and 0.19 for MGD; and 0.89, 0.01, 0.11 and 0.08 for MAD (in participant order). The mean values observed for all subjects in different conditions are reported in Table 7.2.

7.3.3 Influence of Visual Feedback

Figure 7.7 shows results of the comparison between the performance of subjects when using RPC-Net with and without visual feedback. The respective means observed across subjects were 35.6 mm and 34.7 mm for MGD and 11° and 11° for MAD. The Wilcoxon signed-rank test result, where the null hypothesis is that the difference between paired observations (no feedback minus feedback) is symmetrical about $\mu \geq 0$, returned a p-value of 0.44 for both measures, indicating that the null

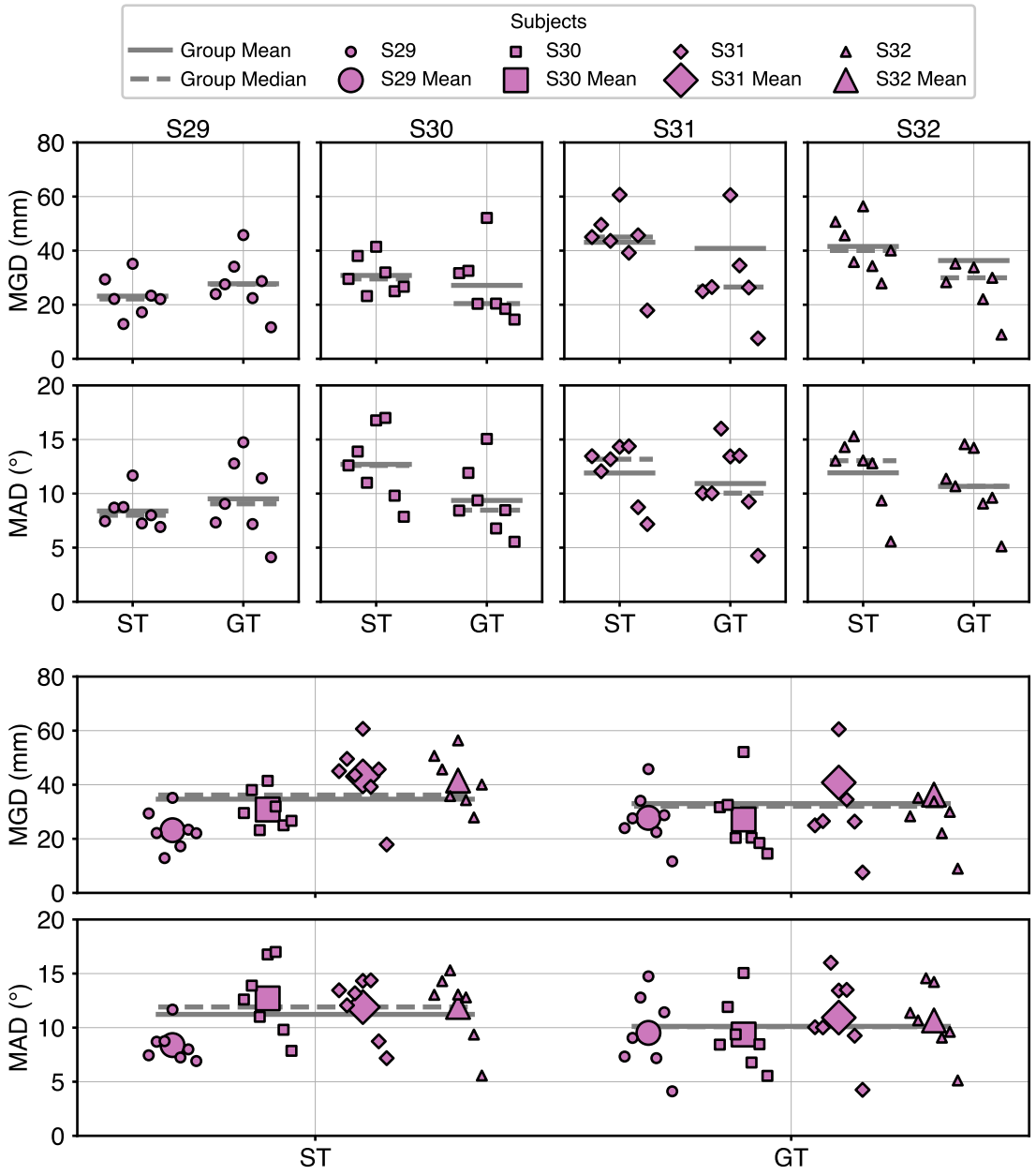

Figure 7.6: Comparison between specific and generalised testing: (Top:) inter-subject comparisons. Wilcoxon signed-rank test results for MGD (H_0: $ST_i - GT_i$ symmetric about $\mu = 0$, H_1: $ST_i - GT_i$ symmetric about $\mu > 0$); S29: $W = 8$, $p = 8.5{\cdot}10^{-1}$; S30: $W = 22$, $p = 1.1{\cdot}10^{-1}$; S31: $W = 21$, $p = 1.5{\cdot}10^{-1}$; S32: $W = 20$, $p = 1.9{\cdot}10^{-1}$. Wilcoxon signed-rank test results for MAD: S29: $W = 7$, $p = 8.9{\cdot}10^{-1}$; S30: $W = 28$, $p = 7.8{\cdot}10^{-3}$; S31: $W = 22$, $p = 1.1{\cdot}10^{-1}$; S32: $W = 23$, $p = 7.8{\cdot}10^{-2}$. (Bottom:) movement-wise means across all subjects. Wilcoxon signed-rank test results for MGD (H_0: $ST_i - GT_i$ symmetric about $\mu = 0$, H_1: $ST_i - GT_i$ symmetric about $\mu > 0$): $W = 7$, $p = 3.1{\cdot}10^{-1}$. Wilcoxon signed-rank test results for MAD: $W = 8$, $p = 1.9{\cdot}10^{-1}$. Mean and median of the distributions are included. GT: Generalised Testing; ST: Specific Testing.

hypothesis could not be rejected. For individual subjects, the p-values for the same hypothesis were 0.47, 1, 0.19 and 0.11 when considering MGD as a performance measure and 0.19, 0.99, 0.53 and 0.08 when considering MAD. The mean values observed for all subjects in different conditions are reported in Table 7.2.

7.4 Discussion

The results from the previous section demonstrate that subjects using the RPC-Net/HDE-Array system achieve robust control of a virtual hand model under conditions that closely approximate real-life scenarios, successfully addressing the limitations identified previously. This study aimed to validate three experimental hypotheses about subject control performance under varying conditions.

The first hypothesis stated that subjects could achieve real-time performance with the RPC-Net/HDE-Array system comparable to the offline, user-independent accuracy previously reported. As shown in Section 7.3.1, MGD remained consistently below 50 mm for both individual movements and subjects, and below 60 mm even for outliers. Similarly, no mean MAD value exceeded 15° and no individual trial exceeded 20°. Although these results are promising, they do not replicate the pure regression accuracy achieved offline by RPC-Net on the same dataset, where the mean MGD and MAD were 25.7 mm (range 4.5 mm) and 8° (range 4°), respectively. As shown in Figure 7.5, only Subject S1 achieved performance within the offline range, while other subjects did so only during rest. Nonetheless, the observed values are comparable to those reported in state-of-the-art studies on EMG-based online control [300, 328, 421].

To interpret these findings, two key aspects merit further discussion. First, as outlined in Section 2.3.1, "perfect" control was defined as achieving outputs within 1-2 mm (or approximately 1-2°) of the target, corresponding to the perceptual resolution of the human sensorimotor system, while "high-quality" control referred to performance within a few millimetres or degrees of that limit. The present results show that no individual value fell below 10 mm and only a minority below 20 mm. Thus, while the system achieves functionally usable and state-of-the-art

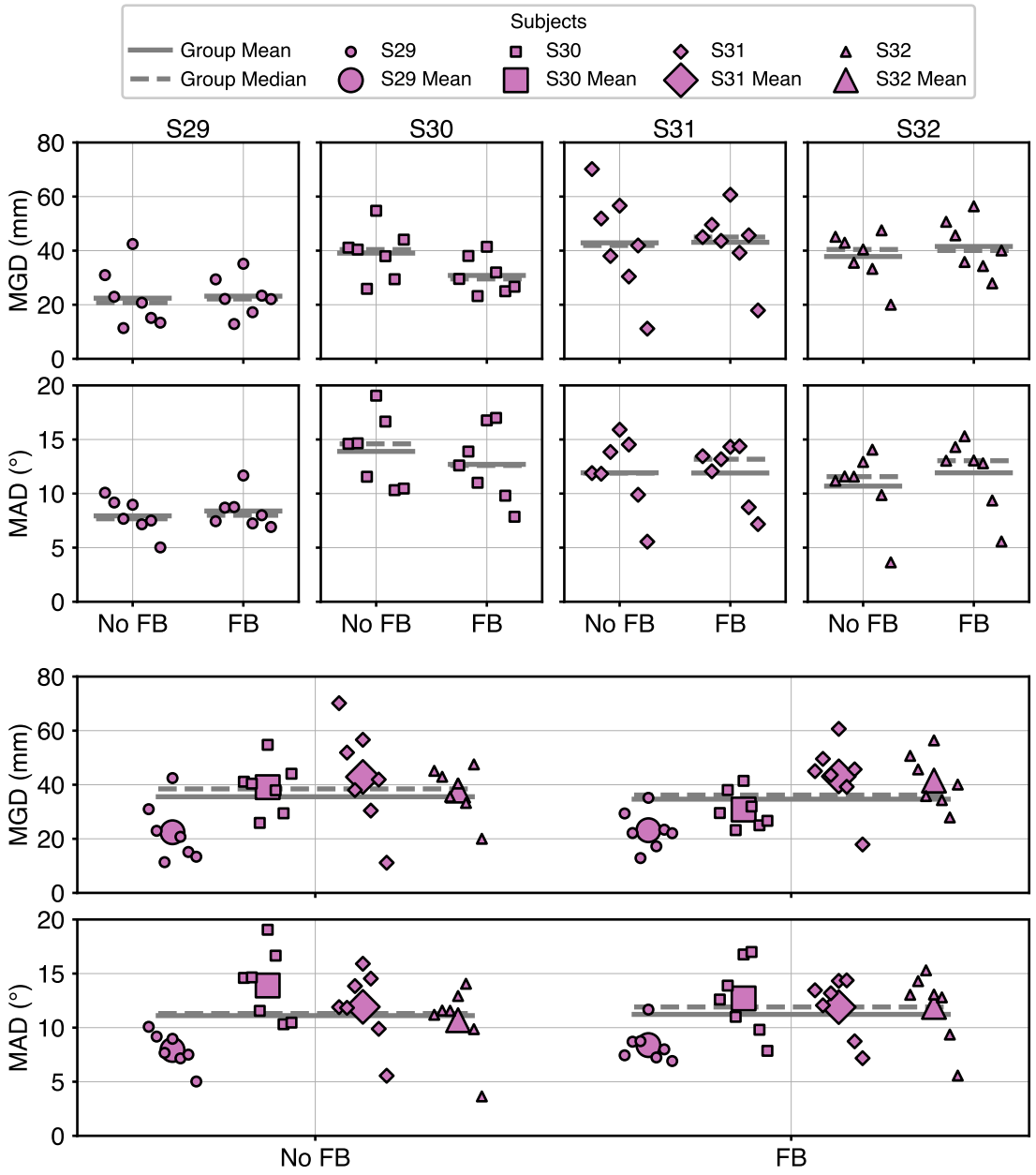

Figure 7.7: Comparison between testing with and without feedback: (Top:) inter-subject comparisons (Wilcoxon signed-rank). Wilcoxon signed-rank test results for MGD (H_0: $NoFB_i - FB_i$ symmetric about $\mu = 0$, H_1: $NoFB_i - FB_i$ symmetric about $\mu < 0$); S29: $W = 13$, $p = 4.7{\cdot}10^{-1}$; S30: $W = 28$, $p = 1.00{\cdot}10^{0}$; S31: $W = 8$, $p = 1.9{\cdot}10^{-1}$; S32: $W = 6$, $p = 1.1{\cdot}10^{-1}$. Wilcoxon signed-rank test results for MAD: S29: $W = 8$, $p = 1.9{\cdot}10^{-1}$; S30: $W = 27$, $p = 9.9{\cdot}10^{-1}$; S31: $W = 14$, $p = 5.3{\cdot}10^{-1}$; S32: $W = 5$, $p = 7.8{\cdot}10^{-2}$. (Bottom:) movement-wise means across all subjects. Wilcoxon signed-rank test results for MGD (H_0: $NoFB_i - FB_i$ symmetric about $\mu = 0$, H_1: $NoFB_i - FB_i$ symmetric about $\mu < 0$): $W = 4$, $p = 4.4{\cdot}10^{-1}$. Wilcoxon signed-rank test results for MAD: $W = 4$, $p = 4.4{\cdot}10^{-1}$. Mean and median of the distributions are included. FB: Feedback; No FB: No Feedback.

performance, it remains below the level of perceptual indistinguishability from natural movement. Second, latency represents a critical factor for naturalistic, closed-loop control. The end-to-end delay of the current RPC-Net/HDE-Array configuration is approximately 75 ms, corresponding to the update rate of the processed RMS signals. This delay originates primarily from the amplifier interface, which transmits RMS values at 15 Hz despite sampling internally at 2 kHz, whereas the inference time of the network is negligible (<2 ms). Although this 75 ms latency exceeds the 30-50 ms range often cited as optimal for intuitive prosthetic control [304, 313], it remains well below the 200 ms perceptual threshold for real-time interaction. Consequently, the system already operates within the acceptable range for natural sensorimotor feedback, and further optimisation of the acquisition interface could bring latency closer to the ideal range.

Taken together, these results do not suggest that subjects were unable to achieve successful control using the RPC-Net/HDE-Array system. Rather, they indicate that introducing the human operator into the control loop inherently introduces additional variability compared to purely offline regression. The encouraging outcome is that this additional variability remains within both the predefined performance threshold and the range reported in contemporary literature. These findings therefore support the feasibility of accurate, real-time multi-DoF control with the RPC-Net/HDE-Array system, even if the first hypothesis is not strictly confirmed.

The second hypothesis proposes that subject performance decreases when the network is trained on pooled data from all subjects rather than on individual-subject data. The results indicate that, when data from all subjects were combined, the null hypothesis of the Wilcoxon signed-rank test could not be rejected for both the MGD and MAD metrics ($p = 0.31$, $p = 0.19$). It is important to note that, given the small sample size, the Wilcoxon signed-rank test has very low power, thereby increasing the likelihood of false negatives. At the individual-subject level, a p-value below the significance threshold ($\alpha = 0.05$) was observed only for MAD in S2, the sole indication of improved performance when using a network trained on multiple subjects. At the same time, the results of the statistical tests performed indicate

that the null hypothesis of equality, under the less conservative two-tailed test, could be rejected in that case only. In summary, no significant difference was detected between training strategies. A performance disadvantage for a network trained on a pool of subjects can therefore be ruled out, meaning that the second experimental hypothesis is not supported. These results are in line with what is observed in the relevant literature and in Chapter 6 [413–415]. The quality of performance is expected to increase with a larger pool of subjects, as the generalisation strength of RPC-Net-G is expected to increase with a broader training population.

The third hypothesis posited that performance would improve with the addition of visual feedback. Contrary to expectation, results across all participants showed no significant effect of feedback ($p = 0.44$ for both metrics), and no individual participant exhibited a significant improvement. Inspection of raw trajectories confirmed that movement patterns, task durations, and correction behaviour remained highly similar across feedback conditions, suggesting that subjects did not meaningfully alter their interaction strategy when visual feedback was provided. These findings imply that the addition of visual feedback did not measurably enhance control quality, thereby not supporting the third hypothesis. This observation contrasts with several prior studies reporting performance gains from visual or electrotactile feedback [422–425]. A number of factors may explain this discrepancy. First, the present task was highly structured and trained under conditions that closely mirrored the testing setup, potentially reducing the marginal benefit of visual information. Second, the non-feedback condition was always performed second, possibly introducing a mild learning or carry-over effect that masked subtle improvements. Third, it is possible that the output dynamics of the system, particularly the inherent difficulty of proportionally controlling a multi-DoF continuous signal, limited the utility of visual cues for online correction. Future work should therefore include counterbalanced or randomised feedback order and task designs specifically aimed at isolating adaptation behaviour. Examining the detailed evolution of MGD and MAD over time, rather than their global averages, may also clarify whether subjects gradually refine their internal control strategies

with or without feedback. Nevertheless, the present results indicate that the RPC-Net/HDE-Array system remains robust even in the absence of visual feedback, an encouraging property for potential clinical or at-home deployment where feedback may not always be available.

7.5 Conclusion

This study validated the RPC-Net/HDE-Array system for online control by evaluating subject performance in control tasks. Real-time performance was comparable to, though lower than, offline benchmarks and similar to values reported in related studies. Furthermore, the influence of visual feedback and inter-subject training on performance was assessed, concluding that no significant deterioration was observed when comparing pooled-data with subject-specific models, and that visual feedback did not significantly affect control quality. These findings suggest that HDE-Array, combined with RPC-Net, offers a viable online control solution, potentially providing a novel control system for prosthetic and other rehabilitation applications. The findings also reinforce earlier evidence on generalised learning. Future work should include real-world validation with prosthetic devices and functional electrical stimulation, investigate how sample size and inter-subject variability influence performance, and extend the framework beyond the proximal forearm to address additional impairments (e.g., tetraplegia, trans-humeral amputation). Overall, the HDE-Array/RPC-Net system shows strong promise for enhancing user experience across a broad range of biomedical-engineering applications.

8

HD-sEMG-Based Control Using Neck Muscles and Shallow Neural Networks: Assessing Performance in Rehabilitation-Oriented Tasks

8.1 Introduction

Cervical-level SCIs, which often result in the loss of upper limb function, were reported at a rate of 10.7 per 100,000 individuals in the High-Income super region as of 2020 [33, 370, 371]. The loss of upper limb functionality profoundly impacts overall quality of life, highlighting the urgent need for advanced rehabilitation strategies [56]. FES, first developed in the 1960s, is a well-established technique that uses electrical stimuli to induce muscle contractions, enabling controlled limb movements with numerous applications for restoring upper limb functionality [149, 426–431]. Depending on the degree and phase of impairment, FES can be employed as a therapeutic intervention, as temporary support during rehabilitation, or as a permanent replacement for lost motor functions through assistive devices known as neuroprostheses. Extensive research has demonstrated the therapeutic efficacy of FES for individuals with SCIs or strokes [426, 432–435]. Recent studies have also highlighted the benefits and functionality of neuroprostheses as permanent

rehabilitative tools [436, 437]. Compared to exoskeletons, neuroprostheses offer a more natural solution by eliminating the need for external mechanical devices. FES has shown significant promise in improving the quality of life for individuals with cervical SCIs, enabling them to perform activities of daily living with minimal assistance and fostering greater independence [438, 439].

While advancements in FES delivery and accessibility for therapeutic purposes have been significant, progress in control methodologies has lagged behind. To enable user independence, operation with minimal assistance should be possible, ideally leveraging residual muscle functions under voluntary control, such as those in the neck or shoulders, depending on the level of impairment [440, 441]. Despite efforts to simplify control systems and training procedures, current clinical applications often require professional operation of FES devices [433, 442–446]. Moreover, the pace of development for control solutions in permanent implants has slowed in recent years [437, 447]. Notably, state-of-the-art solutions are frequently met with user dissatisfaction [448–451].

Among the most promising strategies to overcome control-related limitations is sEMG, a non-invasive technique for detecting residual voluntary muscle activity. sEMG-based systems enable intuitive, online control of assistive devices, such as FES systems, without the need for external assistance by harnessing muscle signals from spared regions of the body. This approach is particularly attractive for individuals with high-level SCIs, as large voluntary muscles such as the sternocleidomastoid and trapezius are innervated by cranial nerves and therefore remain controllable even in cases of very rostral lesions. Recent studies have shown that sEMG can be successfully integrated into FES control systems, including in applications for individuals with tetraplegia, providing a foundation for more autonomous and user-friendly neuroprosthetic control in both long-term and therapeutic settings [452–454]. However, sEMG-controlled FES systems still face several notable challenges. First, they often rely on outdated hardware for EMG acquisition and legacy software for real-time processing, resulting in user discomfort, poor usability, and suboptimal output quality. Second, most studies validating EMG-based approaches focus on

simple tasks, often assessed using Fitts' law, while overlooking more complex motor functions critical for real-time control, such as the manipulation of simulated limbs. These limitations reduce both the practical applicability and user acceptance of such systems, thereby hindering their integration into daily use [447, 455, 456]. Importantly, many of these issues are not exclusive to FES control strategies, but are common across a broad range of rehabilitation devices.

To address these challenges in systems controlled via residual upper limb EMG activity, a solution based on HD-sEMG signals acquired from the forearm of healthy subjects was previously developed and validated: the RPC-Net/HDE-Array system. Although originally intended for prosthetic control, this system addresses many of the same limitations encountered in FES applications. Both domains require intuitive, robust, and responsive user interfaces for online motor control, and face similar issues, including outdated EMG acquisition hardware, limited real-time performance, and poor user comfort. The software component, RPC-Net, was designed to overcome common control algorithm shortcomings, such as instability during online use and sensitivity to signal variation. The hardware component, HDE-Array, complements this by enhancing user comfort, ensuring signal consistency, and improving the overall practicality of EMG acquisition (see Chapters 3 and 4). Subsequent studies confirmed the reliability of the system in online settings, its robustness to electrode displacement and changes in skin condition, and its compatibility with simplified kinematic models (Chapters 5, 6, and 7).

Given the parallels between prosthetic control using residual forearm muscle activity and FES control via neck muscles, and in light of the proven effectiveness of the RPC-Net/HDE-Array system in the former domain, this study aims to evaluate the applicability of the system in the latter. The overarching goal is to develop a comfortable, efficient, and cost-effective solution for accurate FES control in both therapeutic and long-term contexts for tetraplegic subjects. To this end, the suitability of the integrated RPC-Net/HDE-Array system was assessed in the execution of two multi-DoF control tasks, selected as proxies for, and preliminary validation of, control over a multi-site FES system. These tasks were performed by

both healthy and tetraplegic participants to evaluate the relevance of the system for the target population with impaired motor functions. Guided by these aims, the study tests the following hypotheses:

1. Subjects can control a hand kinematic model in real time using neck muscles and the RFC-Net/HDE-Array system, achieving task performance comparable to that observed with forearm muscle control
2. Performance in controlling the hand kinematic model using head and neck muscles, is comparable between tetraplegic and healthy subjects
3. Subjects can successfully use the RFC-Net/HDE-Array system to control three independent cursors in a task-oriented experiment, with 1 DoF per cursor
4. Performance in the cursor-based task is comparable between healthy and tetraplegic subjects

Demonstrating the potential of this system for intuitive multi-site control could contribute to a practical and scalable solution for both short-term therapeutic use and long-term neuroprosthetic applications. To test these hypotheses, a new dataset based on the two tasks was acquired and compared against data from a previous study.

8.2 Materials and Methods

This section details the instrumentation and software used in the study (Section 8.2.1), as well as the experimental procedures implemented to evaluate the stated hypotheses (Section 8.2.2). All procedures were conducted in accordance with the Declaration of Helsinki and approved by the local ethics committee (CEP Unicamp, Approval Reference: 34583120.2.0000.5404). All data used in this study are available online [334].

8.2.1 Instrumentation

The MEACS amplifier and software defined in Chapter 3 (Section 3.2.1) were used for this chapter, along with the HDE-Array defined in Chapter 4 (Section 4.2.1).

For the neck application, the only modification in the HDE-Array configuration was the adjustment of the embedded elastic band to ensure a secure but comfortable fit.

8.2.2 Experimental Protocol

The objective of the experiments was to assess the hypotheses defined in Section 8.1. The following subsections detail the data acquisition protocol, pre-processing pipeline, network training strategy, testing methodology, and performance evaluation metrics for RFC-Net.

Data

Two datasets were used in this study, labelled as DS3 and DS4 within the larger thesis-wide dataset [334]. DS3 was acquired for the study described in Chapter 6 and also used for the study reported in Chapter 7 of this thesis, while DS4 was acquired specifically for this study. For clarity and conciseness, the data collection and processing procedures used for DS4 are described in their entirety, while a summary only of the data acquisition procedure for DS3 is included. DS4 comprises three parts: a training phase (DS4.a) and two online testing phases (DS4.b.s1 and DS4.b.s2). DS4.a was used to train RFC-Net, while DS4.b.s1 and DS4.b.s2 include EMG data and corresponding RFC-Net online outputs recorded during a testing phase, enabling evaluation of the system under test conditions. A thorough description of DS3 acquisition procedures is provided in the relevant chapters.

DS4.a: Training Phase Data Acquisition

For the acquisition of this dataset, 10 tetraplegic (P1-P10) and 8 healthy participants (P11-P18) (age: 21-40 years; weight: 65-90 kg; height: 165-195 cm; neck circumference: 30-40 cm) were recruited. Data collection was conducted at the Department of Orthopaedics, Rheumatology, and Traumatology, State University of Campinas (SP, Brazil), from July to August 2024. All tetraplegic subjects had cervical spinal lesions at the C5 or C4-C5 level. Written informed consent was obtained from all participants. Each subject completed a single trial during the training phase. During this trial, HD-sEMG signals were recorded from the neck

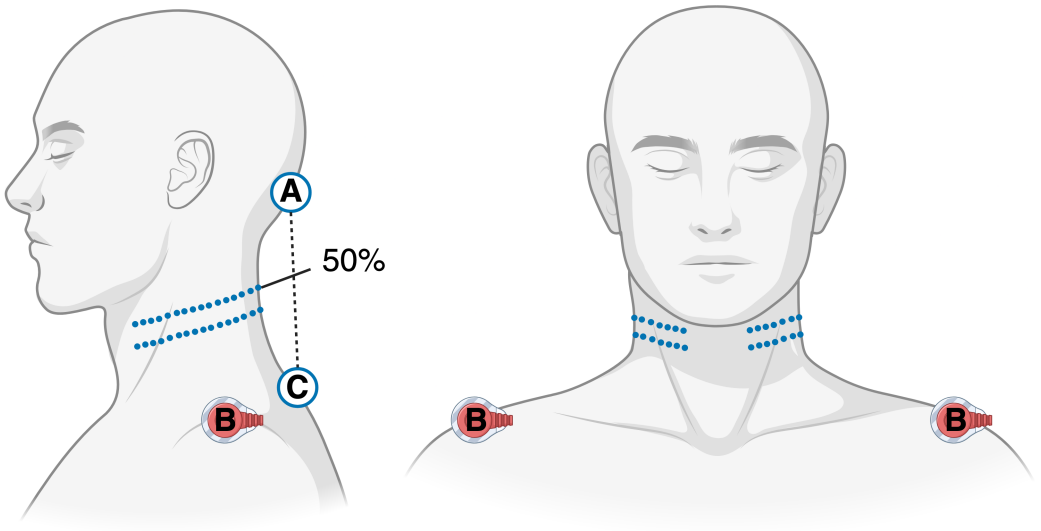

Figure 8.1: Electrode placement: HDE-Array placement around the neck, showing the front and side views. Blue dots represent electrode locations. The array is positioned at 50% of the distance between the vertebra prominens (C) and the inion (A).

while subjects performed a sequence of motor tasks. Prior to recording, participants were seated, and the HDE-Array was positioned and connected to two MEACS SUs. The array, composed of 64 dry electrodes arranged in two circumferential rows, was placed around the neck with a gap over the trachea. The rostral row of electrodes was aligned at 50% of the distance between the inion and the vertebra prominens (points A and C in Figure 8.1). Reference electrodes were placed on the left and right acromia, one per SU (point B in Figure 8.1).

The protocol included 13 distinct motor tasks, each defined by direction, sense, and magnitude.

- Direction was classified as: (1) F: neck flexion/extension (sagittal plane), (2) L: lateral flexion (coronal plane), and (3) R: rotation (transverse plane).
- Sense was labelled as positive (flexion, right lateral flexion, right rotation, indicated with a + sign) or negative (extension, left lateral flexion, left rotation, indicated with a - sign).
- Magnitude was set to either 1 or 2.

The definition of magnitude using discrete values represents a clear departure from the continuous scaling adopted in the first four experimental chapters of this

thesis, but remains consistent with the approach implemented in the previous chapter (Chapter 7). As with the shift in performance measures described in Section 8.2.2 and Section 7.2.2, this methodological change reflects the different nature of the present experiments, which are task- and subject-oriented rather than focused on evaluating algorithmic accuracy over large datasets. For these experiments, defining magnitude as a limited set of discrete targets provided clearer instructions for participants and yielded more repeatable and comparable data across trials and subjects.

An additional rest condition was also included as a baseline task. Each trial consisted of 32 tasks, with each combination of direction, sense, and magnitude presented twice and the rest task repeated eight times. The sequence was randomised. Visual prompts were displayed on a monitor, each lasting 15 seconds (see Figure 8.2). Participants indicated readiness before each prompt; execution began when confirmed. Idle periods between tasks lasted 1-10 seconds, resulting in total trial durations ranging from 8 to 12 minutes. The diversity of tasks enabled robust decoding across neck movement types. After the training trial, the HDE-Array remained in place for the subsequent testing phase while the HD-sEMG signals, together with task labels, were pre-processed and used to train RFC-Net on a per-subject basis.

HD-sEMG Pre-processing

Following the acquisition of training data, the objective of this procedure was to train RFC-Net to estimate continuous neck movement trajectories in the three anatomical directions defined in the experimental protocol, using HD-sEMG signals. Initial HD-sEMG pre-processing was conducted in real time using BP software. Raw signals were converted from bits to volts, offset-corrected, rectified, and transformed into RMS values using a 307-sample (150 ms) sliding window with no overlap. These data were temporarily cached and later used for network training. RMS values were scaled by a factor of 10^4 to standardise input variance and mean. The resulting signals served as the input to RFC-Net during training. The training labels consisted of a three-element array, where each element represented the signed magnitude of

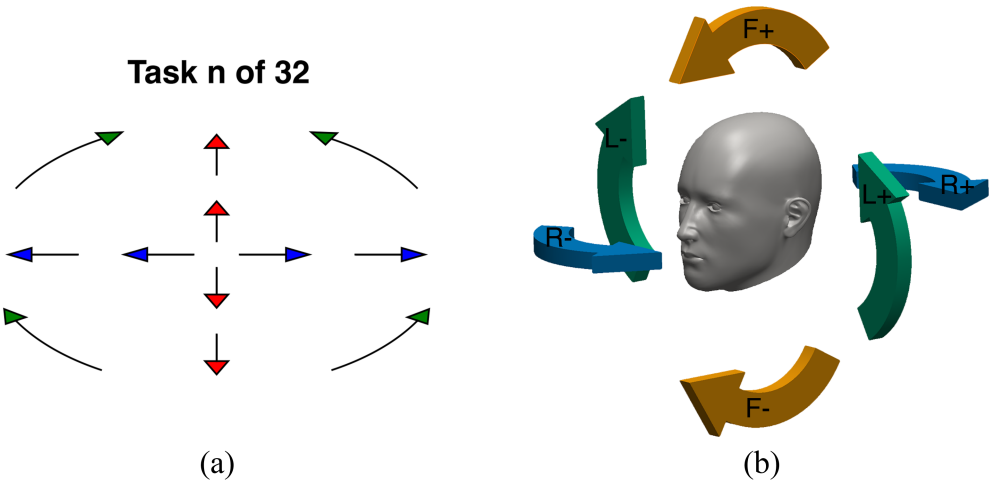

Figure 8.2: Directions of movement and corresponding labels: (a) Overlap of visual prompts shown in the Training Phase: At most two arrows were shown at a time, indicating only one direction and sense. (b) Directions of movement. F: neck flexion/extension (sagittal plane); L: neck lateral flexion (coronal plane); R: neck rotation (transverse plane). Flexion, right lateral flexion, right rotation are indicated by a + sign; extension, left lateral flexion, left rotation are indicated by a − sign.

movement in one of the three anatomical directions. The difference in the width of the sliding window from that of 75 ms used in the previous chapter (Section 7.2.2) is justified by the fact that the 75 ms transmission limit of the software interface is defined per SU. Since two SUs were employed in the present study instead of one, the minimum transmission period was effectively doubled to 150 ms.

RFC-Net Training

RFC-Net is a neural network designed to predict multi-dimensional movement states from neck-acquired HD-sEMG, building upon the earlier RPC-Net model for hand kinematic estimation (Chapter 3). At each inference step, RFC-Net processes the eight most recent samples from 64 EMG channels, producing a 512-dimensional input vector. The network architecture comprises five fully connected layers with 512, 1024, 2048, 1024, and 512 neurons, respectively. All layers use ReLU activation functions, except for the output layer, which generates three continuous outputs corresponding to the three movement directions, with values ranging from -2 to 2. The objective of the training phase was to minimise the mean squared error between the output of RFC-Net and the target label vectors included in the dataset. The training

dataset (DS4.a) was split 90/10 for training and validation. RFC-Net was trained independently for each subject using 100 epochs, with the Adam optimiser (learning rate 10^{-12}, $\varepsilon = 10^{-5}$, $\beta_1 = 0.9$, $\beta_2 = 0.99$, batch size = 400) and a mean squared error loss function, all implemented in PyTorch. The average inference time of RFC-Net was 250 μs ($\pm$22 μs), measured across 10^5 iterations on an Intel(R) Xeon(R) Platinum 8268 CPU (2.90 GHz). Training time per subject was approximately five minutes. The trained network was subsequently used in the testing phase.

DS4.b.s1: Testing Phase Data Acquisition Part 1

The testing phase began immediately after RFC-Net training and resulted in the acquisition of DS4.b. This phase was divided into two parts: cursor control (DS4.b.s1) and hand control (DS4.b.s2). Throughout testing, subjects remained seated in the same position used during training, and the HDE-Array was not repositioned. Both parts of the testing phase were completed by each subject in a single continuous session, using the same experimental setup and electrode placement. In Part 1 (DS4.b.s1), subjects controlled three on-screen cursors in real time via neck muscle activation and RFC-Net, with each cursor corresponding to one of the three movement directions. HD-sEMG signals were streamed through the MEACS system and processed in real time by the BP software, which computed RMS values using a 307-sample (150 ms) sliding window updated every 150 ms. These RMS values were passed to a Python-based application running RFC-Net, which converted them into control signals for the visual interface. The system operated at a refresh rate of 7 frames per second.

Visual tasks were presented alongside the cursors on a monitor. Cursors and task lines were colour-coded by direction using the same scheme as in the training phase (Figure 8.2). Each task involved a target and a constraint requirement. Continuous lines (targets) indicated that the subject needed to push the corresponding cursor beyond a fixed magnitude (set at 1.5). Dashed lines (thresholds), set at a magnitude of 0.5, required the subject to keep the associated cursor below that level. Subjects performed seven distinct task types. The first (N) required maintaining all three

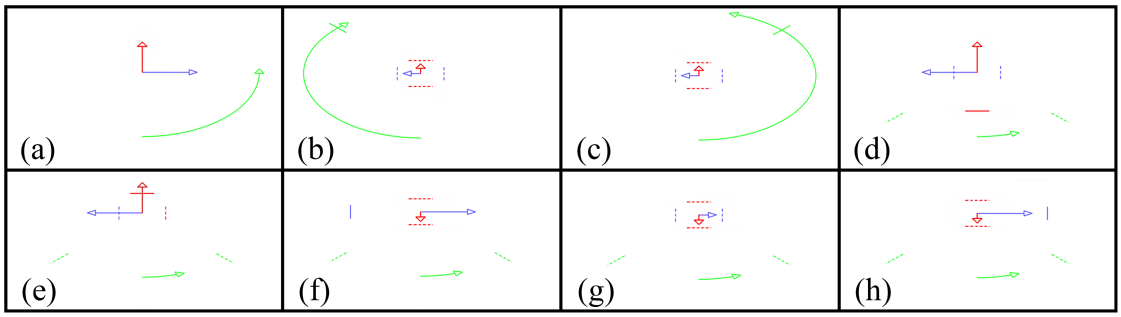

Figure 8.3: Tasks prompted during the first part of the testing phase: (a) No task displayed. (b) "L+", Positive lateral flexion task, subject successfully reached the target while remaining below threshold for the two other directions. (c) "L-", Negative lateral flexion task, subject successfully reached the target while remaining below threshold for the two other directions. (d) "F+", Positive flexion task, subject did not reach the target and failed to stay below threshold for the other two directions. (e) "F-", Negative flexion task, subject reached the target but failed to stay below threshold for the other two directions. (f) "R-" Negative rotation task, subject failed to reach the target but stayed below threshold for the other two directions. (g) Rest task, subject successfully stayed below threshold for all directions. (h) "R+", Positive rotation task, subject failed to reach the target but stayed below threshold for the other two directions.

cursors below their thresholds. The remaining six (R+, R-, F+, F-, L+, L-) each focused on one movement direction as the target, with the other two directions acting as constraints (see Figure 8.3). Each task was performed twice, resulting in a total of 14 trials. Tasks were performed at the own pace of the participants, advancing to the next upon completion. The average duration of a prompt was 13.4 s (± 10.6 s). Each task was classified according to performance:

- failed, if the target was not reached;
- partially completed, if the target was reached but constraint thresholds were violated;
- completed, if the target was reached while staying below both thresholds.

For the rest task (N), outcomes were classified as either completed or failed, since no target was involved (see Figure 8.3 for examples). In addition to categorical outcomes, the distance between the target line and the corresponding cursor was recorded as a continuous measure of task success.

DS4.b.s2: Testing Phase Data Acquisition Part 2

In Part 2 (DS4.b.s2), participants used RFC-Net to control a virtual 3-DoF hand kinematic model. The acquisition, transmission, and processing of HD-sEMG data were identical to those in Part 1. However, instead of moving visual cursors, the three outputs of the RFC-Net model were mapped to control a virtual hand in Three-Dimensional (3D) space.

This mapping was based on results from a previous study in which PCA was applied to a 29-DoF hand kinematic model (Chapter 5). The first three PCs captured 60% of the total variance. The three outputs of RFC-Net were projected onto these three PCs using precomputed PCA coefficients. From the resulting three-dimensional representation, the full 29-DoF joint configuration was reconstructed through inverse PCA and passed through a FKA to compute and render the position of the hand in space. To improve stability and control precision, the outputs were scaled down by a factor of two. Each neck movement direction was associated with one of the three PCs: axial rotation controlled PC1, flexion/extension controlled PC2, and lateral flexion controlled PC3. The resulting output was a virtual hand displayed on the monitor in front of the participant.

As in Part 1, participants completed control tasks by imitating a visual prompt. Three elements were simultaneously shown on the display:

- the target hand configuration, displayed as a skeletal hand model (Figure 8.4.a),
- the live output of the RFC-Net model, also rendered as a skeletal hand (Figure 8.4.a),
- a directional cue indicating the suggested direction of movement, presented as unlabelled arrows (Figure 8.4.b).

Upon appearance of the prompt, participants were instructed to imitate the target pose using the live output as accurately as possible. Seven task types were defined, each corresponding to a specific prompt. The first task (N) represented a rest condition with no PC activation. The remaining six tasks (M1-M6) involved isolated activation of a single PC (positive or negative) with a magnitude of 0.75,

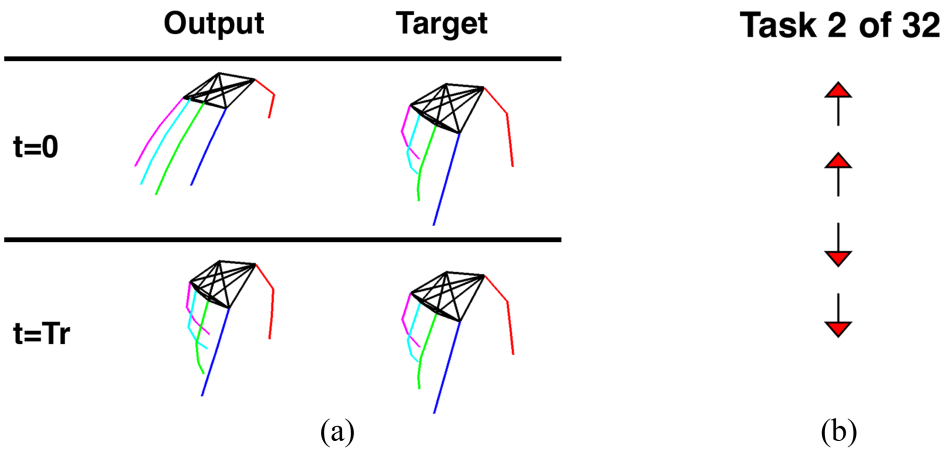

Figure 8.4: Testing phase part 2 example: (a) The left part of the plot shows the prompted task (Target) and the initial output configuration. After the subject was given time to reach the target (time T_r), the two configurations were similar. (b) The second window displays the direction of movement but not its sense.

while the other two PCs remained at zero. The hand configurations associated with each task are illustrated in Figure 8.5. Tasks involving opposite directions along the same PC axis were paired (PC1: M1, M4; PC2: M2, M5; PC3: M3, M6), with the rest pose centred among them. Each task type was presented twice during a session, resulting in a total of 14 prompts. A new prompt appeared upon the request of the participant, and they were allowed to take as much time as needed to match the target pose. The average duration per prompt was 13.6 s ($\pm$ 10.0 s). Task performance was quantified based on the distance between the target and actual hand configurations, rather than using binary success/failure criteria.

DS3: Data from previous study: hand position control via forearm muscles

Evaluation of the first experimental hypothesis used previously recorded HD-sEMG and kinematic data as a benchmark. These data were acquired in a prior study, where the ability of subjects to control a virtual hand kinematic model using proximal forearm muscles through RPC-Net was assessed. This dataset is referred to as DS3 throughout this manuscript. DS3 consists of two subsets, DS3.a and DS3.b. For the purposes of the present study, only DS3.b was used. It includes recordings from four subjects who performed six hand control tasks similar to those

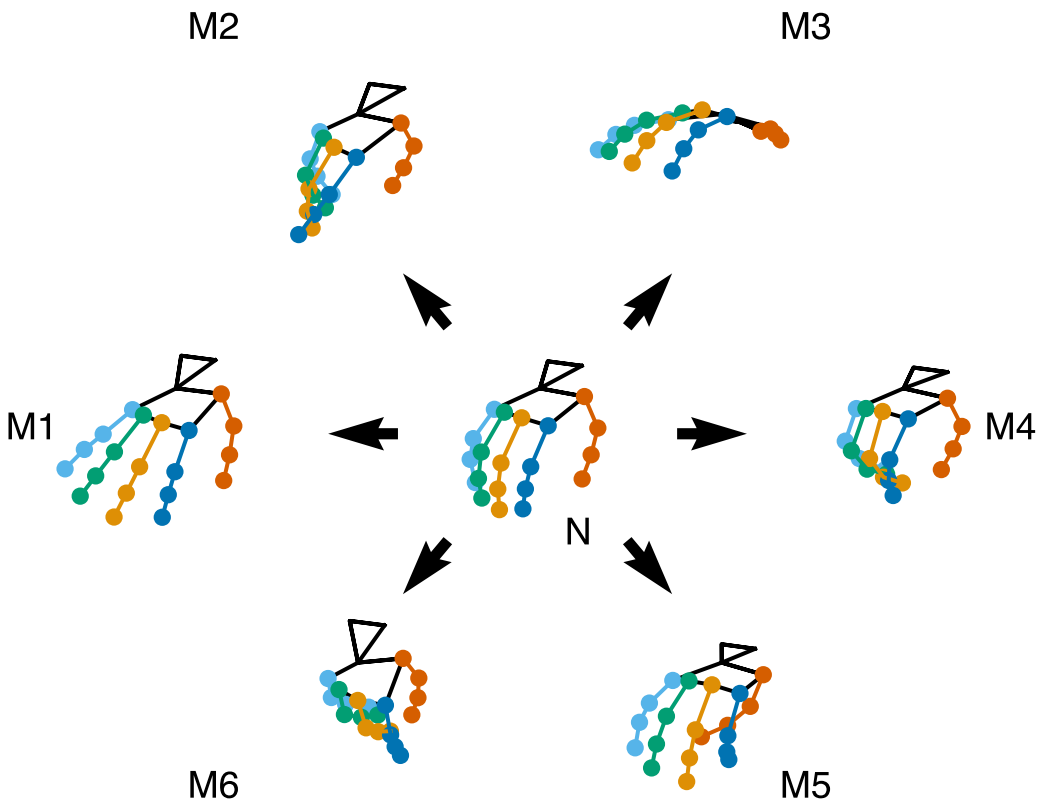

Figure 8.5: Hand control tasks: The figure displays the seven tasks performed by subjects in terms of control of a virtual hand kinematic model. Tasks involving activation of the same PC in opposite directions are aligned along the same axis: PC1 (M1 and M4), PC2 (M2 and M5), and PC3 (M3 and M6). Rest state (N) is centred between them.

in Part 2 of the current testing phase. The aim was to compare the effectiveness of virtual hand control using forearm-acquired signals with results obtained from neck-based control in the present study. Full methodological and technical details of DS3 are provided in Chapter 7.

Performance Assessment

To assess both subject performance and the effectiveness of the RFC-Net/HDE-Array system, different performance metrics were used for Part 1 and Part 2 of the testing phase. For Part 1, performance was evaluated using two metrics: Task Completion Score (TCS) and Normalised Distance (ND). Because Part 1 tasks involved simultaneous target-reaching and constraint-avoidance, simple and complex evaluation metrics were defined to capture different levels of task success. TCS is

defined as the ratio of successfully completed tasks to the total number of tasks, with values ranging from 0 to 1. Higher TCS values indicate better performance.

Two variations of TCS were calculated:

- TCS-Simple (TCS-S): the fraction of tasks that were either completed or partially completed.
- TCS-Complex (TCS-C): the fraction of tasks that were fully completed (i.e., target reached and constraints satisfied).

ND quantifies the spatial closeness between the active cursor and its target in each task. Lower ND values indicate better performance. The following are defined:

- ND-Simple (ND-S): minimum distance between the active cursor and its target line, divided by 1.5.
- ND-Complex (ND-C): calculated as ND-S, but only during time periods when the other two movement directions remained below their respective thresholds.

For the rest task (N), where no active target was present, TCS-S and TCS-C were identical. In this case, ND was computed as the mean minimum distance of all three cursors from zero. All TCS and ND values were averaged across subjects and tasks. Distance and output signals were smoothed using a moving average with a 1.5 s window before metric computation.

For Part 2, performance was evaluated using two metrics: MAD and MGD. Both quantify the deviation between the reconstructed hand output and the target pose, with lower values indicating better performance.

MAD measures the joint-space angular error. At each time step, the absolute difference between the 29 reconstructed joint angles from RFC-Net and the target angles was computed. Target joint angles were derived by applying inverse PCA (with the same coefficients as used during training) to a task activation signal defined as a unit-magnitude step on the relevant principal component. The resulting time series of differences (signal A) was smoothed using a 1.5 s moving average (yielding signal B), and the minimum value of B over the task duration was recorded as the MAD for each subject-task pair.

MGD captures spatial accuracy by comparing full 3D hand poses. At each time point, 29 output angles of RFC-Net were converted to 3D hand positions using the FKA (Chapter 3), producing a set of 20 spatial points. The same transformation was applied to target angles. The Euclidean distances between estimated and target hand position points were computed over time and averaged into a time-varying signal (A). A moving average (1.5 s window) was applied to obtain the smoothed signal (B). For each task, the minimum value of B was recorded as the MGD for the corresponding subject-task combination. MAD and MGD values were also computed for the DS3.b dataset to provide a benchmark for comparison. In DS3.b, four subjects performed six hand control tasks using forearm-based control. For each subject, the mean MAD and MGD values were computed across all tasks. The mean, maximum, and minimum values across subjects are reported in the results section. As discussed in Section 7.2.2, the shift from MD and MPCC to MGD and MAD reflects the use of task-oriented metrics that capture best performance rather than average accuracy, which are more appropriate for task-completion experiments.

Hypotheses Testing

Four hypotheses were tested to evaluate the performance of the RFC-Net/HDE-Array system in enabling control of either on-screen cursors or a virtual hand model using neck muscle activation.

1. Subjects can control a hand kinematic model in real time using neck muscles and the RFC-Net/HDE-Array system, achieving task performance comparable to that observed with forearm muscle control : To assess this, MAD and MGD values from Part 2 of the testing phase were compared with those obtained from the forearm-based dataset (DS3.b). Values from this study were grouped by task (M1-M6 and N), yielding 8 or 10 data points per task depending on group size (8 tetraplegic, 10 healthy subjects). These values were plotted alongside the mean across subjects for each task. In addition, MAD and MGD values were grouped by subject, and both task-wise and subject-wise means

were visualised. A descriptive comparison was conducted to assess relative performance across control modalities.

2. Performance in controlling the hand kinematic model using head and neck muscles, is comparable between tetraplegic and healthy subjects : Unpaired t-tests on MAD and MGD values from Part 2 were conducted to evaluate this. Each data point represented the mean performance of a subject across all tasks. The null hypothesis (H_0) assumed equal means between groups. Prior to testing, normality was assessed using the Shapiro-Wilk test.
3. Subjects can successfully use the RFC-Net/HDE-Array system to control three independent cursors in a task-oriented experiment, with 1 DoF per cursor : This hypothesis was evaluated qualitatively based on aggregate performance scores in Part 1 and visual inspection of TCS and ND metrics. System usability and subject response patterns were assessed descriptively, and outcomes were compared to performance ranges reported in related studies using sEMG-driven cursor control.
4. Performance in the cursor-based task is comparable between healthy and tetraplegic subjects : Group differences in cursor-based task performance were assessed using a Mann-Whitney U test for TCS-S and TCS-C values, as normality assumptions were not met (Shapiro-Wilk test). For ND-S and ND-C values, normality was satisfied and an unpaired t-test was used. In both cases, each data point represented the mean score of a subject across all tasks. The null hypotheses assumed equal distributions for the Mann-Whitney U test and equal means for the t-test.

These hypotheses formed the basis for evaluating both usability and efficacy of the RFC-Net/HDE-Array system across subject populations and task types.

8.3 Results

This section presents the findings from the assessments described in Section 8.2.2. Control performance between tetraplegic and healthy subjects is compared for both cursor and hand position control. Additionally, hand position control using forearm-

and neck-based approaches is contrasted, and feasibility of the cursor control tasks with the RFC-Net/HDE-Array system is assessed.

8.3.1 Assessment of Hand Control Performance

Figure 8.6 shows the values of MGD and MAD for the 18 subjects considered. The plots in the left column present data grouped by task, with black point markers representing individual trials. Square and circular markers indicate the group average for each task. The plots in the right column group individual trials by subject and include the group-wide mean. Additionally, a green line represents the average observed across the four subjects in the study using forearm muscles as the control source (i.e., from DS3.b). The shaded area represents the range (maximum and minimum) observed in DS3.b. Because tasks differed between the two studies, no task-wise distinction was made. For MGD, the mean values observed in both populations (Healthy: 40.2 mm, Tetraplegic: 39.7 mm) fall within the range reported in the previous study (23.1 mm-43.1 mm) and deviate by less than 8 mm from its mean (34.7 mm) in both cases. At the level of individual tasks and subjects, all tasks except M3 and M6 fell within or below this range, and approximately half of subjects in both populations displayed average performance within the reference range. In contrast, results for MAD were notably different. In this case, the mean for both populations (Healthy: 6°, Tetraplegic: 7°) is not only below the mean observed in the previous study (11°) but also outside its reported range (8°-13°). Specifically, only tasks M1 and M4 fall within the reference range, and approximately one-third of the subjects show values within this interval. A summary of the results from this experiment is provided in Table 8.1.

8.3.2 Healthy vs. Tetraplegic Subjects: Hand Position Control

Figure 8.6 presents the comparison of virtual hand position control performance between healthy and tetraplegic subjects using neck muscles. The mean MGD for healthy subjects was 40.2 mm (range: 28.0 mm-61.8 mm), while for tetraplegic

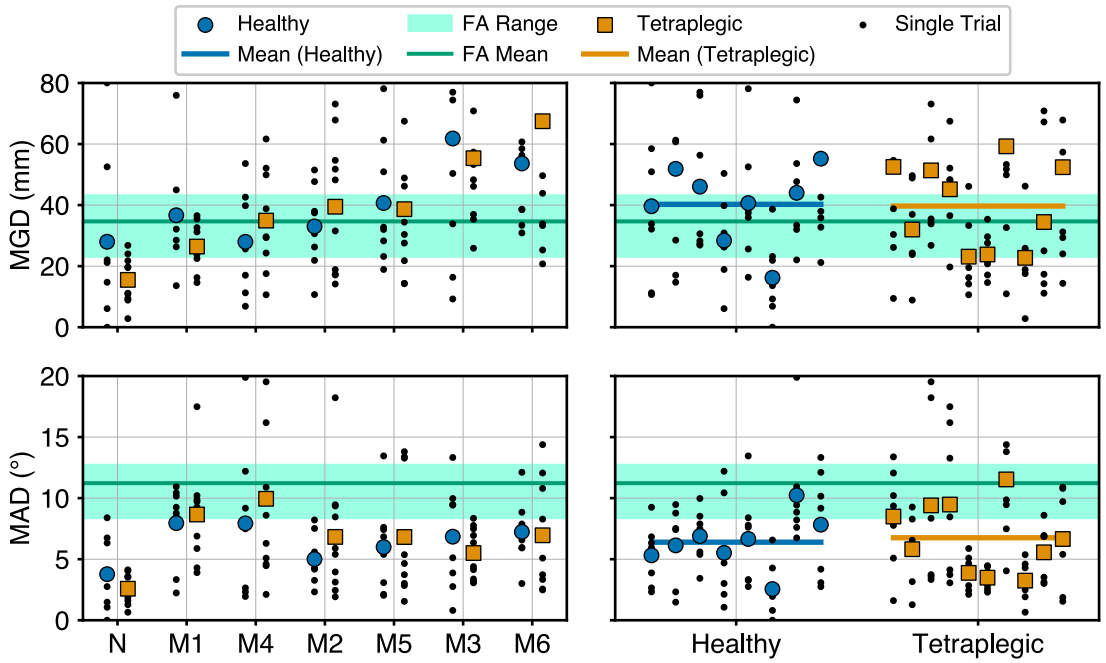

Figure 8.6: Hand control task performance results: This figure shows the results, in terms of MGD and MAD, of the experiment assessing the ability of healthy and tetraplegic subjects to control a virtual hand model. (Left:) Data are grouped by task, as indicated on the x-axis. (Right:) Data are grouped by subject type (healthy or tetraplegic). Unpaired t-test results for MGD (H_0: $\mu_T = \mu_H$): $t(16) = 0.09$, $p = 9.3{\cdot}10^{-1}$). Unpaired t-test results for MAD (H_0: $\mu_T = \mu_H$): $t(16) = -0.30$, $p = 7.7{\cdot}10^{-1}$).

subjects, it was 39.7 mm (range: 15.5 mm-55.3 mm). An unpaired t-test was conducted to assess whether mean values differed between the two groups under the null hypothesis (H_0) of equal means. The test yielded a p-value of 0.93 for MGD and 0.77 for MAD, indicating no statistically significant difference between the groups for either metric. The numerical results are detailed in Table 8.1.

8.3.3 Assessment of Cursor Control Performance

Figure 8.7 presents the results of the experiment assessing the ability of subjects to control a cursor on the screen using neck muscles. The figure reports values for TCS-S, TCS-C, ND-S, and ND-C across tasks and subjects. The corresponding numerical results are detailed in Table 8.2. Results indicated that TCS-S exceeded 50% for all but one task and reached or surpassed 75% in four of the seven tasks. Performance was lower for tasks F and L, while the N task consistently achieved a perfect score. The distribution of values across subjects was broad, with values

Table 8.1: Hand control results

	MGD (mm, Range)		MAD (°, Range)	
Task	Healthy	Tetraplegic	Healthy	Tetraplegic
M1	36.7 (13.6-76)	26.4 (14.6-36.5)	8 (2-11)	9 (4-18)
M2	33.0 (10.7-51.5)	39.5 (14.1-73.1)	5 (2-8)	7 (2-18)
M3	61.8 (9.3-129.5)	55.3 (25.9-94.3)	7 (1-13)	6 (3-8)
M4	28.0 (6.9-53.6)	34.9 (10.6-61.7)	8 (2-20)	10 (2-22)
M5	40.7 (18.9-78.1)	38.7 (14.3-81.3)	6 (2-14)	7 (2-14)
M6	53.7 (30.9-112.2)	67.4 (20.7-142.8)	7 (3-12)	7 (3-14)
N	28.0 (0-80)	15.5 (2.8-26.8)	4 (0-8)	3 (1-4)
All	40.2 (0-129.5)	39.7 (2.8-142.8)	6 (0-20)	7 (1-22)

Forearm Baseline		
Min	23.1 mm	8°
Mean	34.7 mm	11°
Max	43.1 mm	13°

Performance of RFC-Net across tasks for both populations (hand control). Mean and range of MGD and MAD values are shown. Minimum, mean, and maximum values from DS3.b are also included.

evenly spread around the mean (77.8%). A similar pattern was observed for TCS-C, suggesting a uniform decline in performance rather than a pronounced drop in specific subjects or tasks. The mean TCS-C value is 72.2%, representing a 7% decrease from TCS-S. This indicates a modest decline in performance when subjects were also required to constrain movement in the other two directions. A Wilcoxon signed-rank test comparing the two metrics confirmed this difference (H_0: $\mathrm{P(C \geq S)} = \mathrm{P(S \geq C)}$), which yielded $W = 0$, $p = 2.7{\cdot}10^{-2}$.

For ND-S, similar trends were observed. Performance was highest in the rest task and progressively decreased across other tasks. The normalised distance remained below 0.4 for all tasks, indicating relatively high accuracy. For reference, the target was positioned at a distance of 1 from the centre of the dynamic range (after normalisation by 1.5), so a distance of 0.4 corresponded to achieving over 60% of

the required movement. Regarding subject-wise distributions, values for ND-S were normally distributed around the mean, as confirmed by a Shapiro-Wilk test. A slight decrease in performance was observed for ND-C, aligning with trends seen in TCS. Mean ND-S and ND-C values were 0.16 and 0.21 respectively, indicating a 24% increase in normalised distance when subjects were also required to remain below thresholds for the other movement directions. Comparison of ND-S and ND-C values using a paired t-test (H_0: $\mu_S = \mu_C$) returned $t(17)$ = -3.79 ($p = 1.5{\cdot}10^{-3}$), indicating a statistically significant difference between the metrics.

8.3.4 Healthy vs. Tetraplegic Subjects: Cursor Control

Statistical tests assessed whether the four performance metrics differed significantly between the two populations. For TCS-S and TCS-C, a Mann-Whitney U test assessed differences under the null hypothesis (H_0) that both groups followed the same distribution. The test yielded p-values of 0.68 for TCS-S and 0.29 for TCS-C, indicating no statistically significant difference between the groups. For ND-S and ND-C, normality was confirmed by a Shapiro-Wilk test, allowing unpaired two-sided t-tests. The results returned p-values of 0.63 for ND-S and 0.29 for ND-C, again indicating no significant differences between the two populations.

8.4 Discussion

Results presented in the previous section demonstrate that neck muscles can effectively control a 3-DoF hand kinematic model or three independent cursors, with no significant performance difference between healthy and tetraplegic subjects (lesions at C5 or C4-C5 level). This study aimed to validate four experimental hypotheses.

The first stated that subjects can control a hand kinematic model in real time using neck muscles and the RFC-Net/HDE-Array system, achieving task performance comparable to that observed with forearm muscle control. Results in Section 8.3.1 support this hypothesis, indicating that performance was similar between the two control sources, depending on the metric considered. Specifically, mean MGD for most subjects and tasks fell within or below the performance

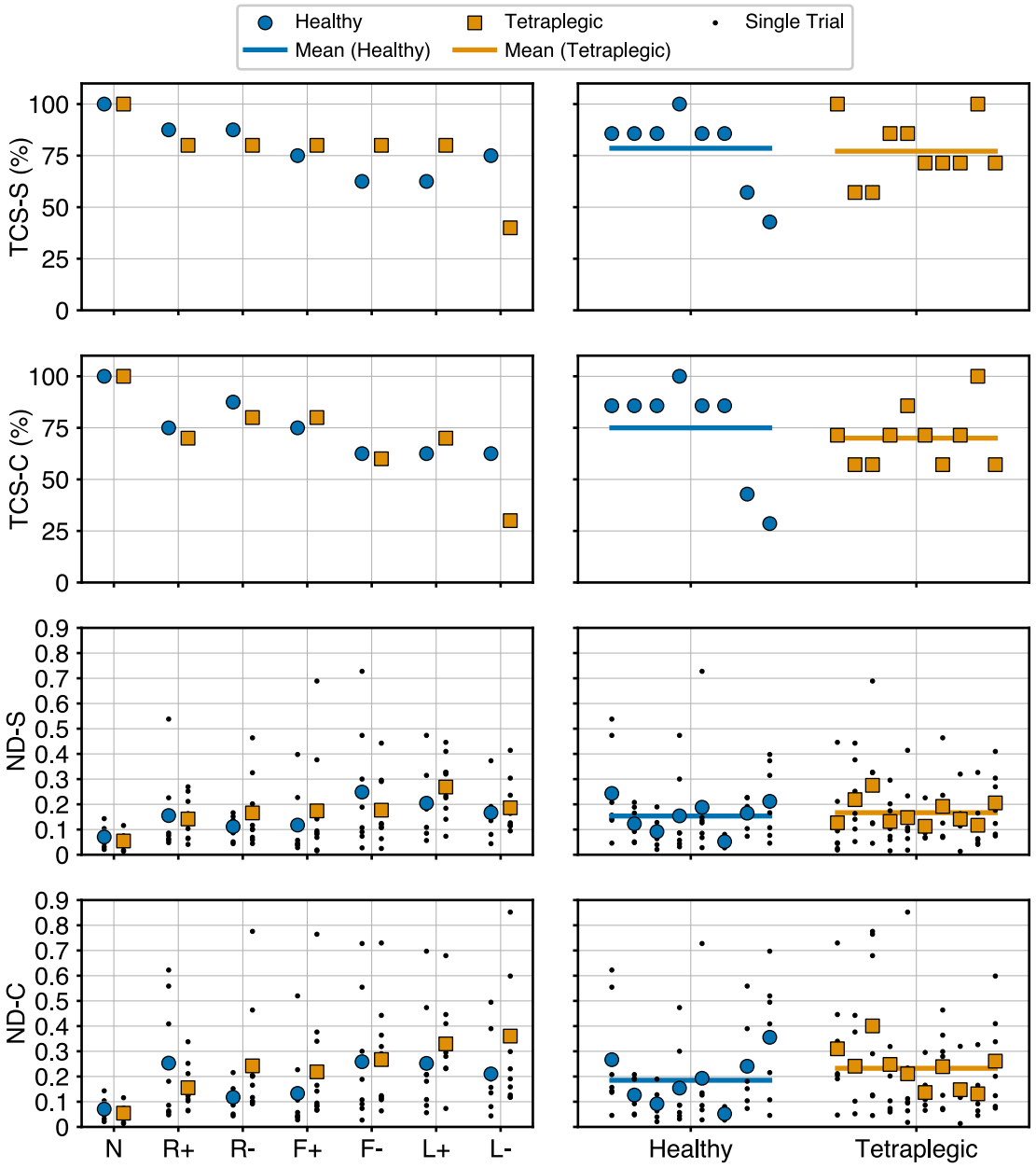

Figure 8.7: Cursor control task performance results: This figure shows the results, in terms of TCS-S, TCS-C, ND-S and ND-C, of the experiment assessing the ability of healthy and tetraplegic subjects to control three independent cursors. (Left:) Data are grouped by task, as indicated on the x-axis. (Right:) Data are grouped by subject type (healthy or tetraplegic). Mann-Whitney U test results for TCS-S (H_0: P(H $\geq$ T) = P(T $\geq$ H)): $U = 45$, $p = 6.8{\cdot}10^{-1}$. Mann-Whitney U test results for TCS-C (H_0: P(H $\geq$ T) = P(T $\geq$ H)): $U = 52$, $p = 2.9{\cdot}10^{-1}$. Unpaired t-test results for ND-S (H_0: $\mu_T = \mu_H$): $t(16) = -0.48$, $p = 6.4{\cdot}10^{-1}$). Unpaired t-test results for ND-C (H_0: $\mu_T = \mu_H$): $t(16) = -1.10$, $p = 2.9{\cdot}10^{-1}$).

range reported for forearm-based control in Chapter 7. A similar trend was seen for all MAD values. While these findings are promising, several factors must be

Table 8.2: Cursor position control results

Task	TCS (%)			
	S		C	
	H	T	H	T
R+	87.5	80	75	70
R-	87.5	80	87.5	80
F+	75	80	75	80
F-	62.5	80	62.5	60
L+	62.5	80	62.5	70
L-	75	40	62.5	30
N	100	100	100	100
All	78.6	77.2	75	70
	ND (Range)			
	S		C	
	H	T	H	T
R+	0.16 (0.05-0.54)	0.14 (0.04-0.27)	0.25 (0.05-0.62)	0.16 (0.06-0.34)
R-	0.11 (0.04-0.17)	0.17 (0.04-0.46)	0.12 (0.04-0.22)	0.24 (0.09-0.78)
F+	0.12 (0.03-0.4)	0.17 (0.02-0.69)	0.13 (0.03-0.52)	0.22 (0.07-0.76)
F-	0.25 (0.03-0.73)	0.18 (0.02-0.44)	0.26 (0.03-0.73)	0.27 (0.06-0.73)
L+	0.20 (0.06-0.47)	0.27 (0.07-0.45)	0.25 (0.06-0.7)	0.33 (0.07-0.68)
L-	0.17 (0.04-0.37)	0.19 (0.09-0.41)	0.21 (0.04-0.49)	0.36 (0.12-0.91)
N	0.07 (0.02-0.14)	0.05 (0.01-0.12)	0.07 (0.02-0.14)	0.05 (0.01-0.12)
All	0.15 (0.02-0.73)	0.17 (0.01-0.69)	0.19 (0.02-0.73)	0.23 (0.01-0.91)

Performance of RFC-Net across tasks for both populations (cursor control). Mean ND-S, ND-C, TCS-S, and TCS-C values are shown. Columns H and T represent healthy and tetraplegic subjects, respectively. Ranges are included for ND.

considered when interpreting them.

A first factor concerns latency, which plays a critical role in determining whether control can be regarded as truly real time. In the present implementation, the total

delay between signal acquisition and output update was approximately 150 ms, corresponding to the sampling period imposed by the amplifier interface. As in the forearm configuration, this limitation arises because the interface transmits root-mean-square (RMS) sEMG values at only 6-7 Hz, despite the underlying amplifier sampling the raw signal at 2 kHz. The computational contribution of the RFC-Net model is negligible, with an inference time of approximately 250 μs. Although the resulting 150 ms loop delay exceeds the 30-50 ms target range generally considered optimal for intuitive prosthetic and rehabilitation control [304, 313], it remains below the 200 ms perceptual threshold for real-time interaction. Thus, the achieved latency is acceptable for interactive applications and indicates that the system operates within a range compatible with natural closed-loop control.

A second factor involves comparability across studies. Experimental setups differed substantially between the present and reference investigations, reported in previous chapters, precluding direct statistical comparison and allowing only qualitative interpretation. The study described in Chapter 7 included a smaller sample size ($n = 4$), omitted dimensionality reduction for kinematic control, and defined tasks in terms of individual joint movements (e.g., index finger flexion), whereas the present study defined tasks by activation of principal components. These methodological differences suggest that the observed similarities in performance should be regarded as indicative rather than conclusive. Moreover, the simpler nature of the tasks used here, single-PC activations, may partially explain the lower MAD values observed. Future work should investigate how task complexity influences accuracy by comparing single-PC activation with more complex, multi-DoF control scenarios.

Third, an obstacle to real-life integration of the RFC-Net/HDE-Array system lies in the interaction between the EMG acquisition chain and any concurrent FES system. This interaction presents challenges at multiple levels. From an engineering and instrumentation perspective, electrical stimulation pulses generate large artefacts in the EMG recording channels, often exceeding the input range of the amplifier and causing signal saturation or recovery delays. The extent of this

interference depends on the relative distance between stimulation and recording sites, the return-electrode configuration, and the grounding strategy of the system. Mitigation requires careful shielding, isolation, and timing control. A common engineering solution is to synchronise stimulation and acquisition, temporarily pausing EMG sampling during stimulation bursts or blanking the amplifier input to avoid contamination of the signal [457, 458]. From a signal-analysis standpoint, stimulation artefacts may overlap with the spectral content of the true EMG signal, corrupting both the amplitude envelope and the features used for inference. Two complementary approaches can be envisaged: (i) explicitly modelling and subtracting the stimulation pattern from the recorded data, or (ii) including stimulation artefacts in the training data so that the network learns to disregard them. The latter strategy would effectively incorporate disturbance robustness into the trained model. Regarding the impact on the trained machine-learning system, un-modelled FES artefacts can lead to misclassification or unstable regression outputs, as the feature distribution during online control no longer matches the training conditions. One possible way to address this discrepancy is to employ adaptive or reinforcement-learning frameworks, allowing the model to refine its parameters in real time as it encounters stimulation-induced disturbances. Overall, successful integration of EMG-based control with FES requires co-design of hardware, timing protocols, and learning algorithms to ensure that stimulation artefacts do not compromise decoding performance or closed-loop stability. In synthesis, while the results should be interpreted with caution, it appears that the first hypothesis is supported.

The second hypothesis proposed that performance in controlling a virtual hand kinematic model would not differ between healthy and tetraplegic subjects. The results support this hypothesis, as indicated by the p-values exceeding the significance threshold from the unpaired two-sided t-tests (0.93 for MGD and 0.77 for MAD). While the results suggest slightly better MGD performance in the tetraplegic group (by 0.5 mm) and slightly better MAD performance in the healthy group (by 1°), these differences were not statistically significant. Analysis of individual task performance also supports this conclusion. Performance trends were consistent

across both groups: tasks M3 and M6 had the highest MGD values (i.e., lowest spatial accuracy), and tasks M1 and M4 had the highest MAD values (i.e., largest angular deviations from target poses). It is important to note that, of the eight healthy participants included in this study, only one had prior partial experience with the system, having also participated in earlier experiments. This minimises the possibility of prior-knowledge bias influencing the comparison between groups.

The third hypothesis stated that subjects could successfully use the RFC-Net/HDE-Array system to control three independent cursors in a task-oriented experiment. The findings support this hypothesis, as evidenced by high task completion rates (TCS-S and TCS-C) and low distances between cursor and target (ND-S and ND-C). A statistically significant but relatively small decrease in performance was observed between TCS-S and TCS-C, suggesting a modest reduction in the ability to precisely control one cursor while suppressing activation in the other two directions. Nonetheless, the small magnitude of this difference reinforces the feasibility of using neck muscles as a control source for managing three independent degrees of freedom. These findings indicate that such a system could serve as a viable and effective method for multidimensional control. These results align with prior work in the literature, which has also explored neck-based control, albeit with notable limitations, as a potential method for multidimensional interface manipulation [447, 455, 456].

When interpreting the effect these results can have on clinical practice, an important consideration is user comfort. In neck-based control, sustained or exaggerated head movements can be tiring, unnatural, and may lead to muscular discomfort or strain, particularly during prolonged use. This limitation could be mitigated by refining the control strategy to rely primarily on light muscle activations or on bilateral contractions that minimise actual head displacement. With appropriate training and tuning of the decoding algorithms, participants may also learn to generate stable control signals through subtle or near-isometric neck activations. While the RFC-Net/HDE-Array system was not validated under such conditions, future studies should investigate this possibility. Nevertheless, given the

limited number of viable control sources available for individuals with high-level spinal cord injuries, some degree of physical effort or mild discomfort may represent an acceptable trade-off for achieving multidimensional control.

Finally, the fourth hypothesis proposed that performance in the cursor-based task would not differ between the two populations. Results support this hypothesis, as indicated by high p-values from Mann-Whitney U tests for TCS-S (0.68) and TCS-C (0.29), showing no significant performance differences between healthy and tetraplegic subjects. Similar outcomes were observed for ND-S and ND-C, where unpaired t-tests yielded p-values of 0.63 and 0.29, respectively. Although tetraplegic subjects exhibited slightly lower performance on average, these differences were not statistically significant and did not affect conclusions drawn from the Mann-Whitney U tests. In conclusion, experimental results support the fourth hypothesis.

8.5 Conclusion

This study evaluated the ability of tetraplegic subjects with lesions at the C5 or C4-C5 level to perform control tasks using neck muscles as a control source and compared their performance to that of healthy subjects and to previously reported tasks involving forearm muscle control. The results showed no significant differences between healthy and tetraplegic participants in either control paradigm. Furthermore, despite differences in experimental protocols, performance achieved using neck muscles was comparable to that obtained from forearm-based control. These findings, combined with the simplicity of the system (requiring less than 30 minutes of training) and its non-invasive nature, underscore the potential of the RFC-Net/HDE-Array system for tetraplegic rehabilitation. All tetraplegic participants reported the device as comfortable, further supporting its practical viability. The system could be adapted to control a three-site FES system from the neck, either for long-term assistive use or as a therapeutic training tool. It also holds potential for integration with other rehabilitation technologies, such as upper limb exoskeletons. Future studies are planned to validate the efficacy of the system in controlling rehabilitation devices in real-time settings. The ability to intuitively

and directly control a rehabilitation device could be transformative for individuals with cervical spinal cord injuries, offering greater autonomy and improved quality of life. Overall, the RFC-Net/HDE-Array system shows strong promise for expanding rehabilitation options and enhancing user experiences for the tetraplegic population.

9
Discussion

This integrated discussion draws the six experimental studies together to show how, collectively, they advance the central aim of this thesis: to demonstrate that the RPC-Net/HDE-Array platform can translate in real-time high-density surface-EMG signals into accurate hand kinematics for upper-limb rehabilitation, addressing the persistent gap in intuitive, user-centred control identified in Chapter 2. Table 9.1 positions each study by summarising its research question, design and headline finding, giving the reader a one-page map of the research arc. Figure 9.1 provides a conceptual map of how each chapter is related to the others. The chapter then proceeds in four steps: Section 9.1 synthesises cross-study findings into three thematic insights; Section 9.2 situates those insights within, and extends, the current neuro-rehabilitation framework; Section 9.3 evaluates methodological strengths and shared limitations; and Section 9.4 discusses practical, theoretical and future-research implications before offering a brief concluding synthesis.

Table 9.1: Summary of the six experimental chapters and their through-line

Ch.	Research question	Design	Headline result
3	Can RPC-Net accurately estimate hand kinematics from HD-sEMG in offline conditions?	Estimation of hand position with HD-sEMG signals and RPC-Net. Assessed overall accuracy of the algorithm and effect of changes in network structure	25 mm MD, 75% MPCC, better than state of the art
4	Can RPC-Net maintain its performance when using dry electrodes (HDE-Array) instead of traditional gel-based electrodes?	Paired offline comparison: gel vs dry HD-sEMG; dry electrode characterisation	Dry array shows non-significant MD ($p = 0.24$) and MPCC ($p = 0.21$) differences; impedance suitable for EMG acquisition
5	Can the kinematic model be effectively reduced to a lower number of DoFs using PCA?	Analysis of PCA results; Assessment of estimation accuracy varying number of PCs (1-29)	12 PCs explain > 90% variance; decoding retains 90% MD with 5 PCs
6	How robust is RPC-Net to electrode repositioning and inter-subject generalisation in offline conditions?	Accuracy assessment with electrode repositioning and multi-subject training data	Including repositioning during training decreases accuracy drop caused by electrode repositioning by 75%; accuracy decreases linearly with the number of subjects used for training.
7	Can subjects use RPC-Net to perform real-time control tasks, and what factors influence their performance during live operation?	Closed-loop real-time tests with/without visual feedback	Real-time performance on par with state of the art; feedback does not improve accuracy ($p = 0.44$); real-time feasibility confirmed.

Continued on next page

Table 9.1 – continued from previous page

Ch.	Research question	Design	Headline result
8	Can the RPC-Net/HDE-Array system enable intuitive, real-time multi-DoF control using neck muscle activity?	3-DoF control task performance with neck-acquired HD-sEMG for healthy and tetraplegic subjects.	Performance within forearm control range; tetraplegic performance non-inferior ($p = 0.93$, MGD; $p = 0.77$, MAD).

Reprising the introduction, the main research question, the study design, and the main finding of each chapter are summarised.

9.1 Integrated Findings and Thematic Insights

This section distils the experimental evidence into three cross-cutting themes that transcend individual chapters. For each theme convergent patterns are identified, points of divergence highlighted, and their implications for upper-limb rehabilitation control systems interpreted.

9.1.1 Theme 1: Decoding Accuracy Across Configurations

Across Chapters 3-5, RPC-Net consistently meets or exceeds state-of-the-art precision. The baseline 96-channel, gel-electrode configuration (Chapter 3) achieves MD = 25 mm and MPCC = 0.75, matching or outperforming state-of-the-art Transformer, CNN and RNN comparators. Switching to the dry HDE-Array (Chapter 4) does not result in a statistically significant difference in either metric ($p = 0.24$, $p = 0.21$). Dimensionality reduction via PCA (Chapter 5) shows that five principal components retain $\geq 90\%$ of full-model accuracy, while twelve PCs already capture $> 90\%$ of signal variance. Performance improves steadily with larger EMG windows, wider hidden layers, more electrodes and more PCs; removing the recursive feedback loop causes a modest accuracy drop, whereas merging the 29 sub-networks into a single network has no statistically significant effect.

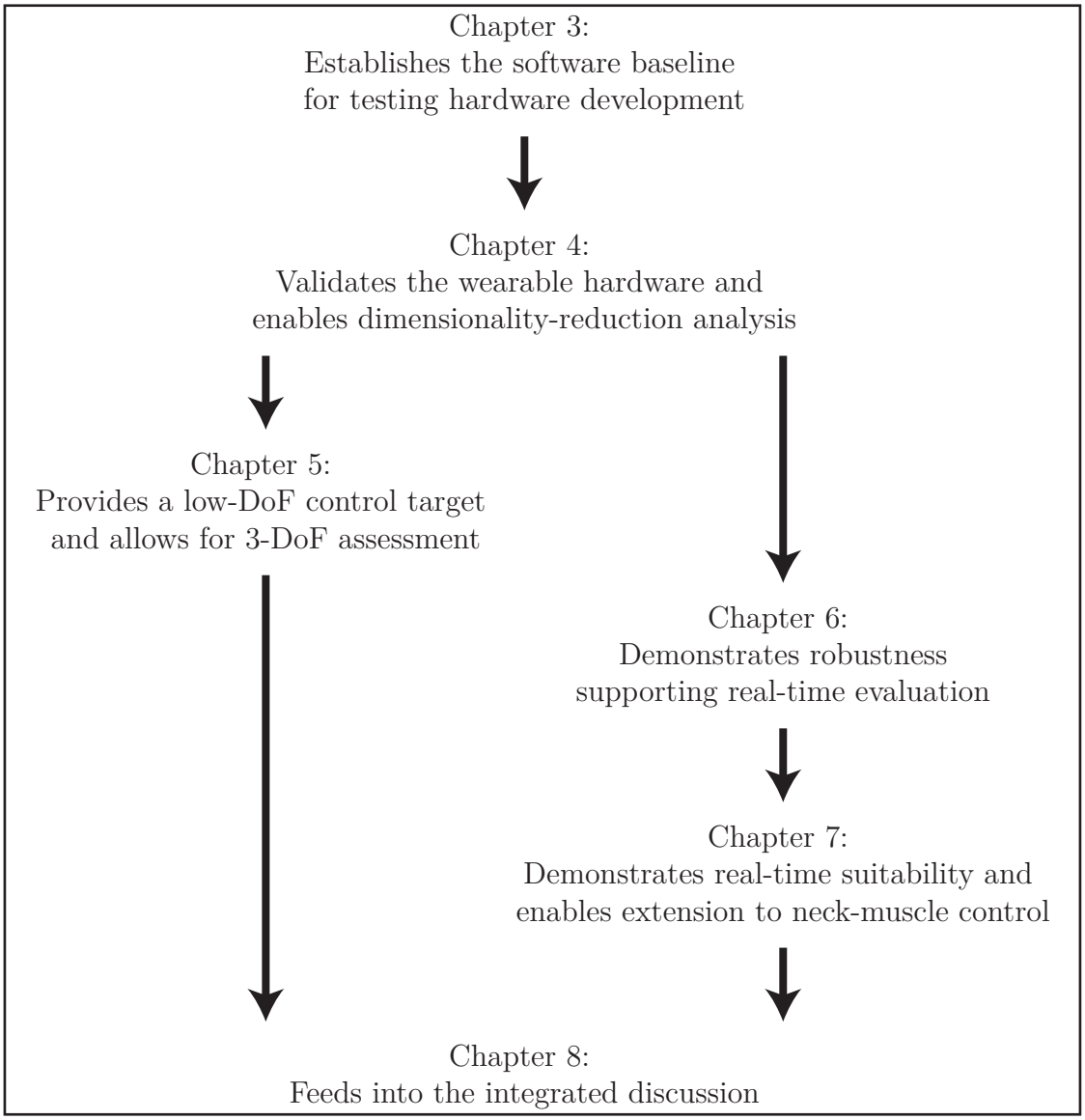

Figure 9.1: Conceptual map of the thesis: Highlighting how each chapter connects to the next.

Several nuances qualify the overall picture. First, when both gel and dry arrays are down-sampled to a 16 × 2 layout, the dry electrodes outperform gel by 4 mm (MD) and 0.07 (MPCC), suggesting that longitudinal channel distribution may compensate for higher skin-electrode impedance. This observation appears to contrast with findings elsewhere in Chapter 4, and indicates that spatial distribution, in addition to material properties, may also be important in influencing decoding performance. Second, the accuracy curves for channel reduction (Figure 3.12) and PCA compression (Figure 5.6) are notably similar, with reductions in EMG inputs

or output DoFs producing nearly linear declines in accuracy. Third, reductions in inference time greatly exceed the magnitude of associated accuracy penalties. For instance, reducing the number of electrodes from 96 to 32 decreases computation time by 85%, while increasing fingertip error by less than 10 mm (28% increase) and reducing MPCC by only 10%. These trade-offs suggest that simplifications in hardware or model architecture can lead to substantial gains in computational efficiency with only limited impact on output quality.

Taken together, these findings characterise RPC-Net as both accurate and adaptable. The model accommodates changes in sensor type, input density and architectural design with minimal compromise in estimation precision. This flexibility allows practical considerations such as comfort, cost or hardware constraints to be taken into account during system deployment, without sacrificing the clinical utility required for integration into rehabilitation settings.

9.1.2 Theme 2: Robustness Under Non-ideal Conditions

A consistent theme across Chapters 4 and 6 is that the RPC-Net/HDE-Array platform retains high decoding accuracy even under conditions that deviate from ideal laboratory setups. In Chapter 4, for example, the dry-electrode bracelet maintains comparable performance to gel-based systems despite operating with much higher skin-electrode impedances. Similarly, in Chapter 6, performance was shown to remain largely consistent when electrodes were shifted between sessions or when signal characteristics varied due to day-to-day changes in skin conductance. This stability was achieved by modifying the training protocol to include representative examples of inputs acquired with different electrode configurations, allowing the system to learn to generalise across such sources of variability. In both cases, the outcome is a system that exhibits substantial robustness to practical sources of inconsistency, such as array placement or skin-electrode interface quality.

There are, however, limitations to this robustness. Adjustments to the training pipeline that compensate for displacement or variability increase training time and complexity, requiring additional data curation and extended calibration procedures.

A more fundamental constraint arises in relation to cross-subject generalisation. Models trained exclusively on a pool of sixteen unrelated participants performed worse than subject-specific models, with MD increasing by 33% and MPCC decreasing by 25%. Furthermore, this degradation in performance worsened as additional subjects were added to the training set, indicating that increased heterogeneity does not compensate for the absence of individualised data. These findings suggest that while the system tolerates many types of signal variability, subject-specific calibration remains indispensable for effective operation.

Taken together, the results position the RPC-Net/HDE-Array system as both resilient and practically viable. With minimal per-user calibration, it can maintain performance in the presence of common real-world disturbances such as skin-electrode impedance variation, array repositioning and inter-session noise. This tolerance represents a critical step towards broader clinical translation, supporting deployment not only in controlled research environments but also in physiotherapy clinics, rehabilitation wards and potentially in domestic settings.

9.1.3 Theme 3: User-centred Control Efficacy

The final theme concerns how well participants, both able-bodied and tetraplegic, were able to use the RPC-Net/HDE-Array system to perform online, multi-DoF control tasks. This aspect is primarily addressed in Chapters 7 and 8, and across both studies the overall picture is encouraging. In Chapter 7, subjects were able to control a virtual hand model with accuracy well within commonly accepted thresholds (50 mm MD), and this remained true even in the absence of visual feedback, as shown in Figure 7.5 and Figure 7.7. Importantly, these results were not limited to forearm-based control. Chapter 8 demonstrates that neck-muscle signals, recorded via HD-sEMG, can be used to achieve similar performance, with average fingertip distances and task success rates falling within the same range as those obtained with forearm recordings. This finding held across both healthy and tetraplegic participants, including individuals with cervical spinal cord injuries

at C5 and C4-C5 levels, suggesting that the system can support online control in populations for whom traditional signal sources are inaccessible or unreliable.

However, despite this overall success, several limitations must be acknowledged. Performance varied considerably between individuals, particularly in more complex control scenarios. While most subjects were able to complete the tasks with reasonable accuracy, Chapter 7 shows a clear spread in performance metrics across participants, even under standardised conditions. A similar trend was observed in Chapter 8, where inter-subject differences persisted even after familiarisation with the interface. Moreover, in Section 8.3.3, a marked drop in performance was recorded as task complexity increased (i.e., when tasks included a threshold as well as a target). This observation is particularly relevant because all experiments were conducted in highly controlled environments. If such performance degradation occurs under optimal conditions, it is likely to be amplified in less structured, real-world settings.

Still, the evidence suggests that, with appropriate setup and a modest learning period, both healthy and tetraplegic users can achieve reliable, multi-DoF control using the RPC-Net/HDE-Array system. The ability to support simultaneous and proportional control using physiological signals from non-traditional sites, such as the neck, broadens the accessibility of the system, and its demonstrated usability across subject groups opens a path towards inclusive rehabilitation technologies. While the observed variability highlights the need for individual calibration and potentially longer familiarisation phases, the overall success of these experiments offers a promising foundation for future user-facing deployments.

9.1.4 Theme Summary

Taken together, the evidence presented across these themes demonstrates that the RPC-Net/HDE-Array system achieves clinically relevant decoding accuracy, accommodates a range of hardware and signal conditions, and enables effective multi-DoF control by both healthy and impaired users. These capabilities provide a strong empirical basis for the theoretical contributions articulated in Section 9.2.

9.2 Theoretical Integration and Contribution

This section distils the integrated findings presented in the six chapters making up this thesis into two tasks: (1) benchmarking them against prevailing work in neuro-rehabilitation and EMG-based control, and (2) pinpointing the genuinely novel insights yielded by the RPC-Net/HDE-Array programme. The goal is to clarify how this thesis shifts the baseline understanding of the field.

9.2.1 Alignment and Divergence with Existing Literature

- **Chapter 3:** The main finding is that the RPC-Net algorithm can translate EMG into hand position with high accuracy (25 mm MD, 0.75 MPCC). While algorithms capable of this exist in the literature, RPC-Net distinguishes itself through the completeness of DoFs controlled [301, 328], the use of proximally placed electrodes only [346], and its low computational requirements [364, 365]. Furthermore, this chapter demonstrates that high-quality regression can be achieved using simple fully connected architectures rather than more complex convolutional ones, as confirmed by comparisons with state-of-the-art CNN-based solutions [293, 360, 361].
- **Chapter 4:** This chapter presents two results that extend prior work. First, the higher signal variability observed around the forearm circumference ($p < 0.001$) aligns with the known anatomical arrangement of forearm muscles [380]. In this context, the HDE-Array provides a higher circumferential resolution than any previous dry-electrode array, leveraging this anatomical feature [330, 393]. Second, the impedance of the electrodes embedded in the HDE-Array, once normalised (median 661 kΩ, area of 12.57 mm^2, resulting in a median normalised impedance of 83 kΩ·cm^2), aligns with the theoretical estimate of 58.50 $\pm$ 64.16 kΩ·cm^2 reported in [377]. Overall, while the dry electrodes exhibit higher impedance across the frequency spectrum, their electrical properties remain within the acceptable range for HD-sEMG acquisition, consistent with previous findings [357, 395].

- **Chapter 5:** This study evaluated the number of PCs needed to account for 90% of hand-movement variance. The results show that this threshold is reached with 12 PCs across subjects and with as few as 8 PCs for individual participants. These findings diverge from earlier studies, which reported higher PC counts to explain similar levels of variance, potentially due to differences in experimental protocols or the greater kinematic complexity of movements examined here [398, 400, 405, 406].
- **Chapter 6:** This study presents two key extensions to the existing literature. First, it quantifies the degradation in performance when a position estimation model is tested on data acquired under different conditions from those used for training. The resulting accuracy (MD = 65.1 mm, MPCC = 0.34) falls well below acceptable thresholds and is significantly worse than comparable approaches reported in the literature [300]. Second, the chapter provides insights into the ability of similar models to generalise across users. These findings align with recent work on sEMG inter-subject generalisation and reinforce the importance of combining personalised calibration with scalable generalisation strategies in the design of muscle-computer interfaces [417].
- **Chapter 7:** This chapter compares subject performance in an HD-sEMG control task using RPC-Net, with and without visual feedback. Results show that the absence of visual feedback does not significantly affect control performance when all subjects are considered together ($p = 0.44$). This finding contrasts with prior studies that reported marked improvements under visual feedback conditions [422–425]. Several factors may account for this discrepancy, including the task-specific nature of the protocol and the high similarity between training and testing setups. Nevertheless, these results suggest that the RPC-Net/HDE-Array system retains usability even in the absence of explicit visual feedback.
- **Chapter 8:** This chapter provides evidence that participants can successfully perform a 3-DoF control task using neck muscles as the input source, with minimal training and a short acquisition protocol. These findings are in

line with previous studies exploring neck-based control interfaces [447, 455, 456]. Notably, performance was comparable between healthy and tetraplegic individuals (with cervical spinal cord injuries at the C5 and C4-C5 levels), extending prior work and demonstrating the accessibility of the system across diverse user groups.

9.2.2 New Insights Beyond the Literature

- **Chapter 3:** The results show that the performance improvement gained by incorporating previous-state information is consistent across both subjects and conditions. This finding is important because temporal recursion is a defining feature of RPC-Net, setting it apart from similar approaches. Additionally, the demonstrated robustness of RPC-Net to variations in input shape (e.g., window length, channel count) represents a novel contribution to the literature on regression-based EMG decoding.
- **Chapter 4:** The findings show that the performance of RPC-Net using the HDE-Array is not significantly different from that achieved with gel electrodes ($p = 0.25$ and $p = 0.21$), with a slight trend towards better performance using the HDE-Array. This trend reaches statistical significance when electrode layouts are matched, with HDE-Array outperforming gel electrodes ($p = 0.04$ and $p = 0.01$). These results provide new evidence that dry, circumferentially distributed arrays can match, or exceed, the decoding performance of standard gel-based configurations.
- **Chapter 5:** This study presents a novel finding regarding dimensionality reduction: only five principal components are required to preserve 90% of estimation accuracy when measured by MD, and eleven PCs suffice to retain 90% of asymptotic MPCC. This significantly lowers previous estimates and highlights the potential of PCA-based compression to simplify inference and reduce hardware demands in practical deployments of RPC-Net.
- **Chapter 6:** A key innovation in this chapter is the introduction of a simple training protocol that significantly mitigates the performance loss caused

by changes in electrode positioning or session variability. By deliberately introducing variability during the training phase, via repeated repositioning and skin preparation, the model learns to generalise across conditions. In this configuration, the performance drop between intra- and extra-session testing is reduced to less than 8 mm, with extra-session MD falling below 45 mm. These values are within the range of viable control and mark a step forward in the robustness of regression-based EMG decoders.

- **Chapter 7:** This chapter provides practical real-time validation of the RPC-Net/HDE-Array system in virtual hand control tasks. The system was validated both in terms of feasibility (e.g., inference time, system stability) and control accuracy. Subjects achieved performance levels comparable to those reported in the literature [300, 328, 421], demonstrating that the architecture is suitable not only for offline decoding but also for interactive control applications in online settings.
- **Chapter 8:** This chapter demonstrates that RPC-Net (or its variant, RFC-Net) can successfully drive a multi-DoF kinematic hand model using a novel control source: neck muscle signals. This is a significant development, as it extends the applicability of the system beyond prosthetic control for amputees to other rehabilitation contexts where traditional EMG sites are inaccessible. Notably, tetraplegic participants (with cervical spinal cord injuries at the C5 and C4-C5 levels) achieved control performance comparable to that of healthy individuals, supporting the feasibility of the system for inclusive, real-world neurorehabilitation applications.

9.2.3 Synthesis

Together, the findings presented in this section demonstrate that the RPC-Net/HDE-Array platform not only aligns with but in several respects advances the current state of the art in EMG-based control. Across all six chapters, the system was shown to achieve competitive or superior accuracy, maintain robustness across sessions and subjects, and extend applicability to new control sites and user groups.

Beyond benchmarking, this thesis contributes several novel insights, ranging from recursive signal integration and PCA-driven dimensionality reduction to training protocols for generalisation and validation in real-time scenarios. Collectively, these advances help close the gap between laboratory-grade performance and practical deployment in inclusive rehabilitation technologies.

9.3 Methodological Strengths and Shared Limitations

This section critically evaluates the methodological foundations of the six experimental chapters, treating them as a unified body of work. It highlights cross-cutting strengths that enhance the credibility, reproducibility, and applicability of the findings, while also acknowledging shared limitations that may constrain generalisability or introduce bias.

9.3.1 Cross-Study Methodological Strengths

1. **Unified end-to-end pipeline (hardware + software + processing):** All six studies used the same HDE-Array hardware, RPC-Net codebase, and pre-processing scripts, minimising cross-study variability.
2. **Well-defined participant inclusion criteria:** Forty able-bodied and ten tetraplegic volunteers met identical age, health, and consent requirements, providing two clearly delineated cohorts.
3. **External benchmarking:** Each chapter benchmarks its results against at least two high-impact studies, using similar metrics for comparison.
4. **User-centred iterative design:** Post-session interviews shaped electrode layout, donning procedures, and interface parameters.
5. **Clear concatenation of aims for subsequent chapters:** Each experiment addresses a research question that logically extends the previous one, reducing duplication and sharpening cumulative evidence.

6. **Pre-clinical validation with end-users:** Online control tasks were performed by both able-bodied and tetraplegic participants, demonstrating usability beyond benchtop testing.
7. **Sensitivity analyses across key parameters:** Systematic sweeps over electrode count, window length, and principal-component number quantified accuracy-latency trade-offs.
8. **Commitment to open science:** Source code (Dropbox) and the annotated HD-sEMG/kinematic dataset (Zenodo) are publicly available, enabling full reproducibility.
9. **Multi-institutional collaboration:** The work integrates expertise from three universities and two clinical centres, enhancing sample diversity and external validity.

9.3.2 Shared Limitations

1. **Subject numbers:** The dataset underlying Chapter 6 and 7 includes only four participants, substantially fewer than those in Chapters 3, 4, and 5. While this reduces the statistical power of the corresponding validation results, this limitation is acknowledged in the respective chapters, and preliminary findings are presented with appropriate caution.
2. **Reliance on external hardware:** All studies relied on a portable EMG amplifier developed externally. Although validating the acquisition and processing pipeline was the primary objective of this thesis, the absence of a proprietary amplifier limits hardware independence. Additionally, the HDE-Array remains a custom prototype and has not yet been scaled for wider deployment.
3. **Manual Assembly and Reproducibility:** The HDE-Array still relies on manual assembly steps, particularly during the embedding of the elastic bands. Although the fabrication of the polyimide electrode layer has been standardised, the integration of the elastic component currently depends on hand alignment and manual securing, which introduces variability and

limits reproducibility. To enable large-scale production, an automated and quality-controlled embedding process is needed to ensure uniform mechanical properties, stable electrode positioning, and consistent electrical performance across units.

4. **Comparison with state of the art:** Due to the novelty of certain research directions, direct comparisons with existing literature were not always feasible. Wherever possible, analogous studies were cited to provide reference points for benchmarking.
5. **Limited ecological validity:** Most experiments were conducted in controlled laboratory settings, using structured tasks. While this approach ensured consistency, it limits the ecological validity of the findings, an issue that should be addressed in future studies involving real-world scenarios.
6. **Participant diversity:** Participants in Chapters 3 through 7 were relatively homogeneous in terms of age and health status. While Chapter 8 partially mitigates this by including individuals with tetraplegia and of a wider age group, broader demographic diversity remains an area for future improvement to strengthen generalisability.

9.3.3 Synthesis

Taken together, the methodological profile of this thesis is robust: a unified hardware-software pipeline, rigorous analytics, open-science practices, and multi-institutional collaboration underpin the credibility of the findings. At the same time, shared constraints, most notably small samples in two chapters, reliance on a bespoke amplifier, and largely laboratory-based tasks, temper the breadth of the conclusions. By explicitly acknowledging these caveats and framing them as targets for future longitudinal, field-based studies with more diverse cohorts, the thesis provides a transparent foundation on which subsequent clinical translation and technological refinement can build.

9.4 Implications and Concluding Synthesis

9.4.1 Practice, Policy, and Management

The RPC-Net/HDE-Array platform represents the first open-source framework capable of decoding high-density surface EMG into multi-DoF kinematics with clinic-level accuracy and sub-second latency. While the current implementation requires a connection to an external computer or embedded processor, the model can be scaled down to operate within the constraints of embedded hardware, highlighting its potential for truly portable deployment. Its most immediate impact lies in rehabilitation technology. For prosthetic users, the system promises quicker fitting, more intuitive control, and at-home calibration, features that can lower abandonment rates and reduce the need for prolonged clinical supervision. For individuals with tetraplegia, the same decoding engine has been validated on neck-muscle signals, opening a low-risk pathway to FES protocols that would otherwise demand constant therapist oversight.

Beyond direct patient care, the HDE-Array itself constitutes a transferable asset. Its unprecedented circumferential resolution and dry-electrode design simplify sensor placement, shorten setup time, and expand recording sites; these characteristics make it attractive not only to rehabilitation engineers but also to researchers in motor-control physiology, sports science, and ergonomics. Finally, the open architecture of the platform invites adaptation for non-medical domains, such as immersive gaming, vehicle teleoperation, and human-robot interaction, where silent, muscle-based interfaces could offer intuitive alternatives to conventional controllers. In sum, the technology validated here equips clinicians, device manufacturers, and policy-makers with a versatile blueprint for inclusive, user-centred assistive solutions.

9.4.2 Directions for Future Research

While this thesis successfully validated the RPC-Net/HDE-Array system in real-time tasks and in motor-impaired participants, further research is required to transition

this solution into clinical and non-clinical real-world settings, the ultimate goal of this work. This section outlines five key directions that emerge from the current findings:

1. **Development of a generalisation framework for RPC-Net training:** Chapters 6 and 7 examined robustness to intra-subject variability and inter-subject generalisation. While the former was mitigated through tailored training protocols, cross-subject generalisation remains a persistent challenge. A practical constraint of the RPC-Net/HDE-Array system lies in the anisotropic distribution of electrodes around the forearm circumference, where repeated applications can yield centimetre-scale shifts even under identical donning procedures. To address this, future work should transition from treating channels as independent inputs to modelling a single, continuous circumferential activation field. The core objective would be to develop an algorithm that, given a 32- or 64-channel acquisition, infers the most likely angular positions of the electrodes on the circumference, reconstructs the underlying activation pattern, and performs decoding based on that pattern rather than on fixed channel indices. A Bayesian formulation would be particularly suitable, combining a prior over plausible electrode layouts with a likelihood informed by spatial smoothness and muscle anatomy to infer the latent circular alignment. A proposed study could involve developing and validating this alignment-and-decoding pipeline using a simple protocol with six hand poses and two to three repetitions per pose, deliberately maximising within-subject repositioning. A target of eight repositionings per subject should introduce sufficient variability, and a cohort of 32 participants would approximately double the scale of the present work while remaining logistically feasible. Primary endpoints would include (i) the ability of the algorithm to accurately reconstruct the original electrode positions and (ii) the performance of an RPC-Net variant trained to use the reconstructed circumferential activation field as input, rather than discrete channel features.
2. **Feasibility of control by amputees:** Although the system was conceived for transradial amputees, all participants in the present studies were either

able-bodied or tetraplegic. Future work should therefore include empirical validation in individuals with unilateral or bilateral upper-limb loss. A dedicated study could recruit transradial amputees with preserved forearm musculature and assess real-time control of a virtual hand using RPC-Net. An initial phase could focus on low-DoF tasks, such as isolated flexion and extension of single joints, within structured, task-based protocols comparable to those used in this thesis. Subsequent phases could progress to multi-joint or grasp-oriented control involving manipulation of virtual objects. Results should be benchmarked against current state-of-the-art algorithms to contextualise performance gains. Because the primary aim is methodological validation rather than clinical generalisation, a small sample size (fewer than ten participants) would be sufficient for preliminary assessment. For transhumeral users, where residual musculature and signal bandwidth are reduced, the RFC-Net variant could be adapted to integrate signals from remaining upper-arm muscles together with auxiliary sources such as the neck, shoulder, or contralateral limb.

3. **Integration with real prosthetic and FES devices:** The present work validated RPC-Net in virtual control tasks; however, translating the algorithm to real actuation hardware represents a critical next step towards clinical deployment. Embedded prototypes could be developed by deploying trained models onto low-power microcontrollers (e.g., ARM Cortex-M or NVIDIA Jetson Nano) integrated within prosthetic sockets. Access to suitable prosthetic hardware would likely be achieved through academic collaborations, enabling flexible interfacing and data acquisition. As in the previous study, early trials could focus on simple, low-DoF movements before progressing to task-oriented protocols involving grasping and manipulation of real or virtual objects. A first feasibility study could include a small cohort (2-4 participants) to verify integration stability, latency, and user control quality, followed by a larger validation study comparing results directly with existing commercial

and research-grade control strategies. For FES-based rehabilitation, RPC-Net could serve as the decoding layer in a closed-loop control architecture that modulates stimulation intensity and timing across a three-site FES system based on decoded motor intent. Initial technical validation should involve a small group of able-bodied volunteers using surface stimulators to assess latency, synchronisation precision, and comfort. Subsequent pilot trials could be conducted with participants with incomplete spinal cord injury or post-stroke hemiparesis to evaluate clinical feasibility. These studies would quantify the correspondence between decoded intention and evoked movement, providing evidence of safety, responsiveness, and user tolerance for self-directed stimulation control.

4. **Effectiveness of user-led FES therapies:** Once safe operation with stimulation hardware is confirmed, a pre-clinical trial could evaluate whether self-administered, RPC-Net-guided FES accelerates functional recovery compared with conventional, therapist-led protocols. This line of research would align with current clinical interest in the therapeutic potential of FES. Participants with subacute stroke or incomplete cervical spinal injury could perform daily home-based sessions in which decoded muscle activity triggers patterned stimulation sequences designed to reinforce voluntary movement. Primary outcomes could include improvements in Fugl-Meyer motor scores, EMG signal coherence, and task-specific dexterity measures across time. A key question would be whether residual motor intent, as decoded by RPC-Net, remains stable or undergoes systematic drift during neuroplastic adaptation. This stability would be crucial for long-term usability and autonomous operation. The study would also pose practical challenges, requiring a large number of participants in a largely unsupervised environment, necessitating robust remote monitoring, adaptive safety thresholds, and automatic signal-quality checks to ensure compliance and participant safety.
5. **User acceptance and device wearability:** With the system now technically validated, the next step is to determine whether it genuinely addresses the

limitations of current rehabilitation devices, specifically unintuitive control, demanding setup, and limited user satisfaction. A dedicated study should therefore assess user acceptance and perceived usability of the RPC-Net/HDE-Array system when used to control an actual prosthetic device. Participants, ideally transradial amputees already experienced with conventional myoelectric control, could perform a series of functional, task-oriented activities of daily living using both their standard control method and the RPC-Net interface in a crossover design. Quantitative measures (e.g., task completion rate, donning time, recalibration frequency) would be complemented by subjective assessments of intuitiveness, comfort, and satisfaction using standardised questionnaires such as the SUS and QUEST scales. A small to medium cohort (10-15 participants) would suffice to identify major usability trends. Comparison against established control algorithms would reveal whether RPC-Net truly reduces cognitive and operational burden, confirming its ability to meet the practical and experiential needs that have long hindered the adoption of upper-limb rehabilitation technologies.

9.5 Concluding Synthesis

Across six experimental studies, this thesis demonstrated that high-density surface EMG signals, captured via a dry, circumferentially distributed array and decoded through a recursive, low-latency neural architecture, can drive accurate, online control of multi-DoF hand kinematics. The RPC-Net/HDE-Array platform proved flexible across hardware configurations, robust under signal variability, and effective in both able-bodied and motor-impaired participants. By addressing long-standing barriers in usability, portability, and signal fidelity, this work helps bridge the gap between laboratory-grade performance and real-world deployment. In doing so, it lays the technical and empirical groundwork for a new generation of assistive technologies, ones that are not only accurate, but inclusive, intuitive, and clinically viable.

10 Conclusion

This thesis was motivated by a clear and pressing challenge: the widespread abandonment of upper-limb assistive technologies due to unintuitive control strategies and burdensome setup procedures. While prosthetic and rehabilitation hardware has advanced considerably, control systems have lagged behind, often relying on classification paradigms and sparse signal acquisition methods that do not align with the way humans naturally move. In response, this work proposed a new solution: the RPC-Net/HDE-Array platform, a joint software-hardware system designed to deliver accurate, user-centred, and practical multi-DoF control via high-density surface electromyography.

The system was evaluated through six experimental studies, each addressing a specific research question formulated in Chapter 2. Together, these studies demonstrate that the RPC-Net/HDE-Array platform delivers state-of-the-art decoding performance using shallow, low-latency neural networks and a wearable dry-electrode interface. The system proved robust across different electrode types, input configurations, and user populations, including individuals with cervical spinal cord injuries. Critically, it enabled online, proportional control using both forearm and neck muscles, underscoring its flexibility and inclusivity.

A summary of all hypotheses tested across the thesis is provided in Table 10.1. Out of eighteen experimental hypotheses, fourteen were supported. The remaining

four were not supported, pointing to key areas for further development, most notably the trade-offs introduced by extreme dimensionality reduction and the limits of cross-subject generalisation without individual calibration. These shortfalls do not undermine the viability of the platform; rather, they delineate the boundaries of current capabilities and define priorities for future optimisation.

Table 10.1: Summary of the hypotheses assessed in the six experimental chapters

Ch.	Hypothesis	Supported?
3	RPC-Net can generate high-quality hand position estimates from HD-sEMG signals, outperforming current state-of-the-art solutions	Yes
3	RPC-Net is robust against changes in input signal length and the number of electromyographic channels used	Yes
3	Information about previous position can improve estimation performance of RPC-Net	Yes
4	The estimation accuracy of RPC-Net using the HDE-Array is statistically indistinguishable from that obtained using gel-based electrodes	Yes
5	Five PCs are sufficient to explain at least 90% of the variance in a representative dataset of natural hand movements	No
5	As the number of principal components increases, the decoding performance of the RPC-Net/HDE-Array system approaches that of the full 29-DoF model, achieving at least 90% of full-model accuracy with five or fewer PCs	Yes
5	The decoding performance obtained, in terms of endpoint effector, using five PCs is non-inferior to that of the full 29-DoF kinematic model within a predefined tolerance of 10 mm	Yes
6	The accuracy of the RPC-Net/HDE-Array system decreases when electrode positioning is inconsistent between the training and testing sessions, compared to the baseline case in which electrode positioning remains consistent	Yes
6	When the RPC-Net/HDE-Array system is tested on data from the same session as the training data, its accuracy remains unchanged regardless of whether electrode repositioning is included during training	Yes

Continued on next page

Table 10.1 – continued from previous page

Ch.	Hypothesis	Supported?
6	The performance degradation observed when the system is trained without electrode repositioning and tested on data from a different session can be mitigated by incorporating electrode repositioning during training	Yes
6	Including inter-subject data in the training set improves the overall performance of the system, providing a valid alternative to an increased amount of subject-specific data	No
7	Subjects can achieve real-time control performance with the RPC-Net/HDE-Array system that mirrors the offline, user-independent accuracy of the system	Yes
7	Generalised training using inter-subject data will yield lower performance compared to training on subject-specific data	No
7	The addition of visual feedback during online control will result in better performance of the system	No
8	Subjects can control a hand kinematic model in real time using neck muscles and the RFC-Net/HDE-Array system, achieving task performance comparable to that observed with forearm muscle control	Yes
8	Performance in controlling the hand kinematic model using head and neck muscles, is comparable between tetraplegic and healthy subjects	Yes
8	Subjects can successfully use the RFC-Net/HDE-Array system to control three independent cursors in a task-oriented experiment, with 1 DoF per cursor	Yes
8	Performance in the cursor-based task is comparable between healthy and tetraplegic subjects	Yes

Of the 18 hypotheses considered, 14 were successfully demonstrated.

The contributions of this thesis are fourfold:

1. it introduces a physiologically inspired, recursive regression architecture for continuous EMG decoding;
2. it presents a dry, adjustable, circumferential HD-sEMG interface suitable for everyday use;
3. it integrates these components into a unified platform validated across offline,

online, and impaired-user settings; and

4. it provides high-quality datasets and an open-source codebase to support reproducibility and further research.

Together, these contributions advance the understanding of the field of muscle-computer interfacing and move the needle closer to user-friendly, clinically viable solutions.

The results also offer broader theoretical and practical insights. They show that shallow networks, when structured recursively, can match or exceed the performance of deeper models, even in high-dimensional control tasks. They also demonstrate that dry-electrode arrays, if carefully designed, can achieve signal quality equivalent to or better than gel-based alternatives. Most importantly, the demonstrated usability of the platform across diverse users and control sites suggests that intuitive, inclusive rehabilitation interfaces are not only feasible but ready for translation.

Nonetheless, the work presented here has limitations. Chapters 6 and 7 involved relatively small samples, and no amputee participants were included. The system was validated in structured laboratory conditions, and the hardware remains at a prototype stage. Future research should address these constraints by

1. developing generalisation frameworks that enable calibration-free operation,
2. conducting trials with amputees and broader clinical cohorts,
3. integrating the decoder with commercial prostheses and FES systems, and
4. evaluating long-term usability and user satisfaction in naturalistic settings.

In sum, this thesis demonstrates that intuitive, proportional, real-time control of upper-limb kinematics is achievable using a lightweight, wearable HD-sEMG platform. By closing the gap between decoding performance and practical usability, the RPC-Net/HDE-Array system lays the groundwork for a new generation of assistive devices, ones that are not only accurate but accessible, adaptable, and truly aligned with the needs of their users.

References

[1] Mark R. Casterline. “Trail Guide to the Body: How to Locate Muscles, Bones and More”. In: *Journal of Athletic Training* 33.3 (1998). Print, pp. 284–285.

[2] Susan Standring. *Gray’s Anatomy: The Anatomical Basis of Clinical Practice*. 42nd ed. Print. New York: Elsevier, 2021.

[3] John E. Hall and Michael E. Hall. *Guyton and Hall Textbook of Medical Physiology*. 14th ed. Print. Philadelphia, PA: Elsevier, 2021.

[4] Frank H. Netter. *Netter Atlas of Human Anatomy: Classic Regional Anatomy Approach*. 8th ed. Print. Philadelphia, PA: Elsevier, 2023.

[5] Jintae Lee and T.L. Kunii. “Model-based analysis of hand posture”. In: *IEEE Computer Graphics and Applications* 15.5 (1995), pp. 77–86.

[6] M.Á. Sánchez-Urán et al. S. Cobos M. Ferre. “Human hand descriptions and gesture recognition for object manipulation”. In: *Computer Methods in Biomechanics and Biomedical Engineering* (2010).

[7] Matthieu Bray et al. “Stochastic optimisation for high-dimensional tracking in dense range maps”. In: *IEE Proceedings-Vision, Image and Signal Processing* 152.4 (2005), pp. 501–512.

[8] Joe Chalfoun et al. “Muscle forces prediction of the human hand and forearm system in highly realistic simulation”. In: *2004 IEEE/RSJ International Conference on Intelligent Robots and Systems (IROS)(IEEE Cat. No. 04CH37566)*. Vol. 2. IEEE. 2004, pp. 1293–1298.

[9] James J Kuch and Thomas S Huang. “Human computer interaction via the human hand: a hand model”. In: *Proceedings of 1994 28th Asilomar Conference on Signals, Systems and Computers*. Vol. 2. IEEE. 1994, pp. 1252–1256.

[10] Huan Du and Edoardo Charbon. “3D hand model fitting for virtual keyboard system”. In: *2007 IEEE Workshop on Applications of Computer Vision (WACV’07)*. IEEE. 2007, pp. 31–31.

[11] M Renault and FB Ouezdou. “Dynamic simulation of hand-forearm system”. In: *Proceedings 10th IEEE International Workshop on Robot and Human Interactive Communication. ROMAN 2001 (Cat. No. 01TH8591)*. IEEE. 2001, pp. 20–25.

[12] Ian Bales and Haohan Zhang. “A six degrees-of-freedom cable-driven robotic platform for head–neck movement”. In: *Scientific Reports* 14.1 (2024), p. 8750.

[13] EANS Edirisinghe et al. “Design and simulation of a human-like robot neck mechanism”. In: *2015 Electrical Engineering Conference [EECon]*. Vol. 1893. 2015.

[14] Renaud Hage et al. “Head pitch angular velocity discriminates (Sub-) Acute neck pain patients and controls assessed with the DidRen laser test”. In: *Sensors* 22.7 (2022), p. 2805.

[15] Zeljka Mihajlovic et al. “A system for head-neck rehabilitation exercises based on serious gaming and virtual reality”. In: *Multimedia Tools and Applications* 77 (2018), pp. 19113–19137.

[16] José Luis Rueda-Arreguín, Marco Ceccarelli, and Christopher René Torres-SanMiguel. “Design of an articulated neck to assess impact head-neck injuries”. In: *Life* 12.2 (2022), p. 313.

[17] Bernadus Kristyanto et al. “Head and neck movement: simulation and kinematics analysis”. In: *Procedia Manufacturing* 4 (2015), pp. 359–372.

[18] Francisco J López-Valdés et al. “The six degrees of freedom motion of the human head, spine, and pelvis in a frontal impact”. In: *Traffic injury prevention* 15.3 (2014), pp. 294–301.

[19] Global Burden of Disease Collaborative Network. *Global Burden of Disease Study 2021 (GBD 2021) Results*. Accessed: April 2025. Seattle, United States, 2024. URL: `https://vizhub.healthdata.org/gbd-results/`.

[20] Global Burden of Disease Collaborative Network. *Global Burden of Disease Study 2021 (GBD 2021) Socio-Demographic Index (SDI) 1950–2021*. Accessed: April 2025. Seattle, United States of America, 2024. URL: `http://ghdx.healthdata.org/record/ihme-data/gbd-2021-sociodemographic-index-sdi-1950-2021`.

[21] S. Gu et al B. Yuan D. Hu. “The global burden of traumatic amputation in 204 countries and territories”. In: *Frontiers in Public Health* (2023).

[22] Kristin Østlie et al. “Prosthesis use in adult acquired major upper-limb amputees: patterns of wear, prosthetic skills and the actual use of prostheses in activities of daily life”. In: *Disability and Rehabilitation: Assistive Technology* 7.6 (2012), pp. 479–493.

[23] Amanda H Sugar, Rebecca Ozelie, and Kristi Turner. “The Occupational Therapy Practitioner Experience and Practice Related to Upper Limb Loss or Difference and Prosthetics.” In: *Journal of Occupational Therapy Education* 8.2 (2024), p. 17.

[24] Sandra L Hubbard Winkler. “Upper limb amputation and prosthetics epidemiology, evidence, and outcomes”. In: *Care of the Combat Amputee* (2009), pp. 597–605.

[25] Timothy R Dillingham, Liliana E Pezzin, and Ellen J MacKenzie. “Limb amputation and limb deficiency: epidemiology and recent trends in the United States”. In: *Southern medical journal* 95.8 (2002), pp. 875–884.

[26] Germain Pomares et al. “Epidemiology of traumatic upper limb amputations”. In: *Orthopaedics & Traumatology: Surgery & Research* 104.2 (2018), pp. 273–276.

[27] Kristin Østlie et al. “Adult acquired major upper limb amputation in Norway: prevalence, demographic features and amputation specific features. A population-based survey”. In: *Disability and rehabilitation* 33.17-18 (2011), pp. 1636–1649.

[28] Elizabeth Inkellis et al. “Incidence and characterization of major upper-extremity amputations in the National Trauma Data Bank”. In: *JBJS Open Access* 3.2 (2018), e0038.

[29] Yasmin Ezzatvar and Antonio García-Hermoso. "Global estimates of diabetes-related amputations incidence in 2010–2020: a systematic review and meta-analysis". In: *Diabetes research and clinical practice* 195 (2023), p. 110194.

[30] Ze-Jian Chen et al. "Effects of repetitive peripheral magnetic stimulation for the upper limb after stroke: Meta-analysis of randomized controlled trials". In: *Heliyon* 9.5 (2023).

[31] Janne M Veerbeek et al. "Early prediction of outcome of activities of daily living after stroke: a systematic review". In: *Stroke* 42.5 (2011), pp. 1482–1488.

[32] Caroline Winters et al. "Generalizability of the proportional recovery model for the upper extremity after an ischemic stroke". In: *Neurorehabilitation and neural repair* 29.7 (2015), pp. 614–622.

[33] Anoushka Singh et al. "Global prevalence and incidence of traumatic spinal cord injury". In: *Clinical epidemiology* (2014), pp. 309–331.

[34] John F Ditunno Jr et al. "Recovery of upper-extremity strength in complete and incomplete tetraplegia: a multicenter study". In: *Archives of physical medicine and rehabilitation* 81.4 (2000), pp. 389–393.

[35] Ralph J Marino et al. "Upper-and lower-extremity motor recovery after traumatic cervical spinal cord injury: an update from the national spinal cord injury database". In: *Archives of physical medicine and rehabilitation* 92.3 (2011), pp. 369–375.

[36] Sonja Von Campenhausen et al. "Prevalence and incidence of Parkinson's disease in Europe". In: *European neuropsychopharmacology* 15.4 (2005), pp. 473–490.

[37] Elaine Kingwell et al. "Incidence and prevalence of multiple sclerosis in Europe: a systematic review". In: *BMC neurology* 13 (2013), pp. 1–13.

[38] Lidwine B Mokkink et al. "The Arm Function in Multiple Sclerosis Questionnaire (AMSQ): development and validation of a new tool using IRT methods". In: *Disability and rehabilitation* 37.26 (2015), pp. 2445–2451.

[39] Davide Cattaneo et al. "Participation restriction in people with multiple sclerosis: prevalence and correlations with cognitive, walking, balance, and upper limb impairments". In: *Archives of physical medicine and rehabilitation* 98.7 (2017), pp. 1308–1315.

[40] Wei Chen et al. "Rest tremor revisited: Parkinson's disease and other disorders". In: *Translational neurodegeneration* 6 (2017), pp. 1–8.

[41] H. Hasan et al. "Objective Decrement in Parkinson's Disease—A New Parameter for the BRAIN Tap Test". In: *20th International Congress of Parkinson's Disease and Movement Disorders*. June 2016.

[42] Juan Manuel Breyer, Pamela Vergara, and Alfonso Perez. "Epidemiology of adult traumatic brachial plexus injuries". In: *Operative Brachial Plexus Surgery: Clinical Evaluation and Management Strategies*. Springer, 2021, pp. 63–68.

[43] Lukas Rasulić et al. "Outcome after brachial plexus injury surgery and impact on quality of life". In: *Acta neurochirurgica* 159 (2017), pp. 1257–1264.

[44] Mukund R Thatte, Sonali Babhulkar, and Amita Hiremath. "Brachial plexus injury in adults: Diagnosis and surgical treatment strategies". In: *Annals of Indian Academy of Neurology* 16.1 (2013), pp. 26–33.

[45] Álvaro Baik Cho et al. “Epidemiological study of traumatic brachial plexus injuries”. In: *Acta ortopedica brasileira* 28.1 (2020), pp. 16–18.

[46] Sheikh Usman Iqbal et al. *The Veterans RAND 12 Item Health Survey (VR-12): What It Is and How It Is Used*. Available online. Boston University School of Public Health. 2007. URL: https://www.bu.edu/sph/files/2015/01/%20veterans%5C_rand%5C_12%5C_item%5C_health%5C_survey%5C_vr-12%5C_2007.pdf.

[47] Linda Resnik et al. “A national study of Veterans with major upper limb amputation: Survey methods, participants, and summary findings”. In: *PloS one* 14.3 (2019), e0213578.

[48] Alfredo J Selim et al. “Updated US population standard for the Veterans RAND 12-item Health Survey (VR-12)”. In: *Quality of life research* 18 (2009), pp. 43–52.

[49] Nathan T Kearns et al. “Posttraumatic stress disorder symptom clusters and substance use among patients with upper limb amputations due to traumatic injury”. In: *Disability and rehabilitation* 41.26 (2019), pp. 3157–3164.

[50] Dorcas E Beaton et al. “Development of the QuickDASH: comparison of three item-reduction approaches”. In: *JBJS* 87.5 (2005), pp. 1038–1046.

[51] Turid Aasheim and Vilhjalmur Finsen. “The DASH and the QuickDASH instruments. Normative values in the general population in Norway”. In: *Journal of Hand Surgery (European Volume)* 39.2 (2014), pp. 140–144.

[52] Deirdre M Desmond. “Coping, affective distress, and psychosocial adjustment among people with traumatic upper limb amputations”. In: *Journal of psychosomatic research* 62.1 (2007), pp. 15–21.

[53] Carolien M Kooijman et al. “Phantom pain and phantom sensations in upper limb amputees: an epidemiological study”. In: *Pain* 87.1 (2000), pp. 33–41.

[54] Christina Lee et al. “Employment status in individuals with upper-limb amputation: a survey of current trends”. In: *JPO: Journal of Prosthetics and Orthotics* 34.2 (2022), pp. 79–88.

[55] Kristin Østlie et al. “Mental health and satisfaction with life among upper limb amputees: a Norwegian population-based survey comparing adult acquired major upper limb amputees with a control group”. In: *Disability and Rehabilitation* 33.17-18 (2011), pp. 1594–1607.

[56] Salwa A Mohammed and Amany M Shebl. “Quality of life among Egyptian patients with upper and lower limb amputation: sex differences”. In: *Advances in medicine* 2014.1 (2014), p. 674323.

[57] R. Sacchetti et al. F. Cordella A. Ciancio. “Literature Review on Needs of Upper Limb Prosthesis Users”. In: *frontiers in Neuroscience* (2016).

[58] P.J. Kyberd and W. Hill. “Survey of upper limb prosthesis users in Sweden, the United Kingdom and Canada”. In: *Prosthetics and Orthotics International* (2011).

[59] Elaine Biddiss, Dorcas Beaton, and Tom Chau. “Consumer design priorities for upper limb prosthetics”. In: *Disability and rehabilitation: Assistive technology* 2.6 (2007), pp. 346–357.

[60] H.E. Yang et al. C.H. Jang H.S. Yang. "A Survey on Activities of Daily Living and Occupations of Upper Extremity Amputees". In: *Annals of Rehabilitation Medicine* (2011).

[61] Christian Pylatiuk, Stefan Schulz, and Leonhard Döderlein. "Results of an Internet survey of myoelectric prosthetic hand users". In: *Prosthetics and orthotics international* 31.4 (2007), pp. 362–370.

[62] Jason Bouffard et al. "Interactions between the phantom limb sensations, prosthesis use, and rehabilitation as seen by amputees and health professionals". In: *JPO: Journal of Prosthetics and Orthotics* 24.1 (2012), pp. 25–33.

[63] Martina Luchetti et al. "Impact of Michelangelo prosthetic hand: Findings from a crossover longitudinal study". en. In: *J. Rehabil. Res. Dev.* 52.5 (2015), pp. 605–618.

[64] E Biddiss and T Chau. "Upper extremity prosthesis use and abandonment: A survey of the last 25 years". In: *Prosthet Orthot Int* (2007).

[65] T. Chau E. Biddiss. "Upper-Limb Prosthetics. Critical Factors in Device Abandonment". In: *American Journal of Physical Medicine and Rehabilitation* (2007).

[66] Heather L Benz et al. "Upper extremity prosthesis user perspectives on unmet needs and innovative technology". In: *2016 38th Annual International Conference of the IEEE Engineering in Medicine and Biology Society (EMBC)*. IEEE. 2016, pp. 287–290.

[67] C. Wilkins L.C. Smail C. Neal. "Comfort and function remain key factors in upper limb prosthetic abandonment: findings of a scoping review". In: *Disability and Rehabilitation: Assistive Technology* (2020).

[68] Ning Jiang et al. "Myoelectric Control of Artificial Limbs - Is There a Need to Change Focus? [In the Spotlight]". In: *IEEE Signal Processing Magazine* 29.5 (2012), pp. 152–150.

[69] L. H. Pichler S. Salminger H. Stino. "Current rates of prosthetic usage in upper-limb amputees – have innovations had an impact on device acceptance?" In: *Disability and Rehabilitation* (2020).

[70] Linda Resnik, Matthew Borgia, and Melissa Clark. "Function and quality of life of unilateral major upper limb amputees: effect of prosthesis use and type". In: *Archives of physical medicine and rehabilitation* 101.8 (2020), pp. 1396–1406.

[71] Timothy Kwok et al. "Quality of life of stroke survivors: a 1-year follow-up study". In: *Archives of physical medicine and rehabilitation* 87.9 (2006), pp. 1177–1182.

[72] Cathy L Bays. "Quality of life of stroke survivors: a research synthesis". In: *Journal of Neuroscience Nursing* 33.6 (2001), pp. 310–316.

[73] Peter Kim et al. "Quality of life of stroke survivors". In: *Quality of life research* 8 (1999), pp. 293–301.

[74] Fiona Coupar et al. "Predictors of upper limb recovery after stroke: a systematic review and meta-analysis". In: *Clinical rehabilitation* 26.4 (2012), pp. 291–313.

[75] Floor Buma, Gert Kwakkel, and Nick Ramsey. "Understanding upper limb recovery after stroke". In: *Restorative neurology and neuroscience* 31.6 (2013), pp. 707–722.

[76] Rosie Goulding, Debbie Thompson, and Chris Beech. “Caring for patients with hemiplegia in an arm following a stroke”. In: *British journal of nursing* 13.9 (2004), pp. 534–539.

[77] Torgeir Bruun Wyller et al. “Subjective well-being one year after stroke”. In: *Clinical rehabilitation* 11.2 (1997), pp. 139–145.

[78] Tamara Bushnik. “Access to equipment, participation, and quality of life in aging individuals with high tetraplegia (C1-C4)”. In: *Topics in Spinal Cord Injury Rehabilitation* 7.3 (2002), pp. 17–27.

[79] K Whalley Hammell. “Exploring quality of life following high spinal cord injury: a review and critique”. In: *Spinal cord* 42.9 (2004), pp. 491–502.

[80] Justyna Frasuńska, Beata Tarnacka, and Piotr Wojdasiewicz. “Quality of life in patients with tetraplegia and paraplegia after traumatic spinal cord injury”. In: *Advances in Psychiatry and Neurology/Postępy Psychiatrii i Neurologii* 29.3 (2020), pp. 143–153.

[81] M Elise Johanson. “Rehabilitation after surgical reconstruction to restore function to the upper limb in tetraplegia: a changing landscape”. In: *Archives of physical medicine and rehabilitation* 97.6 (2016), S71–S74.

[82] Kim D Anderson. “Targeting recovery: priorities of the spinal cord-injured population”. In: *Journal of neurotrauma* 21.10 (2004), pp. 1371–1383.

[83] Govert J Snoek et al. “Survey of the needs of patients with spinal cord injury: impact and priority for improvement in hand function in tetraplegics”. In: *Spinal cord* 42.9 (2004), pp. 526–532.

[84] Lutong Li et al. “A scoping review of design requirements for a home-based upper limb rehabilitation robot for stroke”. In: *Topics in stroke rehabilitation* 29.6 (2022), pp. 449–463.

[85] Shane Forbrigger et al. “Considerations for at-home upper-limb rehabilitation technology following stroke: Perspectives of stroke survivors and therapists”. In: *Journal of Rehabilitation and Assistive Technologies Engineering* 10 (2023), p. 20556683231171840.

[86] Frederik Victor Kobbelgaard, Anne Marie Kanstrup, and Lotte NS Andreasen Struijk. “Exploring user requirements for an exoskeleton arm insights from a user-centered study with people living with severe paralysis”. In: *IFIP Conference on Human-Computer Interaction*. Springer. 2021, pp. 312–320.

[87] Lutong Li, Sarah Tyson, and Andrew Weightman. “Professionals’ views and experiences of using rehabilitation robotics with stroke survivors: A mixed methods survey”. In: *Frontiers in Medical Technology* 3 (2021), p. 780090.

[88] Rosti Readioff et al. “Use and evaluation of assistive technologies for upper limb function in tetraplegia”. In: *The Journal of Spinal Cord Medicine* 45.6 (2022), pp. 809–820.

[89] Sedef Süner-Pla-Cerdà, Batuhan Şahin, and Kutluk Bilge Arikan. “User Requirements and Involvement Methods in the Development of Hand Exoskeletons: A Review”. In: *ACM Transactions on Human-Robot Interaction* 14.1 (2024), pp. 1–30.

[90] N Hutmacher et al. “Identification of needs for an assistive robotic arm in individuals with tetraplegia: a mixed-methods approach”. In: *Journal of NeuroEngineering and Rehabilitation* 22 (2025), p. 113.

[91] Jacob Brackenridge et al. “A review of rehabilitation devices to promote upper limb function following stroke”. In: *Neuroscience and Biomedical Engineering* 4.1 (2016), pp. 25–42.

[92] Revanth Damerla et al. “A review of the performance of extrinsically powered prosthetic hands”. In: *IEEE Transactions on Medical Robotics and Bionics* 3.3 (2021), pp. 640–660.

[93] Vincent Mendez et al. “Current Solutions and Future Trends for Robotic Prosthetic Hands”. In: *Annual Review of Control, Robotics, and Autonomous Systems* 4.1 (2021), pp. 595–627.

[94] D. Plettenburg et al. B. Maat G. Smit. “Passive prosthetic hands and tools: A literature review”. In: *Prosthetics and Orthotics International* (2018).

[95] CM Fraser. “An evaluation of the use made of cosmetic and functional prostheses by unilateral upper limb amputees”. In: *Prosthetics and orthotics international* 22.3 (1998), pp. 216–223.

[96] Ecaterina Golea-Vasluian et al. “Adaptive devices in young people with upper limb reduction deficiencies: Use and satisfaction”. In: *Journal of rehabilitation medicine* 47.4 (2015), pp. 346–355.

[97] Jean Pillet. “The aesthetic hand prosthesis”. In: *Orthopedic Clinics of North America* 12.4 (1981), pp. 961–969.

[98] Dick H Plettenburg. “The WILMER passive hand prosthesis for toddlers”. In: *JPO: Journal of Prosthetics and Orthotics* 21.2 (2009), pp. 97–99.

[99] Gabriel M Kim et al. “Current and emerging prostheses for partial hand amputation: A narrative review”. In: *PM&R* 15.3 (2023), pp. 392–401.

[100] Hooman Soltanian, Genevieve De Bese, and Robert W Beasley. “Passive hand prostheses”. In: *Hand clinics* 19.1 (2003), pp. 177–183.

[101] Cristina Piazza et al. “The softhand pro-h: a hybrid body-controlled, electrically powered hand prosthesis for daily living and working”. In: *IEEE Robotics & Automation Magazine* 24.4 (2017), pp. 87–101.

[102] Gerwin Smit, Dick H Plettenburg, and Frans CT van der Helm. “The lightweight Delft Cylinder Hand: first multi-articulating hand that meets the basic user requirements”. In: *IEEE Transactions on Neural Systems and Rehabilitation Engineering* 23.3 (2014), pp. 431–440.

[103] Stephanie L Carey, Derek J Lura, and M Jason Highsmith. “Differences in myoelectric and body-powered upper-limb prostheses: Systematic literature review.” In: *Journal of Rehabilitation Research & Development* 52.3 (2015).

[104] Federico Tessari A. Marinelli Nicolo Boccardo. “Active upper limb prostheses: a review on current state and upcoming breakthroughs”. In: *Progress in Biomedical Engineering* (2023).

[105] Cristina Piazza et al. “A century of robotic hands”. In: *Annual Review of Control, Robotics, and Autonomous Systems* 2.1 (2019), pp. 1–32.

[106] Össur. *i-Limb Quantum*. https://www.ossur.com/en-in/prosthetics/arms/i-limb-quantum. Accessed: 2025-05-01.

[107] Vincent Systems GmbH. *VINCENTevolution3 / 3+*. https://www.vincentsystems.de/en/vincent-evolution3. Accessed: 2025-05-01.

[108] Masaaki Hioki et al. "Design and control of electromyogram prosthetic hand with high grasping force". In: *2011 IEEE International Conference on Robotics and Biomimetics*. IEEE. 2011, pp. 1128–1133.

[109] Christian Cipriani, Marco Controzzi, and Maria Chiara Carrozza. "The SmartHand transradial prosthesis". In: *Journal of neuroengineering and rehabilitation* 8 (2011), pp. 1–14.

[110] Tommaso Lenzi, James Lipsey, and Jonathon W Sensinger. "The RIC arm—a small anthropomorphic transhumeral prosthesis". In: *IEEE/ASME Transactions on Mechatronics* 21.6 (2016), pp. 2660–2671.

[111] Ottobock. *Greifer—Technical Specifications*. https://shop.ottobock.us/Prosthetics/Upper-Limb-Prosthetics/Myo-Hands-and-Components/Myo-Terminal-Devices/System-Electric-Greifer-DMC-VariPlus/p/8E34~59-1. Accessed: 03 12, 2020.

[112] Immanuel Nicolas Gaiser et al. "The FLUIDHAND III: A multifunctional prosthetic hand". In: *JPO: Journal of Prosthetics and Orthotics* 21.2 (2009), pp. 91–96.

[113] Maria Chiara Carrozza et al. "Design of a cybernetic hand for perception and action". In: *Biological cybernetics* 95 (2006), pp. 629–644.

[114] Konstantinos Andrianesis and Anthony Tzes. "Development and control of a multifunctional prosthetic hand with shape memory alloy actuators". In: *Journal of Intelligent & Robotic Systems* 78 (2015), pp. 257–289.

[115] Kevin B Fite et al. "A gas-actuated anthropomorphic prosthesis for transhumeral amputees". In: *IEEE Transactions on Robotics* 24.1 (2008), pp. 159–169.

[116] Claudia JW Haarman et al. "Mechanical design and feasibility of a finger exoskeleton to support finger extension of severely affected stroke patients". In: *IEEE Transactions on Neural Systems and Rehabilitation Engineering* 31 (2023), pp. 1268–1276.

[117] Naqash Rehmat et al. "Upper limb rehabilitation using robotic exoskeleton systems: a systematic review". In: *International Journal of Intelligent Robotics and Applications* 2 (2018), pp. 283–295.

[118] Muhammad Ahsan Gull, Shaoping Bai, and Thomas Bak. "A review on design of upper limb exoskeletons". In: *Robotics* 9.1 (2020), p. 16.

[119] Yang Shen, Peter Walker Ferguson, and Jacob Rosen. "Upper limb exoskeleton systems—overview". In: *Wearable Robotics* (2020), pp. 1–22.

[120] Hyunki In et al. "Feasibility study of a slack enabling actuator for actuating tendon-driven soft wearable robot without pretension". In: *2015 IEEE International Conference on Robotics and Automation (ICRA)*. IEEE. 2015, pp. 1229–1234.

[121] Dmitry Popov, Igor Gaponov, and Jee-Hwan Ryu. "Portable exoskeleton glove with soft structure for hand assistance in activities of daily living". In: *IEEE/ASME Transactions on Mechatronics* 22.2 (2016), pp. 865–875.

[122] Jose M Ochoa et al. "Use of an electromyographically driven hand orthosis for training after stroke". In: *2011 IEEE international conference on rehabilitation robotics*. IEEE. 2011, pp. 1–5.

[123] Aaron Yurkewich et al. "Hand Extension Robot Orthosis (HERO) Grip Glove: enabling independence amongst persons with severe hand impairments after stroke". In: *Journal of neuroengineering and rehabilitation* 17 (2020), pp. 1–17.

[124] Camille E Proulx, Johanne Higgins, and Dany H Gagnon. "Occupational therapists' evaluation of the perceived usability and utility of wearable soft robotic exoskeleton gloves for hand function rehabilitation following a stroke". In: *Disability and rehabilitation: Assistive technology* 18.6 (2023), pp. 953–962.

[125] Lauri Connelly et al. "A pneumatic glove and immersive virtual reality environment for hand rehabilitative training after stroke". In: *IEEE Transactions on Neural Systems and Rehabilitation Engineering* 18.5 (2010), pp. 551–559.

[126] Aodhán L Coffey, Darren J Leamy, and Tomás E Ward. "A novel BCI-controlled pneumatic glove system for home-based neurorehabilitation". In: *2014 36th Annual International Conference of the IEEE Engineering in Medicine and Biology Society*. IEEE. 2014, pp. 3622–3625.

[127] Tiaan Du Plessis, Karim Djouani, and Christiaan Oosthuizen. "A review of active hand exoskeletons for rehabilitation and assistance". In: *Robotics* 10.1 (2021), p. 40.

[128] John F Farrell et al. "Orthotic aided training of the paretic upper limb in chronic stroke: results of a phase 1 trial". In: *NeuroRehabilitation* 22.2 (2007), pp. 99–103.

[129] Ning Sun, Guotao Li, and Long Cheng. "Design and validation of a self-aligning index finger exoskeleton for post-stroke rehabilitation". In: *IEEE Transactions on Neural Systems and Rehabilitation Engineering* 29 (2021), pp. 1513–1523.

[130] Aaron Yurkewich et al. "Hand extension robot orthosis (HERO) glove: development and testing with stroke survivors with severe hand impairment". In: *IEEE Transactions on Neural Systems and Rehabilitation Engineering* 27.5 (2019), pp. 916–926.

[131] Marco Cempini, Mario Cortese, and Nicola Vitiello. "A powered finger–thumb wearable hand exoskeleton with self-aligning joint axes". In: *IEEE/ASME Transactions on mechatronics* 20.2 (2014), pp. 705–716.

[132] Houcheng Li et al. "Design and control of an underactuated finger exoskeleton for assisting activities of daily living". In: *IEEE/ASME Transactions on Mechatronics* 27.5 (2021), pp. 2699–2709.

[133] Lujain Alrabghi et al. "Stroke types and management". In: *Int J Community Med Public Health* 5.9 (2018), p. 3715.

[134] Robert Bogue. "Rehabilitation robots". In: *Industrial Robot: An International Journal* 45.3 (2018), pp. 301–306.

[135] Ori Ossmy and Roy Mukamel. "Perception as a route for motor skill learning: perspectives from neuroscience". In: *Neuroscience* 382 (2018), pp. 144–153.

[136] Hassan M Qassim and WZ Wan Hasan. "A review on upper limb rehabilitation robots". In: *Applied Sciences* 10.19 (2020), p. 6976.

[137] Xiao Ling Hu et al. "A comparison between electromyography-driven robot and passive motion device on wrist rehabilitation for chronic stroke". In: *Neurorehabilitation and neural repair* 23.8 (2009), pp. 837–846.

[138] Hang Zhang et al. "Feasibility study of robot-assisted stroke rehabilitation at home using RUPERT". In: *The 2011 IEEE/ICME International Conference on Complex Medical Engineering*. IEEE. 2011, pp. 604–609.

[139] JD Sanjuan et al. "Cable driven exoskeleton for upper-limb rehabilitation: A design review". In: *Robotics and Autonomous Systems* 126 (2020), p. 103445.

[140] Rong Song et al. "Assistive control system using continuous myoelectric signal in robot-aided arm training for patients after stroke". In: *IEEE transactions on neural systems and rehabilitation engineering* 16.4 (2008), pp. 371–379.

[141] Md Rasedul Islam et al. "A brief review on robotic exoskeletons for upper extremity rehabilitation to find the gap between research porotype and commercial type". In: *Adv. Robot. Autom* 6.2 (2017), pp. 10–4172.

[142] Rachele Bertani et al. "Effects of robot-assisted upper limb rehabilitation in stroke patients: a systematic review with meta-analysis". In: *Neurological Sciences* 38 (2017), pp. 1561–1569.

[143] Benedetta Cesqui et al. "EMG-based pattern recognition approach in post stroke robot-aided rehabilitation: a feasibility study". In: *Journal of neuroengineering and rehabilitation* 10 (2013), pp. 1–15.

[144] Tobias Nef et al. "Effects of arm training with the robotic device ARMin I in chronic stroke: three single cases". In: *Neurodegenerative diseases* 6.5-6 (2010), pp. 240–251.

[145] Khadijeh Moulaei et al. "Overview of the role of robots in upper limb disabilities rehabilitation: a scoping review". In: *Archives of Public Health* 81.1 (2023), p. 84.

[146] Chao Zhang, Cecilia WP Li-Tsang, and Ricky KC Au. "Robotic approaches for the rehabilitation of upper limb recovery after stroke: a systematic review and meta-analysis". In: *International Journal of Rehabilitation Research* 40.1 (2017), pp. 19–28.

[147] Barbara M Doucet, Amy Lam, and Lisa Griffin. "Neuromuscular electrical stimulation for skeletal muscle function". In: *The Yale journal of biology and medicine* 85.2 (2012), p. 201.

[148] John Chae, Lynne Sheffler, and Jayme Knutson. "Neuromuscular electrical stimulation for motor restoration in hemiplegia". In: *Topics in stroke rehabilitation* 15.5 (2008), pp. 412–426.

[149] John Eraifej et al. "Effectiveness of upper limb functional electrical stimulation after stroke for the improvement of activities of daily living and motor function: a systematic review and meta-analysis". In: *Systematic reviews* 6 (2017), pp. 1–21.

[150] Muhammad Ahmed Khan et al. "A systematic review on functional electrical stimulation based rehabilitation systems for upper limb post-stroke recovery". In: *Frontiers in neurology* 14 (2023), p. 1272992.

[151] Tácia Cotinguiba Machado et al. "Efficacy of motor imagery additional to motor-based therapy in the recovery of motor function of the upper limb in post-stroke individuals: a systematic review". In: *Topics in stroke rehabilitation* 26.7 (2019), pp. 548–553.

[152] Scott H Johnson, Gwen Sprehn, and Andrew J Saykin. "Intact motor imagery in chronic upper limb hemiplegics: evidence for activity-independent action representations". In: *Journal of cognitive neuroscience* 14.6 (2002), pp. 841–852.

[153] Nikhil Sharma, Valerie M Pomeroy, and Jean-Claude Baron. "Motor imagery: a backdoor to the motor system after stroke?" In: *Stroke* 37.7 (2006), pp. 1941–1952.

[154] Rig Das et al. "FBCSP and adaptive boosting for multiclass motor imagery BCI data classification: a machine learning approach". In: *2020 IEEE International Conference on Systems, Man, and Cybernetics (SMC)*. IEEE. 2020, pp. 1275–1279.

[155] Milos R Popovic et al. "Functional electrical stimulation therapy of voluntary grasping versus only conventional rehabilitation for patients with subacute incomplete tetraplegia: a randomized clinical trial". In: *Neurorehabilitation and neural repair* 25.5 (2011), pp. 433–442.

[156] Andrej Kral, Felix Aplin, and Hannes Maier. *Prostheses for the brain: introduction to neuroprosthetics*. Academic Press, 2021.

[157] Yu Tung Lo et al. "Neural interface-based motor neuroprosthesis in post-stroke upper limb neurorehabilitation: An individual patient data meta-analysis." In: *Archives of physical medicine and rehabilitation* (2024).

[158] Solaiman Shokur et al. "A modular strategy for next-generation upper-limb sensory-motor neuroprostheses". In: *Med* 2.8 (2021), pp. 912–937.

[159] Chiara Höhler et al. "The efficacy of hybrid neuroprostheses in the rehabilitation of upper limb impairment after stroke, a narrative and systematic review with a meta-analysis". In: *Artificial Organs* 48.3 (2024), pp. 232–253.

[160] Ejay Nsugbe. "Brain-machine and muscle-machine bio-sensing methods for gesture intent acquisition in upper-limb prosthesis control: a review". In: *Journal of Medical Engineering & Technology* 45.2 (2021), pp. 115–128.

[161] Gerwin Schalk and Eric C Leuthardt. "Brain-computer interfaces using electrocorticographic signals". In: *IEEE reviews in biomedical engineering* 4 (2011), pp. 140–154.

[162] Nitish V Thakor et al. "Neuroprosthetic limb control with electrocorticography: approaches and challenges". In: *2014 36th annual international conference of the IEEE engineering in medicine and biology society*. IEEE. 2014, pp. 5212–5215.

[163] Fabian Herold et al. "Applications of functional near-infrared spectroscopy (fNIRS) neuroimaging in exercise–cognition science: a systematic, methodology-focused review". In: *Journal of clinical medicine* 7.12 (2018), p. 466.

[164] Reza Abiri et al. "A comprehensive review of EEG-based brain–computer interface paradigms". In: *Journal of neural engineering* 16.1 (2019), p. 011001.

[165] María Alvarado et al. "Electroencephalography as an Alternative to Electromyography Prosthesis Control, a Scientific Review". In: *2024 IEEE Central America and Panama Student Conference (CONESCAPAN)*. IEEE. 2024, pp. 1–6.

[166] Cristina-Magda Cazacu and Ioan Doroftei. “Control Advances in Upper Limb Prostheses: A Review. Part I: Invasive Methods”. In: *IFToMM Symposium on Mechanism Design for Robotics*. Springer. 2024, pp. 259–266.

[167] Cristina-Magda Cazacu and Ioan Doroftei. “Control Advances in Upper Limb Prostheses: A Review. Part II: Non-Invasive Methods”. In: *IFToMM Symposium on Mechanism Design for Robotics*. Springer. 2024, pp. 267–278.

[168] Kai J Miller, Dora Hermes, and Nathan P Staff. “The current state of electrocorticography-based brain–computer interfaces”. In: *Neurosurgical focus* 49.1 (2020), E2.

[169] Stefan Salminger et al. “Long-term implant of intramuscular sensors and nerve transfers for wireless control of robotic arms in above-elbow amputees”. In: *Science Robotics* 4.32 (2019), eaaw6306.

[170] Mehrnaz Kh Hazrati and Abbas Erfanian. “An online EEG-based brain–computer interface for controlling hand grasp using an adaptive probabilistic neural network”. In: *Medical engineering & physics* 32.7 (2010), pp. 730–739.

[171] Renling Zou et al. “Effect of the period of EEG signals on the decoding of motor information”. In: *Physical and Engineering Sciences in Medicine* 47.1 (2024), pp. 249–260.

[172] Jianqiang Su et al. “Enhanced Motor Imagery Based Brain-Computer Interface via Vibration Stimulation and Robotic Glove for Post-Stroke Rehabilitation”. In: *International Conference on Neural Information Processing*. Springer. 2023, pp. 326–337.

[173] Pooya Chanu Maibam et al. “Enhancing prosthetic hand control: A synergistic multi-channel electroencephalogram”. In: *Wearable Technologies* 5 (2024), e18.

[174] Marta Gherardini et al. “The myokinetic interface: Implanting permanent magnets to restore the sensory-motor control loop in amputees”. In: *Current Opinion in Biomedical Engineering* 27 (2023), p. 100460.

[175] Robin Rackerby, Stephan Lukosch, and Deborah Munro. “Understanding and measuring the cognitive load of amputees for rehabilitation and prosthesis development”. In: *Archives of Rehabilitation Research and Clinical Translation* 4.3 (2022), p. 100216.

[176] DSV Bandara, Jumpei Arata, and Kazuo Kiguchi. “Towards control of a transhumeral prosthesis with EEG signals”. In: *Bioengineering* 5.2 (2018), p. 26.

[177] Ilham AE Zaeni et al. “Concentration level detection using eeg signal on reading practice application”. In: *2019 International Conference on Electrical, Electronics and Information Engineering (ICEEIE)*. Vol. 6. IEEE. 2019, pp. 354–357.

[178] Jianjun Meng et al. “Noninvasive electroencephalogram based control of a robotic arm for reach and grasp tasks”. In: *Scientific Reports* 6.1 (2016), p. 38565.

[179] Oluwarotimi Williams Samuel et al. “Motor imagery classification of upper limb movements based on spectral domain features of EEG patterns”. In: *2017 39th Annual International Conference of the IEEE Engineering in Medicine and Biology Society (EMBC)*. IEEE. 2017, pp. 2976–2979.

[180] Shalini Stalin et al. “A Machine Learning-Based Big EEG Data Artifact Detection and Wavelet-Based Removal: An Empirical Approach”. In: *Mathematical Problems in Engineering* 2021.1 (2021), p. 2942808.

[181] Fabien Lotte et al. “A review of classification algorithms for EEG-based brain–computer interfaces: a 10 year update”. In: *Journal of neural engineering* 15.3 (2018), p. 031005.

[182] Gernot Müller-Putz. “Toward Non-invasive BCI-Based Movement Decoding”. In: *Neuroprosthetics and Brain-Computer Interfaces in Spinal Cord Injury: A Guide for Clinicians and End Users*. Springer, 2021, pp. 233–249.

[183] Gaetano Gargiulo et al. “A new EEG recording system for passive dry electrodes”. In: *Clinical Neurophysiology* 121.5 (2010), pp. 686–693.

[184] Roman Kusche, Steffen Kaufmann, and Martin Ryschka. “Dry electrodes for bioimpedance measurements—Design, characterization and comparison”. In: *Biomedical Physics & Engineering Express* 5.1 (2018), p. 015001.

[185] Benjamin J Choi and Ji Liu. “A low-cost transhumeral prosthesis operated via an ML-assisted EEG-head gesture control system”. In: *Journal of Neural Engineering* (2025).

[186] Dario Farina, Winnie Jensen, and Metin Akay. *Introduction to neural engineering for motor rehabilitation*. John Wiley & Sons, 2013.

[187] Aimee E Schultz and Todd A Kuiken. “Neural interfaces for control of upper limb prostheses: the state of the art and future possibilities”. In: *Pm&r* 3.1 (2011), pp. 55–67.

[188] Lin Yao et al. “Combining motor imagery with selective sensation toward a hybrid-modality BCI”. In: *IEEE Transactions on Biomedical Engineering* 61.8 (2013), pp. 2304–2312.

[189] Chuyao Jian et al. “Neuromuscular control of the agonist–antagonist muscle coordination affected by visual dimension: An EMG-fNIRS study”. In: *IEEE Access* 8 (2020), pp. 100768–100777.

[190] Haim Abitan, Henrik Bohr, and Preben Buchhave. “Correction to the Beer–Lambert–Bouguer law for optical absorption”. In: *Applied optics* 47.29 (2008), pp. 5354–5357.

[191] Neelum Yousaf Sattar et al. “fNIRS-based upper limb motion intention recognition using an artificial neural network for transhumeral amputees”. In: *Sensors* 22.3 (2022), p. 726.

[192] Umut Mayetin and Serdar Kucuk. “Design and experimental evaluation of a low cost, portable, 3-dof wrist rehabilitation robot with high physical human–robot interaction”. In: *Journal of Intelligent & Robotic Systems* 106.3 (2022), p. 65.

[193] Robert Finnis, Adeel Mehmood, and Jamshed Iqbal. *fNIRS vs. EEG Based Prosthetic Limb Control: A Systematic Literature Review*.

[194] Cynthia A Chestek et al. “Hand posture classification using electrocorticography signals in the gamma band over human sensorimotor brain areas”. In: *Journal of neural engineering* 10.2 (2013), p. 026002.

[195] Oliver Tonet et al. “Defining brain–machine interface applications by matching interface performance with device requirements”. In: *Journal of neuroscience methods* 167.1 (2008), pp. 91–104.

[196] Takufumi Yanagisawa et al. “Real-time control of a prosthetic hand using human electrocorticography signals”. In: *Journal of neurosurgery* 114.6 (2011), pp. 1715–1722.

[197] Takufumi Yanagisawa et al. “Electrocorticographic control of a prosthetic arm in paralyzed patients”. In: *Annals of neurology* 71.3 (2012), pp. 353–361.

[198] Yinfeng Fang et al. “Multi-modal sensing techniques for interfacing hand prostheses: A review”. In: *IEEE Sensors Journal* 15.11 (2015), pp. 6065–6076.

[199] Kadir A Yildiz, Alexander Y Shin, and Kenton R Kaufman. “Interfaces with the peripheral nervous system for the control of a neuroprosthetic limb: a review”. In: *Journal of neuroengineering and rehabilitation* 17 (2020), pp. 1–19.

[200] Ipek Berberoglu et al. “Regenerative peripheral nerve interfaces (RPNIs): an overview of innovative surgical approaches”. In: *Plastic and Aesthetic Research* 11 (2024), N–A.

[201] FA Cuoco and Dominique M Durand. “Measurement of external pressures generated by nerve cuff electrodes”. In: *IEEE Transactions on Rehabilitation Engineering* 8.1 (2000), pp. 35–41.

[202] Sanghoon Lee et al. “Toward bioelectronic medicine—neuromodulation of small peripheral nerves using flexible neural clip”. In: *Advanced Science* 4.11 (2017), p. 1700149.

[203] Angelica M Cobo et al. “Parylene-based cuff electrode with integrated microfluidics for peripheral nerve recording, stimulation, and drug delivery”. In: *Journal of microelectromechanical systems* 28.1 (2018), pp. 36–49.

[204] Katharine H Polasek et al. “Stimulation stability and selectivity of chronically implanted multicontact nerve cuff electrodes in the human upper extremity”. In: *IEEE transactions on neural systems and rehabilitation engineering* 17.5 (2009), pp. 428–437.

[205] Dustin J Tyler and Dominique M Durand. “A slowly penetrating interfascicular nerve electrode for selective activation of peripheral nerves”. In: *IEEE transactions on rehabilitation engineering* 5.1 (1997), pp. 51–61.

[206] Thomas N Nielsen, Cristian Sevcencu, and Johannes J Struijk. “Fascicle-selectivity of an intraneural stimulation electrode in the rabbit sciatic nerve”. In: *IEEE transactions on biomedical engineering* 59.1 (2011), pp. 192–197.

[207] Peter H Veltink et al. “A modeling study of nerve fascicle stimulation”. In: *IEEE transactions on biomedical engineering* 36.7 (1989), pp. 683–692.

[208] Paul Koole et al. “Recruitment characteristics of nerve fascicles stimulated by a multigroove electrode”. In: *IEEE transactions on rehabilitation engineering* 5.1 (1997), pp. 40–50.

[209] Xavier Navarro et al. “Neurobiological evaluation of thin-film longitudinal intrafascicular electrodes as a peripheral nerve interface”. In: *2007 IEEE 10th international conference on rehabilitation robotics*. IEEE. 2007, pp. 643–649.

[210] Silvestro Micera et al. “Hybrid bionic systems for the replacement of hand function”. In: *Proceedings of the IEEE* 94.9 (2006), pp. 1752–1762.

[211] Paolo M Rossini et al. “Double nerve intraneural interface implant on a human amputee for robotic hand control”. In: *Clinical neurophysiology* 121.5 (2010), pp. 777–783.

[212] AE Pena et al. “Mechanical fatigue resistance of an implantable branched lead system for a distributed set of longitudinal intrafascicular electrodes”. In: *Journal of neural engineering* 14.6 (2017), p. 066014.

[213] Natalia Lago et al. “Neurobiological assessment of regenerative electrodes for bidirectional interfacing injured peripheral nerves”. In: *IEEE transactions on biomedical engineering* 54.6 (2007), pp. 1129–1137.

[214] Jennifer L Seifert et al. “Normal molecular repair mechanisms in regenerative peripheral nerve interfaces allow recording of early spike activity despite immature myelination”. In: *IEEE Transactions on neural systems and Rehabilitation Engineering* 20.2 (2011), pp. 220–227.

[215] Akhil Srinivasan et al. “Microchannel-based regenerative scaffold for chronic peripheral nerve interfacing in amputees”. In: *Biomaterials* 41 (2015), pp. 151–165.

[216] Jinwoo Jeong et al. “64-channel double-layered sieve electrode with increased porosity for improved axon regeneration and high spatial resolution”. In: *2016 6th IEEE International Conference on Biomedical Robotics and Biomechatronics (BioRob)*. IEEE. 2016, pp. 1148–1153.

[217] Isaac P Clements et al. “Regenerative scaffold electrodes for peripheral nerve interfacing”. In: *IEEE Transactions on neural systems and rehabilitation engineering* 21.4 (2012), pp. 554–566.

[218] Kshitija Garde et al. “Early interfaced neural activity from chronic amputated nerves”. In: *Frontiers in neuroengineering* 2 (2009), p. 299.

[219] Marco JM Hoozemans and Jaap H Van Dieen. “Prediction of handgrip forces using surface EMG of forearm muscles”. In: *Journal of electromyography and kinesiology* 15.4 (2005), pp. 358–366.

[220] M Bilodeau et al. “EMG frequency content changes with increasing force and during fatigue in the quadriceps femoris muscle of men and women”. In: *Journal of electromyography and kinesiology* 13.1 (2003), pp. 83–92.

[221] R. Reiter. “Eine neue Elektrokunsthand”. In: *Grenzgebiete der Medizin* 1.4 (1948), pp. 133–135.

[222] AE Kobrinski et al. “Problems of bioelectric control”. In: *IFAC Proceedings Volumes* 1.1 (1960), pp. 629–633.

[223] Drishti Yadav and Karan Veer. “Recent trends and challenges of surface electromyography in prosthetic applications”. In: *Biomedical Engineering Letters* 13.3 (2023), pp. 353–373.

[224] Mamun Bin Ibne Reaz, M Sazzad Hussain, and Faisal Mohd-Yasin. “Techniques of EMG signal analysis: detection, processing, classification and applications”. In: *Biological procedures online* 8 (2006), pp. 11–35.

[225] Claudio Castellini and Patrick Van Der Smagt. "Surface EMG in advanced hand prosthetics". In: *Biological cybernetics* 100 (2009), pp. 35–47.

[226] David J Hewson et al. "Evolution in impedance at the electrode-skin interface of two types of surface EMG electrodes during long-term recordings". In: *Journal of Electromyography and Kinesiology* 13.3 (2003), pp. 273–279.

[227] Kevin L Kilgore et al. "An implanted upper-extremity neuroprosthesis using myoelectric control". In: *The Journal of hand surgery* 33.4 (2008), pp. 539–550.

[228] P Hunter Peckham et al. "Efficacy of an implanted neuroprosthesis for restoring hand grasp in tetraplegia: a multicenter study". In: *Archives of physical medicine and rehabilitation* 82.10 (2001), pp. 1380–1388.

[229] James P Uhlir et al. "Performance of epimysial stimulating electrodes in the lower extremities of individuals with spinal cord injury". In: *IEEE Transactions on neural systems and rehabilitation engineering* 12.2 (2004), pp. 279–287.

[230] Enzo Mastinu et al. "Grip control and motor coordination with implanted and surface electrodes while grasping with an osseointegrated prosthetic hand". In: *Journal of neuroengineering and rehabilitation* 16 (2019), pp. 1–10.

[231] Janis J Daly et al. "Performance of an intramuscular electrode during functional neuromuscular stimulation for gait training post stroke." In: *Journal of Rehabilitation Research & Development* 38.5 (2001).

[232] Wigand Poppendieck et al. "A new generation of double-sided intramuscular electrodes for multi-channel recording and stimulation". In: *2015 37th Annual International Conference of the IEEE Engineering in Medicine and Biology Society (EMBC)*. IEEE. 2015, pp. 7135–7138.

[233] Christopher M Frost et al. "Regenerative peripheral nerve interfaces for real-time, proportional control of a Neuroprosthetic hand". In: *Journal of neuroengineering and rehabilitation* 15 (2018), pp. 1–9.

[234] Gregory A Dumanian et al. *Targeted muscle reinnervation treats neuroma and phantom pain in major limb amputees: a randomized clinical trial*. 2019.

[235] J Byers Bowen et al. "Targeted muscle reinnervation to improve pain, prosthetic tolerance, and bioprosthetic outcomes in the amputee". In: *Advances in Wound Care* 6.8 (2017), pp. 261–267.

[236] Theodore A Kung et al. "Regenerative peripheral nerve interface viability and signal transduction with an implanted electrode". In: *Plastic and reconstructive surgery* 133.6 (2014), pp. 1380–1394.

[237] Philip P Vu et al. "Closed-loop continuous hand control via chronic recording of regenerative peripheral nerve interfaces". In: *IEEE Transactions on Neural Systems and Rehabilitation Engineering* 26.2 (2017), pp. 515–526.

[238] Ziming Chen et al. "A review of myoelectric control for prosthetic hand manipulation". In: *Biomimetics* 8.3 (2023), p. 328.

[239] Gary Kamen and David A Gabriel. *Essentials of electromyography*. Human Kinetics Publishers, 2009.

[240] Sanjeev D Nandedkar, Erik V Stalberg, and Donald B Sanders. "Simulation techniques in electromyography". In: *IEEE Transactions on biomedical engineering* 10 (1985), pp. 775–785.

[241] K. Mukund and S. Subramaniam. "Skeletal muscle: A review of molecular structure and function, in health and disease". In: *Wiley Interdiscip Rev Syst Biol Med* 12.1 (Jan. 2020).

[242] Elwood Henneman. "Relation between size of neurons and their susceptibility to discharge". In: *Science* 126.3287 (1957), pp. 1345–1347.

[243] Jacques Duchateau and Roger M Enoka. "Human motor unit recordings: origins and insight into the integrated motor system". In: *Brain research* 1409 (2011), pp. 42–61.

[244] R. Merletti and D Farina. *Surface Electromyography: Physiology, Engineering, and Applications*. The Institute of Electricaland Electronics Engineers, Inc., 2016.

[245] R. Fitzhugh. *Mathematical Models of Excitation and Propagation in Nerve*. Publisher Unknown, 1966.

[246] Roberto Merletti and Philip J Parker. *Electromyography: physiology, engineering, and non-invasive applications*. Vol. 11. John Wiley and Sons, 2004.

[247] Lauren H Smith and Levi J Hargrove. "Comparison of surface and intramuscular EMG pattern recognition for simultaneous wrist/hand motion classification". In: *2013 35th annual international conference of the IEEE engineering in medicine and biology society (EMBC)*. IEEE. 2013, pp. 4223–4226.

[248] R. Merletti and S. Muceli. "Tutorial. Surface EMG detection in space and time: Best practices". In: *Journal of Electromyography and Kinesiology* 49 (2019), p. 102363.

[249] Roberto Merletti, Aleš Holobar, and Dario Farina. "Analysis of motor units with high-density surface electromyography". In: *Journal of electromyography and kinesiology* 18.6 (2008), pp. 879–890.

[250] Texas Instruments. *Noise Analysis in Operational Amplifier Circuits*. Dallas, Texas, SLVA043B. 2007. URL: `https://www.ti.com/`.

[251] R. Merletti and G.L. Cerone. "Tutorial. Surface EMG detection, conditioning and pre-processing: Best practices". In: *Journal of Electromyography and Kinesiology* 54 (Oct. 2020), p. 102440. URL: `https://doi.org/10.1016/j.jelekin.2020.102440`.

[252] D. Farina, D. F. Stegeman, and R. Merletti. "Biophysics of the Generation of EMG Signals". In: *Surface Electromyography : Physiology, Engineering, and Applications*. John Wiley and Sons, Ltd, 2016. Chap. 2, pp. 1–24.

[253] G.L. Cerone M. Knaflitz M. Gazzoni. *Strumentazione Biomedica*. LEVROTTO and BELLA, 2022.

[254] Vera Lucia Da Silveira Nantes Button. *Principles of Measurement and Transduction of Biomedical Variables*. Academic Press, 2015.

[255] Amine Nait-Ali. *Advanced Biosignal Processing*. Springer, 2009.

[256] A.J. Nimunkar J.G. Webster. *Medical Instrumentation: Application and Design*. John Wiley and Sons, 2020.

[257] John XJ Zhang and Kazunori Hoshino. *Molecular sensors and nanodevices: principles, designs and applications in biomedical engineering*. Academic Press, 2018.

[258] Dario Farina et al. “High-density EMG E-textile systems for the control of active prostheses”. In: *2010 Annual international conference of the IEEE engineering in medicine and biology*. IEEE. 2010, pp. 3591–3593.

[259] T Finni et al. “Measurement of EMG activity with textile electrodes embedded into clothing”. In: *Physiological measurement* 28.11 (2007), p. 1405.

[260] Siyeon Kim, Sojung Lee, and Wonyoung Jeong. “EMG measurement with textile-based electrodes in different electrode sizes and clothing pressures for smart clothing design optimization”. In: *Polymers* 12.10 (2020), p. 2406.

[261] Steffi L Colyer and Polly M McGuigan. “Textile electrodes embedded in clothing: A practical alternative to traditional surface electromyography when assessing muscle excitation during functional movements”. In: *Journal of sports science & medicine* 17.1 (2018), p. 101.

[262] Stuart J Russell and Peter Norvig. *Artificial intelligence: a modern approach*. pearson, 2016.

[263] Christopher M Bishop and Nasser M Nasrabadi. *Pattern recognition and machine learning*. Vol. 4. 4. Springer, 2006.

[264] Ian Goodfellow et al. *Deep learning*. Vol. 1. 2. MIT press Cambridge, 2016.

[265] Michael A Nielsen. *Neural networks and deep learning*. Vol. 25. Determination press San Francisco, CA, USA, 2015.

[266] Md. Zahangir Alom et al. “The History Began from AlexNet: A Comprehensive Survey on Deep Learning Approaches”. In: *arXiv preprint* (Mar. 2018).

[267] F. Rosenblatt. “The perceptron: A probabilistic model for information storage and organization in the brain”. In: *Psychological Review* 65.6 (1958), pp. 386–408. URL: https://doi.org/10.1037/h0042519.

[268] Johnny LG Nielsen et al. “Simultaneous and proportional force estimation for multifunction myoelectric prostheses using mirrored bilateral training”. In: *IEEE Transactions on Biomedical Engineering* 58.3 (2010), pp. 681–688.

[269] Md Zahangir Alom et al. “A State-of-the-Art Survey on Deep Learning Theory and Architectures”. In: *Electronics* 8.3 (Mar. 2019), p. 292. URL: http://dx.doi.org/10.3390/electronics8030292.

[270] Yann LeCun et al. “Gradient-based learning applied to document recognition”. In: *Proceedings of the IEEE* 86.11 (1998), pp. 2278–2324.

[271] David E Rumelhart, Geoffrey E Hinton, and Ronald J Williams. “Learning representations by back-propagating errors”. In: *nature* 323.6088 (1986), pp. 533–536.

[272] Michael I Jordan. “Serial order: A parallel distributed processing approach”. In: *Advances in psychology*. Vol. 121. Elsevier, 1997, pp. 471–495.

[273] Jeffrey L Elman. “Finding structure in time”. In: *Cognitive science* 14.2 (1990), pp. 179–211.

[274] Ashish Vaswani et al. *Attention Is All You Need*. 2017. URL: https://arxiv.org/abs/1706.03762.

[275] T. Hastie, R. Tibshirani, and J. Friedman. *The elements of statistical learning*. 2. Springer New York, NY, Aug. 2009.

[276] Vladimir N Vapnik. "A note on one class of perceptrons". In: *Automat. Rem. Control* 25 (1964), pp. 821–837.

[277] Leo Breiman. "Random forests". In: *Machine learning* 45 (2001), pp. 5–32.

[278] Evelyn Fix and Joseph L Hodges. "Discriminatory analysis". In: *Nonparametric discrimination: Small sample performance. Report A* 193008 (1951).

[279] Ronald A Fisher. "The use of multiple measurements in taxonomic problems". In: *Annals of eugenics* 7.2 (1936), pp. 179–188.

[280] F Ray Finley and Roy W Wirta. "Myocoder studies of multiple myopotential response". In: *Archives of physical medicine and rehabilitation* 48.11 (1967), pp. 598–601.

[281] K. Englehart E. Scheme. "Electromyogram pattern recognition for control of powered upper-limb prostheses: State of the art and challenges for clinical use". In: *Journal of Rehabilitation Research and Development* (2011).

[282] A. Cloutier and J. Yang. "Control of Hand Prostheses: A Literature Review". In: *IDETC-CIE* (Portland, OR). 2013.

[283] A. L. Ciancio et al. "Control of prosthetic hands via the peripheral nervous system". In: *Front. Neurosci.* 10 (Apr. 2016), p. 116.

[284] Kamalraj Subramaniam Nisheena V. Iqbal and Shaniba Asmi P. "A Review on Upper-Limb Myoelectric Prosthetic Control". In: *IETE Journal of Research* (2017).

[285] Daniel Graupe, Javad Salahi, and DeSong Zhang. "Stochastic analysis of myoelectric temporal signatures for multifunctional single-site activation of prostheses and orthoses". In: *Journal of biomedical engineering* 7.1 (1985), pp. 18–29.

[286] Michael F Kelly, Philip A Parker, and Robert N Scott. "The application of neural networks to myoelectric signal analysis: A preliminary study". In: *IEEE Transactions on Biomedical Engineering* 37.3 (1990), pp. 221–230.

[287] Bernard Hudgins, Philip Parker, and Robert N Scott. "A new strategy for multifunction myoelectric control". In: *IEEE transactions on biomedical engineering* 40.1 (1993), pp. 82–94.

[288] Aimee Cloutier and James Yang. "Design, control, and sensory feedback of externally powered hand prostheses: a literature review". In: *Critical Reviews™ in Biomedical Engineering* 41.2 (2013).

[289] Dario Di Domenico et al. "Hannes prosthesis control based on regression machine learning algorithms". In: *2021 IEEE/RSJ International Conference on Intelligent Robots and Systems (IROS)*. IEEE. 2021, pp. 5997–6002.

[290] Triwiyanto Triwiyanto et al. "State of the art methods of machine learning for prosthetic hand development: a review". In: *Proceeding of the 3rd International Conference on Electronics, Biomedical Engineering, and Health Informatics: ICEBEHI 2022, 5–6 October, Surabaya, Indonesia*. Springer. 2023, pp. 555–574.

[291] Mohamed Zine-El-Abidine Amrani et al. "Artificial neural networks based myoelectric control system for automatic assistance in hand rehabilitation". In: *2017 26th IEEE International Symposium on Robot and Human Interactive Communication (RO-MAN)*. IEEE. 2017, pp. 968–973.

[292] Muhammad Shahzaib and Sadia Shakil. “Hand electromyography circuit and signals classification using artificial neural network”. In: *2018 14th International Conference on Emerging Technologies (ICET)*. IEEE. 2018, pp. 1–6.

[293] Alexander E Olsson et al. “Extraction of multi-labelled movement information from the raw HD-sEMG image with time-domain depth”. In: *Scientific reports* 9.1 (2019), p. 7244.

[294] Wei Li, Ping Shi, and Hongliu Yu. “Gesture recognition using surface electromyography and deep learning for prostheses hand: state-of-the-art, challenges, and future”. In: *Frontiers in neuroscience* 15 (2021), p. 621885.

[295] Alessio Burrello et al. “Bioformers: Embedding transformers for ultra-low power semg-based gesture recognition”. In: *2022 Design, Automation & Test in Europe Conference & Exhibition (DATE)*. IEEE. 2022, pp. 1443–1448.

[296] Simon Ferguson and G Reg Dunlop. “Grasp recognition from myoelectric signals”. In: *Proceedings of the Australasian Conference on Robotics and Automation, Auckland, New Zealand*. Vol. 1. 2002, p. 6.

[297] Janne M Hahne et al. “Linear and nonlinear regression techniques for simultaneous and proportional myoelectric control”. In: *IEEE Transactions on Neural Systems and Rehabilitation Engineering* 22.2 (2014), pp. 269–279.

[298] Silvia Muceli and Dario Farina. “Simultaneous and proportional estimation of hand kinematics from EMG during mirrored movements at multiple degrees-of-freedom”. In: *IEEE transactions on neural systems and rehabilitation engineering* 20.3 (2011), pp. 371–378.

[299] Ning Jiang et al. “EMG-based simultaneous and proportional estimation of wrist/hand kinematics in uni-lateral trans-radial amputees”. In: *Journal of neuroengineering and rehabilitation* 9 (2012), pp. 1–11.

[300] Raul C Sıˆmpetru, Michael März, and Alessandro Del Vecchio. “Proportional and simultaneous real-time control of the full human hand from high-density electromyography”. In: *IEEE Transactions on Neural Systems and Rehabilitation Engineering* 31 (2023), pp. 3118–3131.

[301] A. Ameri et al. “Regression convolutional neural network for improved simultaneous EMG control”. In: *J. Neural Eng.* 16.3 (Apr. 2019), p. 036015.

[302] Peng Xia, Jie Hu, and Yinghong Peng. “EMG-based estimation of limb movement using deep learning with recurrent convolutional neural networks”. In: *Artificial organs* 42.5 (2018), E67–E77.

[303] Ricardo V Godoy, Anany Dwivedi, and Minas Liarokapis. “Electromyography based decoding of dexterous, in-hand manipulation motions with temporal multichannel vision transformers”. In: *IEEE Transactions on Neural Systems and Rehabilitation Engineering* 30 (2022), pp. 2207–2216.

[304] Dario Farina et al. “The extraction of neural information from the surface EMG for the control of upper-limb prostheses: emerging avenues and challenges”. In: *IEEE Transactions on Neural Systems and Rehabilitation Engineering* 22.4 (2014), pp. 797–809.

[305] Bingbin Wang et al. “Unravelling influence factors in pattern recognition myoelectric control systems: The impact of limb positions and electrode shifts”. In: *Sensors* 24.15 (2024), p. 4840.

[306] Bo Lv et al. “Channel selection against electrode shift enables robust myoelectric control without retraining”. In: *Science China Technological Sciences* 64.8 (2021), pp. 1653–1662.

[307] Ann M Simon et al. “Implications of EMG channel count: enhancing pattern recognition online prosthetic testing”. In: *Frontiers in Rehabilitation Sciences* 5 (2024), p. 1345364.

[308] Linda Resnik. “Development and testing of new upper-limb prosthetic devices: research designs for usability testing.” In: *Journal of Rehabilitation Research & Development* 48.6 (2011).

[309] Nawadita Parajuli et al. “Real-time EMG based pattern recognition control for hand prostheses: A review on existing methods, challenges and future implementation”. In: *Sensors* 19.20 (2019), p. 4596.

[310] Miguel Simao et al. “A review on electromyography decoding and pattern recognition for human-machine interaction”. In: *Ieee Access* 7 (2019), pp. 39564–39582.

[311] Andrés Jaramillo-Yánez, Marco E Benalcázar, and Elisa Mena-Maldonado. “Real-time hand gesture recognition using surface electromyography and machine learning: A systematic literature review”. In: *Sensors* 20.9 (2020), p. 2467.

[312] Tala Zaim et al. “Machine Learning-and Deep Learning-Based Myoelectric Control System for Upper Limb Rehabilitation Utilizing EEG and EMG Signals: A Systematic Review”. In: *Bioengineering* 12.2 (2025), p. 144.

[313] Kevin Englehart and Bernard Hudgins. “A robust, real-time control scheme for multifunction myoelectric control”. In: *IEEE transactions on biomedical engineering* 50.7 (2003), pp. 848–854.

[314] Ning Jiang et al. “Effect of arm position on the prediction of kinematics from EMG in amputees”. In: *Medical & biological engineering & computing* 51.1 (2013), pp. 143–151.

[315] BL Day et al. “Electric and magnetic stimulation of human motor cortex: surface EMG and single motor unit responses.” In: *The Journal of physiology* 412.1 (1989), pp. 449–473.

[316] Daniel M Wolpert, R Chris Miall, and Mitsuo Kawato. “Internal models in the cerebellum”. In: *Trends in cognitive sciences* 2.9 (1998), pp. 338–347.

[317] Stephen H Scott. “Optimal feedback control and the neural basis of volitional motor control”. In: *Nature Reviews Neuroscience* 5.7 (2004), pp. 532–545.

[318] David W Franklin and Daniel M Wolpert. “Computational mechanisms of sensorimotor control”. In: *Neuron* 72.3 (2011), pp. 425–442.

[319] Gea Drost et al. “Clinical applications of high-density surface EMG: a systematic review”. In: *Journal of Electromyography and Kinesiology* 16.6 (2006), pp. 586–602.

[320] Hanadi Abbas Jaber, Mofeed Turky Rashid, and Luigi Fortuna. "Robust hand gesture identification using envelope of HD-sEMG signal". In: *Proceedings of the International Conference on Information and Communication Technology*. 2019, pp. 203–209.

[321] Giacinto Luigi Cerone, Alberto Botter, and Marco Gazzoni. "A modular, smart, and wearable system for high density sEMG detection". In: *IEEE Transactions on Biomedical Engineering* 66.12 (2019), pp. 3371–3380.

[322] Nicholas Tacca et al. "Wearable high-density EMG sleeve for complex hand gesture classification and continuous joint angle estimation". In: *Scientific Reports* 14.1 (2024), p. 18564.

[323] Lennart Heim et al. "Measuring what really matters: Optimizing neural networks for tinyml". In: *arXiv preprint arXiv:2104.10645* (2021).

[324] Ji Lin et al. "Mcunet: Tiny deep learning on iot devices". In: *Advances in neural information processing systems* 33 (2020), pp. 11711–11722.

[325] Eric R Kandel et al. *Principles of neural science*. Vol. 4. McGraw-hill New York, 2000.

[326] Maryam Khoshkhooy Titkanlou, Duc Thien Pham, and Roman Mouček. "Classification of EEG Signal Using Deep Learning Architectures Based Motor-Imagery for an Upper-Limb Rehabilitation Exoskeleton". In: *SN Computer Science* 6.3 (2025), p. 193.

[327] Md Rabiul Islam et al. "S-ConvNet: A shallow convolutional neural network architecture for neuromuscular activity recognition using instantaneous high-density surface EMG images". In: *2020 42nd Annual International Conference of the IEEE Engineering in Medicine & Biology Society (EMBC)*. IEEE. 2020, pp. 744–749.

[328] M. Nowak et al. "Simultaneous and Proportional Real-Time Myocontrol of Up to Three Degrees of Freedom of the Wrist and Hand". In: *IEEE T. Bio-Med. Eng.* 70.2 (Feb. 2023), pp. 459–469.

[329] Roberto Merletti, Dario Farina, and Marco Gazzoni. "The linear electrode array: a useful tool with many applications". In: *Journal of Electromyography and Kinesiology* 13.1 (2003), pp. 37–47.

[330] S. Tam et al. Félix Chamberland Étienne Buteau. "Novel Wearable HD-EMG Sensor With Shift-Robust Gesture Recognition Using Deep Learning". In: *IEEE TRANSACTIONS ON BIOMEDICAL CIRCUITS AND SYSTEM* (2023).

[331] John Z Wu et al. "Simulation of mechanical responses of fingertip to dynamic loading". In: *Medical engineering & physics* 24.4 (2002), pp. 253–264.

[332] Uwe Proske and Simon C Gandevia. "The proprioceptive senses: their roles in signaling body shape, body position and movement, and muscle force". In: *Physiological reviews* (2012).

[333] Giovanni Rolandino. *Code Repository for RPC-Net and HDE-Array System*. `https://www.dropbox.com/scl/fo/nkvbse7evo0k8ou1utn7i/AMDh_MOZQJ6gCwDXGPadmZ0?rlkey=ynoix3anpc81v24hogn3fymb4&st=xrqx07q2&dl=0`. Accessed May 2025. 2025.

[334] G. Rolandino et al. *RPC-Net Dataset. Simultaneous HD-sEMG Recordings on the Forearm and angles of a 29-DoF Hand Kinematic Model*. available: 10.5281/zenodo.14246378. Nov. 2024.

[335] Institute for Health Metrics and Evaluation (IHME). *GBD Compare Data Visualization*. Available from: http://vizhub.healthdata.org/gbd-compare. (Accessed May 2023). Jan. 2020.

[336] M.G. Catalano et al. "Adaptive synergies for the design and control of the Pisa/IIT SoftHand". In: *Int. J. Robot. Res.* 33.5 (Apr. 2014), pp. 768–782.

[337] M. Controzzi et al. "The SSSA-MyHand: A Dexterous Lightweight Myoelectric Hand Prosthesis". In: *IEEE T. Neur. Sys. Reh.* 25.5 (June 2016), pp. 459–468.

[338] J. Fajardo et al. "Galileo Hand: An Anthropomorphic and Affordable Upper-Limb Prosthesis". In: *IEEE Access* 8 (Apr. 2020), pp. 81365–81377.

[339] P. J. Kyberd. "Assessment of Functionality of Multifunction Prosthetic Hands". In: *J. Prosthet. Ortoht.* 29.3 (July 2017), pp. 103–111.

[340] D. D'Accolti et al. "Online Classification of Transient EMG Patterns for the Control of the Wrist and Hand in a Transradial Prosthesis". In: *IEEE Robotic. Autom. L.* 8.2 (Feb. 2023), pp. 1045–1052.

[341] E. A. Biddiss and T. T. Chau. "Upper limb prosthesis use and abandonment: A survey of the last 25 years". In: *Prosthet. Orthot. Int.* 31.3 (Sept. 2007), pp. 236–257.

[342] C. Ahmadizadeh et al. "Human machine interfaces in upper-limb prosthesis control: A survey of techniques for pre-processing and processing of biosignals". In: *IEEE Signal Proc. Mag.* 38.4 (June 2021), pp. 12–22.

[343] M. Cognolato M. Atzori and H. Müller. "Deep Learning with Convolutional Neural Networks Applied to Electromyography Data: A Resource for the Classification of Movements for Prosthetic Hands". In: *Frontiers in neurorobotics* (2016).

[344] Y. Hu et al. "A novel attention-based hybrid CNN-RNN architecture for sEMG-based gesture recognition". In: *PLOS One* 13.10 (Oct. 2018), e0206049.

[345] I. Vujaklija and D. Farina. "Prosthetics and Innovation". In: *Blast Injury Science and Engineering: A Guide for Clinicians and Researchers*. Cham, CH: Springer, 2022, pp. 421–435.

[346] R. C. Sîmpetru et al. "Accurate Continuous Prediction of 14 Degrees of Freedom of the Hand from Myoelectrical Signals through Convolutive Deep Learning". In: *IEEE-EMBC* (Glasgow, UK). 2022, pp. 702–706.

[347] N. Thomas et al. "The Utility of Synthetic Reflexes and Haptic Feedback for Upper-Limb Prostheses in a Dexterous Task Without Direct Vision". In: *IEEE T. Neur. Sys. Reh.* 31 (Jan. 2023), pp. 169–179.

[348] J. A. George et al. "Biomimetic sensory feedback through peripheral nerve stimulation improves dexterous use of a bionic hand". In: *Sci. Robot.* 4.32 (July 2019), eaax2352.

[349] C. Castellini et al. "Surface EMG for force control of mechanical hands". In: *IEEE-ICRA* (Pasadena, CA). 2008, pp. 725–730.

[350] A. Cimolato et al. “Hybrid Machine Learning-Neuromusculoskeletal Modeling for Control of Lower Limb Prosthetics”. In: *IEEE RAS/EMBS BioRob* (New York, NY). 2020, pp. 557–563.

[351] Y. J. Choo and M. C. Chang. “Use of machine learning in the field of prosthetics and orthotics: A systematic narrative review”. In: *Prosthet. Orthot. Int.* 47.3 (June 2023), pp. 226–240.

[352] M. Atzori and H. Müller. “Control Capabilities of Myoelectric Robotic Prostheses by Hand Amputees: A Scientific Research and Market Overview”. In: *Front. Syst. Neurosci.* 9 (Nov. 2015), p. 162.

[353] C. Castellini et al. “Multi-subject/daily-life activity EMG-based control of mechanical hands”. In: *J. Neural. Eng. Rehab.* 6.1 (Nov. 2009), pp. 1–11.

[354] C. J. De Luca. “The Use of Surface Electromyography in Biomechanics”. In: *J. Appl. Biomech.* 13.2 (Mar. 1997), pp. 135–163.

[355] V. G. Tenore et al. “Decoding of Individuated Finger Movements Using Surface Electromyography”. In: *IEEE T. Bio-Med. Eng.* 56.5 (May 2009), pp. 1427–1434.

[356] O. Fukuda et al. “A human-assisting manipulator teleoperated by emg signals and arm motions”. In: *IEEE T. Robotic. Autom.* 19.2 (Apr. 2003), pp. 210–222.

[357] T. Vieira et al. G. L. Cerone A. Botter. “Design and Characterization of a Textile Electrode System for the Detection of High-Density sEMG”. In: *IEEE Transactions on Neural Systems and Rehabilitation Engineering* 29.12 (2021), pp. 1110–1119.

[358] Jorge Nocedal and Stephen J Wright. “Quadratic programming”. In: *Numerical optimization* (2006), pp. 448–492.

[359] Kaiming He et al. “Deep residual learning for image recognition”. In: *Proceedings of the IEEE conference on computer vision and pattern recognition*. 2016, pp. 770–778.

[360] F. Quivira et al. “Translating sEMG signals to continuous hand poses using recurrent neural networks”. In: *IEEE EMBS BHI* (Las Vegas, NV). 2018, pp. 166–169.

[361] N. A. S. Putro et al. “Estimating finger joint angles by surface EMG signal using feature extraction and transformer-based deep learning model”. In: *Biomed. Signal Proces.* 87.B (Jan. 2024), p. 105447.

[362] Sheldon M. Ross. “Hypothesis Tests Concerning Two Populations”. In: *Introductory Statistics (Fourth Edition)*. Oxford, UK: Academic Press, 2017, pp. 433–488.

[363] Ronald J Feise. “Do multiple outcome measures require p-value adjustment?” In: *BMC medical research methodology* 2.1 (2002), p. 8.

[364] S. Xie et al. T. Bao S.A.R. Zaidi. “A CNN-LSTM Hybrid Model for Wrist Kinematics Estimation Using Surface Electromyography”. In: *IEEE Transactions on Instrumentation and Measurement* (2020).

[365] X. Hu et al. “Extracting extensor digitorum communis activation patterns using high-density surface electromyography”. In: *Front. Psychol.* 6 (Oct. 2015), p. 279.

[366] C. Amma et al. “Advancing muscle-computer interfaces with high-density electromyography”. In: *ACM CHI* (Seul, ROK). 2015, pp. 929–938.

[367] M. Rojas-Martínez et al. “Identification of isometric contractions based on High Density EMG maps”. In: *J. Electromyogr. Kines.* 23.1 (Feb. 2013), pp. 33–42.

[368] Cody L McDonald et al. “Global prevalence of traumatic non-fatal limb amputation”. In: *Prosthetics and orthotics international* 45.2 (2021), pp. 105–114.

[369] Alan D Lopez and Christopher CJL Murray. “The global burden of disease, 1990–2020”. In: *Nature medicine* 4.11 (1998), pp. 1241–1243.

[370] W. Ding et al. “Spinal cord injury: The global incidence, prevalence, and disability from the global burden of disease study 2019”. In: *Spine* 47.21 (Nov. 2022), p. 1532.

[371] National Spinal Cord Injury Statistical Center. *SCIMS 2022 Annual Report - Complete Public Version*. Annual Statistical Report. Birmingham, AL: National Spinal Cord Injury Statistical Center, 2022.

[372] Eko Wahyu Abryandoko et al. “Literature review: User interface of system functional electrical stimulation (FES) and arm robotic rehabilitation”. In: *Journal of Applied Engineering Science* (2024), pp. 1–14.

[373] C. Igual et al. “Myoelectric Control for Upper Limb Prostheses”. In: *Electronics* 8.11 (Oct. 2019), p. 1244.

[374] J. He et al. N. Jiang C. Chen. “Bio-robotics research for non-invasive myoelectric neural interfaces for upper-limb prosthetic control: a 10-year perspective review”. In: *National Science Review* (2023).

[375] S. van Twillert et al. N. Kerver C.K. van der Sluis. “Towards assessing the preferred usage features of upper limb prostheses: most important items regarding prosthesis use in people with major unilateral upper limb absence—a Dutch national survey”. In: *Disability and Rehabilitation* (2021).

[376] D. Yao et al. A.K. Einfeldt F. Rebmann. “What do users and their aiding professionals want from future devices in upper limb prosthetics? A focus group study”. In: *PLoS ONE* (2023).

[377] Guangli Li, Sizhe Wang, and Yanwen Y Duan. “Towards gel-free electrodes: A systematic study of electrode-skin impedance”. In: *Sensors and Actuators B: Chemical* 241 (2017), pp. 1244–1255.

[378] Xi Tang et al. “Using microneedle array electrodes for non-invasive electrophysiological signal acquisition and sensory feedback evoking”. In: *Frontiers in Bioengineering and Biotechnology* 11 (2023), p. 1238210.

[379] Claudia Lopes et al. “Nanostructured (Ti, Cu) N dry electrodes for advanced control of the neuromuscular activity”. In: *IEEE Sensors Journal* 23.4 (2023), pp. 3629–3639.

[380] Richard Drake et al. *Gray’s basic anatomy*. Elsevier Health Sciences, 2012.

[381] Todd C Pataky. “One-dimensional statistical parametric mapping in Python”. In: *Computer methods in biomechanics and biomedical engineering* 15.3 (2012), pp. 295–301.

[382] Todd Pataky. *spm1d*. Available from: https://spm1d.org/ (Accessed Sep 2024). 2022.

[383] Robert S Witte and John S Witte. *Statistics*. John Wiley & Sons, 2017.

[384] George Casella and Roger Berger. *Statistical inference*. CRC Press, 2024.

[385] R. Merletti. "The electrode–skin interface and optimal detection of bioelectric signals". In: *Physiol. Meas.* 31.10 (Oct. 2010), pp. 1–4.

[386] C.M. van Rijn et al. "High-quality recording of bioelectric events. Part 1. Interference reduction, theory and practice". In: *Med. Biol. Eng. Comput.* 28.5 (Sept. 1990), pp. 389–397.

[387] A. Botter et al. R. Merletti M. Aventaggiato. "Advances in Surface EMG: Recent Progress in Detection and Processing Techniques". In: *Critical Reviews in Biomedical Engineering* (2010).

[388] J.C. Huhta et al. "60-Hz interference in electrocardiography". In: *IEEE Trans. Biomed. Eng.* BME-20.2 (Mar. 1973), pp. 91–101.

[389] Y.M. Chi et al. "Dry-contact and noncontact biopotential electrodes: methodological review". In: *IEEE Rev Biomed Eng* 3 (2010), pp. 106–119.

[390] G. Piervirgili et al. "A new method to assess skin treatments for lowering the impedance and noise of individual gelled Ag–AgCl electrodes". In: *Physiol. Meas.* 35.10 (Sept. 2014).

[391] G. L. Cerone et al. "Design and Validation of a Wireless Body Sensor Network for Integrated EEG and HD-sEMG Acquisitions". In: *IEEE Transactions on Neural Systems and Rehabilitation Engineering* 30 (2022), pp. 61–71.

[392] Marco Barbero, Roberto Merletti, and Alberto Rainoldi. "Atlas of Muscle Innervation Zones". In: *Atlas of Muscle Innervation Zones* (2012).

[393] Thalmic Labs. *myo.js README*. `https://github.com/thalmiclabs/`. Accessed: 2024-05-18.

[394] Liangtao Yang et al. "Insight into the contact impedance between the electrode and the skin surface for electrophysical recordings". In: *ACS omega* 7.16 (2022), pp. 13906–13912.

[395] Paolo Cattarello and Roberto Merletti. "Characterization of dry and wet Electrode-Skin interfaces on different skin treatments for HDsEMG". In: *2016 IEEE International Symposium on Medical Measurements and Applications (MeMeA)*. IEEE. 2016, pp. 1–6.

[396] Marco Santello et al. "Hand synergies: Integration of robotics and neuroscience for understanding the control of biological and artificial hands". In: *Physics of life reviews* 17 (2016), pp. 1–23.

[397] Carolyn R Mason, Jose E Gomez, and Timothy J Ebner. "Hand synergies during reach-to-grasp". In: *Journal of neurophysiology* 86.6 (2001), pp. 2896–2910.

[398] Marco Santello, Martha Flanders, and John F Soechting. "Postural hand synergies for tool use". In: *Journal of neuroscience* 18.23 (1998), pp. 10105–10115.

[399] Mark L Latash. "One more time about motor (and non-motor) synergies". In: *Experimental Brain Research* 239.10 (2021), pp. 2951–2967.

[400] Emanuel Todorov and Zoubin Ghahramani. "Analysis of the synergies underlying complex hand manipulation". In: *The 26th Annual International Conference of the IEEE Engineering in Medicine and Biology Society.* Vol. 2. IEEE. 2004, pp. 4637–4640.

[401] Felipe L Gewers et al. "Principal component analysis: A natural approach to data exploration". In: *ACM Computing Surveys (CSUR)* 54.4 (2021), pp. 1–34.

[402] Andrea Cimolato et al. "EMG-driven control in lower limb prostheses: A topic-based systematic review". In: *Journal of NeuroEngineering and Rehabilitation* 19.1 (2022), p. 43.

[403] Zixuan Qin et al. "A CW-CNN regression model-based real-time system for virtual hand control". In: *Frontiers in Neurorobotics* 16 (2022), p. 1072365.

[404] Alain De Cheveigné and Jonathan Z Simon. "Denoising based on time-shift PCA". In: *Journal of neuroscience methods* 165.2 (2007), pp. 297–305.

[405] Vrajeshri Patel et al. "Linear and nonlinear kinematic synergies in the grasping hand". In: *Journal of Bioengineering & Biomedical Sciences* 5.3 (2015), p. 1.

[406] Néstor J Jarque-Bou et al. "Kinematic synergies of hand grasps: a comprehensive study on a large publicly available dataset". In: *Journal of neuroengineering and rehabilitation* 16 (2019), pp. 1–14.

[407] Deanna H Gates, Susannah M Engdahl, and Alicia Davis. "Recommendations for the successful implementation of upper limb prosthetic technology". In: *Hand Clinics* 37.3 (2021), pp. 457–466.

[408] Linda J Resnik et al. "Measuring satisfaction with upper limb prostheses: orthotics and prosthetics user survey revision that includes issues of concern to women". In: *Archives of physical medicine and rehabilitation* 103.12 (2022), pp. 2316–2324.

[409] Cosimo Gentile and Emanuele Gruppioni. "A perspective on prosthetic hands control: From the brain to the hand". In: *Prosthesis* 5.4 (2023), pp. 1184–1205.

[410] Jongman Kim et al. "SEMG-based hand posture recognition considering electrode shift, feature vectors, and posture groups". In: *Sensors* 21.22 (2021), p. 7681.

[411] Jiayuan He et al. "Position identification for robust myoelectric control against electrode shift". In: *IEEE transactions on neural systems and rehabilitation engineering* 28.12 (2020), pp. 3121–3128.

[412] Ziyou Li et al. "Electrode shifts estimation and adaptive correction for improving robustness of sEMG-based recognition". In: *IEEE Journal of Biomedical and Health Informatics* 25.4 (2020), pp. 1101–1110.

[413] Jianfeng Li et al. "Deep end-to-end transfer learning for robust inter-subject and inter-day hand gesture recognition using surface EMG". In: *Biomedical Signal Processing and Control* 100 (2025), p. 106892.

[414] Yucheng Long et al. "A transfer learning based cross-subject generic model for continuous estimation of finger joint angles from a new user". In: *IEEE Journal of Biomedical and Health Informatics* 27.4 (2023), pp. 1914–1925.

[415] Di Wu, Jie Yang, and Mohamad Sawan. "Transfer Learning on Electromyography (EMG) Tasks: Approaches and Beyond". In: *IEEE Transactions on Neural Systems and Rehabilitation Engineering* 31 (2023), pp. 3015–3034.

[416] Xiang Chen et al. “Hand gesture recognition based on surface electromyography using convolutional neural network with transfer learning method”. In: *IEEE Journal of Biomedical and Health Informatics* 25.4 (2020), pp. 1292–1304.

[417] Md Rabiul Islam et al. “Surface EMG-based inter-session/inter-subject gesture recognition by leveraging lightweight all-ConvNet and transfer learning”. In: *IEEE Transactions on Instrumentation and Measurement* (2024).

[418] Chen Chen et al. “Simultaneous and proportional control of wrist and hand movements by decoding motor unit discharges in real time”. In: *Journal of Neural Engineering* 18.5 (2021), p. 056010.

[419] Dapeng Yang and Hong Liu. “An EMG-based deep learning approach for multi-DOF wrist movement decoding”. In: *IEEE Transactions on Industrial Electronics* 69.7 (2021), pp. 7099–7108.

[420] Sumit A Raurale, John McAllister, and Jesus Martinez del Rincon. “Real-time embedded EMG signal analysis for wrist-hand pose identification”. In: *IEEE Transactions on Signal Processing* 68 (2020), pp. 2713–2723.

[421] Qin Zhang et al. “Simultaneous and proportional estimation of multijoint kinematics from EMG signals for myocontrol of robotic hands”. In: *IEEE/ASME Transactions on Mechatronics* 25.4 (2020), pp. 1953–1960.

[422] Sean Sanford et al. “Effects of Visual Feedback Complexity on the Performance of a Movement Task for Rehabilitation”. In: *Journal of Motor Behavior* 53.2 (2021), pp. 243–257.

[423] Meike A Schweisfurth et al. “Electrotactile EMG feedback improves the control of prosthesis grasping force”. In: *Journal of neural engineering* 13.5 (2016), p. 056010.

[424] Jack Tchimino, Jakob Lund Dideriksen, and Strahinja Dosen. “EMG feedback outperforms force feedback in the presence of prosthesis control disturbance”. In: *Frontiers in Neuroscience* 16 (2022), p. 952288.

[425] Strahinja Dosen et al. “EMG Biofeedback for online predictive control of grasping force in a myoelectric prosthesis”. In: *Journal of neuroengineering and rehabilitation* 12 (2015), pp. 1–13.

[426] Cesar Marquez-Chin and Milos R Popovic. “Functional electrical stimulation therapy for restoration of motor function after spinal cord injury and stroke: a review”. In: *Biomedical engineering online* 19.1 (2020), p. 34.

[427] Yuan-xing Wang and Zhi-zeng Luo. “Research on the effect of MT+ FES training on sensorimotor cortex”. In: *Neural Plasticity* 2022.1 (2022), p. 6385755.

[428] Siddeshwar Patil et al. “Functional electrical stimulation for the upper limb in tetraplegic spinal cord injury: a systematic review”. In: *Journal of medical engineering & technology* 39.7 (2015), pp. 419–423.

[429] Jheng-Dao Yang et al. “Effectiveness of electrical stimulation therapy in improving arm function after stroke: a systematic review and a meta-analysis of randomised controlled trials”. In: *Clinical rehabilitation* 33.8 (2019), pp. 1286–1297.

[430] Mei Sun et al. “Meta-Analysis of Functional Electrical Stimulation Combined with Occupational Therapy on Post-Stroke Limb Functional Recovery and Quality of Life”. In: *Cerebrovascular Diseases* 53.6 (2025), pp. 743–752.

[431] Owen A Howlett et al. "Functional electrical stimulation improves activity after stroke: a systematic review with meta-analysis". In: *Archives of physical medicine and rehabilitation* 96.5 (2015), pp. 934–943.

[432] Andrés F Ruiz Olaya and Alberto López Delis. "Emerging technologies for neuro-rehabilitation after stroke: Robotic exoskeletons and active fes-assisted therapy". In: *Assistive Technologies for Physical and Cognitive Disabilities* (2015), pp. 1–21.

[433] Mingxu Sun et al. "FES-UPP: a flexible functional electrical stimulation system to support upper limb functional activity practice". In: *Frontiers in Neuroscience* 12 (2018), p. 449.

[434] Anelise Ventura et al. "Design and fast-fabrication of a system for functional electrical stimulation in upper limb of people with tetraplegia". In: *Spinal Cord Series and Cases* 8.1 (2022), p. 54.

[435] Marco Crepaldi et al. "FITFES: A wearable myoelectrically controlled functional electrical stimulator designed using a user-centered approach". In: *IEEE Transactions on Neural Systems and Rehabilitation Engineering* 29 (2021), pp. 2142–2152.

[436] Philipp Müller et al. "Adaptive multichannel FES neuroprosthesis with learning control and automatic gait assessment". In: *Journal of neuroengineering and rehabilitation* 17 (2020), pp. 1–20.

[437] Dejan B Popović and Lana Popović-Maneski. "Neuroprosthesis and Functional Electrical Stimulation (Peripheral)". In: *Handbook of Neuroengineering*. Springer, 2022, pp. 1–40.

[438] Mehdi Khantan, Mikael Avery, Phyo Thuta Aung, et al. *The NuroSleeve, A User-Centered 3D Printed Orthosis and Functional Electrical Stimulation System for Individuals with Upper Extremity Impairment*. `https://doi.org/10.21203/rs.3.rs-2451365/v1`. Preprint, Research Square, Version 1. Jan. 2023.

[439] Amanda Noonan et al. "A Portable, User-Controlled FES System for Upper Limb Reanimation in Individuals with Tetraplegia". In: *Archives of Physical Medicine and Rehabilitation* 101.11 (2020), e89–e90.

[440] Elizabeth Heald et al. "Myoelectric signal from below the level of spinal cord injury as a command source for an implanted upper extremity neuroprosthesis-a case report". In: *Journal of neuroengineering and rehabilitation* 16 (2019), pp. 1–6.

[441] Matija Milosevic et al. "Why brain-controlled neuroprosthetics matter: mechanisms underlying electrical stimulation of muscles and nerves in rehabilitation". In: *Biomedical engineering online* 19 (2020), pp. 1–30.

[442] Francisco Anaya, Pavithra Thangavel, and Haoyong Yu. "Hybrid FES–robotic gait rehabilitation technologies: a review on mechanical design, actuation, and control strategies". In: *International journal of intelligent robotics and applications* 2 (2018), pp. 1–28.

[443] Junlin Zhou, Christopher T Freeman, and William Holderbaum. "Multiple-model iterative learning control with application to stroke rehabilitation". In: *Control Engineering Practice* 154 (2025), p. 106134.

[444] Christina Salchow-Hömmen et al. “User-centered practicability analysis of two identification strategies in electrode arrays for FES induced hand motion in early stroke rehabilitation”. In: *Journal of NeuroEngineering and Rehabilitation* 15 (2018), pp. 1–19.

[445] Nathan Dunkelberger, Eric M Schearer, and Marcia K O’Malley. “A review of methods for achieving upper limb movement following spinal cord injury through hybrid muscle stimulation and robotic assistance”. In: *Experimental neurology* 328 (2020), p. 113274.

[446] Morufu Olusola Ibitoye et al. “Restoring prolonged standing via functional electrical stimulation after spinal cord injury: A systematic review of control strategies”. In: *Biomedical Signal Processing and Control* 49 (2019), pp. 34–47.

[447] Matthew R Williams and Robert F Kirsch. “Evaluation of head orientation and neck muscle EMG signals as three-dimensional command sources”. In: *Journal of neuroengineering and rehabilitation* 12 (2015), pp. 1–16.

[448] Luis Felipe Reséndiz Domínguez et al. “Results of a Survey Applied to Potential Users of a Functional Electrical Stimulation Device and Its Use to Design a User Interface Based on IEC 62366 and IEC 62304 Standards”. In: *Congreso Nacional de Ingeniería Biomédica*. Springer. 2024, pp. 113–121.

[449] Roberta Mazzone. “cycling induced by functional electrical stimulation: user experience evaluation and long-term performances assessment”. MA thesis. Politecnico di Milano, 2021.

[450] Bastien Moineau et al. “End-user and clinician perspectives on the viability of wearable functional electrical stimulation garments after stroke and spinal cord injury”. In: *Disability and Rehabilitation: Assistive Technology* 16.3 (2021), pp. 241–250.

[451] Yalian Pei et al. “Consumer views of functional electrical stimulation and robotic exoskeleton in SCI rehabilitation: A mini review”. In: *Artificial Organs* (2024).

[452] Guang Dai et al. “Electromyography Acquisition and Intervention in Healthcare for Older Adults: A HCI Scoping Review”. In: *International Symposium on World Ecological Design*. IOS Press. 2024, pp. 570–581.

[453] Hye-Kang Park et al. “A wearable electromyography-controlled functional electrical stimulation system improves balance, gait function, and symmetry in older adults”. In: *Technology and Health Care* 30.2 (2022), pp. 423–435.

[454] Chiara Höhler et al. “Contralaterally EMG-triggered functional electrical stimulation during serious gaming for upper limb stroke rehabilitation: a feasibility study”. In: *Frontiers in Neurorobotics* 17 (2023), p. 1168322.

[455] Matthew R Williams and Robert F Kirsch. “Evaluation of head orientation and neck muscle EMG signals as command inputs to a human–computer interface for individuals with high tetraplegia”. In: *IEEE Transactions on Neural Systems and Rehabilitation Engineering* 16.5 (2008), pp. 485–496.

[456] Thomas Schauer. “Sensing motion and muscle activity for feedback control of functional electrical stimulation: Ten years of experience in Berlin”. In: *Annual Reviews in Control* 44 (2017), pp. 355–374.

[457] Zheng-Yang Bi et al. “A hybrid method for real-time stimulation artefact removal during functional electrical stimulation with time-variant parameters”. In: *Journal of Neural Engineering* 18.4 (2021), p. 046028.

[458] Lachlan R McKenzie et al. “Low-cost stimulation resistant electromyography”. In: *HardwareX* 9 (2021), e00178.

[459] A Richards. *University of Oxford Advanced Research Computing*. 2015.

Plus Ultra

Appendices

A

Ethics and Acknowledgments

A.1 Acknowledgment Chapter 3

The author would like to thank the members of ONIG in Oxford and of LISiN in Turin for the valuable guidance provided during the writing of this chapter and to acknowledge the use of the University of Oxford Advanced Research Computing (ARC) facility in carrying out this work [459]. Figure 3.1 was created with BioRender.com.

A.1.1 Publication acknowledgment

This chapter is based on research previously published by G. Rolandino, M. Gagliardi, T. Vieira, G. L. Cerone, B. Andrews and J. J. FitzGerald in IEEE Transactions on Biomedical Engineering (vol. 71, no. 5, pp. 1617-1627, May 2024; doi: 10.1109/TBME.2023.3346192), with the title: "Developing RPC-Net: Leveraging High-Density Electromyography and Machine Learning for Improved Hand Position Estimation". The material is incorporated here with minor modifications and in accordance with university guidelines. Co-author permission statements are included below.

A.2 Acknowledgment Chapter 4

The author would like to thank the members of ONIG in Oxford and of LISiN in Turin for the valuable guidance provided during the writing of this chapter and to acknowledge the use of the University of Oxford Advanced Research Computing (ARC) facility in carrying out this work [459]. Figure 4.2 and Figure 4.1 were created with BioRender.com.

A.2.1 Publication acknowledgment

This chapter is based on research previously published (G. Rolandino, C. Zangrandi, T. Vieira, G. L. Cerone, B. Andrews and J. J. FitzGerald, "HDE-Array: Development and Validation of a New Dry Electrode Array Design to Acquire HD-sEMG for Hand Position Estimation," in IEEE Transactions on Neural Systems and Rehabilitation Engineering, vol. 32, pp. 4004-4013, 2024, doi: 10.1109/TNSRE.2024.3490796.). The material is incorporated here with minor modifications and in accordance with university guidelines. Co-author permission statements are included below.

A.3 Acknowledgment Chapter 5

The author would like to thank the members of ONIG in Oxford and of LISiN in Turin for the valuable guidance provided during the writing of this chapter and to acknowledge the use of the University of Oxford Advanced Research Computing (ARC) facility in carrying out this work [459]. Figure 5.1 was created with BioRender.com.

A.3.1 Publication acknowledgment

This chapter is based on research previously presented as a conference contribution (G. Rolandino, T. Vieira, G. L. Cerone, B. Andrews, and J. J. FitzGerald, "Performance of a ML-Based 3-DoF Kinematic Model in Estimating Hand Position from High-Density EMG," presented at the IFESS Conference, Bath, UK, September 2024). The material has been substantially revised and adapted in accordance

with university guidelines. A statement confirming permission from all co-authors is provided below.

A.4 Acknowledgment Chapter 6

The author would like to thank the members of ONIG and ORI in Oxford, of LISiN in Turin, and of the Department of Orthopaedics, Rheumatology and Traumatology at the University of Campinas for the valuable guidance provided during the writing of this chapter. The author would like to acknowledge the contribution of Matt Towlson from ORI to the data acquisition phase, and to acknowledge the use of the University of Oxford Advanced Research Computing (ARC) facility in carrying out this work [459]. Figure 6.1 and Figure 6.2 were created with BioRender.com. This chapter arises from research funded by the John Fell Oxford University Press Research Fund.

A.4.1 Publication acknowledgment

This chapter is based on research submitted for publication (G. Rolandino, L. Lion, T. Vieira, G. L. Cerone, B. Andrews and J. J. FitzGerald, "Artificial Neural Networks for HD-sEMG-Based Hand Position Estimation: Addressing Inter- and Intra-Subject Variability,") to IEEE Transactions on Neural Systems and Rehabilitation Engineering, in July 2025. The material is incorporated here with minor modifications and in accordance with university guidelines. The co-author permission statement from all authors involved is included below.

A.5 Acknowledgment Chapter 7

The author would like to thank the members of ONIG and ORI in Oxford, of LISiN in Turin, and of the Department of Orthopaedics, Rheumatology and Traumatology at the University of Campinas for the valuable guidance provided during the writing of this chapter. The author would like to acknowledge the contribution of Matt Towlson from ORI to the data acquisition phase, and to acknowledge the use of the University of Oxford Advanced Research Computing (ARC) facility in carrying out this work

[459]. Figure 7.1 and Figure 7.2 were created with BioRender.com. This chapter arises from research funded by the John Fell Oxford University Press Research Fund.

A.5.1 Publication acknowledgment

This chapter is based on research submitted for publication (G. Rolandino, G. Parisi, T. Vieira, G. L. Cerone, B. Andrews and J. J. FitzGerald, "Real-Time Hand Kinematic Estimation with HD-sEMG and Artificial Neural Networks: Feasibility and Effects of Multi-Subject Training and Visual Feedback,") to IEEE Transactions on Neural Systems and Rehabilitation Engineering, in July 2025. The material is incorporated here with minor modifications and in accordance with university guidelines. The co-author permission statement from all authors involved is included below.

A.6 Acknowledgment Chapter 8

The author would like to thank the members of ONIG in Oxford and of the Department of Orthopaedics, Rheumatology and Traumatology at the University of Campinas for the valuable guidance provided during the writing of this chapter. The author would like to acknowledge the use of the University of Oxford Advanced Research Computing (ARC) facility in carrying out this work [459]. Figure 8.1 was created with BioRender.com. This chapter arises from research funded by the John Fell Oxford University Press Research Fund.

A.6.1 Publication acknowledgment

This chapter is based on research submitted for publication (G. Rolandino, V. Taboni Lisboa, T. Vieira, A. Cliquet Jr., B. Andrews and J. J. FitzGerald, "HD-sEMG-Based Control Using Neck Muscles and Shallow Neural Networks: Assessing Performance in Rehabilitation-Oriented Tasks,") to IEEE Transactions on Neural Systems and Rehabilitation Engineering, in July 2025. The material is incorporated here with minor modifications and in accordance with university guidelines. The co-author permission statement from all authors involved is included below.

A.7 Ethics Documentation

Ethics approval for the studies described in Chapters 6-8 was granted by the local ethics committee, the "Comitê de Ética em Pesquisa" (CEP), at the State University of Campinas (Universidade Estadual de Campinas, UNICAMP), SP, Brazil. Approval reference: 34583120.2.0000.5404.

The following pages include the original ethics approval documents for two additional applications (granted in Italy and UK, respectively), as well as the co-authorship acknowledgment. The ethics approval granted in Italy is included in the original Italian and in the English translation.

VALUTAZIONE ETICA

PREMESSE:

Il Comitato Etico per la Ricerca del Politecnico di Torino (CER-Polito), sulla scorta delle competenze stabilite dal proprio Regolamento emanato dal Senato Accademico il 3 luglio 2020 (D.R. 622), ha esaminato la richiesta di valutazione etica del protocollo n. 107460/2023 inviata dal Prof. Taian, responsabile scientifico del progetto "*Sviluppo di una tecnica di elaborazione di segnali per il controllo di protesi di mano articolate basata sul deep learning"* e afferente al Dipartimento di Elettronica e Telecomunicazioni (DET). Tale richiesta è stata esaminata dal Comitato Etico in occasione della seduta del 24.11.2023, riunione a seguito della quale è emanata la presente valutazione. Tale protocollo risulta essere una versione aggiornata rispetto a quello valutato nella riunione del 27/10/2023 (n. 86843/2023).

DESCRIZIONE DEL PROGETTO:

Lo studio si pone l'obiettivo di migliorare le condizioni di vita di soggetti amputati degli arti superiori cercando di sviluppare delle soluzioni di controllo dei dispositivi protesici minimamenti soddisfacenti poiché mentre i dispositivi hanno raggiunto livelli di prestazione pressoché inquantificabili, portando ad avere dei apparati capaci di replicare o addirittura di eccedere le capacità degli arti originali, le soluzioni di controllo sono ancora molto lontane dall'essere soddisfacenti. La comunità scientifica si trova, di conseguenza, nella complicata situazione di avere dispositivi sofisticati ma non un modo per controllarli. Il presente progetto si colloca nel contesto di questa ricerca di strategie di controllo ottimale, inserendosi nel contesto più ampio della collaborazione tra il Politecnico di Torino (LISiN) e l'Università di Oxford (Nuffield Department of Surgical Sciences). La collaborazione è centrata intorno alla ricerca di dottorato di Giovanni Rolandino (Università di Oxford), che sta valutando in modo più ampio le potenzialità del *machine learning* per il controllo protesico. I dati utilizzati per il presente progetto saranno acquisiti nel contesto più ampio dell'intera collaborazione e i risultati ottenuti nell'ambito di esso potranno contribuire alla ricerca nella sua interezza. L'obiettivo principale del progetto di ricerca è valutare la performance di diversi tipi di algoritmi di *machine learning* nelle applicazioni riguardanti il controllo di dispositivi protesici di mano. Più precisamente, lo scopo del progetto è valutare come diversi tipi di algoritmo possano tradurre l'attività elettromiografica, ottenuta sulla superficie dell'avambraccio, in attività cinematica della mano. Uno scopo aggiuntivo del progetto è realizzare un'interfaccia in grado di tradurre l'attività elettromiografica, ottenuta sulla superficie dell'avambraccio, in attività cinematica della mano in tempo reale. Nel contesto di questo progetto sarà necessario acquisire dati elettromiografici di superficie e cinematici da un campione di soggetti sani.

VALUTAZIONE ETICA:

Il Comitato Etico rileva che il razionale del protocollo n. 97022/2023 è ben articolato e formulato e che il progetto di ricerca in esame non presenta aspetti critici di tipo etico o di tipo tecnico che necessitino di ulteriori approfondimenti.

Tutto ciò considerato, il Comitato approva il Protocollo n. 107460/2023.

La Presidentessa del Comitato Etico per la Ricerca del Politecnico di Torino

(Ing. Augusta Tralli)

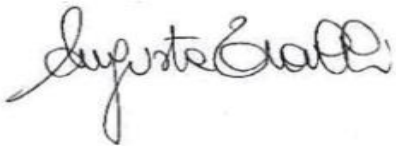

Ethical Evaluation

PREMISES:

The Ethical Committee for Research at the Politecnico di Torino (CER-Polito), based on the competencies established by its own Regulation issued by the Academic Senate on July 3, 2020 (D.R. 622), has examined the request for ethical evaluation of protocol no. 107460/2023 submitted by Prof. Taian, the scientific coordinator of the project "Development of a Signal Processing Technique for the Control of Articulated Hand Prostheses Based on Deep Learning," affiliated with the Department of Electronics and Telecommunications (DET). This request was reviewed by the Ethical Committee during the session on 11/24/2023, following which this evaluation was issued. This protocol is an updated version of the one reviewed in the meeting on 10/27/2023 (no. 86843/2023).

PROJECT DESCRIPTION:

The study aims to improve the living conditions of individuals with upper limb amputations by developing minimally satisfactory control solutions for prosthetic devices. While these devices have achieved performance levels that are almost unquantifiable, capable of replicating or even exceeding the abilities of original limbs, the control solutions are still far from satisfactory. Consequently, the scientific community is in the complicated situation of having sophisticated devices but not a way to control them. This project is part of the search for optimal control strategies and fits within the broader context of the collaboration between the Politecnico di Torino (LISiN) and the University of Oxford (Nuffield Department of Surgical Sciences). The collaboration is centered around the doctoral research of Giovanni Rolandino (University of Oxford), who is broadly evaluating the potential of machine learning for prosthetic control. The data used for this project will be acquired within the broader context of the entire collaboration, and the results obtained will contribute to the overall research. The main objective of the research project is to evaluate the performance of different types of machine learning algorithms in applications related to the control of hand prosthetic devices. More specifically, the project aims to assess how different types of algorithms can translate electromyographic activity, obtained from the surface of the forearm, into hand kinematic activity. An additional goal of the project is to create an interface capable of translating electromyographic activity, obtained from the surface of the forearm, into hand kinematic activity in real time. Within the context of this project, it will be necessary to acquire surface electromyographic and kinematic data from a sample of healthy subjects.

ETHICAL EVALUATION:

The Ethical Committee notes that the rationale of protocol no. 97022/2023 is well articulated and formulated and that the research project under review does not present any ethical or technical critical aspects that require further investigation. Considering all this, the Committee approves Protocol no. 107460/2023.

The President of the Ethical Committee for Research at the Politecnico di Torino *(Dr. Augusta Tralli)*

MEDICAL SCIENCES INTERDIVISIONAL RESEARCH ETHICS COMMITTEE
Research Services, Boundary Brook House, Churchill Drive, Headington, Oxford, OX3 7GB
Tel: +44(0)1865 616575
ethics@medsci.ox.ac.uk

CONFIDENTIAL

Professor James FitzGerald & Giovanni Rolandino
Nuffield Department of Surgical Sciences
University of Oxford
John Radcliffe Hospital
Oxford

7 June 2024

Dear Professor FitzGerald and Giovanni,

Research Ethics Approval - CUREC 1

Ethics Approval Reference: R93729/RE001

Study title: Assessing the Potential of Deep Learning and High-Density Surface Electromyography Signals from Residual Muscles to Restore Hand Movement Control in Tetraplegic Patients

Short title: Restoration of Hand Movement Control Using Deep Learning Applied to surface EMG

The above application has been considered on behalf of the Medical Sciences Interdivisional Research Ethics Committee (MS IDREC) in accordance with the University's procedures for ethical approval of all research involving human participants.

I am pleased to inform you that, on the basis of the information provided to the IDREC, the proposed research has been judged as meeting appropriate ethical standards, and approval has been granted from **7th June 2024** until **6th June 2026.**

Insurance-provided indemnity arrangements are in place for the duration of the approval stated above. It is your responsibility to ensure that you request an extension to the end date for indemnity to remain in place should you continue the research beyond the dates covered.

Amendments

Should there be any subsequent changes to the study, you should submit details to the MS IDREC for consideration and approval. Details of changes must be listed on an amendment form.

Yours Sincerely

DocuSigned by:
Leah Butts
9F14889D2BC549A...

Mrs Leah Butts
Research Ethics Administrator

for
Dr Helen Barnby-Porritt
Research Ethics Manager

NUFFIELD DEPARTMENT OF SURGICAL SCIENCES
Medical Sciences Division
UNIVERSITY OF OXFORD

Confirmation of Authorship

According to divisional and departmental guidance, we confirm that Giovanni Rolandino wrote and produced the material included in the following papers and contributions, with no input or advice from us beyond what is considered appropriate or acceptable for a doctoral thesis:

1) G. Rolandino, M. Gagliardi, T. Martins, G. L. Cerone, B. Andrews and J. J. FitzGerald, “Developing RPC-Net: Leveraging High-Density Electromyography and Machine Learning for Improved Hand Position Estimation,” in *IEEE Transactions on Biomedical Engineering*, vol. 71, no. 5, pp. 1617-1627, May 2024, doi: 10.1109/TBME.2023.3346192.
2) G. Rolandino, C. Zangrandi, T. Vieira, G. L. Cerone, B. Andrews and J. J. FitzGerald, “HDE-Array: Development and Validation of a New Dry Electrode Array Design to Acquire HD-sEMG for Hand Position Estimation”, in *IEEE Transactions on Neural System and Rehabilitation Engineering, vol. 32, pp. 4004-13, 2024, doi: 10.1109/TNSRE.2024.3490796.*
3) G. Rolandino, T. Vieira, G. L. Cerone, B. Andrews, and J. J. FitzGerald, “Performance of a ML-Based 3-DoF Kinematic Model in Estimating Hand Position from High-Density EMG,” presented at the IFESS Conference, Bath, UK, September 2024.
4) G. Rolandino, L. Lion, T. Vieira, I. Havoutis, B. Andrews and J. J. FitzGerald, "Artificial Neural Networks for HD-sEMG-Based Hand Position Estimation: Addressing Inter- and Intra-Subject Variability", submitted to IEEE Transactions on Neural Systems and Rehabilitation Engineering
5) G. Rolandino, G. Parisi, T. Vieira, I. Havoutis, B. Andrews and J. J. FitzGerald, "Real-Time Hand Kinematic Estimation with HD-sEMG and Artificial Neural Networks: Feasibility and Effects of Multi-Subject Training and Visual Feedback", submitted to IEEE Transactions on Neural Systems and Rehabilitation Engineering
6) G. Rolandino, V. Taboni Lisboa, T. Vieira, A. Cliquet Jr., B. Andrews and J. J. FitzGerald, "HD-sEMG-Based Control Using Neck Muscles and Shallow Neural Networks: Assessing Performance in Rehabilitation-Oriented Tasks", submitted to IEEE Transactions on Neural Systems and Rehabilitation Engineering

We also grant him permission to reuse portions or the entirety of the previously mentioned papers or contributions in his DPhil thesis.

Signatures:

Name	Date	Signature
Marco **Gagliardi**	23/07/2025	
Chiara **Zangrandi**	23/07/2025	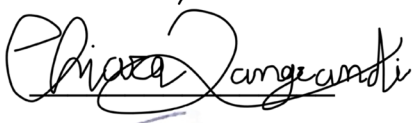
Leonardo **Lion**	23/07/2025	
Giuseppe **Parisi**	23/07/2025	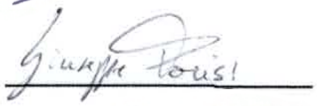
Vinicius **Taboni Lisboa**	23/07/2025	
Taian **Martins Viera**	23/07/2025	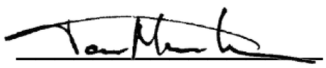
Giacinto Luigi **Cerone**	23/07/2025	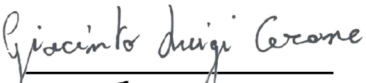
Ioannis **Havoutis**	23/07/2025	
Alberto **Cliquet Jr.**	23/07/2025	
Brian **Andrews**	23/07/2025	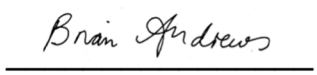
James J. **FitzGerald**	23/07/2025